

9-15-2011

Increasing the Performance of a Sliding Discharge Actuator Through the Application of Multiple Potentials

Steven D. Seney Jr.

Follow this and additional works at: <https://scholar.afit.edu/etd>

Part of the [Aerospace Engineering Commons](#)

Recommended Citation

Seney, Steven D. Jr., "Increasing the Performance of a Sliding Discharge Actuator Through the Application of Multiple Potentials" (2011). *Theses and Dissertations*. 1354.
<https://scholar.afit.edu/etd/1354>

This Thesis is brought to you for free and open access by the Student Graduate Works at AFIT Scholar. It has been accepted for inclusion in Theses and Dissertations by an authorized administrator of AFIT Scholar. For more information, please contact richard.mansfield@afit.edu.



INCREASING THE PERFORMANCE OF A SLIDING
DISCHARGE ACTUATOR
THROUGH THE APPLICATION OF MULTIPLE
POTENTIALS

THESIS

LCDR Steven D Seney Jr, Lieutenant Commander, USN

AFIT/GA/GAE/ENY/11-S01

DEPARTMENT OF THE AIR FORCE
AIR UNIVERSITY

AIR FORCE INSTITUTE OF TECHNOLOGY

Wright-Patterson Air Force Base, Ohio

APPROVED FOR PUBLIC RELEASE; DISTRIBUTION UNLIMITED.

The views expressed in this thesis are those of the author and do not reflect the official policy or position of the United States Air Force, United States Navy, Department of Defense, or the United States Government. This material is declared a work of the U.S. Government and is not subject to copyright protection in the United States.

AFIT/GA/GAE/ENY/11-S01

INCREASING THE PERFORMANCE OF A SLIDING DISCHARGE
ACTUATOR
THROUGH THE APPLICATION OF MULTIPLE POTENTIALS

THESIS

Presented to the Faculty
Department of Aeronautical Engineering
Graduate School of Engineering and Management
Air Force Institute of Technology
Air University
Air Education and Training Command
In Partial Fulfillment of the Requirements for the
Degree of Master of Science in Aeronautical Engineering

LCDR Steven D Seney Jr, BS, MSOM
Lieutenant Commander, USN

September 2011

APPROVED FOR PUBLIC RELEASE; DISTRIBUTION UNLIMITED.

AFIT/GA/GAE/ENY/11-S01

INCREASING THE PERFORMANCE OF A SLIDING DISCHARGE ACTUATOR
THROUGH THE APPLICATION OF MULTIPLE POTENTIALS

LCDR Steven D Seney Jr, BS, MSOM
Lieutenant Commander, USN

Approved:

LtCol Richard E. Huffman, PhD
(Chairman)

Date

Dr. William Bailey (Member)

Date

Dr. Mark Reeder (Member)

Date

Abstract

A comparison between a sliding discharge DBD actuator with grounded and AC biased sliding electrode driven at kHz frequency is presented. The induced velocity in the bulk flow was recorded with PIV and compared for multiple potential splits between two test configurations and a baseline sliding discharge actuator over three test phases. In the first test phase, varying potential splits were examined between the primary and secondary electrode with the sliding electrode grounded. The potential splits yielded a thicker induced jet than the baseline case with similar peak velocities on the order of 1.25 m/s at the 61 mm test point.

The second test phase encompassed an examination of the effects of varying the potentials applied to the primary and sliding discharge electrode with the difference between the electrodes maintained at 15 kV. Induced velocities ranged from a low of 0.17 m/s to a high of 1.87 m/s. The data suggests that the induced velocity is essentially determined by the primary to secondary electrode potential difference.

Phase three examined the effect of applying an AC potential to the sliding discharge electrode 180° out of phase with the AC potential of the primary electrode. The applied potential to the sliding electrode affects the induced jet velocity and morphology. The induced jet decreases in height and the vertical velocity component decreases with an increasing bias on the sliding discharge electrode. Peak jet velocity increases with increasing bias on the sliding electrode until such bias reaches the ionization threshold of the bulk flow. Any further increase in potential results in an induced small secondary wall jet which acts as a boundary layer trip, then steers the jet away from the wall. The highest induced velocity improvement for a 10 kV sliding electrode bias at 41 mm downstream was 22% greater than the baseline case and the induced wall jet thicknesses varied from 21% thicker for the zero bias configurations to 10% thinner than the base case for the 7 kV sliding electrode bias.

Acknowledgements

First and foremost, I owe a large debt of gratitude to my wife. Her support and infinite patience cannot be overstated. Next I would like to thank my advisor, LtCol Richard Huffman, whose guidance and willingness to let me explore the aspects that I found interesting were essential to all I have learned and completed. During my investigations, Dave Liu and Joshua Stults were ever gracious in the donation of their time and efforts to aid in my many trouble shooting efforts and attempts to find a way forward. I would also like to thank my reading committee, Dr. William Bailey and Dr. Mark Reeder, for their patience and grace in guiding me to the answers of my many questions on plasma physics and PIV operations. Thanks to the AFIT model shop who were instrumental in the design and construction of the enclosed test section utilized here. Jay Anderson, John Hixenbaugh, and Christopher Zickefoose were instrumental in the infrastructure and logistics support that was required for this work. Without their never ending support much of this work could not have been completed.

Finally, the author would like to acknowledge the support of AFOSR with contract monitor Dr. John Schmisser for the support of this research. Any opinions, findings and conclusions or recommendations expressed in this materail are those of the author and do not necessarily reflect the views of AFOSR.

LCDR Steven D Seney Jr

Table of Contents

	Page
Abstract	iv
Acknowledgements	v
List of Figures	viii
List of Tables	xv
List of Symbols	xvi
List of Abbreviations	xvii
I. Introduction	1
1.1 Objective	3
1.2 Research Focus	4
II. Background	6
2.1 Atmospheric Plasma	6
2.2 Atmospheric Plasma Discharges	10
2.3 DBD Configurations	15
2.4 DBD Theory of Operation	16
2.5 DBD Research	19
2.6 Plasma Flow Interaction Models	23
2.7 Performance Measurement Techniques	26
2.8 DBD Limitations	28
III. Methodology	31
3.1 Sliding Discharge Actuator Design	31
3.2 Test Potentials	34
3.3 Waveform Generation	38
3.4 Particle Image Velocimetry	39
3.5 Actuator Power	48
3.6 Efficiency Metric	50
3.7 Error Analysis	51
IV. Results	54
4.1 Test Design Selection	55
4.2 Phase I	62
4.3 Phase II	69
4.4 Phase III	75
4.5 Summary	85

	Page
V. Conclusions	87
5.1 Findings Review	87
5.2 Future Work Recommendations	88
Appendix A. Equipment and Settings	91
A.1 Waveform Generation Equipment Settings	91
A.2 Equipment List	92
Appendix B. Data Compendium	93
B.1 Design of Experiment	94
B.2 Phase I	102
B.3 Phase II	131
B.4 Phase III	154
Appendix C. Matlab Code	183
C.1 Vector Continuity Check	183
Bibliography	186
Vita	190

List of Figures

Figure		Page
1.1	Single DBD Configuration for Flow Control	2
1.2	Finger Arrayed DBD Actuators	3
1.3	Three Electrode Sliding Discharge Actuator	4
2.1	Plasma Classifications	8
2.2	Paschen Curve for Air	12
2.3	Streamer to Filament Progression	12
2.4	DBD Discharge	14
2.5	Volumetric Versus Surface DBD Configurations	15
2.6	Surface DBD Electrode Configurations	17
2.7	Electron Flow During Discharge	19
2.8	Sliding Discharge Actuator Plasma Discharge At Saturation Potential	21
2.9	Surface Potential vs Time and Longitudinal Distance	23
2.10	Boundary Layer Profile	30
3.1	Test Actuator	31
3.2	Actuator After 1 Billion Cycles	32
3.3	Dielectric Failure	33
3.4	Adjustable Test Stand	34
3.5	Actuator Wiring Schematic	37
3.6	Function Generator and Amplifier	39
3.7	CMI 5530 Transformer	40
3.8	Lexan Test Section	40
3.9	TSI Model 9306 Atomizer	41
3.10	Plasma Discharge Detected By PIV	41
3.11	Laser and Camera Setup	42
3.12	Sample Focus Image	43
3.13	Flow Map System Hub and Test Setup Schematic	44

Figure		Page
3.14	Matlab Continuity Check Example	45
3.15	Wall Jet Build Profile	47
3.16	Power Measurement Equipment	49
3.17	Sample Voltage and Current Readings	50
4.1	Velocity Measurement coordinate System	54
4.2	12 kV SDBD and Sliding Discharge Induced Wall Jet Vector Contours	56
4.3	12 kV SDBD and Sliding Discharge Induced Wall Jet Profiles . . .	57
4.4	12 kV SDBD and Sliding Discharge Induced Wall Jet Profiles . . .	58
4.5	Large Gap Versus Small Gap Vertical Wall Jet Velocity Profiles . .	59
4.6	Vertical Wall Jet Velocity Versus Phase	60
4.7	Encapsulated Electrode Width Comparisons	61
4.8	Phase I Velocity Contour Map Results	63
4.9	Phase I Normalized Velocity Profiles. 61 mm Test Point	65
4.10	Phase I Normalized Efficiency Profiles. 61 mm Test Point.	66
4.11	Phase I Plasma Discharges	67
4.12	Phase I Plasma Discharge Photographs	68
4.13	Phase I Plasma Induced Boundary Layer Trip	68
4.14	Case 7 Vector Contour Map	69
4.15	Case 8 Vector Contour Map	69
4.16	Case 9 Vector Contour Map	70
4.17	Case 10 Vector Contour Map	70
4.18	Case 11 Vector Contour Map	70
4.19	Phase II Normalized Velocity Profiles. 61 mm Test Point.	71
4.20	Phase II Normalized Efficiency Profiles. 61 mm Test Point.	73
4.21	Case 9 Plasma Secondary Discharge	74
4.22	Phase II Plasma Discharge Photographs	74
4.23	Case 12 Velocity Contour Map Results	75
4.24	Case 13 Velocity Contour Map Results	76

Figure		Page
4.25	Case 14 Velocity Contour Map Results	76
4.26	Case 15 Velocity Contour Map Results	76
4.27	Case 16 Velocity Contour Map Results	77
4.28	Case 17 Velocity Contour Map Results	77
4.29	Case 18 Velocity Contour Map Results	77
4.30	Phase III Normalized Velocity Profiles. 61 mm Test Point	78
4.31	Phase III Velocity Components	80
4.32	Phase III Normalized Efficiency Profiles. 61 mm Test Point	81
4.33	Phase III Boundary Layer Profiles	82
4.34	Phase III Plasma Discharge Lengths	83
4.35	Vertical Wall Jet	84
4.36	Phase Comparison: 31 and 61 mm Test Points	86
B.1	Sliding Discharge Versus Standard DBD Wall Jet Profile. 0° Starting Phase Angle.	94
B.2	Sliding Discharge Versus Standard DBD Wall Jet Profile. 90° Start- ing Phase Angle.	95
B.3	Sliding Discharge Versus Standard DBD Wall Jet Profile. 180° Start- ing Phase Angle.	95
B.4	12 kV SDBD Velocity Vector and Contour Maps	96
B.5	12 kV Sliding Discharge Actuator Velocity Vector and Contour Maps	97
B.6	Case A Sliding Discharge Actuator: Waveform Velocity Contour Plots	98
B.7	Case B Sliding Discharge Actuator: Waveform Velocity Contour Plots	99
B.8	Vertical Wall Jet Velocity Profile Comparisons	100
B.9	Case A Vertical Wall Jet Velocity Contours and Vectors	101
B.10	Case B Vertical Wall Jet Velocity Contours and Vectors	101
B.11	Phase I Velocity Profiles: 31 mm Point	102
B.12	Phase I Velocity Profiles: 41 mm Point	103
B.13	Phase I Velocity Profiles: 51 mm Point	104
B.14	Phase I Velocity Profiles: 61 mm Point	105

Figure		Page
B.15	Phase I Efficiency Profiles: 31 mm Point	106
B.16	Phase I Efficiency Profiles: 41 mm Point	107
B.17	Phase I Efficiency Profiles: 51 mm Point	108
B.18	Phase I Efficiency Profiles: 61 mm Point	109
B.19	Baseline Case: U vs Height	110
B.20	Baseline Case: Discharge Plume	110
B.21	Baseline Case: Velocity Vectors and Components	111
B.22	Baseline Case: Turbulent Intensity	112
B.23	Case 1: U vs Height	113
B.24	Case 1: Discharge Plume	113
B.25	Case 1: Velocity Vectors and Components	114
B.26	Case 1: Turbulent Intensity	115
B.27	Case 2: U vs Height	116
B.28	Case 2: Discharge Plume	116
B.29	Case 2: Velocity Vectors and Components	117
B.30	Case 2: Turbulent Intensity	118
B.31	Case 3: U vs Height	119
B.32	Case 3: Discharge Plume	119
B.33	Case 3: Velocity Vectors and Components	120
B.34	Case 3: Turbulent Intensity	121
B.35	Case 4: U vs Height	122
B.36	Case 4: Discharge Plume	122
B.37	Case 4: Velocity Vectors and Components	123
B.38	Case 4: Turbulent Intensity	124
B.39	Case 5: U vs Height	125
B.40	Case 5: Discharge Plume	125
B.41	Case 5: Velocity Vectors and Components	126
B.42	Case 5: Turbulent Intensity	127

Figure		Page
B.43	Case 6: U vs Height	128
B.44	Case 6: Discharge Plume	128
B.45	Case 6: Velocity Vectors and Components	129
B.46	Case 6: Turbulent Intensity	130
B.47	Phase II Velocity Profiles: 31 mm Point	131
B.48	Phase II Velocity Profiles: 41 mm Point	132
B.49	Phase II Velocity Profiles: 51 mm Point	133
B.50	Phase II Velocity Profiles: 61 mm Point	134
B.51	Phase II Efficiency Profiles: 31 mm Point	135
B.52	Phase II Efficiency Profiles: 41 mm Point	136
B.53	Phase II Efficiency Profiles: 51 mm Point	137
B.54	Phase II Efficiency Profiles: 61 mm Point	138
B.55	Case 7: U vs Height	139
B.56	Case 7: Discharge Plume	139
B.57	Case 7: Velocity Vectors and Components	140
B.58	Case 7: Turbulent Intensity	141
B.59	Case 8: U vs Height	142
B.60	Case 8: Discharge Plume	142
B.61	Case 8: Velocity Vectors and Components	143
B.62	Case 8: Turbulent Intensity	144
B.63	Case 9: U vs Height	145
B.64	Case 9: Discharge Plume	145
B.65	Case 9: Velocity Vectors and Components	146
B.66	Case 9: Turbulent Intensity	147
B.67	Case 10: U vs Height	148
B.68	Case 10: Discharge Plume	148
B.69	Case 10: Velocity Vectors and Components	149
B.70	Case 10: Turbulent Intensity	150

Figure		Page
B.71	Case 11: U vs Height	151
B.72	Case 11: Discharge Plume	151
B.73	Case 11: Velocity Vectors and Components	152
B.74	Case 11: Turbulent Intensity	153
B.75	Phase III Velocity Profiles: 31 mm Point	154
B.76	Phase III Velocity Profiles: 41 mm Point	155
B.77	Phase III Velocity Profiles: 51 mm Point	156
B.78	Phase III Velocity Profiles: 61 mm Point	157
B.79	Phase III Efficiency Profiles: 31 mm Point	158
B.80	Phase III Efficiency Profiles: 41 mm Point	159
B.81	Phase III Efficiency Profiles: 51 mm Point	160
B.82	Phase III Efficiency Profiles: 61 mm Point	161
B.83	Case 12: U vs Height	162
B.84	Case 12: Discharge Plume	162
B.85	Case 12: Velocity Vectors and Components	163
B.86	Case 12: Turbulent Intensity	164
B.87	Case 13: U vs Height	165
B.88	Case 13: Discharge Plume	165
B.89	Case 13: Velocity Vectors and Components	166
B.90	Case 13: Turbulent Intensity	167
B.91	Case 14: U vs Height	168
B.92	Case 14: Discharge Plume	168
B.93	Case 14: Velocity Vectors and Components	169
B.94	Case 14: Turbulent Intensity	170
B.95	Case 15: U vs Height	171
B.96	Case 15: Discharge Plume	171
B.97	Case 15: Velocity Vectors and Components	172
B.98	Case 15: Turbulent Intensity	173

Figure		Page
B.99	Case 16: U vs Height	174
B.100	Case 16: Discharge Plume	174
B.101	Case 16: Velocity Vectors and Components	175
B.102	Case 16: Turbulent Intensity	176
B.103	Case 17: U vs Height	177
B.104	Case 17: Discharge Plume	177
B.105	Case 17: Velocity Vectors and Components	178
B.106	Case 17: Turbulent Intensity	179
B.107	Case 18: U vs Height	180
B.108	Case 18: Discharge Plume	180
B.109	Case 18: Velocity Vectors and Components	181
B.110	Case 18: Turbulent Intensity	182

List of Tables

Table		Page
2.1	Ionization Energy for Selected Atoms and Molecules	7
2.2	Electron Affinity For Selected Atoms and Molecules	9
2.3	DBD Operating Parameters	19
2.4	Boundary Layer Thicknesses	30
3.1	Test Phases	36
3.2	Dantec Dynamics PIV Software Settings	46
4.1	Encapsulated Electrode Width and Potential Split Comparison . .	58
4.2	Phase I Jet Heights	64
4.3	Phase I Jet Peak Velocities	64
4.4	Phase I Power Consumption Results	65
4.5	Phase II Jet Peak Velocities	71
4.6	Phase II Jet Heights	72
4.7	Phase II Power Consumption Results	72
4.8	Phase III Jet Peak Velocities	78
4.9	Phase III Jet Heights	79
4.10	Phase III Power Consumption Results	81
A.1	Test Equipment Settings: Function Generators	91
A.2	Test Equipment	92

List of Symbols

Symbol		Page
M	Mach Number	2
e	Electron Charge	7
m_e	Electron Mass	7
n_e	Electron Density	7
α_i	Degree of Ionization	7
n_n	Neutral Density	7
T_i	Ion Temperature	9
T_0	Neutral Gas Temperature	9
EA	Electron Affinity	9
α	Townsend ionization coefficient	10
γ	Secondary Emission Coefficient	11
V_{br}	Breakdown Voltage	11
\mathbf{f}_i	Collisional Body Force, Electron Neutral	24
\mathbf{f}_e	Collisional Body Force, Ion Neutral	24
n_s	Specie Number Density	24
ν_{sm}	Momentum Transfer Collision Frequency	24
μ_s	Particle Mobility	24
j_s	Specie Current Density	24
D_s	Specie Diffusion Coefficient	25
ρ_c	Plasma Charge Density	26
$u_{x,std}$	Horizontal Velocity Component Standard Deviation	51
$u_{y,std}$	Vertical Velocity Component Standard Deviation	51

List of Abbreviations

Abbreviation		Page
DBD	Dielectric Barrier Discharge	1
SDBD	Single Dielectric Barrier Discharge	2
DC	Direct Current	16
AC	Alternating Current	16
PIV	Particle Image Velocimetry	27

INCREASING THE PERFORMANCE OF A SLIDING DISCHARGE ACTUATOR THROUGH THE APPLICATION OF MULTIPLE POTENTIALS

I. Introduction

With aircraft performance continuing to improve and UAV's operating in low Reynolds number environments being developed, a need has emerged for better methods of flow control for stall avoidance, recovery, and aircraft maneuvering. The current generation of flow control and generation devices such as suction and blowing devices are impractical due to the eventual clogging of the small diameter tubes involved, and leading edge slats increase the aircraft's drag profile and have demonstrated a tendency to cause undesirable vibrations [1], and ailerons and other control surfaces utilize heavy mechanical mechanisms. Over the last decade, interest in the atmospheric plasma created by dielectric barrier discharges (DBD) has grown tremendously due to the DBD's ability to maintain its discharge at atmospheric pressures while not progressing into an arc discharge [2,3]. Research has demonstrated the ability of this discharge to energize, accelerate, and reattach separated fluid flows [2–16]. DBD actuators have the advantages over other flow control devices of having no moving parts, capable of being flush mounted into an airfoil, able to operate at very high frequencies and having a very low power requirement on the order of 60 - 120 W/linear meter of array [1,2,7,17].

The plasma created from a DBD actuator is a non-thermal plasma that is stable at atmospheric pressures [2,17] and has been used in commercial applications for the generation of ozone since 1857 [1,2,17,18]. Significant amounts of research are currently being conducted on DBD's for flow control due to the simplicity of their design, lack of moving parts, ability to be operated at atmospheric pressures under non-equilibrium conditions, and their ability to both impart momentum and excite

instabilities in the surrounding flow fields [2, 10, 18]. The standard DBD configuration, as shown in Figure 1.1, consists of a dielectric material interposed between two electrodes that are powered by either a high voltage, high frequency AC potential or by DC nanopulses. The dielectric material that separates the electrodes both precludes pure DC operation [19] and prevents the discharge from producing a spark and transitioning from a filamentary cascade into an arc discharge.

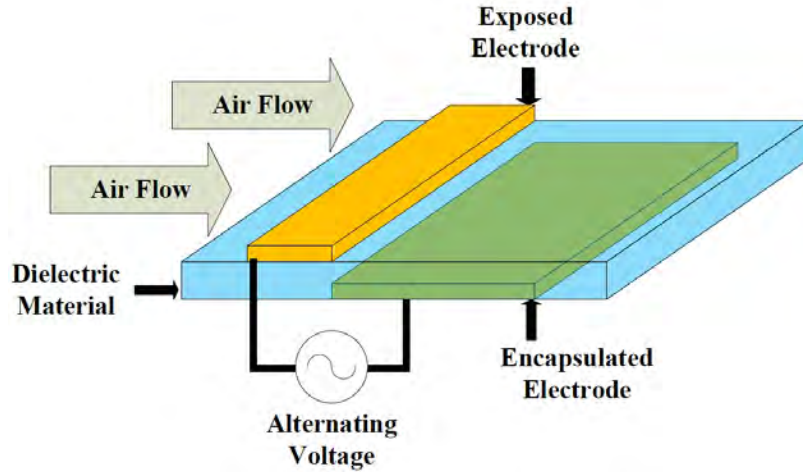


Figure 1.1: Single DBD configuration for flow control

But, the short length and shallow depth of the plasma discharge coupled with the small relative velocity imparted during the discharge limit the actuators effectiveness at higher Mach Numbers, M [1, 2, 17]. The relatively small body force and the experimentally demonstrated induced velocities of only up to 10 m/s [6, 17, 20] produced by the single DBD (SDBD) actuator are very low in comparison to the dynamic pressures of the flow at Mach numbers above 0.2 [21]. With SDBD discharges having discharge lengths of less than 35 mm [1, 2, 17], it is vital to have them precisely located at the point of boundary layer separation, the stagnation line, or in a span wise array designed to create vortices across a wider swath of the airfoil surface similar to that tested by Poggie et. al as shown in Figure 1.2 [22].

Sliding discharge actuators, DBD arrays (both standard and finger arrays), and three electrode configurations negate some of these concerns. Sliding discharges and three electrode actuators can create sliding surface sparks that can cover linear dis-



Figure 1.2: Chordwise arrayed DBD actuators increase the span wise effective area of the DBD plasma. From Poggie et. al. [22]

tances of up to 1 m [19] and create a longer more homogeneous plasma than the standard DBD actuator for the same input power and waveform [23]. Sliding discharges, depending on electrode configuration also deliver a higher induced velocity and thrust [24]. Arrays of SDBD's or of sliding discharges can also be constructed to cover the entire airfoil span in question, offering actuation across the entire airfoil generating coverage for a wider range of stagnation lines. This enables excitation of stagnation points across the entire airfoil and not just a 3-5 cm span.

1.1 Objective

For DBD actuators to become viable flow control devices the performance envelope must be broadened. A sliding discharge actuator, as seen in Figure 1.3, consists of the standard DBD actuator but with a third exposed electrode that is normally grounded. The sliding discharge actuator produces a more homogeneous plasma with a higher induced velocity than the SDBD for similar power consumption. But, sliding discharge actuators plasma discharge lengths are limited and display very shallow induced wall jets. While the sliding discharge design overcomes many of the SDBD's failings, research needs to be done to maximize its ionic wind, thrust output, and efficiency.

The goal of this research was to quantify the improvement in the performance of a sliding discharge actuator operating under multiple potential splits. To investigate how the third electrode affects the induced velocity caused by the potential difference between the primary and secondary electrodes, split potentials were applied to the

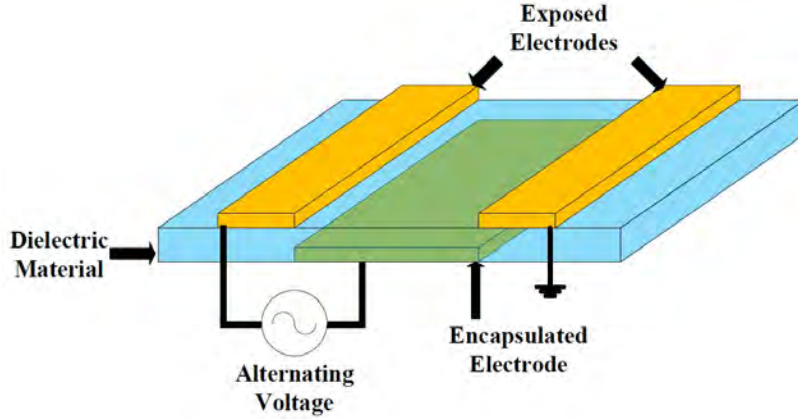


Figure 1.3: Three electrode sliding discharge actuator on a silica glass dielectric.

electrodes of a silica glass based sliding discharge DBD actuator with the sliding discharge electrode grounded. The effects of the application of an AC potential applied to the third electrode in order to maximize actuator efficiency and peak performance were then examined. The induced velocity profiles of all test cases measured were compared to that of a standard 15 kV potential powered sliding discharge actuator in terms of both magnitude and efficiency in terms of induced flow versus consumed power. Finally, a potential split method that offers performance improvements in terms of both peak induced velocity and efficiency over the standard sliding discharge actuator was finally developed. The final potential scheme examined delivered an actuator that was throttlable and capable of inducing a steerable wall jet. This allows the three potential actuator to be used as a stall control device energizing the flow to reattach separated boundary layers, as a flight control device similar to a spoiler, and as a blower with a steerable jet.

1.2 Research Focus

For this research a 15 kV primary AC potential powered sliding discharge actuator constructed upon a 1.8 mm thick silica glass dielectric was utilized. A dual pulsed Nd:YAG laser PIV system and a 4 megapixel CCD camera with a field of regard of 85 mm by 85 mm was used to record the induced flow fields. Varying potentials and

biases between the three electrodes were tested to develop performance curves on each test potential. The examination was conducted over three distinct phases. In Phase I, the effects of splitting the 15 kV primary to secondary potential between the primary and secondary electrodes were examined. In Phase II, the effects of splitting a 15 kV potential between the primary to sliding discharge electrode were examined utilizing potential splits similar to those found in Phase I. After Phase II, a comparison was conducted on the performance results for the first 11 test cases. The data suggested that a primary to secondary electrode potential split of 13 - 2 kV would be the optimum case for Phase III. In Phase III, the selected potential was modified by adding a third potential to the sliding discharge electrode in an attempt to further accelerate the bulk flow. Finally, an examination was conducted on the performance metrics of induced flow magnitude, longevity, and power consumption.

Chapter 2 of this work entails a review of the physics of DBD operations and prior research conducted on the mechanisms of momentum coupling by AC actuated DBD actuators. Chapter 3 discusses the final actuator design and the methodology used to test the actuator. In Chapter 4 the results from the experimental design and the three final test phases are presented and analyzed. Finally, Chapter 5 contains the overall conclusions and lessons learned and proposes a road map forward for future research.

II. Background

This section begins with a review of plasma basics as they apply to DBD actuators. A review of plasmas generated at from air at pressures near one atmosphere and the types of discharge that pertain to DBD's is presented. DBD actuator types, construction, and prior research are then examined. A simplified model is then developed to gain a better understanding of DBD operations. Finally, DBD limitations and measurement techniques are reviewed.

2.1 Atmospheric Plasma

Plasma is the state of matter that is comprised of electrically charged, gaseous particles. Ionization, the process of plasma formulation, occurs when a neutral molecule or atom is split into an electron and positive ion pair or when an electron attaches to the neutral molecule forming a negative ion. The separation of an electron from a neutral molecule is caused when energy in excess of that molecule's ionization energy is applied. This can be accomplished in several ways such as through the application of an electromagnetic field of sufficient strength, addition of large amounts of thermal energy, or photon bombardment [17, 19]. In the case of DBD actuators, ionization is most often achieved through the application of a high potential electric field. Free electrons, either present in the neutral gas or seeded by a charged electrode, are then accelerated by the electric field. The high velocity electrons then collide with molecules in the air above the actuator. If the collisional energy is greater than the required ionization energy, ions are created. The required ionization energies of selected gas species are found in Table 2.1. For atmospheric plasma, the four most important species are nitrogen, oxygen, carbon dioxide, and water vapor. Of the major components of air, water has one of the lowest ionization energies and is among the first particles to ionize leading to the formation of H_2O^+ and OH^- , explaining the high acidity and oxidative ability of air and why DBD's tend to have very limited duty life cycles before the exposed electrodes begins to decay [2, 17, 19].

Table 2.1: Ionization Energy for Selected Atoms and Molecules [19]

Gas	Ionization Energy	Gas	Ionization Energy
$e+N_2=N_2^++e+e$	$I = 15.6 \text{ eV}$	$e+CO_2=CO_2^++e+e$	$I = 13.8 \text{ eV}$
$e+H_2O=H_2O^++e+e$	$I = 12.6 \text{ eV}$	$e+O_2=O_2^++e+e$	$I = 12.2 \text{ eV}$

DBD generated plasma consists of a mixtures of four types of particles: electrons, positive ions, negative ions, and neutral particles. Electrons are the elementary negative particle found in plasma. Their charge is the elementary one electron charge, $e = -1.6 \cdot 10^{-19} \text{ C}$, and have a mass, m_e , of $m_e = 9.11 \cdot 10^{-31} \text{ kg}$. This low mass, combined with a relatively large charge to mass ratio, in comparison to heavier charged particles, gives the electron a high mobility and results in it being the first type of particle to react to external electromagnetic fields. Through their movement, electrons will initiate ionization, dissociation and recombination through interactions with the other plasma particle species. The rates of these interactions are dependent upon the electron density, distribution, and average energy level. The electron distribution in plasma is often highly dependent upon the strength and layout of the electric field.

Due to the fundamental role of electrons in plasma interactions, plasmas are often classified by their electron densities, n_e [17,19,25], and their degree of ionization, α_i :

$$\alpha_i = \frac{n_e}{n_e + n_n} \quad (2.1)$$

Where n_n is the neutral density. Figure 2.1 illustrates where various types of plasmas fall in terms of electron density and temperature. If $\alpha_i > 10^{-3}$, the plasma is considered fully ionized. If $\alpha_i < 10^{-3}$ then the plasma is considered weakly ionized, often called a cold plasma [17]. Pavon and Fridman [17,19] note that weakly ionized plasmas are then furthered categorized by the relative thermodynamic states of their species. In a plasma that is in thermal equilibrium, also known as thermal plasmas, the temperature of the species are all approximately equal. In a non-thermal, or non-

equilibrium plasma, the electron temperatures exceed that of the neutral particles, positive ions, and negative ions: $T_e > T_i \approx T_n$ [17, 19]. DBD discharges are of the weakly ionized, non-thermal variety with $T_e \approx 10$ eV [17, 19].

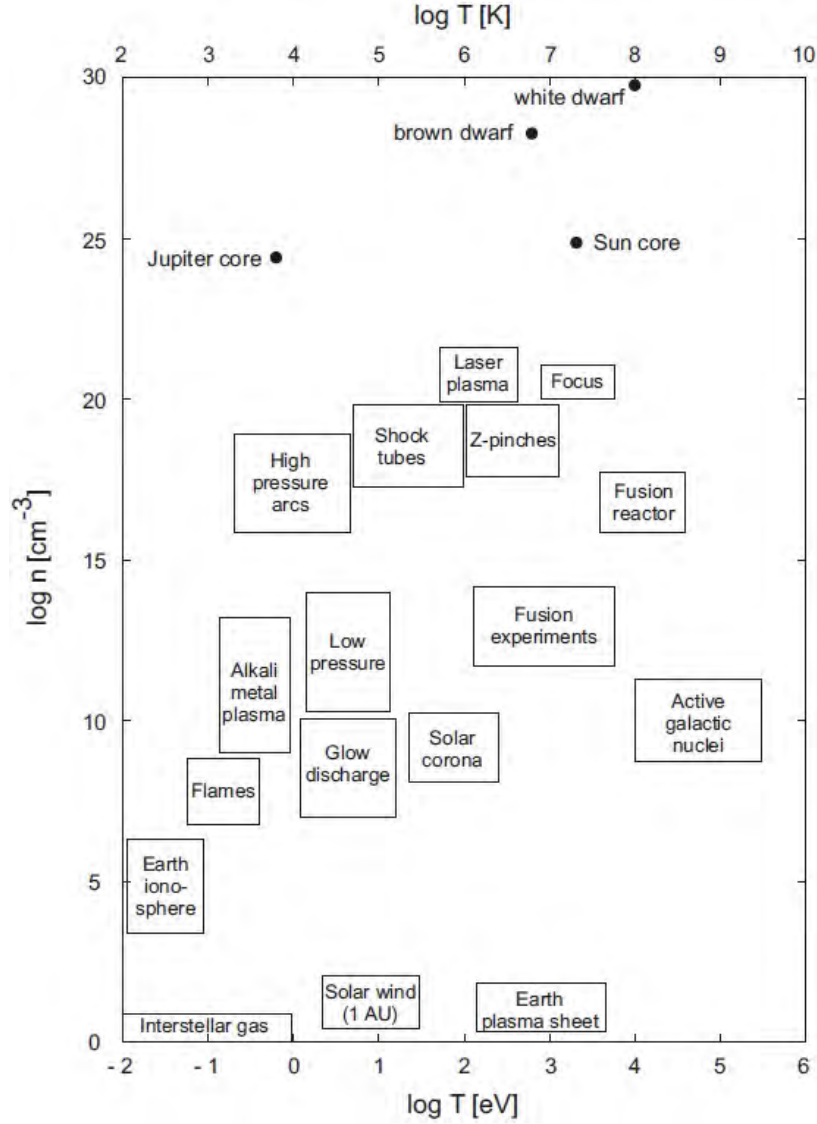


Figure 2.1: Classifications of different types of plasmas [25].

When an electron collides with a molecule with enough energy to cause ionization, the collision most often results in the formation of a positive ion, such as: $e + N_2 = N_2^+ + e + e$. In non-thermal, quasi-neutral plasmas of DBD's, positive ions are most often singly ionized and have a charge of $1.6 \cdot 10^{-19}$ C, the positive equivalent

charge of losing one electron. Positive ions are heavy particles, in comparison with electrons, and are not accelerated as quickly by external electromagnetic fields. Positive ion velocities are furthered slowed by the collisional energy lost during elastic collisions with the other plasma particles. In a non-thermal plasma, the nature of these collisions results in an ion temperature, T_i , close the to the neutral gas temperature, T_0 [19].

Some gases, after undergoing a molecule-electron collision do not release an extra electron and form positive ions, but instead absorb the electron and form negative ions: $e + O_2 = O_2^-$. These gases, such as O_2 , Cl_2 , SF_6 and $TiCl_4$, are referred to as “electronegative gases.” Singly charged negative ions formed in this process are heavy charged particles with a charge of $-1.6 \cdot 10^{-19}$ C. A molecule’s affinity to absorb an electron is called its electron affinity, EA ; the binding energies for some common gases are listed in Table 2.2. As can be seen in Table 2.2, the most prevalent atmospheric “electronegative gases” is O_2 , comprising approximately 21% of the atmosphere at sea level. Experimental results have shown that the presence of oxygen, and the negative ions produced from it, does not degrade actuator performance in terms of momentum coupling and thrust generation at 1 atm of pressure, and improves the actuator’s performance at lower pressures [4]. It has also been suggested that the presence of the negative oxygen ions is one of the main factors in the disparities observed between the induced velocities and imparted momentums of the positive exposed electrode and negative exposed electrode parts of the DBD cycle [26].

Table 2.2: Electron Affinity For Selected Atoms and Molecules

Gas	Electron Affinity	Gas	Electron Affinity
$O_2^- + e$	0.44 eV	$CH_2^- + e$	16.2 eV
$OH^- + e$	1.8 eV	$O_3^- + e$	2.0 eV
$Cl_2^- + e$	2.4 eV	$NO_3^- + e$	4.9 eV

2.2 Atmospheric Plasma Discharges

When the electric field reaches a potential in excess of the breakdown voltage of the surrounding gas, a breakdown occurs and the plasma discharge is then initiated [2]. The breakdown voltage is dependent upon the composition of the surrounding gas, the electrode design of the actuator, the distance between the electrodes, and the type of current [2, 4, 17]. Pavon [17] lists four main categories of stable plasma discharges:

- Dark Townsend Discharge
- Glow Discharges
- Corona Discharges
- Arc Discharges

and three processes that can initiate/sustain the discharge at atmospheric pressures [17]:

- Townsend Breakdown
- Streamer Breakdown
- Spark Breakdown

with Townsend and Streamer breakdowns being relevant to DBD actuators discharges, which are usually composed of micro-filaments at atmospheric pressures [3, 17].

In a Townsend breakdown, an electric field is created between two electrodes separated by a distance, d . Electrons located in this gap between the electrodes, either naturally occurring or intentionally seeded, are accelerated by the electric field, traveling from the cathode to the anode. If the electric field is of sufficient magnitude, the electrons will have sufficient energy to ionize some of the gas particles through inelastic collisions, causing the formation of ions in the gap. The ions impacting the cathode cause the secondary release of additional electrons. It is this secondary release that sustains the Townsend breakdown [17, 19]. The degree of ionization caused by the electron motion is given by the Townsend ionization coefficient α :

$$\alpha = \frac{1}{n_e} \frac{dn_e}{dx} \quad (2.2)$$

Where $n_e(x) = n_{e0}e^{\alpha x}$. If x is assumed to be the gap length, d , between the electrodes, and electronegative gases and recombination factors are ignored, this results in the formation of $e^{\alpha d} - 1$ positive ions in the gap between electrodes. Upon impact the positive ions cause the release of $\gamma [e^{\alpha d} - 1]$ electrons, where γ , the secondary emission coefficient, is dependent upon the electrode material, smoothness, the electric field, and the type of gas being ionized. For a breakdown at a given voltage, $V \geq V_{br}$, to be self-sustaining, $\gamma [e^{\alpha d} - 1] > 1$ [17, 19].

The minimum breakdown voltage, V_{br} for this type of discharge depends upon the type of gas, the pressure, electrode material, humidity, frequency of the applied voltage and the distance between electrodes [17, 19]. The Paschen curve, named for Frierdrich Paschen who studied the breakdown voltage of parallel plates in a gas [17], showing the breakdown voltages for for air in terms of pd , is shown in Figure 2.2. This curve follows the form of:

$$V_{br} = \frac{B * pd}{\ln(A) - \ln(\ln(1/\gamma) + 1) + \ln(pd)} \quad (2.3)$$

with A and B being gas dependent constants and γ being the secondary emission coefficient of the electrode material. For the actuator under examination, the breakdown voltage for a discharge to form between the two exposed electrodes at one atmosphere is on the order of 70 kV. But as can be seen in Figure 2.2, as the gap width is maintained constant and the pressure is dropped to 200 Torr, equivalent to a flight altitude of approximately 30,000 feet, the voltage necessary for a discharge between the exposed electrodes decreases to on the order of 20 kV. This decrease in breakdown voltage can be seen in the lengthening discharge plumes observed for DBDs tested at lower pressures. The lower breakdown voltage also drives the maximum potential split between the two exposed electrodes in the tested actuator.

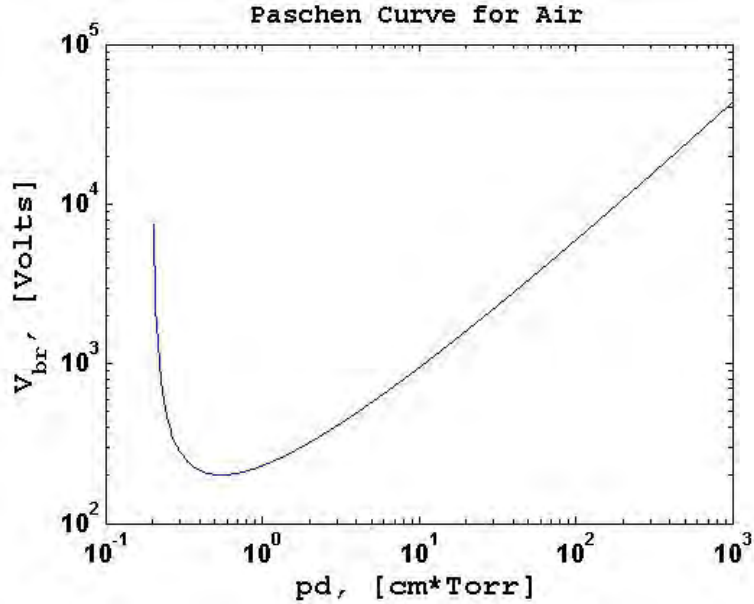


Figure 2.2: Paschen Curve For Air with $A = 15$, $B = 365$, and $\gamma = 0.15$. Adapted from Fridman and Kennedy [19].

As the voltage is increased beyond the minimum breakdown voltage for a given $p * d$, humidity, and gas type, the breakdown progresses from a Townsend breakdown to a streamer breakdown. This progression to a streamer is caused by a build up of the local surface charge due to the electron avalanche [17]. Pavon [17] describes the streamer to filament progression as a series of three steps as shown in Figure 2.3:

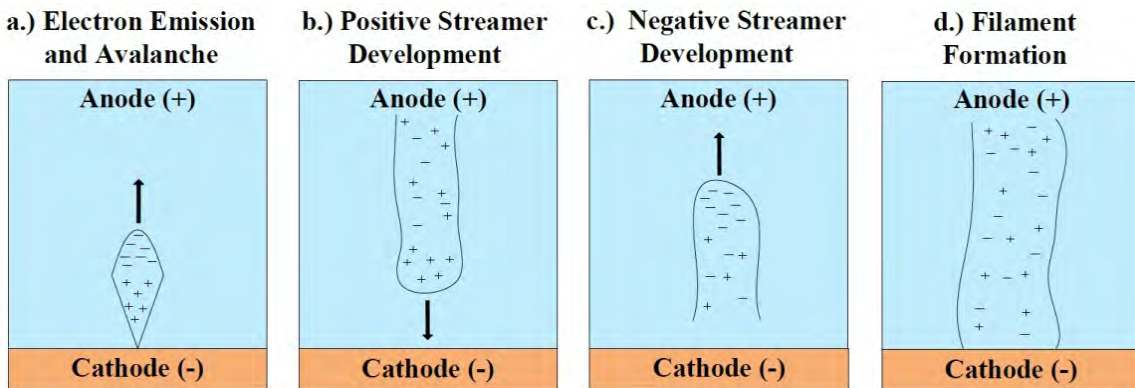


Figure 2.3: Electron Avalanche to filament development. Adapted from Pavon [17]

- Electron Avalanche to Streamer: As the electrons accelerate away from the cathode they ionize the neutral particles in their path creating an electron avalanche

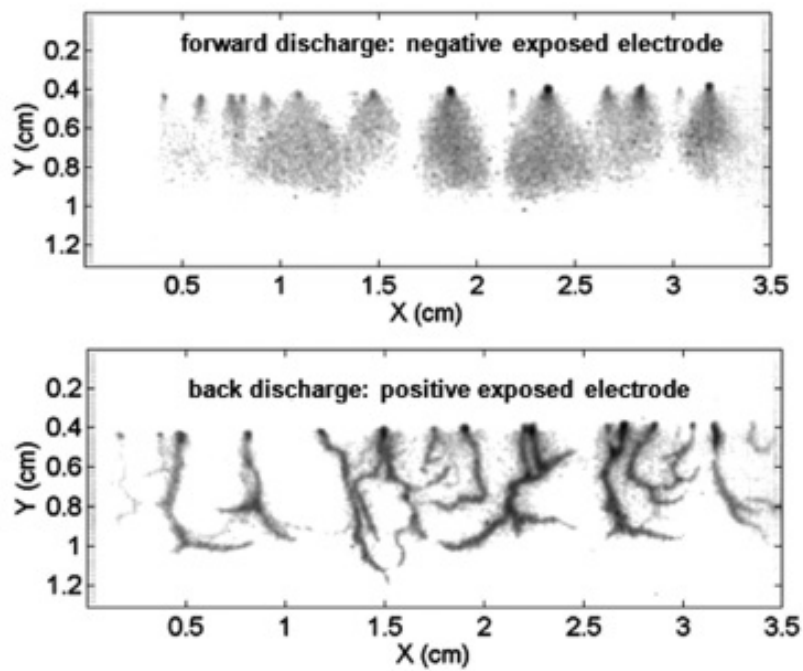
and form a localized electric field in their wake. When this localized electric field becomes stronger than the external electric field, a weakly ionized region will develop and initiate a streamer as seen in Figure 2.3 (a) [17].

- **Streamer Propagation:** The streamer, once formed, then propagates towards the cathode. For small to moderate gaps and voltages, the streamer will propagate from the anode to the cathode after the electron avalanche has reached the anode as shown in Figure 2.3 (b). For larger gaps and overvoltages, the streamer will develop before the electron avalanche has reached the anode and then will propagate towards both the cathode and the anode; see Figure 2.3 (c) [17].
- **Filament Stage:** The breakdown stage ends once the streamer connects the two electrodes. Filaments, or ionized plasma channels, then form to bridge the gap between the two electrodes. The filaments then balance out and negate the localized electric field caused by the electron avalanche. The dielectric in DBD's prevent a filament to arc progression and cause the self-limiting nature of the DBD discharge. Figure 2.3 (d) [17]. In DBD's, if the amplitude of external electric field is not continually increased, the deposition of the charges on the dielectric forms a virtual electrode negating the potential difference between the anode and cathode and causing the discharge to quench.

To the naked eye, SDBD discharges, in surface configuration, appear to exhibit a diffuse glow discharge as seen in Figure 2.4. But, the nature of the discharge actually varies across the plasma period. During the negative exposed electrode cycle and a strong filamentary discharge during the positive exposed electrode part of the cycle [2, 3, 17] as can be seen in Figure 2.4 (b). Orlov, Font, and Edelstein [3] concluded that the different discharge natures between the positive and negative exposed electrode parts of the cycle are due to the negative charge build up on the dielectric surface during the negative exposed electrode part of the cycle and the overall downstream (greater than 5 mm in their set up) positive surface charge on the actuator.



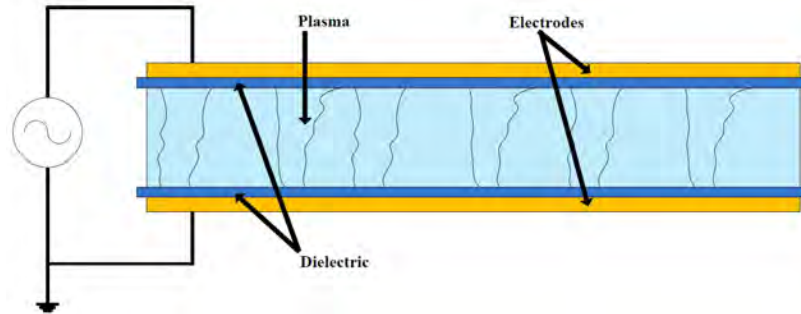
(a) Glow discharge as seen with a 30 Hz shutter speed for a 15 kV potential DBD.



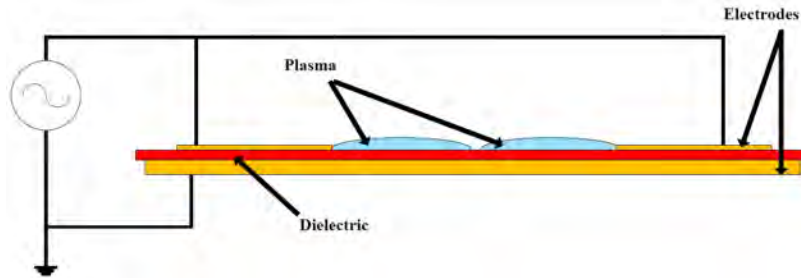
(b) High speed photography shot illustrating the differing nature of the discharge between the positive and negative periods. Taken from Orlov, Font, and Edelstein [3].

Figure 2.4: Full period discharge and half cycle discharge.

2.3 DBD Configurations



(a) Volumetric Discharge Configuration



(b) Surface Discharge Configuration

Figure 2.5: Volumetric Versus Surface DBD Configurations

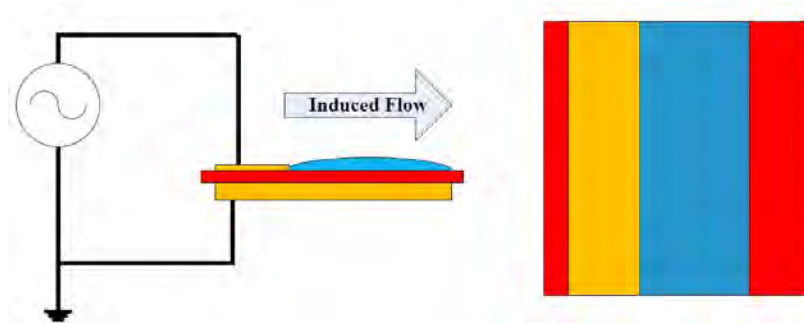
The DBD actuator normally consists of electrodes separated by a dielectric barrier. The electrodes vary from wire to metallic meshes and are normally flat metal plates that are either glued, printed, or electroplated onto the dielectric surface. The dielectric can be any non conductive material that prohibits the breakdown from progressing from a glow discharge to an arc discharge. DBD actuators have two main configurations, volumetric discharge configurations and the surface discharge configurations. While the volumetric discharge configuration has been the most studied [17], the surface discharge configuration is the most commonly used for aerospace applications. Figure 2.5 illustrates the differences between the two types of discharges.

Surface DBD actuators can then be further categorized by their electrode configuration and geometry. The asymmetric electrode configuration, as shown in Figure 2.6 (a), is the standard DBD actuator that is used for thrust and ionic wind creation. Ionic wind can be defined as the flow induced by the acceleration of charged ions

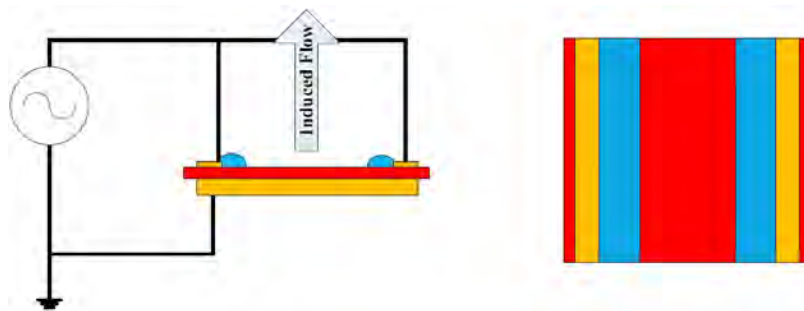
by the actuator's electric field. The ions then transfer their momentum to the bulk flow through momentum transfer collisions. The symmetric configuration, as shown in Figure 2.6 (b), can be used to create a vertical jet or vortices between the encapsulated electrodes. These actuators can be placed in parallel with the free stream flow to excite flow instabilities and reattach separated flows more efficiently than the standard DBD [22]. The electrodes can also be arranged in such a manner as to create a plasma pump or jet by having the induced thrust and wind be created through a cylindrical geometry as shown in Figure 2.6 (c). These configurations can be used individually or in arrays to manipulate the flow as desired.

2.4 DBD Theory of Operation

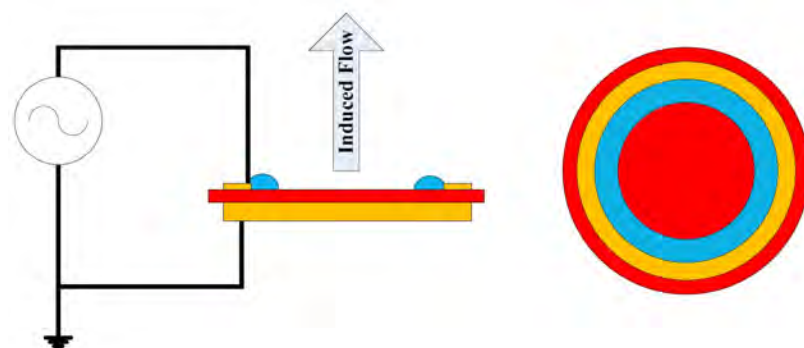
DBD plasma is formed through the application of a high potential, most often in the multiple kV range, to the air exposed electrode. This potential can take the form of DC nanopulses, sawtooth, triangular, or AC waveforms, with AC (standard sine wave) waveforms being examined in this work. DBD's in surface configuration operate by applying a potential of sufficient magnitude to induce the ionization of the ambient air near the exposed electrode(s), producing an extremely thin plasma, less than one mm [17] in height, in the air above the dielectric encapsulated electrode [2]. The DBD cycle, for AC waveform, consists of two half periods, the negative period when the exposed electrode is negative and the positive period when the exposed electrode is positive. During the cycle, electrons are accelerated to and from the exposed electrode, depending upon electrode potential [11]. At high enough potentials ($V > V_{br}$, around 6 kV for this experimental set up), the electron-neutral collisions are sufficiently energetic to initiate breakdown and plasma formation. During the negative half-period, electrons are accelerated from the exposed electrode and gather on the dielectric surface creating a local surface charge and orienting themselves to cancel out the electric field between the exposed and encapsulated electrode, quenching of the discharge [2, 11, 17, 26, 27]. During the positive half-period, the charges on the dielectric are accelerated towards the exposed electrode, initiating the second



(a) Asymmetric SDBD designed for the generation of thrust and ionic wind.



(b) Symmetric SDBD designed for the generation of a vertical jet or vortex.



(c) Circular SDBD designed for the generation of a vertical jet.

Figure 2.6: Various Surface DBD Electrode Configurations. Adapted from [1]

discharge of the cycle [2, 11, 17]. Figure 2.7 illustrates typical charge movement during one DBD cycle. Measurements have been taken of the electric field above the dielectric throughout the DBD cycle showing that the potential difference between the exposed electrode and the dielectric surface is up to three times larger during the positive exposed electrode part of the cycle. Enloe, Font, McLaughlin, and Orlov [26] have also shown that after a few AC cycles a positive DC biased charge develops on the dielectric surface a small distance downstream of the exposed electrode. The implication of adding a third potential to the SDBD actuator to minimize these differences, as has been tested in this Thesis, will be discussed further in future sections [3, 26, 27].

The discharge produces a quasi-neutral ionized gas during both the positive and negative half-cycle. During the negative half-cycle, the discharge is comprised of overlapping micro discharges that develop at the edge of the exposed electrode and traverse outwards and deposit negative charges on the dielectric surface. The longevity of these streamers is determined by the capacitance of dielectric material and the frequency and amplitude of the applied waveform. During the positive half-cycle the discharge is comprised of streamers that propagate perpendicularly from the exposed electrode parallel to the virtual electrode that was created from the deposition of negative charges on the dielectric surface. Figure 2.7 shows the charge flow during the different parts of the actuator period [2, 3, 10, 11, 26, 28].

The plasma generated by the actuator is accelerated by the external electric field and local electric field created by the charge build up on the dielectric surface. The actuator thrust is a result of the force of the electric field on the positive and negative ions and electrons. The interaction between the plasma and the applied electric field is responsible for the body force and momentum transfer to the neutral fluid, and subsequently generated ionic wind, through the ion-neutral particle collisions [2, 11, 20, 26, 27].

DBD actuators operate effectively across a wide range of voltages, frequencies, and pressures. An optimal waveform, frequency, voltage, electrode configuration,

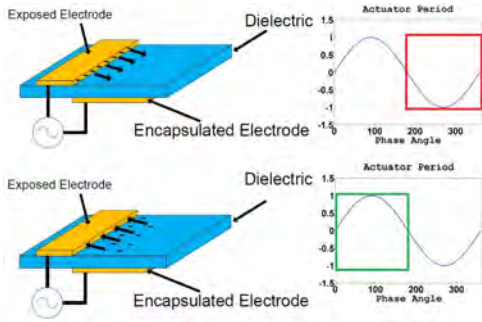


Figure 2.7: Surface charge accumulation on the dielectric causes the DBD to be self-limiting and stable at atmospheric pressures. When the exposed electrode applied voltage is negative the negative charges accumulate on the dielectric. When the exposed electrode voltage reverses and goes positive the electron flow reverses and the electrons flow from the dielectric back to the exposed electrode. Adapted from Enloe [10].

dielectric constant, and dielectric thickness has yet to be determined. Table 2.3 lists the normal range of DBD operating parameters.

Table 2.3: Normal Operating Characteristics of DBD Actuators. Adapted from [2, 17, 19].

Parameter	DBD	
Pressure [bar]	10^{-3}	- 1
Current [A]	10^{-4}	- 10^{-1}
Voltage [kV]	1	- 20
E [$\frac{kV}{cm}$]	30	- 100
T_0 [K]	300	- 600
T_e [eV]	1	- 10
n_e [$\frac{1}{cm^3}$]	10^{11}	- 10^{14}

2.5 DBD Research

The current body of research on DBD actuators for aeronautical use can be categorized into two main areas: optimization research and mechanism research. The optimization research is focused on trying to optimize the DBD parameters and configuration to maximize the induced ionic wind, delivered thrust, region of flow reattachment, or actuator efficiency in terms of consumed power to delivered thrust

[7–9,13,16,24,28–37]. Most of the DBD research for aeronautical applications is being conducted with SDBD’s operating in a frequency range of 1 - 25 kHz, voltage ranges of 1 - 20 kV_{pp}, and at free stream velocities below Mach 0.2. Optimization studies have shown that for a given voltage, an increase in the frequency and a decrease in the thickness of the dielectric material results in increased thrust and momentum coupling [20,29,35], with the optimum frequency being dependent upon the gas species and static pressure [2]. Increasing the amplitude of the applied waveform has also shown to deliver an increase in plasma discharge length, induced velocity, and thrust as long as the amplitude applied is below the saturation amplitude [4,11,28]. For amplitudes in excess of the saturation point of the actuator being tested there is little increase in the induced thrust and momentum coupling. The saturation point, as defined by Thomas [31], is the point at which the discharge transitions from a uniform glow discharge to a discharge that is dominated by filaments as shown in Figure 2.8. It has also been shown that for dielectrics with lower dielectric constants, an increase in thickness results in an improved performance in terms of thrust generation, exceeding the thrust generated by actuators constructed on thinner dielectric materials with higher dielectric constants. This is due primarily to the higher potentials that can be applied to these actuators before the saturation point is reached. In all cases, the optimum performance point is achieved when the plasma is fully developed but has yet to transition to a fully filamentary discharge. Once the discharge has reached the saturation point, further increases in applied potential yield negligible increases in induced velocity and thrust while incurring marked increases in the amount of consumed power [31].

DBDs can be operated either continuously or in a pulsed manner designed to excite instabilities in the free stream flow. The magnitude of the power consumed during actuator operation is dependent upon the mode of operation, with the lower frequency pulsed operation consuming less power [28]. Some models have been developed supporting these results and suggesting that at potentials on the lower end of the spectrum, 1.5-2 kV, a sinusoid signal is ineffective due to the positive ion attraction



Figure 2.8: 1.8mm thick silica dielectric based sliding discharge actuator at its saturation potential of 19 kV.

to the exposed electrode in the negative half-cycle. Differing waveforms have been used to overcome the lack of performance at lower voltages. Sawtooth and triangular waves with long rise times corresponding to the negative portion of the AC frequency cycle have produced more induced thrust than comparable to sine waves [2]. Work by He et. al. [13] and Corke et. al. [8] also demonstrated that DBD actuators are capable of increasing the coefficient of lift of the airfoil it is attached to, although the magnitude of the increase decreases with increasing free stream velocity [7, 8, 13, 28].

Electrode configuration and optimization work has also shown how improvements in the thrust and induced velocity performance can be achieved through the use of multiple encapsulated electrode configurations. Hale [32, 33] was able to achieve induced velocity improvements of up to 91.2%. This work also showed an optimum driving frequency of 10 kHz for performance improvements by multiple encapsulated electrodes.

The thickness and type of dielectric, in terms of dielectric constant, also plays a role in actuator performance. Thinner dielectrics deliver better performance for a given waveform, in terms of induced velocity and thrust, than thicker dielectrics of the with similar properties [6, 10]. Conversely, thicker dielectrics, while less efficient

in comparison to thinner ones in terms of thrust per volt applied, can handle a higher peak voltage before becoming saturated and have a longer duty life before thermal breakdown [29,31]. For this reason, and the superior thermal qualities of silica glass over Kapton, a 1.8 mm thick glass dielectric was selected for this study.

The breakdown mechanism research has been focused on the nature of the breakdown, effects of various gas species, and the development of mathematical models that can be used to develop optimized electrode configurations and for use in flow solvers. The breakdown has been characterized as a four stage process that occurs once every DBD duty cycle:

- Stage One: Electrons migrate away from the negatively charged exposed electrode and deposit themselves on the dielectric surface above the encapsulated electrode creating a local surface potential [26,27,38,39]. This surface potential is dependent upon the plasma/surface interactions and the capacitive voltage division from the actuator's geometry and fluctuates in both space and time. This surface potential can be seen in Figure 2.9 [27].
- Stage Two: When the potential is greater than the breakdown potential, breakdown occurs. The discharge then deposits charges on the dielectric surface negating the potential difference between the exposed and encapsulated electrode. The discharge then quenches, thus self limiting the duration of the discharge to a few nanoseconds [2, 3, 11, 26].
- Stage Three: After the discharge, when the exposed electrode goes positive, the deposited surface charges move back towards the exposed electrode.
- Stage Four: The electric field from the positively charged electrode and the movement of these electrons causes a second ionization that lasts until the electrode begins to negatively charge for the next duty cycle [3].

Research has demonstrated that the residual surface charge plays a role in both the self limiting nature of the discharge and in the amount of generated thrust and that performance improvements can be achieved by optimizing the amount and rate of

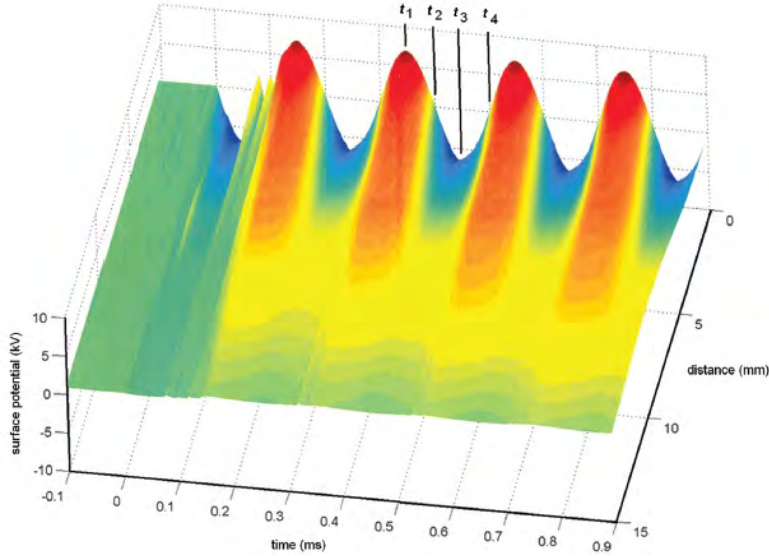


Figure 2.9: Surface charge build up on the dielectric of a two electrode SDBD with a Macor dielectric. The charge accumulation generates a surface potential on the dielectric surface that varies across the dielectric surface during actuator operation. Taken from [26].

surface charge build up [27,38,39]. Other research conducted on the gas species effects has shown that the presence of oxygen increases the thrust to power performance of the actuator. This suggests that the negative ions generated by oxygen increases the actuators performance during the negative half cycle [4,40]. Low pressure examination of DBD performance shows that this trend increases with a decrease of pressure and that DBD actuators are more effective for aircraft flying up at altitude as the generated thrust and reaction region both increase with a decrease in pressure [4,5]. As will be discussed in Chapter 3, PIV was used to determine the extent of induced velocity disparities between half cycles of an SDBD and the sliding discharge actuator under test.

2.6 Plasma Flow Interaction Models

DBD plasma is an ionized quasi-neutral plasma that can be assumed to be quasi steady if the AC period is longer than the time required for the plasma charges to

redistribute themselves [28] and can be modeled by Maxwell's equations [2, 11, 28]. Humble gives the force equation for a charged particle as [41]:

$$m_i \frac{d\vec{u}_i}{dt} = q_i \vec{E} + q_i \cdot (\vec{u}_i \times \vec{B}) + \sum P_{ik} \quad (2.4)$$

where:

$$\begin{aligned} m_i &= \text{Particle Mass (kg)}, \\ q_i &= \text{Particle Charge}, \\ \vec{u}_i &= \text{Particle Velocity (m/s)}, \\ \vec{E} &= \text{Electric Field (V/m)}, \\ \vec{B} &= \text{Magnetic Field (Tesla)}, \\ \vec{P}_{ik} &= \text{Collisional Force (N)}, \\ q_i (\vec{u}_i \times \vec{B}) &= \text{Lorentz Force (N)}, \end{aligned}$$

In the absence of an external magnetic field and a static flow, these equations can be used to develop the body force generated by the actuator. The force per unit volume on the neutrals can be expressed in terms of collisions between the neutral particles and the electrons and ions, \mathbf{f}_i and \mathbf{f}_e respectively [42]:

$$\mathbf{f}_i = \mathbf{n}_i \mathbf{m}_i \nu_{in} \mathbf{u}_i \quad (2.5)$$

And:

$$\mathbf{f}_e = \mathbf{n}_e \mathbf{m}_e \nu_{en} \mathbf{u}_e \quad (2.6)$$

Where n_s is the respective specie number density, m_s is the respective specie mass, and ν_{sm} is the momentum transfer collision frequency. Boeuf [42] then uses the particle mobility, $\mu_s = e/m_s \nu_s$, and the charged particle current density, j_s , to characterize the total body force acting on the neutral molecules in the control volume as:

$$\mathbf{f}_b = \frac{\mathbf{j}_i}{\mu_i} - \frac{\mathbf{j}_e}{\mu_e} \quad (2.7)$$

Utilizing drift-diffusion equations the current densities can be defined as:

$$\mathbf{j}_i = e (\mathbf{n}_i \mu_i \mathbf{E} - \mathbf{D}_i \nabla \mathbf{n}_i) \quad (2.8)$$

And:

$$\mathbf{j}_e = e (\mathbf{n}_e \mu_e \mathbf{E} - \mathbf{D}_e \nabla \mathbf{n}_e) \quad (2.9)$$

The Einstein relation can then be used to define the diffusion coefficients, D_s :

$$D_s = \frac{\mu_s k T_s}{q} \quad (2.10)$$

If the ions are assumed to all be singly ionized, equations 2.8, 2.9, and 2.10 can be substituted into equation 2.7 to obtain an equation for the body force acting on the neutral gas per unit volume:

$$\mathbf{f}_b = e (\mathbf{n}_i - \mathbf{n}_e) \mathbf{E} - k T_i \nabla \mathbf{n}_i - k T_e \nabla \mathbf{n}_e \quad (2.11)$$

In the non-neutral region of the plasma, the edge of the discharge as it travels to/from the exposed electrode(s), and neglecting charged particle gradients, equation 2.11 can be simplified to [3, 11, 15, 42]:

$$\mathbf{f}_b \approx e (\mathbf{n}_i - \mathbf{n}_e) \mathbf{E} \quad (2.12)$$

The ion density in the non-neutral region is generally much greater than the electron density, $n_i \gg n_e$, and making the assumption that electron neutral collisions impart negligible momentum, the body force equation can be simplified to [42]:

$$\mathbf{f}_b \approx e (\mathbf{n}_i) \mathbf{E} \quad (2.13)$$

Substituting in the charge density of the plasma, $\rho_c = e(n_i)$, and utilizing Poisson's equation for an electric field:

$$\nabla \cdot \mathbf{E} = \frac{\rho_c}{\epsilon_0} \quad (2.14)$$

The force can be also be represented as the gradient of the electrostatic pressure [15]:

$$\mathbf{f}_b = \frac{1}{2} \epsilon_0 \vec{\nabla} (\mathbf{E}^2) \quad (2.15)$$

If the viscous and gravitational forces are assumed to be much less then the electric force, then the above body force can be utilized to calculate the imparted velocity:

$$\frac{1}{2} \rho u^2 = \int \mathbf{f}_b \cdot d\mathbf{s} + \frac{1}{2} \rho \mathbf{u}_\infty^2 \quad (2.16)$$

Where u_∞ is the bulk free stream velocity upstream of the actuator and u is the downstream velocity downstream after actuation. For actuators operating in a quiescent flow such as was examined in this work (i.e. $u_\infty = 0$, integrating across the control volume and the solving for u yields an expression for the imparted velocity:

$$\mathbf{u} = \sqrt{\frac{\epsilon_0 \mathbf{E}^2}{\rho}} \quad (2.17)$$

This indicates that the direction and magnitude of the velocity imparted by the actuator can be controlled by modifications of the electric field. It should also be noted that the residual surface charge that develops on the dielectric surface [26, 27] will affect the electric field.

2.7 Performance Measurement Techniques

DBD actuator performance and effectiveness as a flow control and momentum impart device is primarily measured using direct velocity measurements, thrust stand

measurements, and flow visualization techniques, Velocity measurement techniques can be broken down into two main categories, probe measurements and particle image velocimetry (PIV). In probe measurement techniques a probe, either a pitot static probe or a CTA hot wire probe, is inserted into the flow downstream of the actuator. The method is capable of delivering good spacial resolutions of the flow and temporal resolution in the cases of hot wire probes. But, the probes are intrusive in the flow field, must be adequately spaced from the exposed electrode to prevent arcing, and can accumulate a charge build up modifying the electric field of the actuator.

Force balances and thrust stands are used to directly measure the thrust output of an actuator. In balance measurement techniques, the DBD actuator is mounted on either a scale [31, 40], fulcrum [11, 24, 36], or pendulum setup and the generated thrust is measured. The thrust stand data is often time averaged to give an average thrust per DBD cycle. Fulcrum and pendulum set ups offer the ability to measure the thrust generated per plasma half cycles and allow the comparison of thrust generation between the negative and positive half cycles. Due to the large applied potentials, the thrust stand is often encased in a Faraday cage or otherwise electrically isolated to reduce the signal noise [36, 38, 39], with fulcrum and pendulum arms made of non-conductive materials.

One of the most common flow visualization techniques is smoke flow visualization. In smoke flow visualization, particles small enough to track the fluid motion (size $\leq 1\mu\text{m}$) are suspended in the air, or other gas. The smoke is then released into the flow, to form either fog or streamlines, and is then used to identify flow boundaries and characteristics. Smoke flows have the advantages of being relatively simple and easy to set up and having the capability of showing complex flow structures. Smoke flows have the disadvantage of causing accumulations in the test apparatus and obscuring the observation windows, requiring occasional cleaning. Burning, condensation/vaporization, aerosol generation are the most common methods for smoke generation [43] Smoke flows for BDB actuators have been used to show the reattachment of a separated boundary layer from high AOA airfoils [44].

PIV is a non intrusive technique that employs a laser that is modified to create a light plane through a lightly particle seeded fluid. The laser illuminates the field of regard and a digital camera records images at a given time interval. Distinct particles on the frames are then compared and tracked to calculate the velocity and direction of the flow. The main disadvantage of the 2-D PIV technique is the required two dimensionality of the flow. Any particles moving into or out of the laser light plane will skew the results and out of plane velocity won't be measured or tracked [43]. The type of seeding material must be chosen with care, as the seeding material itself may become charged and accelerated by the actuator skewing the results. Stanfield compared the induced velocity of a nanopulsed DBD using PIV and pitot probes and noted the differences that resulted between the probe results and the PIV results by seeding material type [20]. The PIV setup for this work will be examined in greater detail in Chapter 3.

2.8 DBD Limitations

Despite the ease of construction and operation, DBDs have inherent limitations which need to be overcome. The first limitation is one of materials. Ionization of atmospheric oxygen and water vapor causes extensive etching of the exposed electrode and dielectric material eventually leading to thermal breakdown of the actuator. The ionization of the water vapor increases the acidity above the exposed electrode and the dielectric, eroding both surfaces. Oxidation of the copper electrodes used in this work can be seen in Chapter 3. This places a limitation on the duration for which an actuator can be continually run [17]. In addition to the degraded life-cycle caused by the acidity, increases in the relative humidity of the surrounding air also result in decreasing actuator performance [45].

Effectiveness is further limited by the short plasma discharge duration in terms of the linear length of the discharge. AC driven SDBD's have demonstrated discharge lengths of only 20 mm [23, 24], with multiple encapsulated electrodes showing slight improvements in discharge duration and strength [32, 33]. Sliding discharge actuators

and nano-pulsed DC driven actuators have demonstrated an ability to maintain a stable discharge of up to 50% longer than the standard DBD, but those discharges are still less than 50 mm in length [23]. As a result, a single DBD actuator is only capable of accelerating the airflow over a very small chordwise region of the wing [22].

The shallow vertical height of discharge further limits the actuator effectiveness. DBD discharges only extend upwards from the dielectric surface to a maximum height of 1 mm [3, 15]. The majority of the plasma, and induced flow, is trapped in the boundary layer. Due to this lack of height in the discharge, the flows generated separate and dissipate quickly as they exist purely in the shear region of the boundary layer [1]. This effect may be slightly mitigated by actuating two offset SDBDs slightly out of phase to create an elevated pulse away from the dielectric barrier or by creating a steerable vertical wall jet that can be used to excite instabilities in the flow [46]. The boundary layer thickness for a flat plate actuator examined can be calculated with Equation 2.18.

$$\delta_{99} = \frac{5.5x}{\sqrt{Re_x}} \quad (2.18)$$

Where:

x	Distance from plate leading edge
Re_x	$\frac{\rho \cdot v \cdot x}{\mu}$
ρ	Air density [$\text{kg}\backslash\text{m}^3$]
v	Free stream velocity [$\text{m}\backslash\text{s}$]
μ	Dynamic viscosity

The boundary layer thicknesses for the actuator for varying velocities 5 cm downstream are shown in Table 2.4 and a layer visualization can be seen in Figure 2.10.

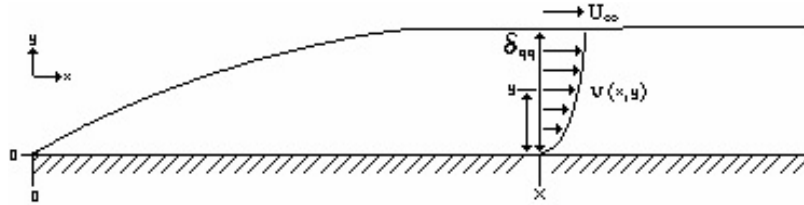


Figure 2.10: Boundary layer profile across a flat plat. Adapted from [1].

Table 2.4: Boundary layer thicknesses for varying velocities at $x = 5.0$ cm with $\rho = 1.20$ kg/m³ and $\mu = 1.983 \cdot 10^{-5}$ kg/(ms)

Velocity $\frac{m}{s}$	Re	δ_{99} (m)
1	3,025	0.0050
3	9,077	0.0029
5	15,129	0.0022
7	21,180	0.0019
9	27,231	0.0017

III. Methodology

3.1 Sliding Discharge Actuator Design

The plasma actuator examined in this thesis consists of two exposed electrodes and one electrode encapsulated underneath a glass dielectric. The electrodes are constructed of copper foil tape with adhesive on one side. The encapsulated electrode is 25 mm wide, 25 μm thick, and 150 mm long. The encapsulated electrode is affixed to the underside of the silica dielectric and is then encased in 75 μm thick Kapton. The two exposed copper electrodes are 6 mm wide, 25 μm thick, and 150 mm long. The exposed electrodes are affixed to the upper surface of the silica dielectric and are aligned such that there is no gap or overlap with respect to the encased electrode. The first 3 mm of upstream electrode for electrode one and the last 3 mm of downstream exposed electrode for electrode two are then covered in 25 μm thick Kapton. This is done to eliminate secondary discharges in these directions. Figure 3.1 illustrates the actuator design.

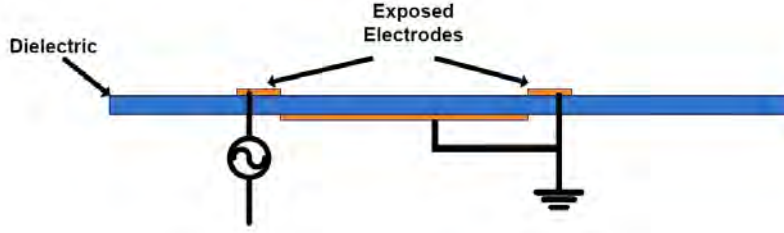


Figure 3.1: Test Actuator Design

The final actuator design, as well as test potentials, was selected after sampling several other design cases. Kapton dielectrics of varying thickness, exposed electrodes with no Kapton coatings, an encapsulated electrode of 12 mm width, a single DBD actuator, and various potential splits were also sampled for performance. Appendix B contains selected results from these trials with the key design stages discussed further in Chapter 4. The two primary considerations in the final design selections were induced velocity performance and actuator robustness. The selected design exhibits a minimum actuator robustness, measured in cycles, of over 200 million cycles at

primary-secondary potential splits of 15 kV and a frequency of 10 kHz. Dielectric heating was present at these potentials, but was insufficient to cause actuator failure. Figure 3.2 shows one of the test actuators after 1 billion cycles, approximately 28 hours of cycling. That actuator was cycled for both PIV and power measurements and oxidation of the exposed copper electrodes is beginning to become evident.

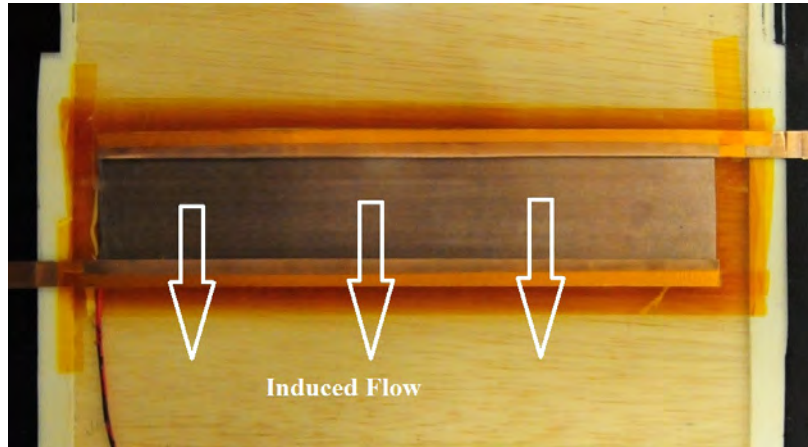
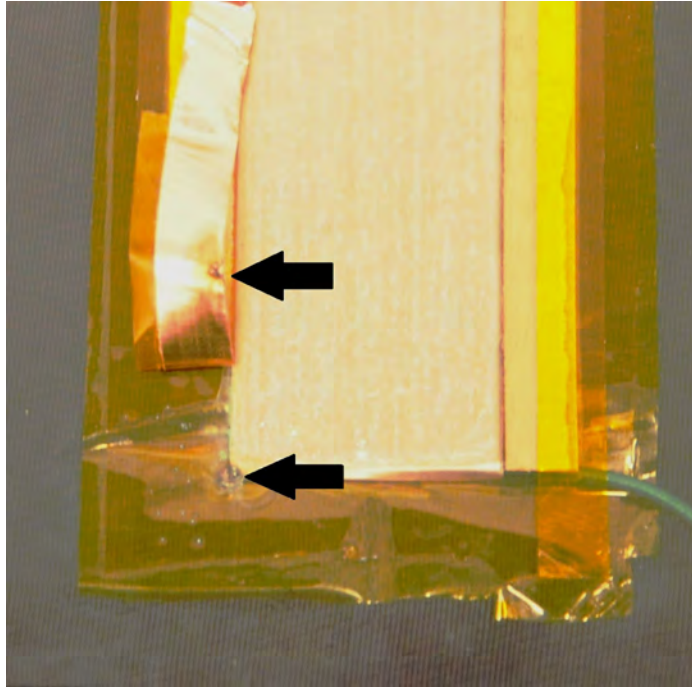


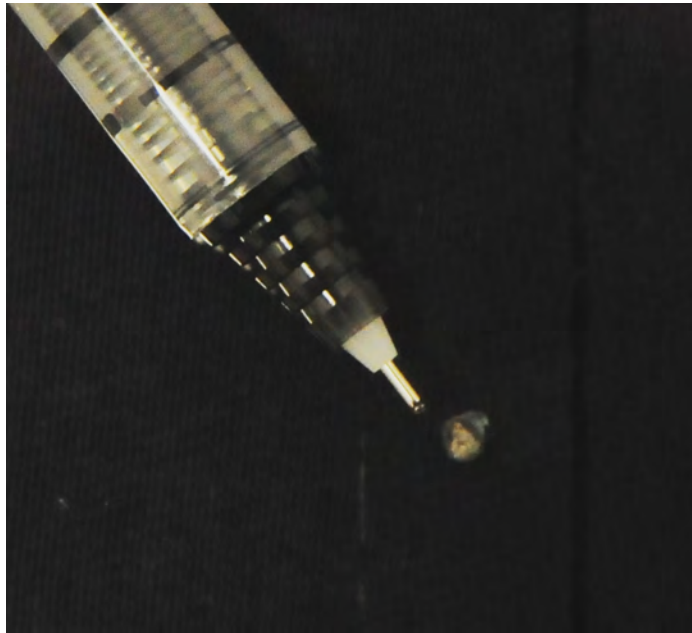
Figure 3.2: Sliding discharge actuator after 1 billion cycles, approximately 28 hours of cycling. Actuator was operated intermittently with a maximum continuous cycling time of 30 minutes.

For primary to secondary electrode potential splits in excess of 15 kV, actuator lifespans were greatly diminished. The observed actuator failures were all due to dielectric failure, with small burn through holes appearing in the silica dielectric. The failure points always appeared on the immediate downstream edge of the primary electrode with no apparent trend as to where on the electrode the failure would occur. There were no observed failures on either the upstream edge of the sliding electrode or in the middle of the dielectric above the encapsulated electrode. Figure 3.3 shows the dielectric failure that occurred at the end of the encapsulated electrode, with subfigure (b) showing a 0.5 mm tipped pen for perspective.

The actuator was mounted on a wooden platform to protect the wiring to the encapsulated electrode. The wooden base prevented the encapsulated electrode's wiring from coming into contact with the test stand and causing an unintentional glow discharge or a full arc. The wooden platform was then mounted on a micrometer



(a) Dielectric failure at the end of the encapsulated electrode.



(b) Dielectric failure point with a 0.5 mm tipped pen for perspective

Figure 3.3: Dielectric failure after less than 120,000 cycles for a 20 kV primary electrode potential. The failure burned through the dielectric and caused scorching and some erosion of the primary electrode as can be seen in the subfigure (a).

adjustable test stand in the test section. The test stand enabled the raising, lowering, and leveling of the test actuator within the test section. Prior to each PIV test, the test actuator was bubble leveled to minimize any gravitational effects on the induced jet's velocity. Figure 3.4 shows the adjustable test stand.

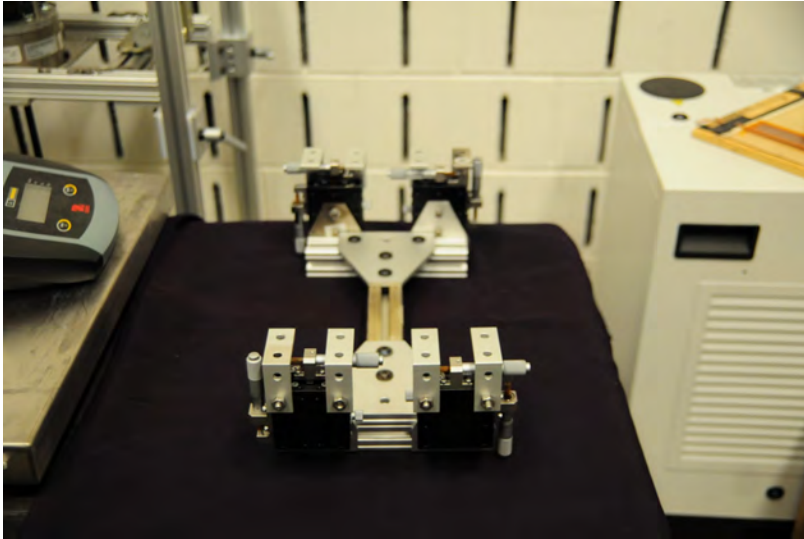


Figure 3.4: Micrometer adjustable test stand for the actuator

3.2 Test Potentials

The primary experiment was carried out in 19 tests over three distinct phases. All test cases are compared to a Baseline case of a standard sliding discharge actuator powered by a 15 kV - 10 kHz primary electrode potential, with the encapsulated electrode and the sliding electrode grounded. Phase one examined the effects of splitting the 15 kV potential between the primary and secondary electrode. The examined potential splits began at potentials of 18-3-0 kV and terminated at a split of 7.5-7.5-0 kV, primary and secondary electrode potentials respectively. In the test cases where with primary electrode potential exceeded of 15 kV, the secondary electrode potential is in phase with the primary electrode potential. For cases where the primary electrode potential was below 15 kV, the primary and secondary electrode potentials were 180° out of phase. The final case, a potential split of 7.5-7.5-0 kV, was selected after noting that applying a greater potential to the encapsulated electrode than was

applied to the primary electrode no longer resulted in a single induced wall jet, but a pair of competing wall jets. This is discussed further in the design of experiments results section in Chapter 4.

Phase two examined the effects of splitting a 15 kV potential between the primary and sliding discharge electrodes with the secondary electrode grounded. The potential splits began at potentials of 18 kV - 0- 3 kV and terminate at a split of 9-0-6 kV. The phase differences between the applied potentials remains the same as conducted in Phase one. A potential split of 7.5-0-7.5 kV was not fully investigated, as it resulted in a pair of competing wall jets vice the desired single induced wall jet. Appendix B contains the results illustrating the effects of two competing wall jets generated by nearly equi-potential electrodes.

Phase three explored the effects of applying an AC bias potential to the sliding electrode. The primary electrode potential of 13 kV and a secondary electrode potential of 2 kV was selected after examining and comparing the induced velocity performances of the Phase one and Phase two test potentials. The 18 kV primary potentials induced the highest peak observed velocities but resulted in a decreased actuator life cycle and were therefore not considered for Phase three. Biases of between 2 kV and 12 kV were then applied to the sliding electrode in order to further accelerate the bulk flow. Table 3.1 lists the Phases of the conducted study and Figure 3.5 illustrates the electrode naming convention.

Table 3.1: Experiment Phases. Potentials are listed in kV - Phase Angle.

Phase	Test Case Number	Primary Potential	Secondary Potential	Potential	Actual Potentials
Phase 1	Baseline	15 - 0°	0 - 0°	0 - 0°	15-0-0
	1	13 - 0°	2 - 180°	0 - 0°	12.6-2.7-0
	2	11 - 0°	4 - 180°	0 - 0°	10.6-4.6-0
	3	9 - 0°	6 - 180°	0 - 0°	9.1-6.3-0
	4	7.5 - 0°	7.5 - 180°	0 - 0°	7.6-7.8-0
	5	17 - 0°	2 - 0°	0 - 0°	17.9-2.6-0
Phase 2	6	18 - 0°	3 - 0°	0 - 0°	18.6-3.4-0
	7	13 - 0°	0 - 0°	2 - 180°	13.5-0-2.2
	8	11 - 0°	0 - 0°	4 - 180°	11.4-0-4.4
	9	9 - 0°	0 - 0°	6 - 180°	9.7-0-6.2
	10	17 - 0°	0 - 0°	2 - 0°	18-0-1.8
Phase 3	11	18 - 0°	0 - 0°	3 - 0°	18.8-0-2.7
	12	13 - 0°	2 - 180°	2 - 180°	13-1.6-2.25
	13	13 - 0°	2 - 180°	4 - 180°	12.9-1.6-3.75
	14	13 - 0°	2 - 180°	6 - 180°	12.7-1.6-5.4
	15	13 - 0°	2 - 180°	7 - 180°	13.3-1.6-7.0
	16	13 - 0°	2 - 180°	9 - 180°	13.2-1.6-9.3
	17	13 - 0°	2 - 180°	11 - 180°	13.0-1.5-11.0
	18	13 - 0°	2 - 180°	12 - 180°	12.9-1.5-12.0

A wiring difference existed between the Baseline Case, Cases 1 - 11, and Cases 12 - 18. The Baseline case was wired in a similar manner to other sliding discharge actuators tested in the literature [23, 24, 47] to establish a baseline performance estimate. The baseline actuator was wired with only the primary electrode connected to a transformer, the secondary and sliding discharge electrodes were both connected to ground. In Cases 1 - 11, the primary and secondary electrodes were wired to individual transformers with the sliding discharge electrode grounded. In Cases 12 - 18, all three actuator electrodes are wired to and powered by independent transformers. Figure 3.5 illustrates the different wiring configurations between Phases I, II, and III.

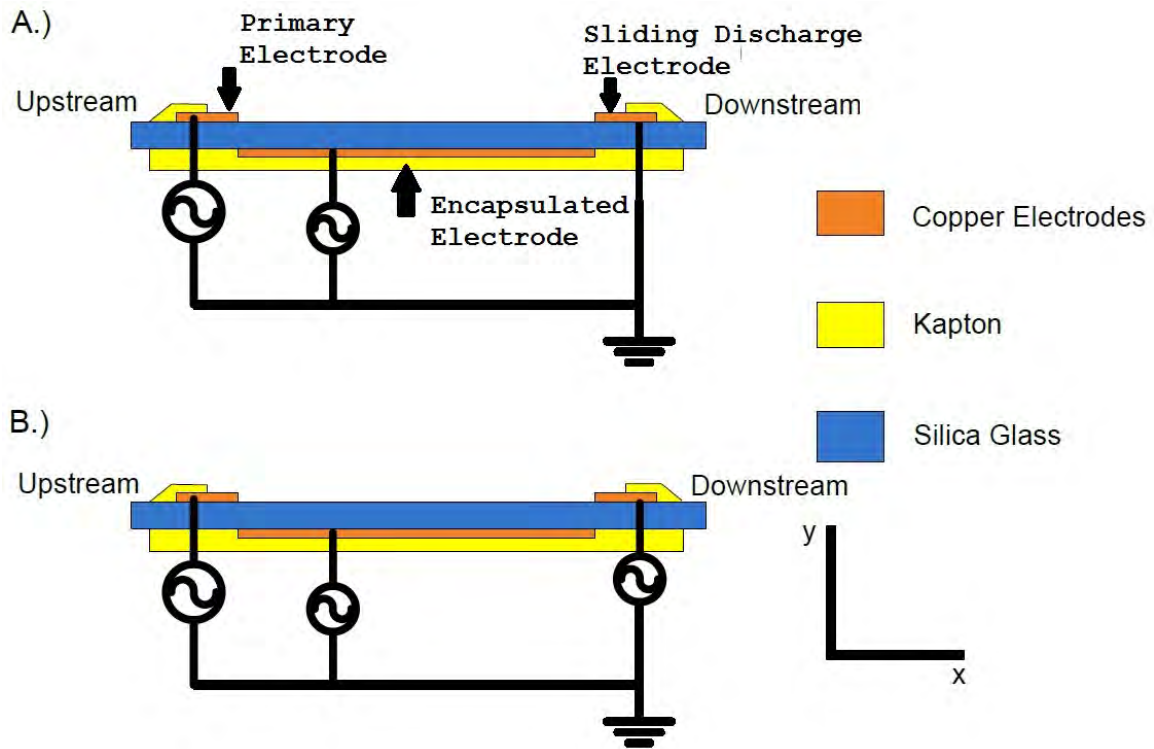


Figure 3.5: Test Actuators. A.) Phase I and II (Cases 1 - 11): Primary and secondary electrodes are set to receive potentials. Sliding electrode is grounded.
 B.) Phase III (Cases 12-18): All three electrodes are receiving a potential from their respective transformers.

3.3 Waveform Generation

Independent channels of signal generation and amplification were utilized to create the potentials applied to the electrodes. Two Agilent 3522A two channel function generators provided the selected voltage required for the potential to be applied to its respective electrode. The experimentally determined settings are listed in Appendix A, Table A.1 for all the test Cases. Burst mode, the number of cycles, and the proper start phase, 0 degrees or 180 degrees, were programmed for each channel. For the PIV data collects, The burst length was 300,000 cycles for the PIV data collects and 900,000 cycles for the power consumption data collects. The determination for the numbers of cycles per burst is discussed further in the PIV and power data sections. Next, the trigger for each respective channel was set to activated by an external trigger generated by the PIV computer that was coupled to the capture of Frame 1 of the PIV image pairs. The channel outputs were then turned on utilizing the channel menus. This resulted in the actuator being synchronized for the first image pair in the 30 second PIV run, and then running independently of the camera timing signal for the remainder of the data collection.

Two Crown XLS 1000 stereo amplifiers then amplified the signals output by the function generators. Each amplifier channel was set in stereo mode on an amplification of 13, out of a maximum of 20, with the high-pass filter set to 3 kHz to minimize low frequency noise. Each channel has a maximum output of 350 Watts at these settings and was used to amplified a single waveform. In Cases 5 and 6, the amplifiers were operated in bridged mode in order to deliver a clean sinusoidal input to the electrodes. In bridged mode, with the same filter settings, the amplifier provided 1000 Watts of amplification, but only to a single channel. Figure 3.6 shows the function generator and amplifier used in this research.

The amplified signals were then powered individual Corona Magnetic transformers. The CMI-5530 transformers output potentials in the range of 2 - 10 kV_{rms} and 4

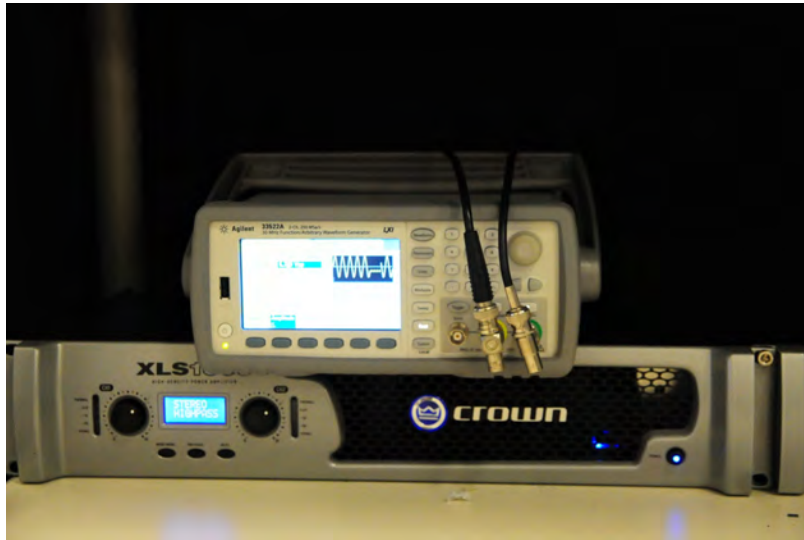


Figure 3.6: Function generator and corresponding amplifier.

- 24 kHz. The output high voltage signals are then routed to the respective electrodes on the sliding discharge actuator. Figure 3.7 shows one of the CMI 5530 transformers.

3.4 Particle Image Velocimetry

A dual pulsed laser PIV system recorded the plasma actuator induced wall jet velocity profiles. In this test, the actuators ran in a quiescent environment inside of a 30 cm x 30 cm x 60 cm Lexan test section. Figure 3.8 shows the test box with actuator in place prior to a PIV data collect.

The test box was equipped 3/4 inch thick quartz glass optical windows for the laser and the PIV camera. Through fittings were created for the eight individual high voltage inputs, eight ground lines, seeding inlet, and a 200 psi compressed air fitting to vent and clear the test section between tests. As the test box itself is highly reflective, matte black felt was placed inside the test section to reduce the level of spurious reflections and maximize image contrast and quality.

A TSI Model 9306 Six Jet Atomizer, as seen in Figure 3.9, seeded the test section with olive oil. The atomizer created droplets that average 1 μm in diameter. Olive oil was selected as the seeding material due to its inert nature and ease of acquisition.



Figure 3.7: CMI 5530 Transformer.

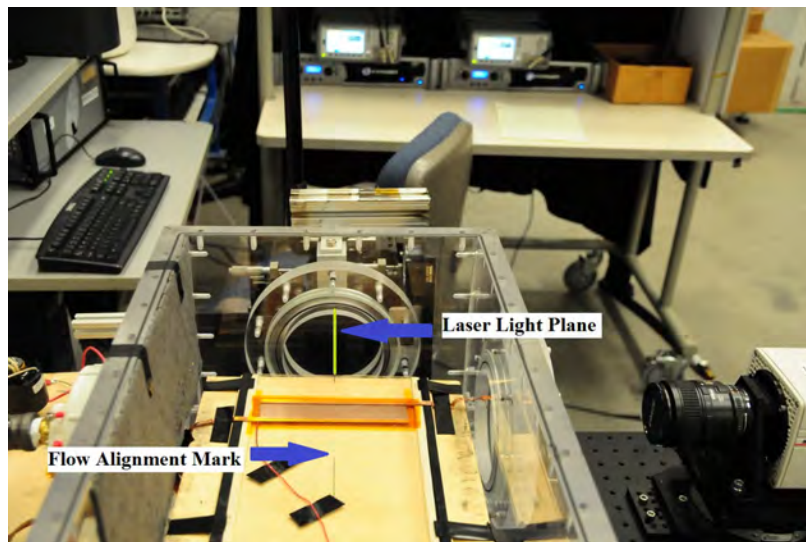


Figure 3.8: 30 cm x 30 cm x 60 cm Lexan test box with actuator in place. Induced flow is from top to bottom. The actuator contained an alignment mark, as highlighted, to ensure the laser light plane was parallel to the induced flow direction for each test case.



Figure 3.9: TSI Model 9306 Six Jet Atomizer

The Dantec Dynamics Flow Map System Hub PC captured the PIV image pairs. A New Wave Research Solo PIV-120 120 mJ at 532 nm Nd:YAG Q-switched laser attached to a Dantec Dynamics laser light arm provided the light source and a Megaplus Model ES 4.0/E4 megapixel CCD camera captured the images. A 532 nm +/- 5nm bandpass filter was used on the camera to prevent interference from background light sources from distorting the results. The filter also helped to minimize the effects of the plasma discharge itself, though the discharge plumes were still apparent in the PIV images. Figure 3.10 shows the residual pick up of the plasma discharge by the PIV camera.

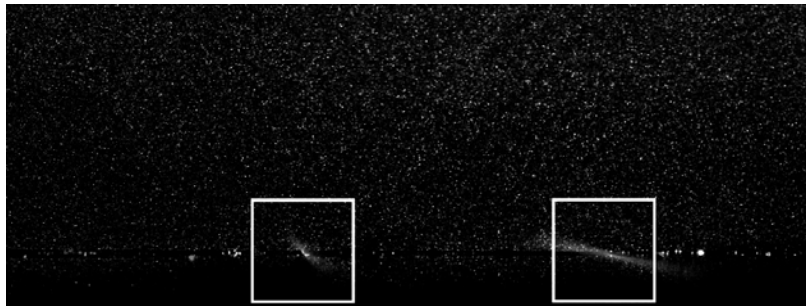


Figure 3.10: Competing plasma discharges from Test Case 18. Though minimized by the 532 nm filter, the two discharges still illuminated the surrounding area.

The camera, equipped with a 60 mm Micro Nikkor lens, has a resolution of 2048 x 2048 pixels and was positioned at a distance of 14 inches from the laser light plane. Placing the camera at a distance of 14 inches yielded a field of regard of 85 mm x 85 mm and a resolution of 24.09 pixels/mm. The fstop was set to 2.8 for all focus images and to 5.6 for all PIV collects. Figure 3.11 shows the camera and laser light head positioning.

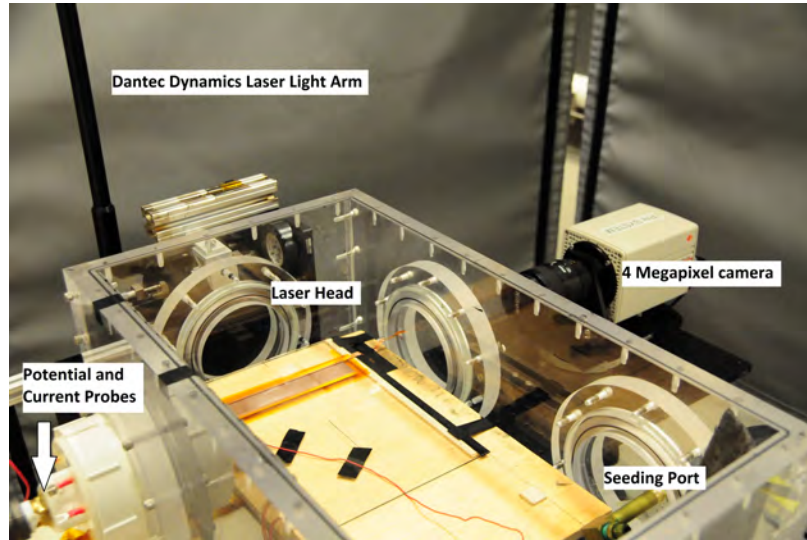


Figure 3.11: Laser and Camera Setup. The induced flow in the test section is from top left to bottom right.

Focus images of a millimeter demarcated ruler, as seen in Figure 3.12, were taken prior to all data collects to ensure proper actuator placement within the 85 mm test section. In all tests, the actuator was placed with the upstream edge of the primary electrode 10 mm \pm 0.5 mm from the edge of the field of regard. The distance between the two points on the focus image was then measured to ensure the proper scale factor was set for each data collect. Improper setting of the scale factor results in inaccurate velocity reporting by the PIV software. The velocity reported in pixels/second will remain accurate, but the velocity in meters/second will be inaccurate proportional to the inaccuracy of the scale factor.

The acquisition software was set to record five image pairs per second, a 5 Hz sampling rate, with 50 μ s between image one and image two in each image pair.

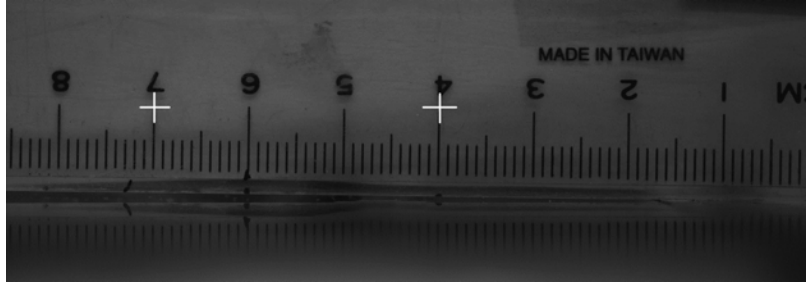
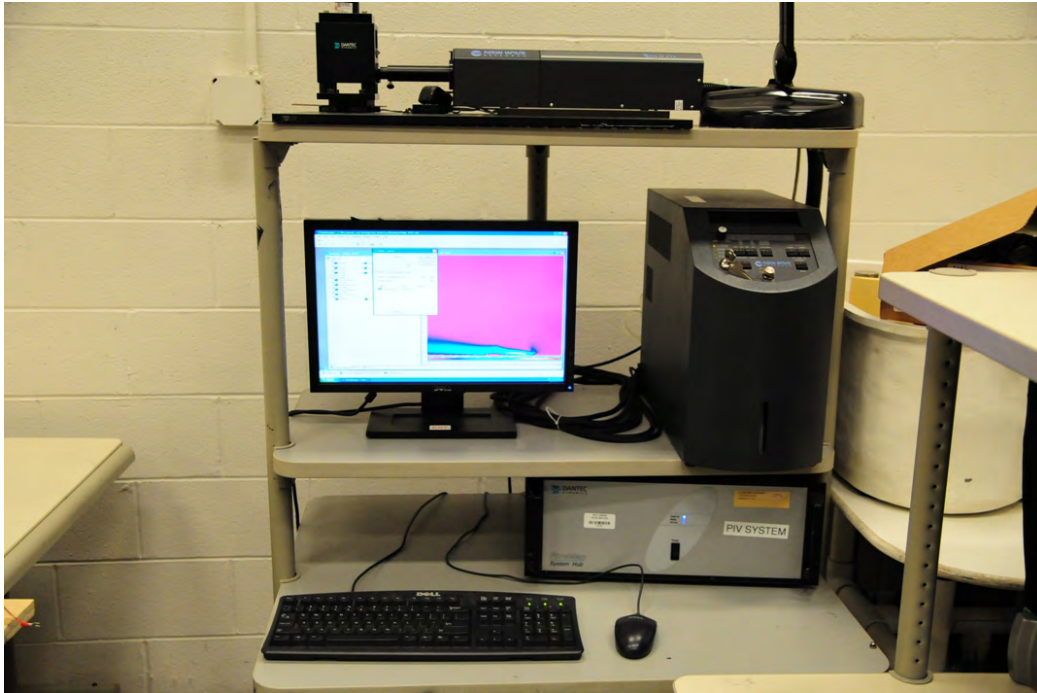


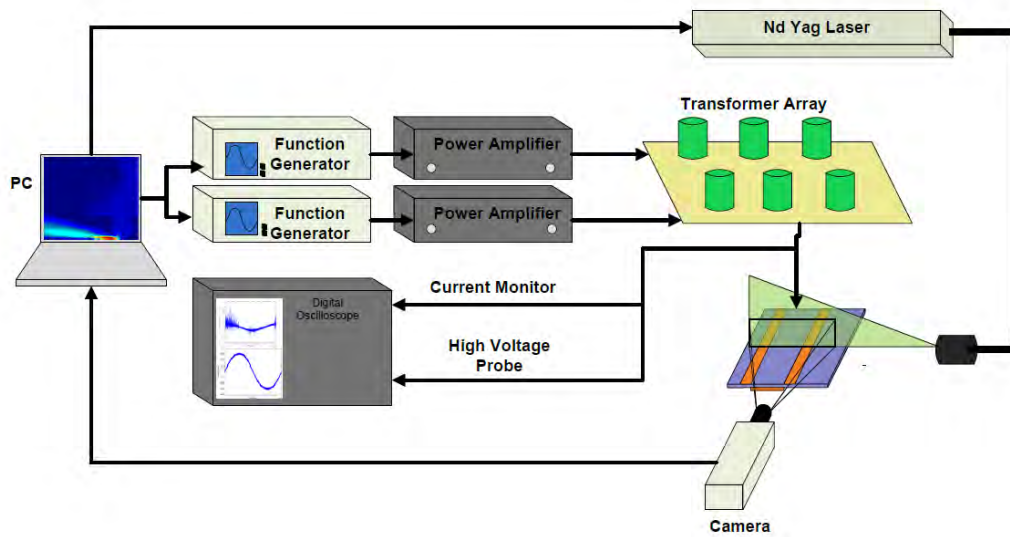
Figure 3.12: Focus Image. Two white crosses on the image were utilized to measure the scale factor for field of regard determination.

Hardware limitations determined the 5 Hz sampling rate, with 5 Hz being the fastest collection rate achievable with the laser-camera combination utilized. The 50 μ s frame rate was selected as this was 0.5 DBD cycles. This enabled measurement of the induced velocity of the actuator at the sub period level and is discussed further in the DOE section of Chapter 4. With the 5 Hz sampling rate, the data collection runs lasted 30 seconds per collection, dictating the 300,000 cycle burst set for the actuator as described previously. Hardware limitations required that the data collection be done in bursts of 150 images pairs per collect. 2100 image pairs were collected for each test case in 14 - 150 image pair bursts for Phases I and II and 1050 image pairs were collected for each Phase III test case in 7 - 150 image pair bursts. To ensure consistency, the test section was vented and reseeded every fourth run to prevent an ozone build up from adversely affecting the results. Table 3.2 lists the PIV software acquisition and processing settings and Figure 3.13 shows the test and measurement equipment schematic and Dantec Dynamics Flow Map System.

Dantec Dynamics Flow Manager software processed all image pairs to produce the initial vector maps utilizing an adaptive correlation method with two step downs. The initial interrogation region contained 32 pixels by 64 pixels and after 2 step downs the final interrogation region was 8 pixels by 16 pixels. All interrogation regions contained a 50% overlap. These settings delivered a spatial resolution of 0.168 mm/vector (6 vectors/mm) in the vertical component and 0.333 mm/vector (3 vectors/mm) in the horizontal component. The peak to peak correlation filter was



(a) Dantec Dynamics Flow Map System Hub



(b) Test Setup Schematic

Figure 3.13

set to 1.5 and the peak size filter was set to 1.75 to 5.75 pixels. To reduce processing time, only the 1000 x 2048 pixels of each image pair in the useful region of the image are processed, resulting in a map of 249 x 255 vectors encompassing a 42 mm x 85 mm test section. After initial vector processing, a 10 m/s maximum range filter was then applied to each vector map before the vector maps were further processed in Matlab.

In Matlab, a momentum continuity check was performed on the vector maps using an eight nearest neighbor approach. Any vector that was outside of four sigma from the eight vectors around it was discarded and replaced with NaN in Matlab [48]. This method helps to minimize any errors induced by invalid correlations. Figure 3.14 illustrates this technique and the accompanying Matlab code can be found in Appendix C.

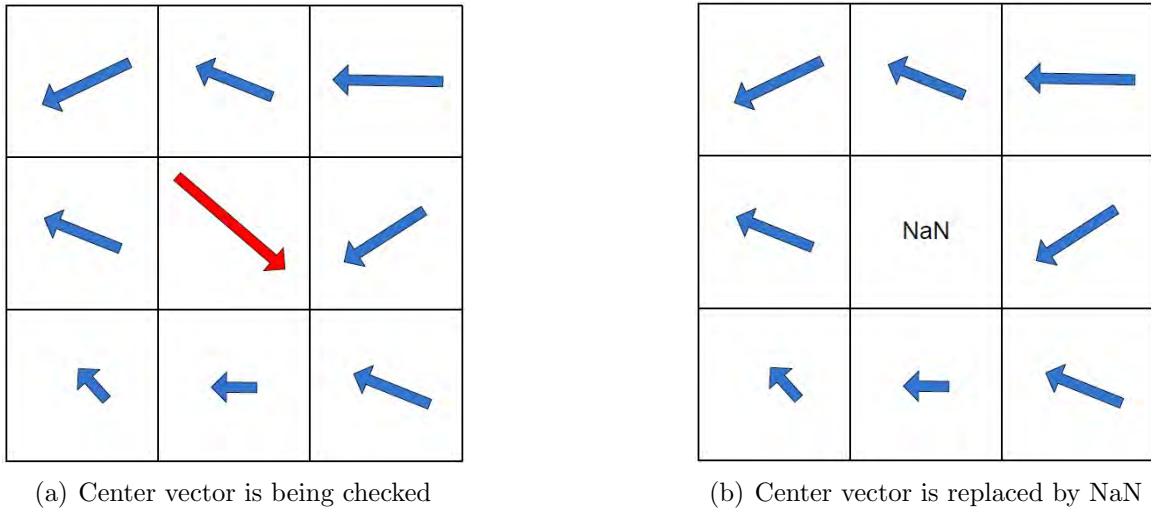


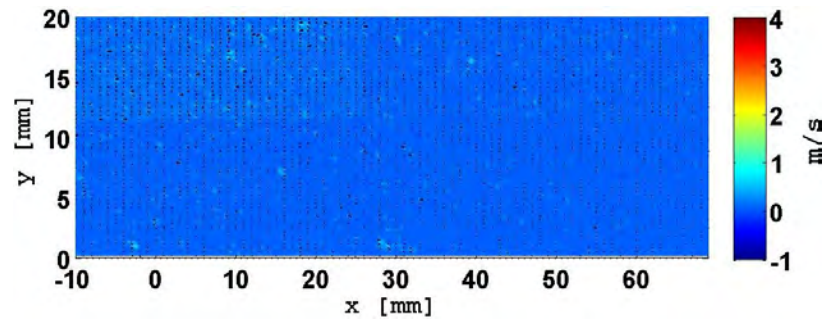
Figure 3.14: a.) Center vector is checked for continuity with the eight vectors surrounding it.
 b.) Vector falls outside of 4σ and has been discarded as an improper correlation and replaced with NaN.

After all the vector maps were processed in this manner, the vector maps were averaged for horizontal and vertical velocity components and the horizontal and vertical velocity component standard deviations calculated. The data presented in Chapter 4 is an average of 2044 image pairs for Phases I and II and 1022 image pairs for Phase

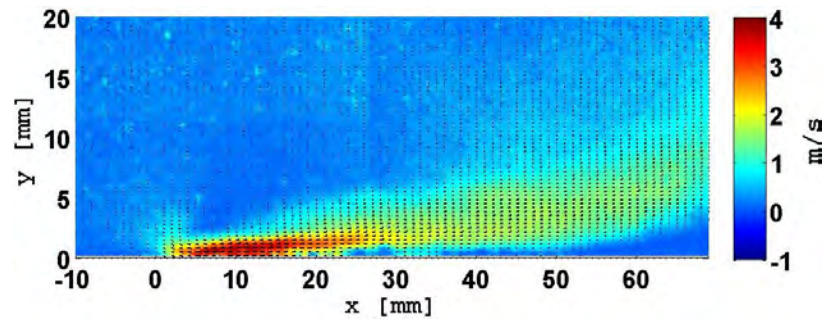
Table 3.2: Image acquisition and processing software settings.

Acquisition Settings		
	Time Between Frames	50 μs
	Time Between Image Pairs	200 ms
	Image Pairs Per Burst	150
	Burst Initiation	User Command Via PC
Processing Settings		
Adaptive Correla- tion:	Image Processing Area	1000 x 2048 (pixels)
	Final Interrogation Region (Pixels)	8 x 16
	Region Overlap	50%
	Steps	2
	Peak to Peak Correlation Requirement	1.5
Range Val- idation:	Peak Width Filter	1.75 (min) to 5.5 (max)
	Vector Length Filter	-10 to 10 [m/s]
	U Length Filter	None
	V Length Filter	None

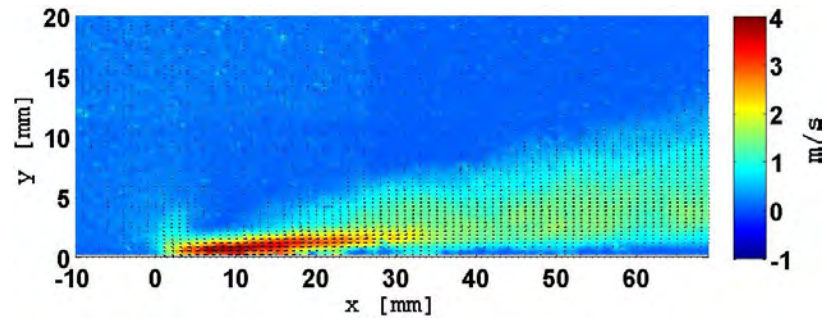
III. The first 4 image pairs of each run discarded from the averaging process to allow the wall jet profile time to fully develop. Figure 3.15 shows how the wall jet becomes fully formed within the first 600 ms of actuation. In the build profiles shown in Figure 3.15 it can be seen that as the induced jet becomes fully formed that height off of the wall at which it interacts with the flow decreases. After 600 ms, the induced jet reaches steady state, the air above the flow is quiescent, and the flow direction is nearly parallel to the wall.



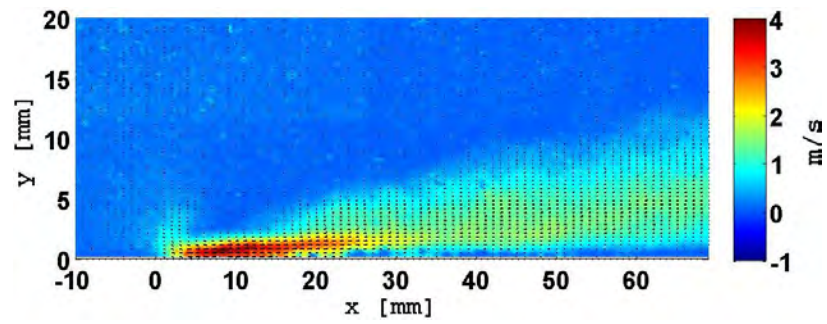
(a) $t = 50 \mu s$



(b) $t = 200 \text{ ms}$



(c) $t = 400 \text{ ms}$



(d) $t = 600 \text{ ms}$

Figure 3.15: Induced wall jet growth over time.

3.5 Actuator Power

A Tektronix DPO 4032 digital oscilloscope recorded the potential and current of the electrodes to enable the calculation of each test case's consumed power. Tektronix P6015A high voltage probes recorded the potential measurements for each electrode. The probe was placed on directly on the high voltage electrodes just after their connection to the transformer. The P6015A probe has a bandwidth of 75 MHz and is capable of recording voltages up to 20 kV_{rms} with an accuracy of 3% when terminated in a $1 \text{ M}\Omega$ load. Measurements of 10 data sets were taken per test case with 100 ksamples taken per data collection and 10 zero data sets were taken for probe bias calculations. Figure 3.16 shows the high voltage probe and current monitor used. The order in which the electrodes were sampled for potential measurements was randomized and will be discussed further in the error analysis section.

Current measurements for each electrode were taken using a Pearson Electronics Model 2100 current monitor. The Model 2100 is a loop type current monitor that was placed around the high voltage line leading into the electrode that was being recorded. The current monitor is not insulated, so only insulated conductors were used and the high voltage lines were run through the center of the current monitor with care taken to ensure that no unintentional glow discharge occurred. The Model 2100 current monitor has a bandwidth of 20 MHz and is capable of recording amperages up to 7.5 A_{rms} with a manufacturer calibrated accuracy of 0.53% at a sensitivity of 1 V/A when terminated in a $1 \text{ M}\Omega$ load. Currents for 10 data collects per test case with 100 ksamples taken per sample.

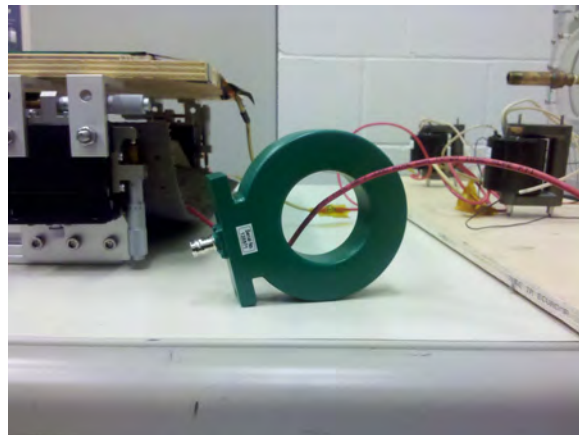
The average actuator power consumption was calculated using Equation 3.1:

$$Power = \sum_{i=1}^n \frac{1}{T} \int_{t_1}^{t_2} V(t) I(t) dt - \sum_{i=1}^n \frac{1}{T} \int_{t_1}^{t_2} V_{bias}(t) I_{bias}(t) dt \quad (3.1)$$

Where T is the number of data samples in the time interval Δt , n is the number of electrodes, and V and I are the instantaneous potential and current. V_{bias} and I_{bias}



(a) Tektronix P6015A High Voltage Probe.



(b) Pearson Model 2100 Current Monitor

Figure 3.16: Voltage Probe and Current Monitor

are the measured instantaneous bias potential and current. Bias measurement will be discussed further in the error analysis section. The power consumptions calculated for the 10 collects were then averaged to produce an average power consumption for each test case. Figure 3.17 shows the current and voltage results from one of the Baseline case measurements.

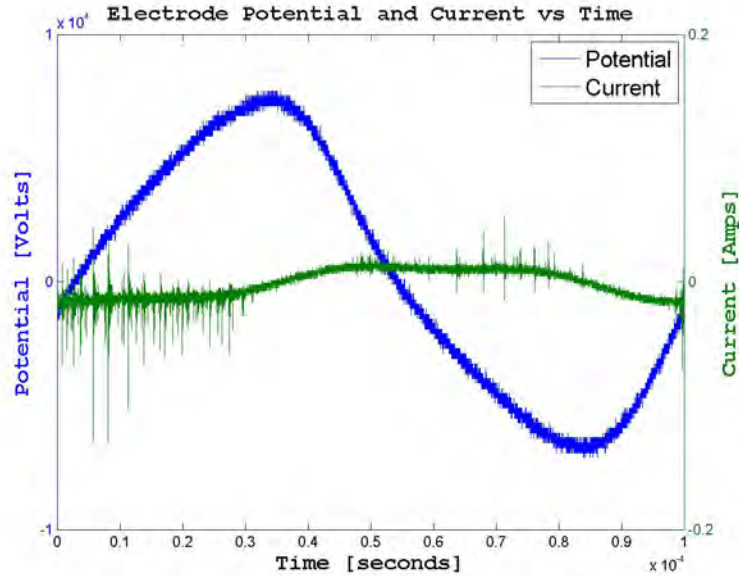


Figure 3.17: Sample voltage and current readings for the Baseline test Case Waveform of 15-0-0 kV. Note the high frequency spikes in the current readings caused by the micro-discharges in the the plasma.

3.6 Efficiency Metric

To enable a comparison between the different test cases a performance metric of induced velocity per Watt [$\frac{m/s}{W}$], similar to that utilized by Forte et. al. [49], of consumed power was utilized:

$$\eta = \frac{U_{Test Case}}{P_{Test Case}} \quad (3.2)$$

This efficiency metric was selected as it normalizes for fluctuations in electrode potentials that deviate from the exact desired test potentials. The efficiencies for all

test cases were calculated at the four evaluation points of $x = 31, 41, 51,$ and 61 mm. A comparison of the 61 mm test point was used as the final evaluation point for determination of the optimum test case.

3.7 Error Analysis

The first error that was quantified was PIV data errors. All PIV collects were collected in the sealed test section with the actuator electrodes powered with the settings listed in Table A.1. To reduce the effects of ozone accumulation in the test section the test section was vented and reseeded every fourth data collection run. PIV errors were the result of camera jitter, sub-pixel resolution error, and function generator jitter. To account for these errors, the standard error in the mean flow field was calculated using Equation 3.3

$$Velocity_{Error} = 1.96 \cdot \frac{\sqrt{u_{x,std}^2 + u_{y,std}^2}}{\sqrt{n}} \quad (3.3)$$

Where n is the number of vectors and $u_{x,std}$ and $u_{y,std}$ are the horizontal and vertical velocity component's standard deviations. The factor of 1.96 was used to obtain a 95% confidence factor on the error in the flow field velocity results [50].

The error for the consumed actuator power is comprised of four parts: instrument bias for both the current monitor and high voltage probe and instrument error for both the current monitor and the high voltage probe. To determine the bias, ten data collections were taken with the actuator electrodes connected to the transformers but under no load. The bias to be subtracted from the calculated power was then found using Equation 3.1 as previously discussed.

The error associated resulting from equipment accuracies was calculated using the quadrature technique shown in Equation 3.4:

$$Error_{test\ run} = \frac{1}{T} \sum_{i=1}^T V_{test\ run}(t) * I_{test\ run}(t) * \sqrt{(error_{vp})^2 + (error_{cm})^2} \quad (3.4)$$

Where $error_{cm}$ is the current monitor accuracy of 0.53%, $error_{vp}$ is the high voltage probe accuracy of 3.0%, and T is again the number of samples in the data collection, 100 ksamples for this study. Using this error for each of the 10 data collections per test case, the mean error for the data collections and bias can be calculated:

$$mean\ error = \frac{\sum_{i=1}^n (error_{test\ run})}{n} \quad (3.5)$$

With n being the number of data collections, 10 for each test case and the bias.

The total error for each power data collection is therefore the sum of the mean error for the test case and the bias:

$$Power_{Error} = error_{data} + error_{bias} \quad (3.6)$$

It was observed during data collection that actuator heating affected the results of power consumption. Two steps were taken to minimize the effects actuator heating would have on power consumption recordings. The actuator was first run for 10 minutes to warm the dielectric. The data was then collected in a randomized fashion both in terms of test cases and electrodes. The order of the test cases was randomized and then the order of the electrodes measured, primary, encapsulate and sliding electrode as applicable, was further randomized to try and minimize and dielectric warming effects.

The efficiency error was then calculated using the power and velocity errors. The quadrature of errors technique was again used and is shown in Equation 3.7.

The error results are contained in the Results Tables for the appropriate section in Chapter 4.

$$Efficiency_{Error} = \sqrt{Power_{Error}^2 + Velocity_{Error}^2} \quad (3.7)$$

IV. Results

This chapter is broken down into 5 main sections. The first Section discusses the analysis that went into the selection of the final actuator design, PIV settings, and test potential selections. Some analysis and commentary is conducted on these results mainly focusing on results that deviate from the trends seen in prior DBD research. In Sections 2-4, the sections that cover the main test potentials examined, the analysis is limited to trends noticed in those sections only with comparisons made to any trends seen in other published DBD research. In Section 5, the 3 test potentials phase results are compared and final conclusions drawn about the effects of the addition of a third AC potential to a sliding discharge actuator.

All wall jet profiles were measured at the same relative points: 31, 41, 51, and 61 mm downstream as measured from the trailing edge of the primary exposed electrode. The 31 mm point was chosen as the first test point because it was the first point at which no plasma was ever visible in the PIV imagery to obscure the results. Figure 4.1 illustrates the coordinate system convention that is used in this analysis.

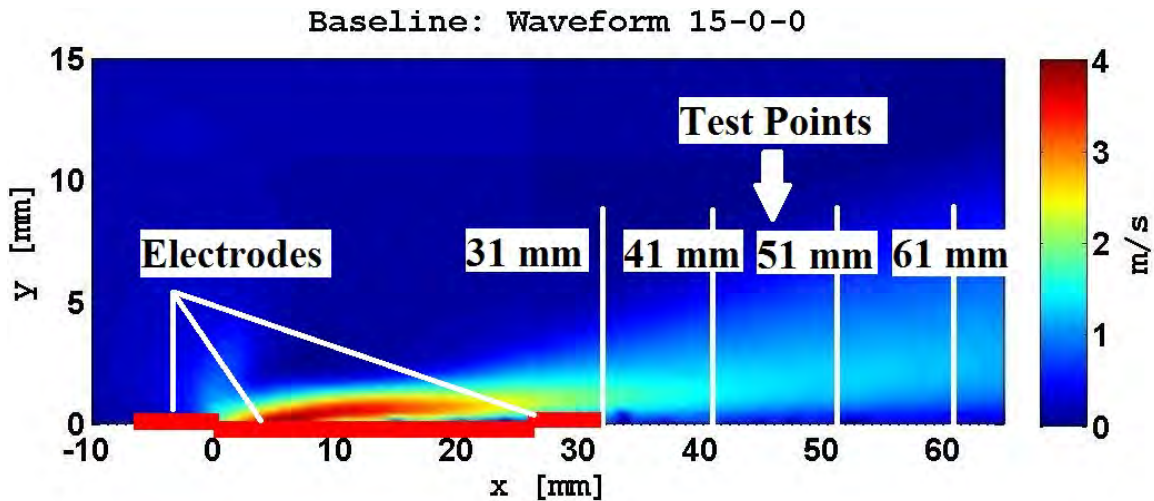
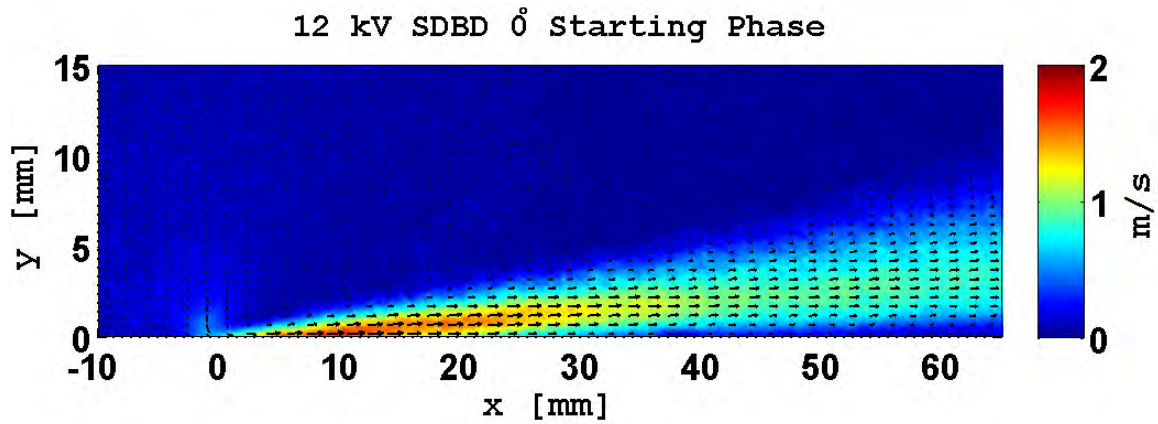


Figure 4.1: Coordinate system used to extract wall jet velocity profiles. Actuator electrodes are in red, velocity profile cross section locations are in denoted in white. The waveform tested in this image consisted of a 15 kV primary electrode potential with the encapsulated and sliding discharge electrodes grounded.

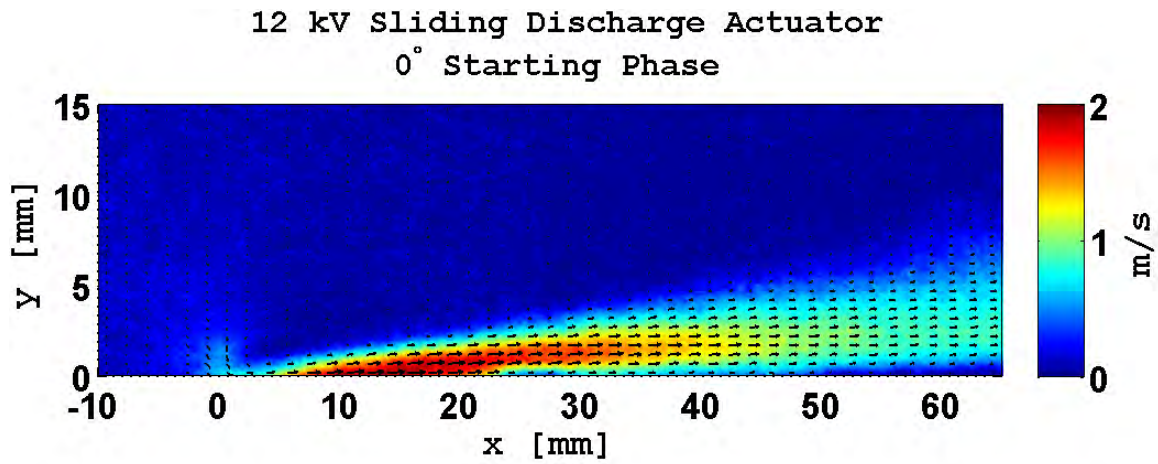
4.1 Test Design Selection

The final test design was selected after an extensive examination of several design parameters. The first parameter examined was the effects of adding the third electrode, in essence the performance improvement achieved by a sliding discharge actuator over a standard DBD. The tests were conducted at a primary to encapsulated potential of 12 kV and a frequency of 10 kHz. All images are captured utilizing the settings listed in Table 3.2 and were taken for input waveforms with initial phase angles of 0, 90, and 180°. Full contour map and vector results highlighting the difference between the starting phase angles are provided in Appendix B with selected results seen below.

The two actuators produced velocity profiles with similar morphologies at all starting phase angles. Both induced flows began 1-2 mm downstream from the primary electrode and had small suction zones in the same locations. Figure 4.2 shows the induced velocity contours and magnitude of the two actuators for a 0° starting phase angle. A rarefied vector map showing every 5th velocity vector in the horizontal direction and every third direction in the vertical direction was overlaid onto the contour plot to further aid in a comparison between the performance of the two actuators.



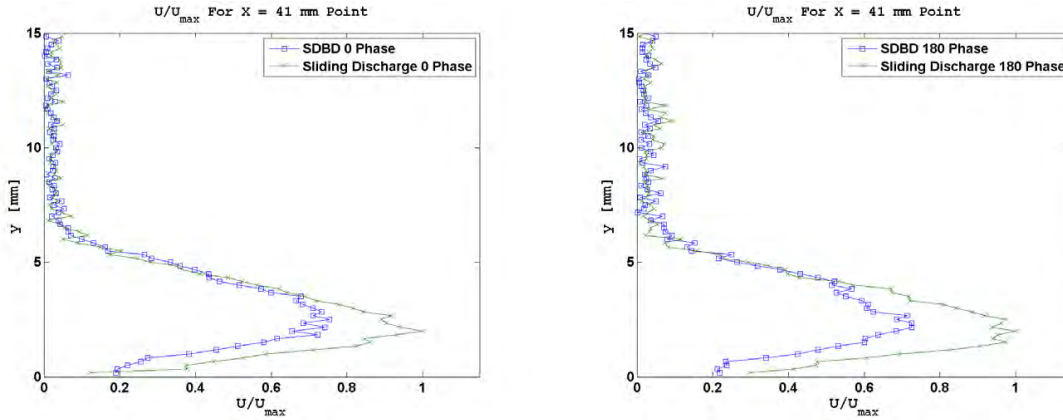
(a) SDBD Vectors and Contour Map



(b) Sliding Discharge Vectors and Contour Map

Figure 4.2: 12 kV SDBD versus 12 kV Sliding Discharge Actuator Comparison. 0° Start Phase

While the induced flow shapes were similar, the two actuators imparted different velocities to the bulk flow. The sliding discharge actuator imparted a peak velocity 25% greater than the standard DBD at the 41 mm point for a phase angle of 0° and 28% greater for a phase angle of 180° . A comparison of the two actuators for starting Phase Angles of 0° and 180° is made in Figure 4.3.

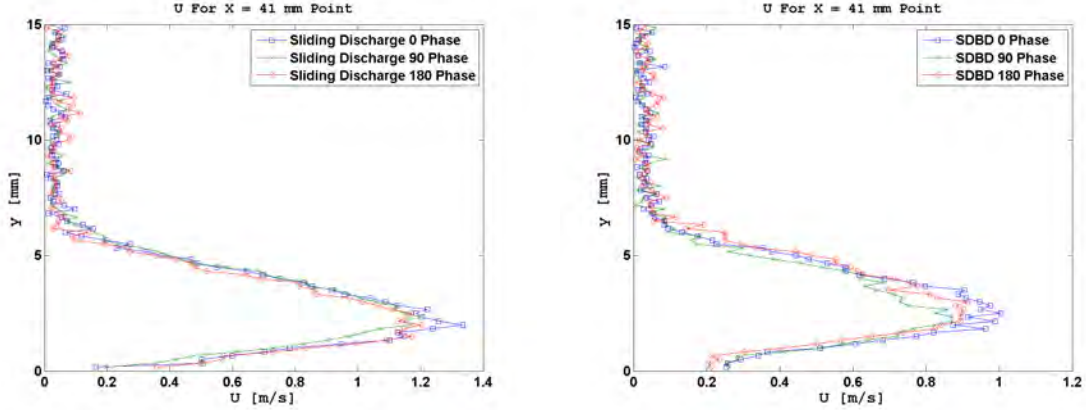


(a) 0° Degree Starting Phase Angle. $U_{max} = 1.33$ m/s. (b) 180° Degree Starting Phase Angle. $U_{max} = 1.20$ m/s.

Figure 4.3: 12 kV SDBD versus 12 kV Sliding Discharge Actuator comparison for various starting phase angles at the 41 mm point.

Next, a comparison was made between the induced flows of the actuators as a function of phase angle. The SDBD actuator had a peak performance over the positive half cycle of the applied waveform producing a peak velocity of 1 m/s. The performance of the negative half cycle was 10% below that of the positive half cycle with a peak velocity of 0.90 m/s. The sliding discharge actuator exhibited a similar drop off, but if the one peak vector of 1.38 m/s is discounted there is a negligible performance difference between the two starting phases. The induced velocity results by phase for the two actuator designs can be seen in Figure 4.4. All future tests were conducted for an initial phase angle of 0° .

Next an examination was conducted on the range of the potential splits and encapsulated electrode width to be examined in the final three phases. The tests examined sliding discharge actuators with encapsulated electrodes of widths of 25 mm



(a) Sliding Discharge Phase Velocity Comparison (b) SDBD Phase Velocity Comparison

Figure 4.4: 12 kV SDBD versus 12 kV Sliding Discharge Actuator Comparison for various starting phase angles at the 41 mm point. Both actuators produced higher velocities during the positive half cycle.

and 12.5 mm, Cases A and B respectively, and three potential splits. The exposed electrode dimensions remained the same. The waveforms examined are listed in Table 4.1.

Table 4.1: Velocity Comparisons between sliding discharge actuators of varying geometries and potentials. Velocity reported in m/s, Potentials in kV.

Test Case	Electrode Potentials [kV]			Phase Difference
	Primary	Encapsulated	Sliding	
Case A	17	0	3	180°
	12	0	8	180°
	10	0	10	0°
	10	0	10	180°
Case B	17	0	3	180°
	12	0	8	180°
	10	0	10	0°
	10	0	10	180°

For both cases a symmetric potential applied to the exposed electrodes induced a vertical wall jet. The vertical wall jet, similar to the one generated by Porter [46] and Fleming [51], developed regardless of the phase difference between the potentials applied to the electrodes. The phase differences did impart differing peak velocities

to the vertical wall jet. The 180 degree phase difference between the two exposed electrodes created the largest accelerating electric field and thus the greatest vertical velocities. Case A induced a greater vertical jet velocity than Case B for all potential phase differences. The results for the 180 degree potential phase difference for Case A and B can be seen in Figure 4.5.

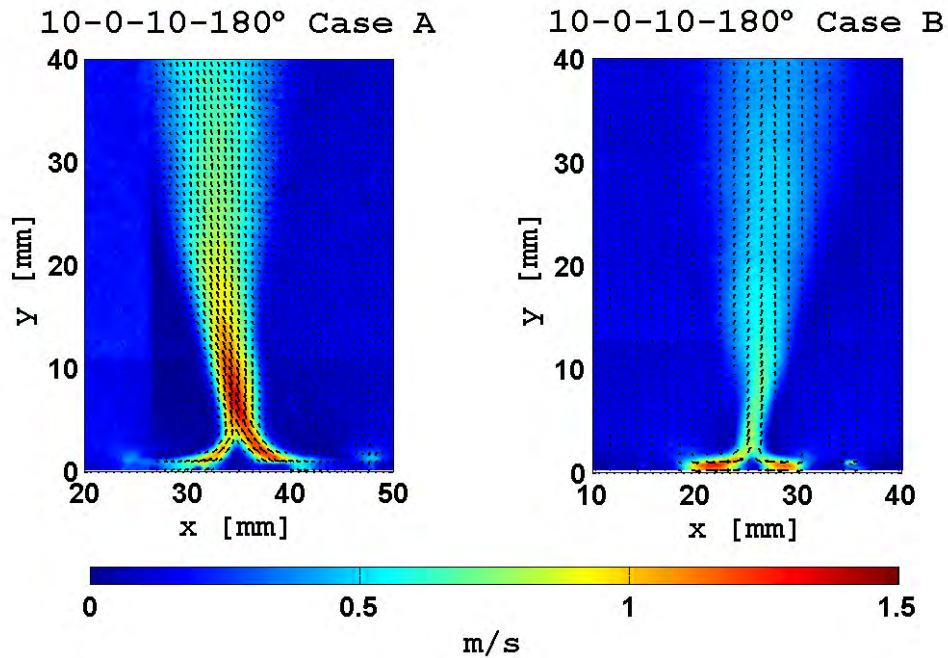


Figure 4.5: Vertical jets induced by competing discharges over the same encapsulated electrode. Small potential mismatches between the two exposed electrodes caused the induced jets to angle away from the higher potential.

Changes in phase between the potentials applied to the electrodes resulted in changing vertical velocities. Figure 4.6 illustrates the levels of the differing vertical velocity components as a function of phase angle between the two electrodes for Case A, with similar Case B profiles found in Appendix B. After observing this trend, Phase 2 potential splits were stopped at a split of 9 kV - 0 - 6 kV since a waveform

split of 7.5 - 0 - 7.5 kV resulted in a vertical jet and not the desired horizontal wall jet.

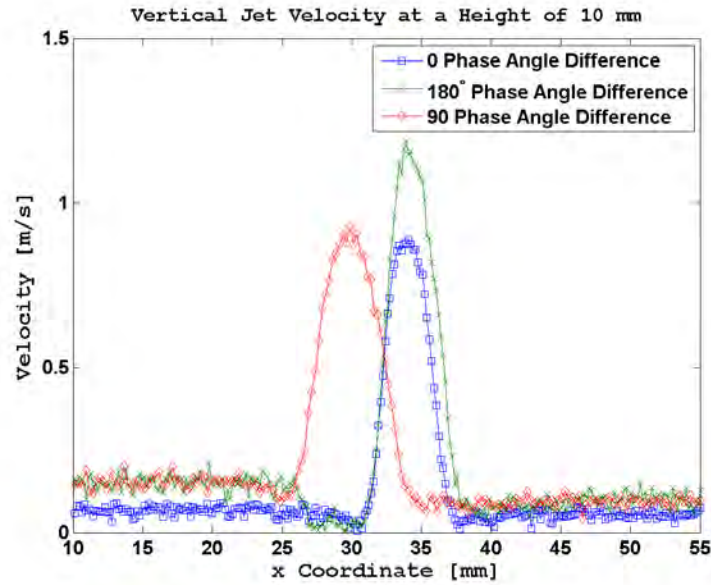


Figure 4.6: Vertical jets velocity profile versus electrode phase angle difference at 10 mm above the actuator surface.

The data for the asymmetric potentials showed that the larger gap produced better wall jet velocities. These results reaffirmed other published optimizations [28, 31, 33, 35]. The narrower encapsulated actuator also exhibited a tendency to form an arc across the gap between the electrodes vice a glow discharge and experienced dielectric failure faster than the large gap actuator. Due to these undesirable tendencies of the narrower encapsulated electrode the wider encapsulate electrode was selected for examination in Phases I-III. Figure 4.7 shows the velocity profiles of the two test widths for the two test potentials.

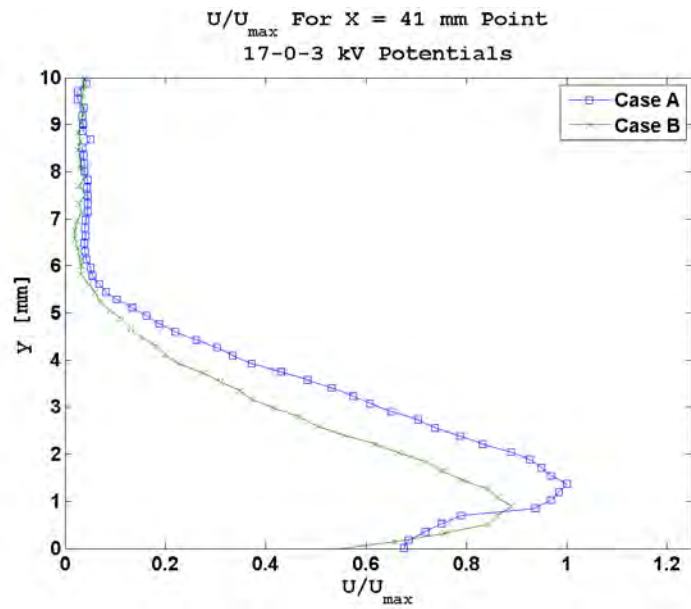
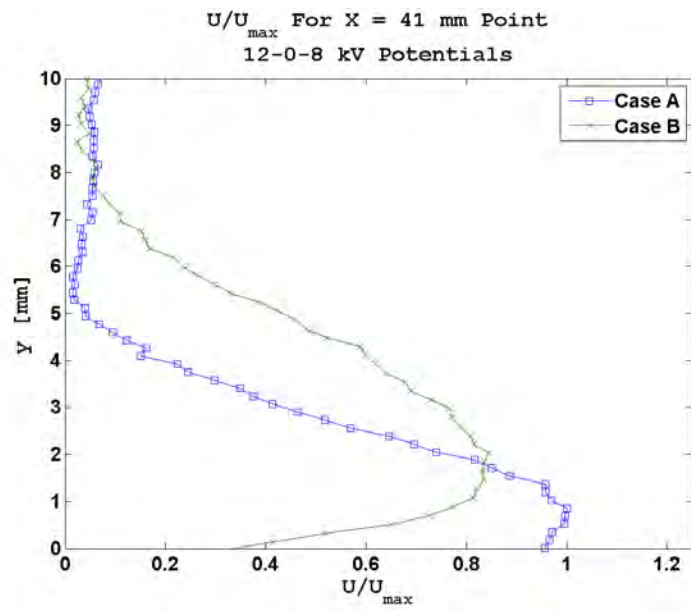


Figure 4.7: 12-0-8 and 17-0-3 kV induced velocity profiles at the 41 mm point.

4.2 Phase I

The velocity profiles for the Phase I Test Cases and the Baseline Case were recorded for a $15 kV_{pp}$ primary to secondary electrode potential and a 10 kHz frequency with the sliding discharge electrode grounded. The plasma discharges of the Test Cases created wall jets that formed at the edge of the primary electrode and a small suction zone over the plasma discharge itself. The suction zone extended to a height of approximately 7 mm above the plasma discharge and had a peak velocity of -1 m/s. Cases III and IV also created secondary discharges that disrupted the primary wall jet inducing a bump into the wall jet profile. Figure 4.8 contains velocity contour plots overlaid with velocity vectors to aid in visualization. Only the Baseline Case and Case 4 are shown as the other Case profiles are similar to that of the Baseline Case. The remaining profiles and x and y component contours can be found in Appendix B.

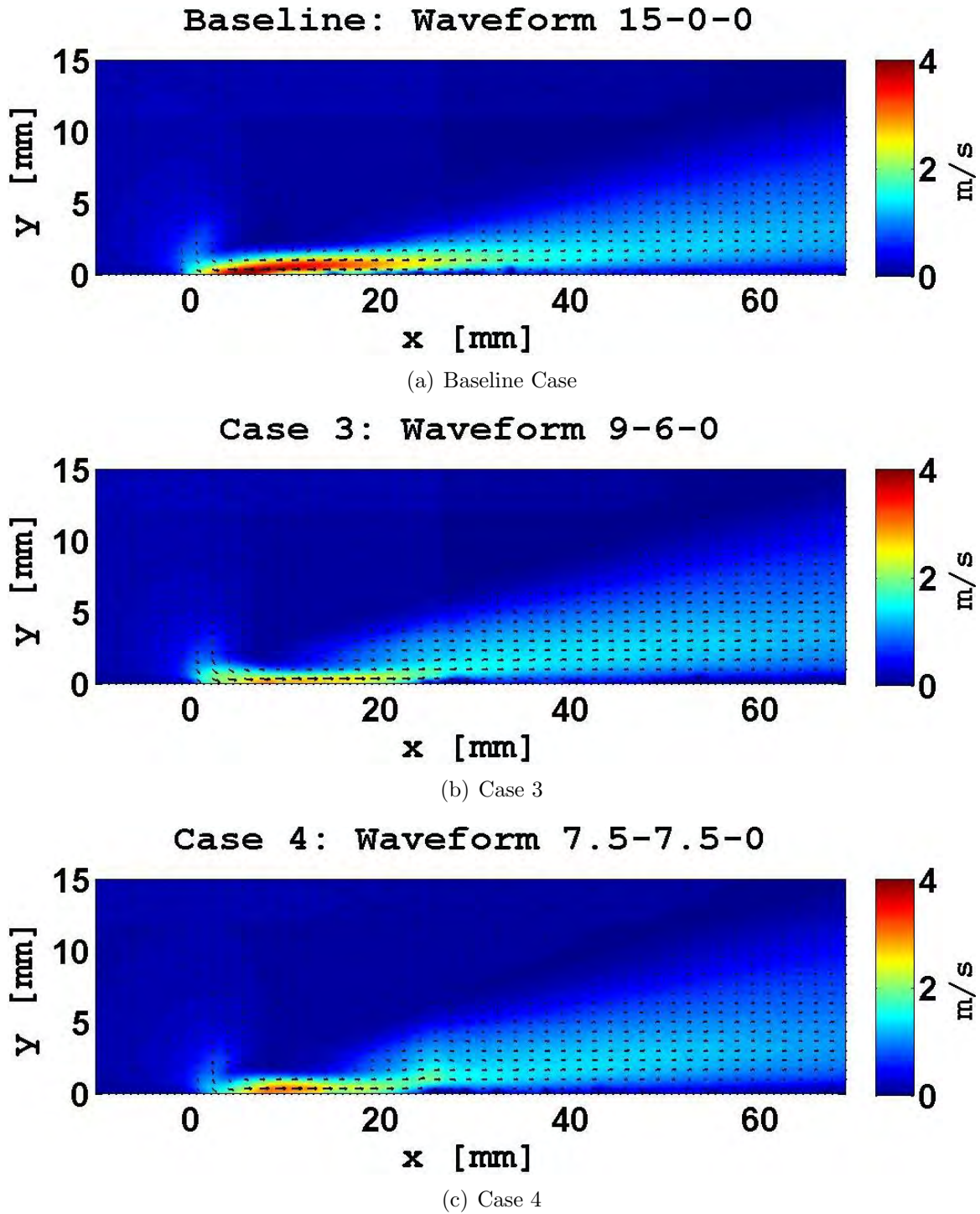


Figure 4.8: Velocity contour map results for Baseline, Case 3, and Case 4. The small suction zone can be seen at x locations of 0-5 mm, forming directly above the discharge. The secondary discharges in Cases 3 and 4 cause a redirection in induced velocity that can be seen at x locations of 25-30 mm.

The results for all Test Cases were examined at the downstream edge of the tertiary electrode and then in 10 mm increments for the next 30 mm. Induced wall jet heights were calculated at the 31 mm positions and are defined as the maximum height at which $U \geq 0.1*U_{max}$. These results were used to examine induced wall jet morphology and are found in Table 4.2.

Table 4.2: Phase I Wall Jets Heights at 31 mm test point.

Test Case	Potential	Induced Jet Height [mm]
Baseline	15-0-0	5.33
Case 1	13-2-0	6.83
Case 2	11-4-0	6.50
Case 3	9-6-0	6.50
Case 4	7.5-7.5-0	6.67
Case 5	17-2-0	5.50
Case 6	18-3-0	5.50

The data suggests that the vertical height of the induced wall jet affects the rate of velocity dissipation over distance. The Baseline Case had the highest peak induced velocity but also the smallest induced jet height. This resulted the fastest velocity dissipation of all the Phase I Test Cases. Figure 4.9 shows the U/U_{max} profiles for the 61 mm test point location illustrating the results of the velocity dissipation. The peak velocities for all the Test Cases and test points are tabulated in Table 4.3. Jet profiles for the remaining test points can be found in Appendix B.

Table 4.3: Phase I peak wall jet velocities. Peak velocity and error reported in m/s.

Test Case	Potential [kV]	31 mm		41 mm		51 mm		61 mm	
		Vel.	Err.	Vel.	Err.	Vel.	Err.	Vel.	Err.
Baseline	15-0-0	1.89	0.022	1.45	0.022	1.30	0.018	1.20	0.018
Case 1	13-2-0	1.62	0.023	1.40	0.019	1.34	0.017	1.26	0.018
Case 2	11-4-0	1.71	0.020	1.48	0.018	1.38	0.021	1.24	0.017
Case 3	9-6-0	1.50	0.021	1.36	0.025	1.30	0.018	1.19	0.019
Case 4	7.5-7.5-0	1.45	0.023	1.33	0.021	1.26	0.018	1.14	0.022
Case 5	17-2-0	1.63	0.110	1.58	0.054	1.49	0.039	1.33	0.022
Case 6	18-3-0	1.59	0.101	1.65	0.045	1.46	0.028	1.29	0.020

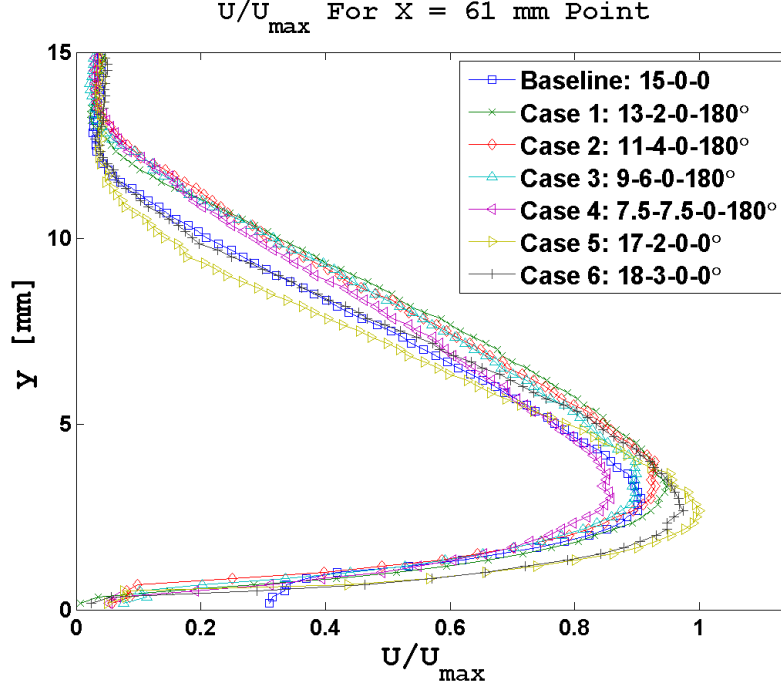


Figure 4.9: Phase I Normalized Velocity Profiles. $U_{max} = 1.33$ m/s.

To enable an efficiency comparison to be made, the power consumed by the actuators was calculated as discussed previously. The data showed that the power consumed by the actuator was related to the length and nature of the primary plasma discharge and the presence of any secondary discharges. Power consumption increased with increasing discharge lengths and the presence of a secondary discharge and if the primary discharge started to make a filamentary transition. Table 4.4 contains the Phase I power consumption results.

Table 4.4: Phase I Power Consumption Results. Power and power error reported in Watts.

Test Case	Potential [kV]	Power	Power Error
Baseline	15-0-0	13.1773	0.4014
Case 1	13-2-0	12.0363	0.3667
Case 2	11-4-0	12.0600	0.3674
Case 3	9-6-0	13.0505	0.3976
Case 4	7.5-7.5-0	14.6500	0.4463
Case 5	17-2-0	31.8900	0.9715
Case 6	18-3-0	37.0896	1.1299

The efficiency results were then plotted at the test points 31, 41, 51, and 61 mm to examine any performance trends. The higher power consumption and velocity dissipation of the Baseline Case coupled with a higher power consumption resulted in decreased efficiency performance, despite having induced the peak induced velocity. Cases 2 and 3 had nearly identical efficiencies and were 20% more efficient than the Baseline Case. The 61 mm test point results are contained in Figure 4.10.

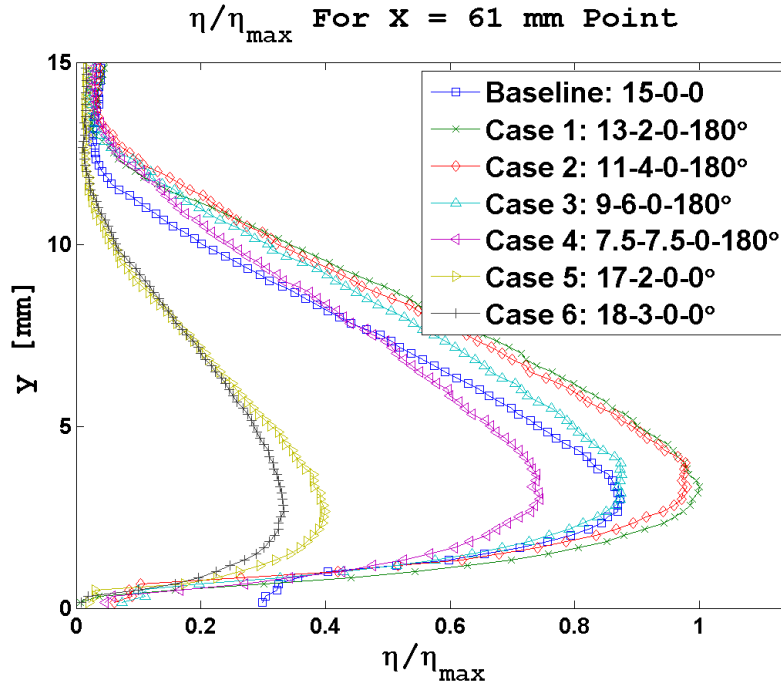


Figure 4.10: Phase I Normalized Efficiency Profiles

Analysis of the Phase I results revealed four trends. First, the Baseline Case, while inducing a higher initial velocity than the Phase I cases, also had the shallowest jet height which had an impeding affect on its duration and by 61 mm downstream its velocity only exceeded that of Cases 3 and 4. Second, downstream velocity appears unaffected by potential split between the primary and secondary electrode as long as there is no secondary discharge formation on the sliding discharge electrode. Third, power consumption was unaffected by the potential split, and only varied with the extent of the discharge and the presence of any secondary discharges along the sliding discharge electrode. Test Cases 3 and 4 both exhibited a secondary discharge along

the edge of the sliding discharge electrode opening up a another channel for current flow and increasing the power consumption for those Cases. The secondary discharge effect was more prominent in some of the later Phase III Cases and will be discussed in further in section 4. Cases 5 and 6 both exhibited a longer discharge that was more filamentary in nature, indicating the discharge was approaching the saturation point. Figures 4.11 and 4.13 show 10 second time averaged plasma discharge lengths for the Phase I Cases.

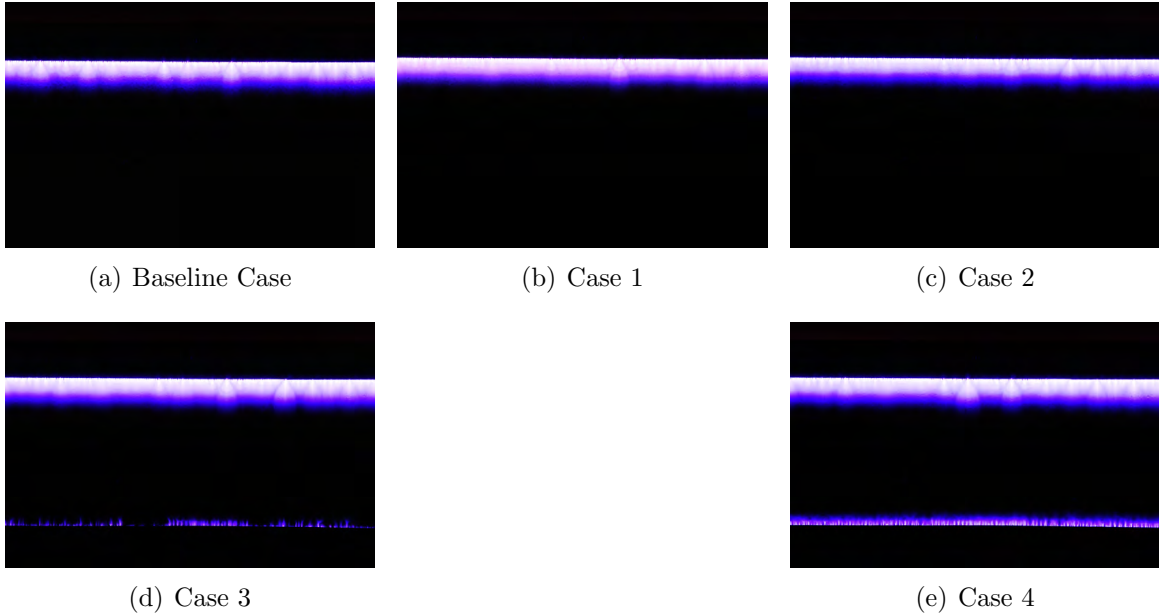


Figure 4.11: Secondary discharges are present in Cases 3 and 4. The intensity of the secondary discharge grew as the potential applied to the secondary electrode was increased.

In Cases 3 and 4, the secondary discharge initiated a small jet in the upstream direction impeding the desired flow and degrading performance. In Case 4, the beginnings of a small plasma induced boundary layer trip can be seen in the vector contour plot. In all Test Cases increased power consumption resulted in much lower efficiencies as there was no corresponding increase in induced velocity. The last trend noticed was in the apparent morphology changes in the jet itself. In Case 1 - 4, the Cases involving a biased encapsulated electrode with the 180° phase difference, the induced jet was 20% taller then the Base Case and the Cases involving a repelling

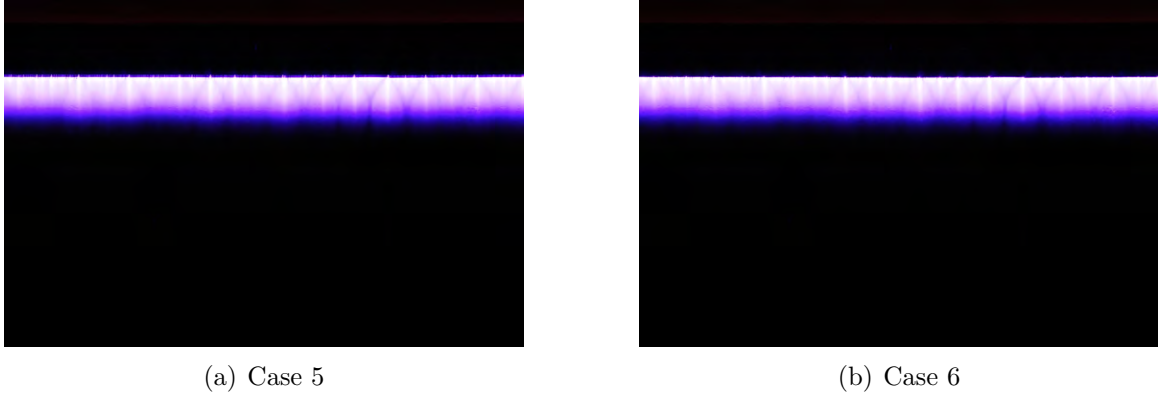


Figure 4.12: The filamentary discharges developing in Cases 5 and 6 indicate the actuators are operating near the saturation point.

encapsulated electrode. Case 6 and Case 7 with the 15 kV potential created by impeding the primary potential with the encapsulated electrode both had induced jet heights nearly identical to the Baseline Case.

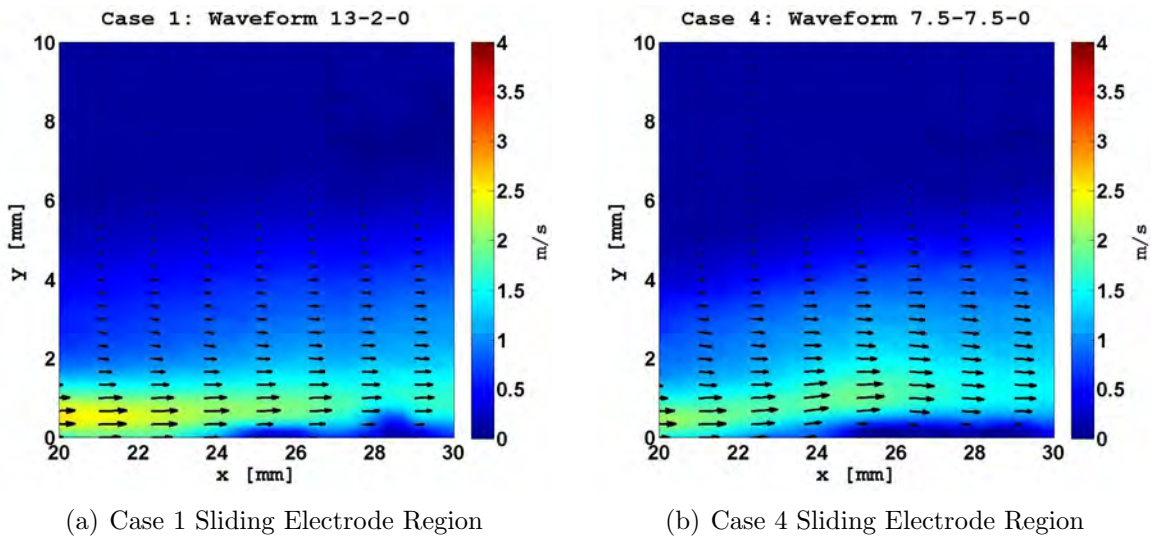


Figure 4.13: Case 1 has no secondary discharge and no change in flow direction over the sliding discharge electrode region. The secondary discharge in Case 4 created a small plasma induced boundary layer trip that redirected the flow and reduced its magnitude.

4.3 Phase II

The Phase II Test Cases involved potential differences of $15 kV_{pp}$ between the primary and sliding electrodes and a 10 kHz frequency. This examination conducted examined the effects of adding a potential bias to the sliding electrode and whether the above the dielectric potential split has as significant an effect as the primary to secondary electrode potential split. The primary factor in velocity generation appears to be the primary to secondary electrode potential difference. Decreasing primary potentials resulted in decreased induced velocities despite increasing sliding discharge electrode potentials. By Case 9 the induced velocity is only 0.35 m/s. Figures 4.14 through 4.18 contain velocity vector and contour plots similar to the Phase I cases.

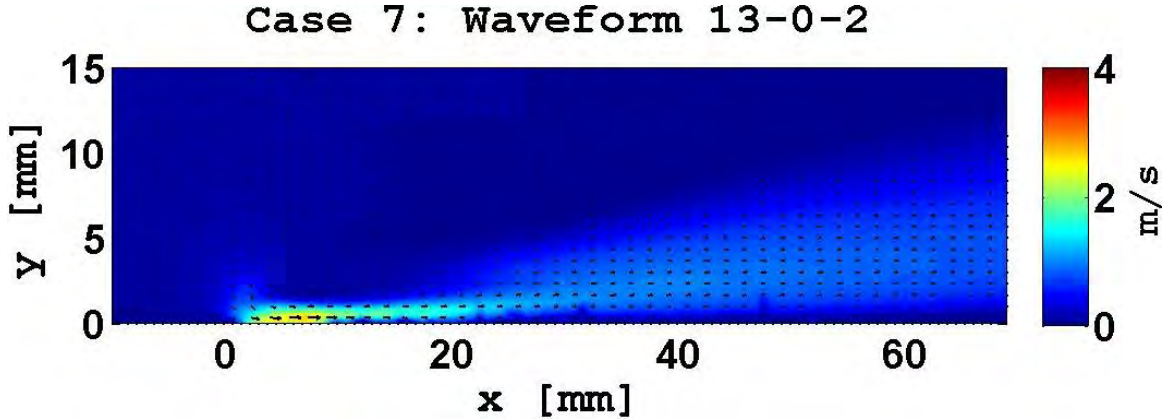


Figure 4.14: Case 7 Vector Contour Map

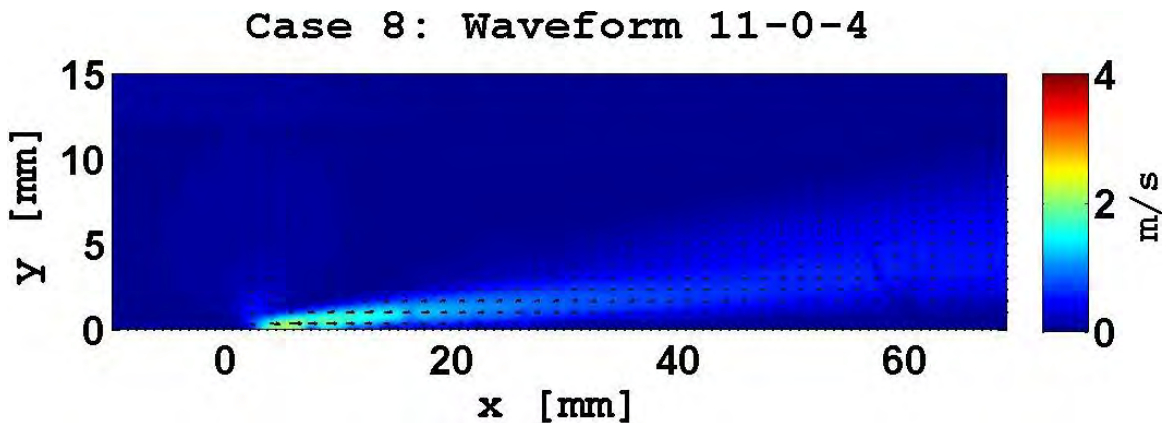


Figure 4.15: Case 8 Vector Contour Map

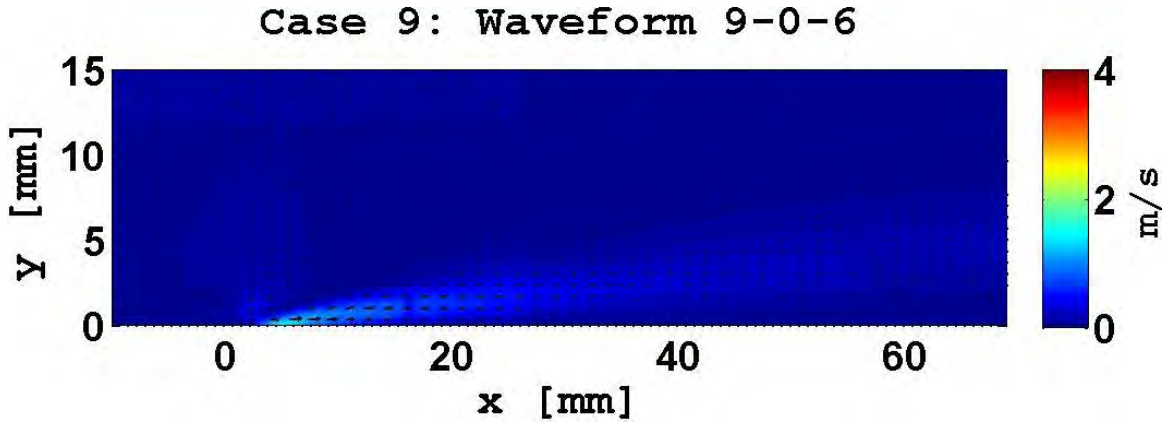


Figure 4.16: Case 9 Vector Contour Map

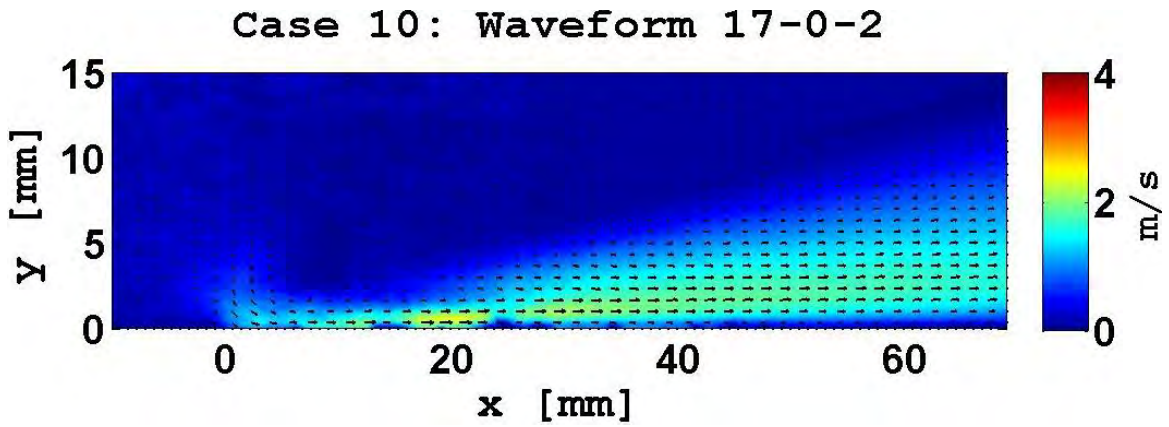


Figure 4.17: Case 10 Vector Contour Map

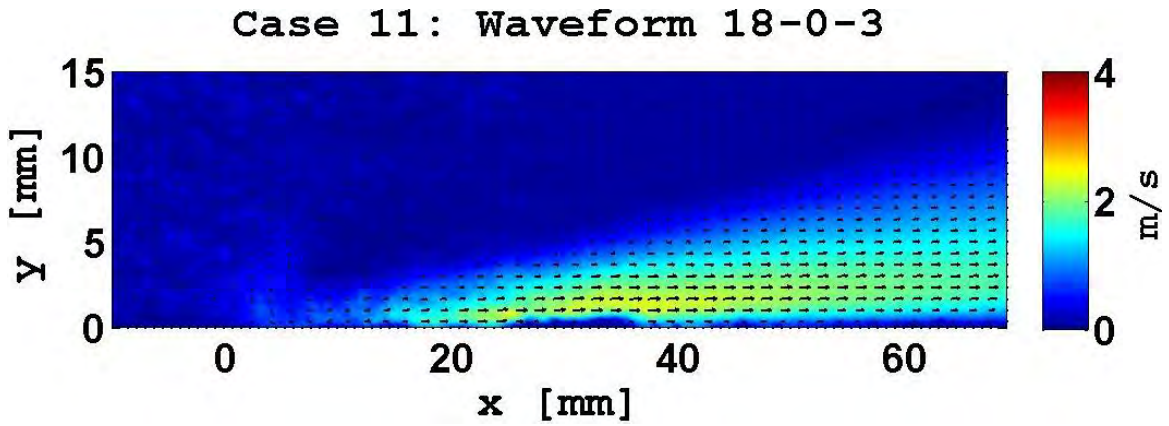


Figure 4.18: Case 11 Vector Contour Map

The normalized performance comparison of the Phase II cases shown in Figure 4.19 further illustrates the correlation between a decrease in the primary to secondary electrode potential split and decreases in induced velocity. At the 61 mm Test Point, Test Case 18 with a primary potential of 18 kV generated an induced velocity that was double the magnitude of Case 7 and nearly four times the magnitude of Case 8. The peak velocities for all of the Test Points and Cases are contained in Table 4.5.

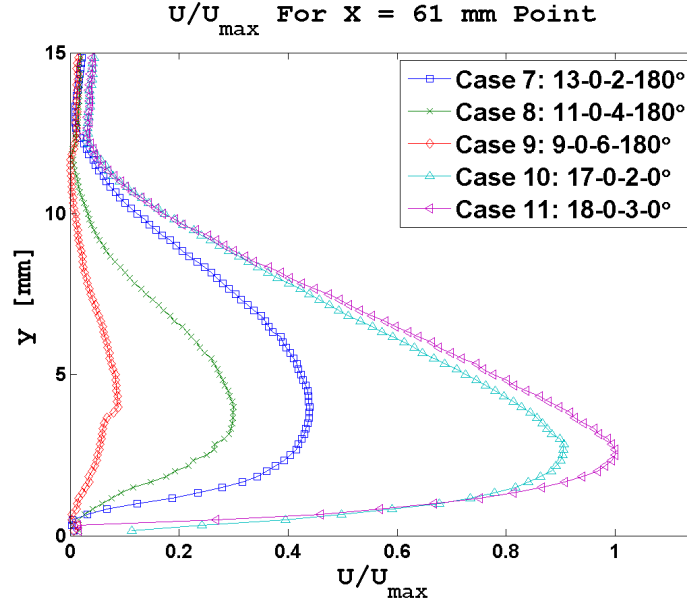


Figure 4.19: Phase II Normalized Velocity Profiles. $U_{max} = 1.87$ m/s.

Table 4.5: Phase II peak wall jet velocities. Peak velocity and error reported in m/s.

Test Case	Potential [kV]	31 mm		41 mm		51 mm		61 mm	
		Vel.	Err.	Vel.	Err.	Vel.	Err.	Vel.	Err.
Case 7	13-0-2	1.03	0.021	0.96	0.012	0.88	0.011	0.82	0.008
Case 8	11-0-4	0.80	0.005	0.67	0.007	0.61	0.008	0.56	0.011
Case 9	9-0-6	0.35	0.009	0.25	0.007	0.20	0.007	0.17	0.012
Case 10	17-0-2	2.05	0.048	1.87	0.033	1.80	0.024	1.70	0.023
Case 11	18-0-3	2.28	0.089	2.27	0.045	2.05	0.029	1.87	0.022

Induced wall jet heights were calculated in the previously described manner and are presented in Table 4.6. No apparent trend in jet height was discernible as all Test Cases induced jets of similar height. The similarity in jet height also yielded similar velocity dissipations with only Case 9 having a dissipation in excess of 25%.

Table 4.6: Phase II Wall Jets Heights at 31 mm test point.

Test Case	Potential	Induced Jet Height [mm]
Case 7	13-0-2	5.83
Case 8	11-0-4	5.50
Case 9	9-0-6	5.67
Case 10	17-0-2	5.83
Case 11	18-0-3	5.50

To enable an efficiency comparison to be made, the power consumed by the actuators was recorded and calculated as discussed previously. Table 4.7 contains the power consumption results and Figure 4.20 illustrates the efficiencies at the 61 mm Test Point. Several trends were apparent in the examination and comparison between the normalized velocity profile curves and the efficiency curves. First, the potential split between the primary and sliding electrodes does not appear to play as large a role in the induced velocity performance of the actuator as does the potential difference between the primary and secondary electrode. This is evident in the velocity profile curve at the 61 mm test point where the performance drops off in the same order as the drop off of primary to secondary potential regardless of the exposed electrodes potential split.

Table 4.7: Phase II Power Consumption Results. Power and power error reported in Watts.

Test Case	Potential [kV]	Power	Power Error
Case 7	13-0-2	10.0906	0.3074
Case 8	11-0-4	5.8022	0.1768
Case 9	9-0-6	3.7700	0.1149
Case 10	17-0-2	27.5260	0.8386
Case 11	18-0-3	39.0896	1.1897

The second trend observed was the change in efficiency. Unlike in Phase I where the efficiency curves were similar for the non-secondary discharge inducing Test Cases, in Phase II, Case 8, which exhibited only 28% of the induced velocity of the Case 11 and half the induced velocity of Case 7, had the best efficiency. This indicated that

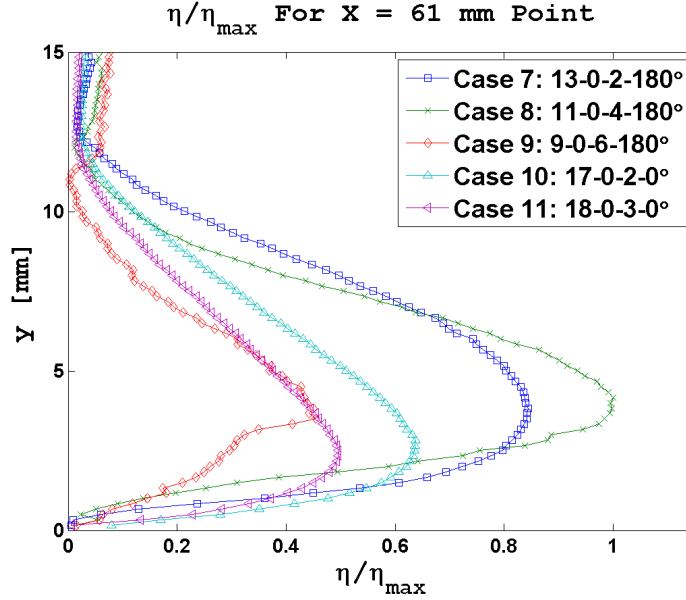
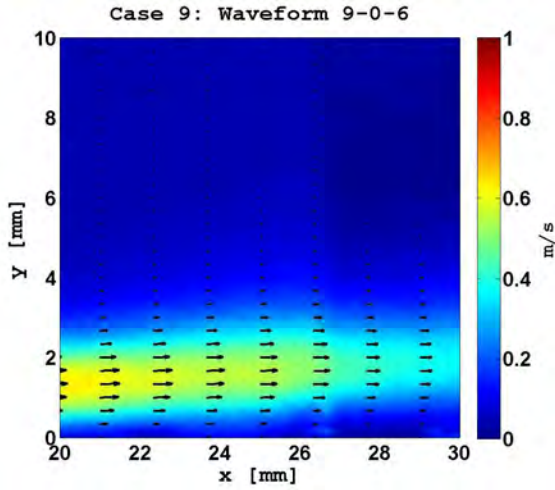


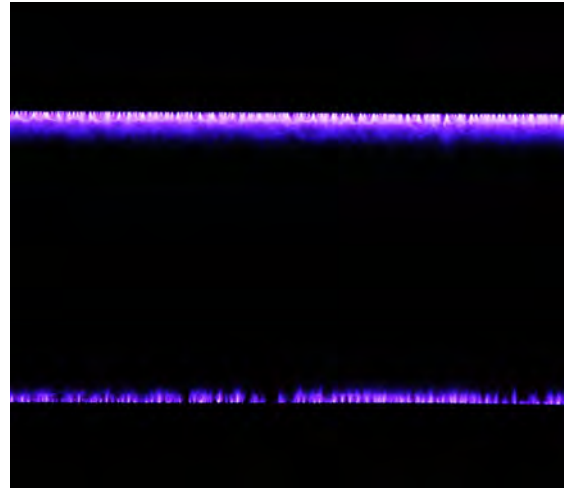
Figure 4.20: Phase 2 Normalized Efficiency Profiles

applying a large, sub-ionization level potential to the sliding electrode will improve the actuators performance and this was examined further in Phase III.

The third trend apparent was the relationship between primary electrode potential, plasma discharge length, and power consumption. Decreasing primary potentials yielded decreasing power consumptions and decreased plasma discharge lengths but not in a linear manner. A 15% decrease in primary potential from Case 7 to 8 delivered a 50% decrease in power consumption and discharge length. The change in plasma discharge lengths are illustrated in Figures 4.22 and 4.21. The secondary discharge in Case 9 is illustrated in Figure 4.21. The secondary discharge was smaller in size than that of Case 4 in Phase I, and no boundary layer trip was observed in the flow field. This results, coupled with the lack of boundary layer trip in Case 3 seems to suggest that a minimum potential induced discharge of 7.5 kV is required to initiate a boundary layer trip. This was again seen in Phase III.

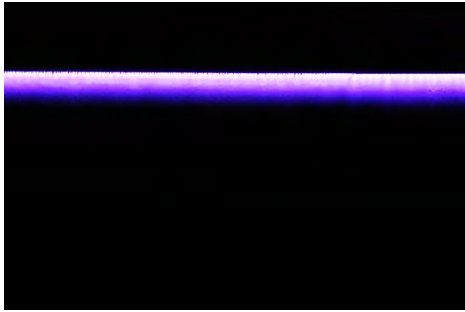


(a) Case 9 Sliding Electrode Region

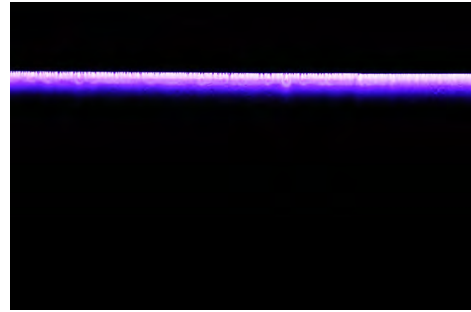


(b) Case Secondary Discharge

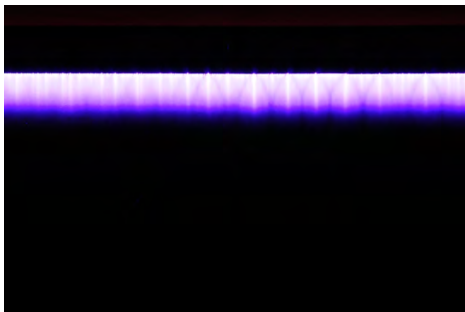
Figure 4.21: The secondary discharge is similar to that of Case 4 but is insufficient to generate a secondary jet. Subfigure (a) illustrates the lack of a secondary jet induce boundary layer trip.



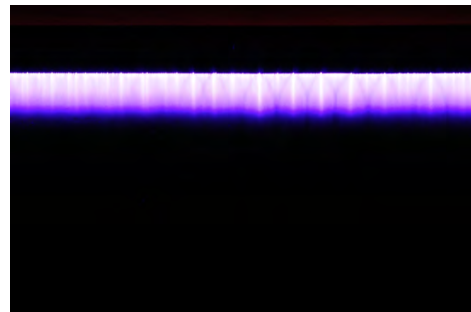
(a) Case 7



(b) Case 8



(c) Case 10



(d) Case 11

Figure 4.22: Cases 10 and 11 displayed a longer discharge that was filamentary in nature, approaching saturation. This resulted in better induced velocity but at the cost of a much higher power consumption.

4.4 Phase III

The primary and secondary electrode potential split of 13 - 2 kV with a 180° phase difference utilized for Phase III Test Case was selected after reviewing the results from Phase I and II. This potential exhibited the best performance in Phase I in terms of maximum downstream velocity and efficiency, although it was noted that the difference between this Case and Case 2 was negligible. Case 7 also developed a 50% higher induced velocity than Case 8 in Phase II, albeit at a sacrifice of efficiency. The velocity profiles of the Phase 3 Cases are presented in Figures 4.23 through 4.29. The profiles show a decreasing jet height with an increase in sliding discharge electrode potential until a secondary discharge was initiated. Increasing the sliding discharge electrode further resulted in a secondary induced jet strong enough to perform as a boundary layer trip, eventually leading to a vertical wall jet.

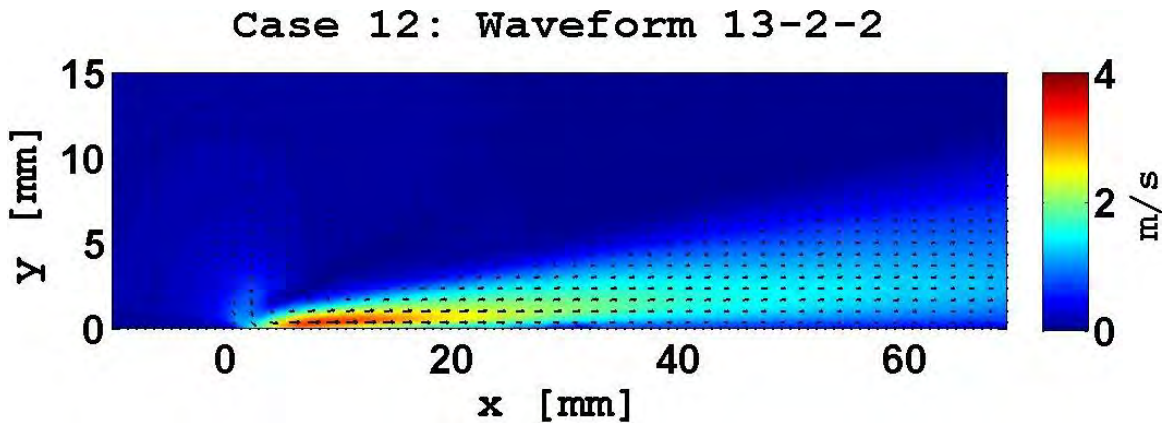


Figure 4.23: Case 12 Velocity Contour Map Results

Case 13: Waveform 13-2-4

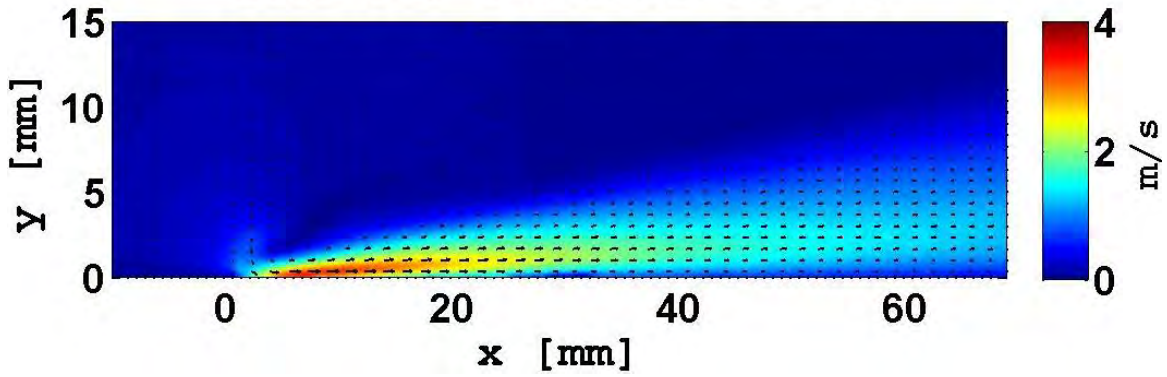


Figure 4.24: Case 13 Velocity Contour Map Results

Case 14: Waveform 13-2-6

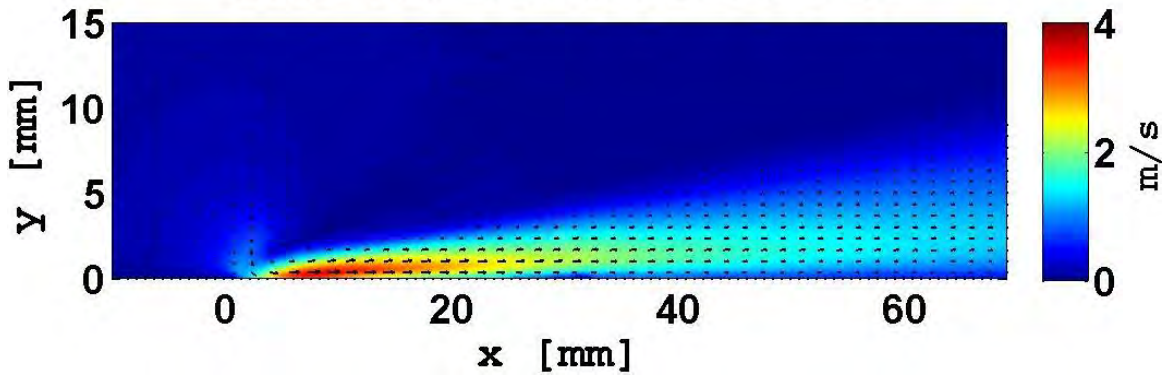


Figure 4.25: Case 14 Velocity Contour Map Results

Case 15: Waveform 13-2-7.5

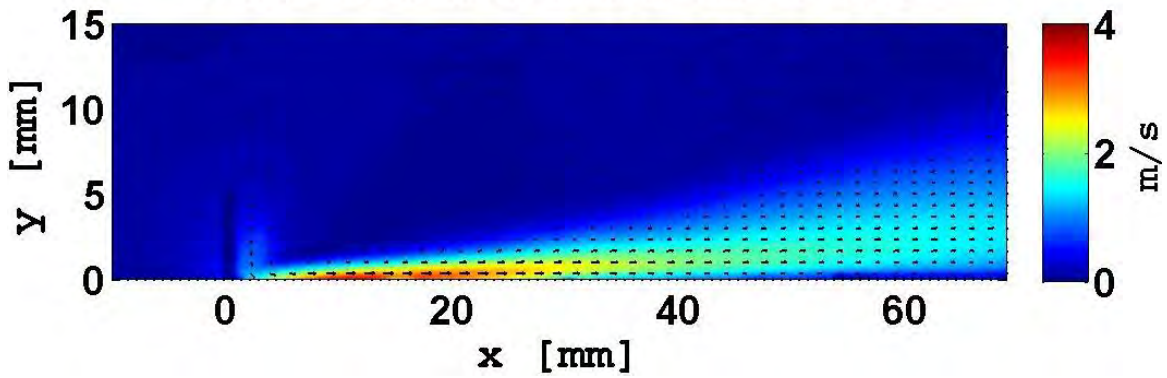


Figure 4.26: Case 15 Velocity Contour Map Results

Case 16: Waveform 13-2-9

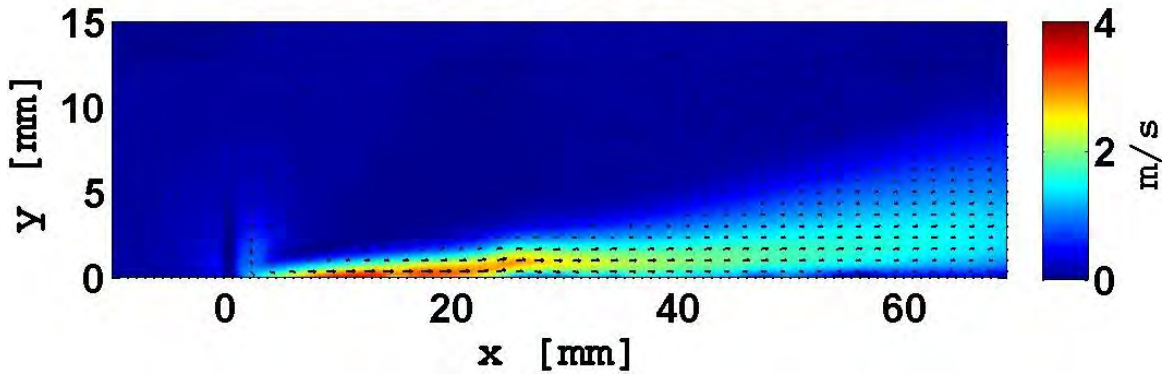


Figure 4.27: Case 16 Velocity Contour Map Results

Case 17: Waveform 13-2-11

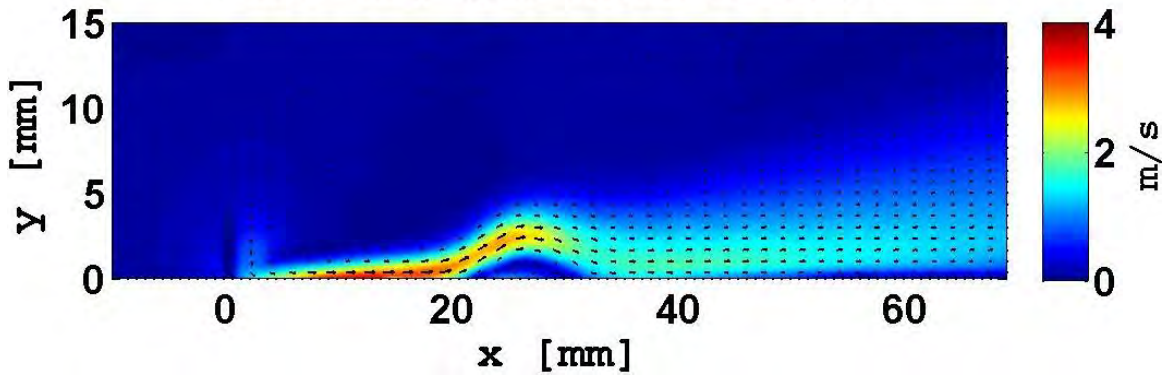


Figure 4.28: Case 17 Velocity Contour Map Results

Case 18: Waveform 13-2-12

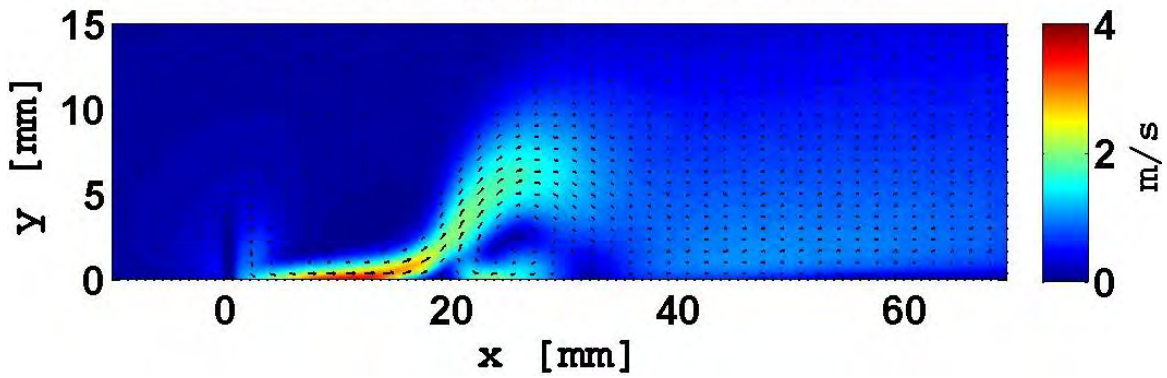


Figure 4.29: Case 18 Velocity Contour Map Results

The results for the Phase III Cases were also examined at the 31, 41, 51, and 61 mm test points except for Case 18 as it produced a near vertical vice horizontal jet. Increases in sliding discharge electrode potentials yielded direct increases in the induced jet velocity until a separation bubble was formed above the sliding discharge electrode. The peak observed velocity was 27% greater than the Baseline Case and 50% greater Case 1. The U/U_{max} profiles for the 61 mm test point are shown in Figure 4.30 and the peak velocities at the other Test Points are tabulated in Table 4.8.

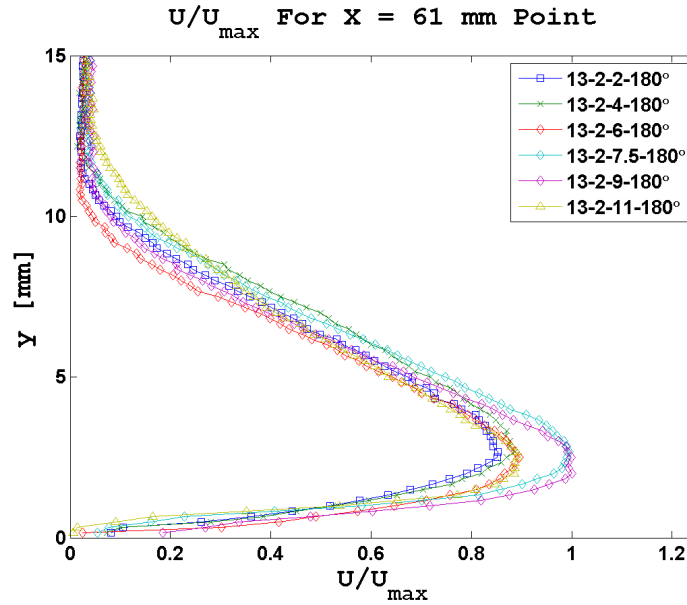


Figure 4.30: Phase III Normalized Velocity Profiles. $U_{max} = 1.52$ m/s.

Table 4.8: Phase III peak wall jet velocities. Peak velocity and error reported in m/s. Case 18 reported as N/A as no wall jet was produced.

Test Case	Potential [kV]	31 mm		41 mm		51 mm		61 mm	
		Vel.	Err.	Vel.	Err.	Vel.	Err.	Vel.	Err.
Case 12	13-2-2	1.96	0.029	1.61	0.026	1.44	0.022	1.30	0.028
Case 13	13-2-4	2.10	0.034	1.71	0.032	1.51	0.029	1.35	0.028
Case 14	13-2-6	2.16	0.030	1.75	0.029	1.54	0.025	1.37	0.025
Case 15	13-2-7.5	2.41	0.030	1.97	0.033	1.70	0.029	1.52	0.027
Case 16	13-2-9	2.40	0.031	1.98	0.032	1.71	0.028	1.52	0.029
Case 17	13-2-11	1.79	0.048	1.75	0.031	1.55	0.028	1.36	0.024
Case 18	13-2-12	NA	NA	NA	NA	NA	NA	NA	NA

Induced wall jet heights were calculated as discussed previously to see if the applied waveform had any affect on jet morphology. Increasing the sliding discharge electrode potential resulted in a shallower induced velocity profile. The Case 16 wall jet was 38% shallower than the jet for Case 1 (the 13-2-0 kV potential). This indicated that the potential on the sliding discharge electrode affected both the wall jet velocity and shape. To further examine the effects on the induced velocity of the wall jets the individual x and y components of the velocity were examined. The data showed that increasing the potential yielded an increase in the x component velocity and a corresponding decrease in y component velocity. This indicates that the induced velocity is more parallel to the dielectric. The Phase III velocity component breakdowns are shown in Figure 4.31. Phase III wall jet heights are listed in Table 4.9.

Table 4.9: Phase III Wall Jets Heights at 31 mm test point.

Test Case	Potential	Induced Jet Height [mm]
Case 12	13-2-2	5.33
Case 13	13-2-4	5.67
Case 14	13-2-6	4.83
Case 15	13-2-7.5	4.33
Case 16	13-2-9	4.17
Case 17	13-2-11	6.17

Electrode potentials and currents were again recorded and used to calculate Test Case power consumption and used to calculate Test Case efficiencies. Case 18 was omitted for the same reason as before. Power consumed increased for all Test Cases that exhibited a secondary discharge. Increased secondary discharge lengths corresponded increases in power consumption. Cases 12-14 consumed nearly the same power despite increasing potentials between those Cases. Table 4.10 contains the Phase III power consumption results.

The most efficient Test Case was Case 14 (13-2-6 kV potential). This Test Case had the largest sliding discharge electrode potential prior to the initiation of a secondary discharge. Case 15 exhibited the largest velocity but consumed a dis-

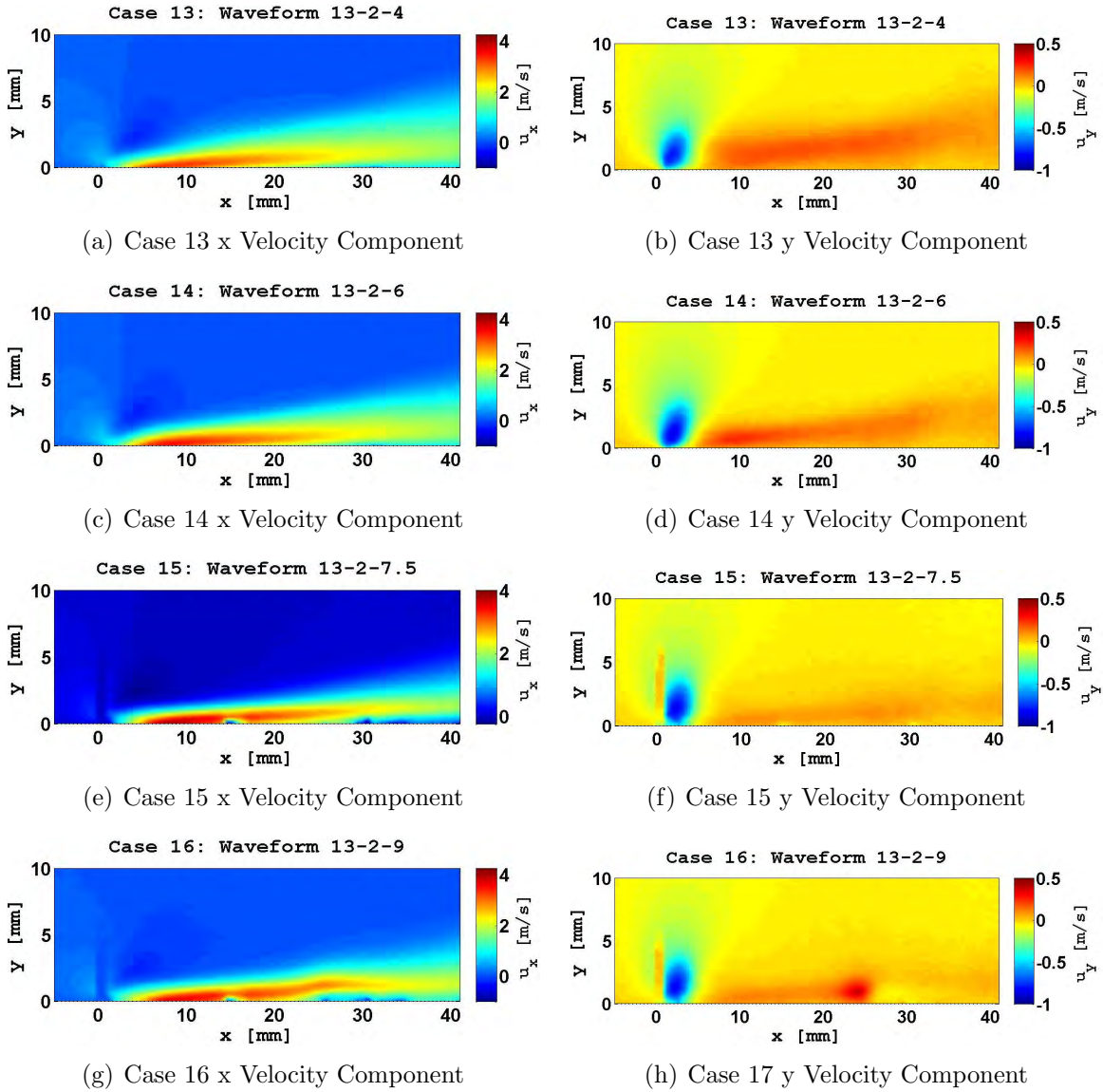


Figure 4.31: Cases 13-16 all exhibit an increasing x component velocity and decreasing y component velocity as the potential on the sliding discharge electrode is increased. Case 16 exhibited an increase in the y component velocity near the sliding discharge electrode caused by the secondary discharge.

Table 4.10: Phase III Power Consumption Results. Power and power error reported in Watts.

Test Case	Potential [kV]	Power	Power Error
Case 12	13-2-2	12.6646	0.3858
Case 13	13-2-4	12.1950	0.3715
Case 14	13-3-6	12.1299	0.3695
Case 15	13-2-7	15.3395	0.4673
Case 16	13-2-9	17.0826	0.5204
Case 17	13-2-11	19.4802	0.5935

proportionate amount of power with the observed secondary discharge. Figure 4.32 shows the normalized Phase III efficiencies at the 61 mm test point.

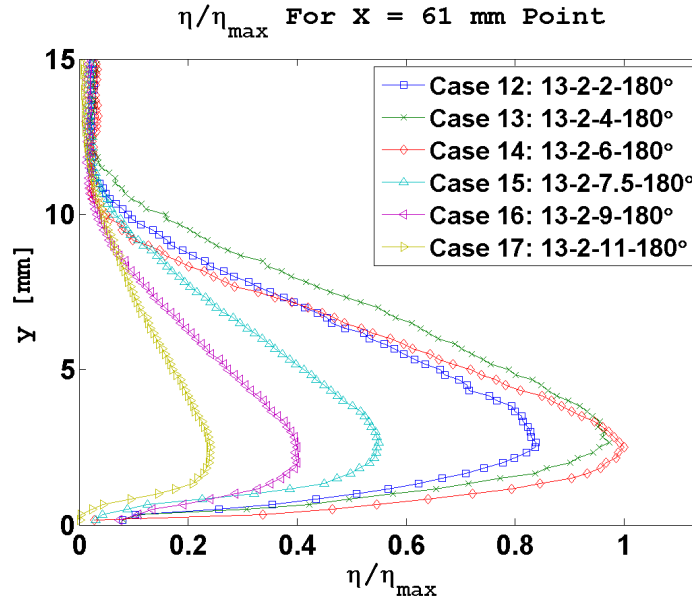
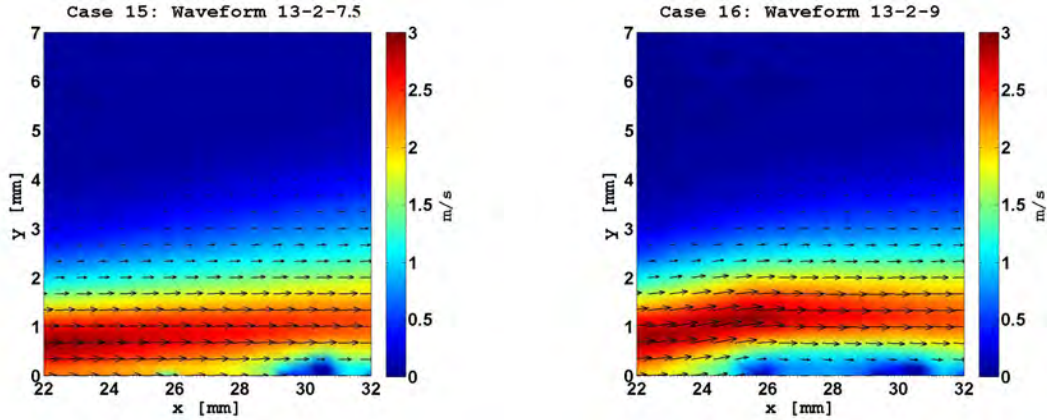


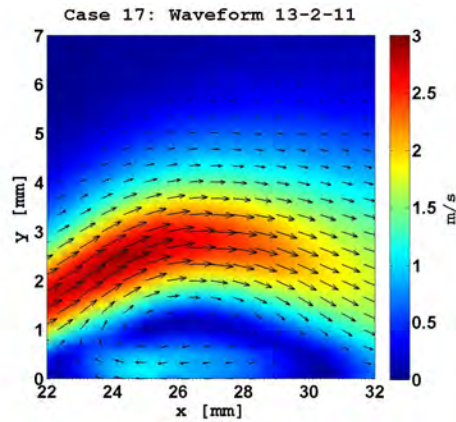
Figure 4.32: Phase 3 Normalized Efficiency Profiles

In the Phase III tests, several trends in the data were apparent that reinforced observations from Phase I and II. First, actuator power consumption and efficiency can be correlated directly to the presence, or lack thereof, of a secondary discharge. Case 16 exhibited the greatest induced velocity performance with the 9 kV bias applied to the sliding discharge electrode. But, this bias also induced a strong secondary discharge that resulted in a 40% increase in the consumed power over the the cases

in which a secondary discharge was not present. The secondary discharges were also strong enough to firmly establish a plasma induced trip in the boundary layer. This trip fully developed boundary layer separation by Case 17. The secondary discharge that developed a suction that drew in bulk air from downstream and tripped the wall jet induced by the primary discharge. A comparison of the sliding discharge electrode regions of Case 15-17 is shown in Figure 4.33.



(a) Case 15 Sliding Discharge Electrode Region (b) Case 16 Sliding Discharge Electrode Region



(c) Case 17 Sliding Discharge Electrode Region

Figure 4.33: Phase 3 Boundary Layer Profiles. As the secondary discharge increased in intensity the flow disruption also increased. By Case 17, subfigure (c), a secondary jet had formed that separated the primary jet away from the dielectric surface.

The discharges of the Phase III Test Cases were similar to those of Test Case 1 which utilized the same primary to secondary electrode potentials. There was no

discernible difference between Case 1 and Cases 12-14, despite the increase in sliding discharge electrode potential. The secondary discharges of Cases 15-18 intensified as the potential on the sliding discharge electrode was increased. Figure 4.34 shows the Phase III discharges in comparison to the discharge of Test Case 1.

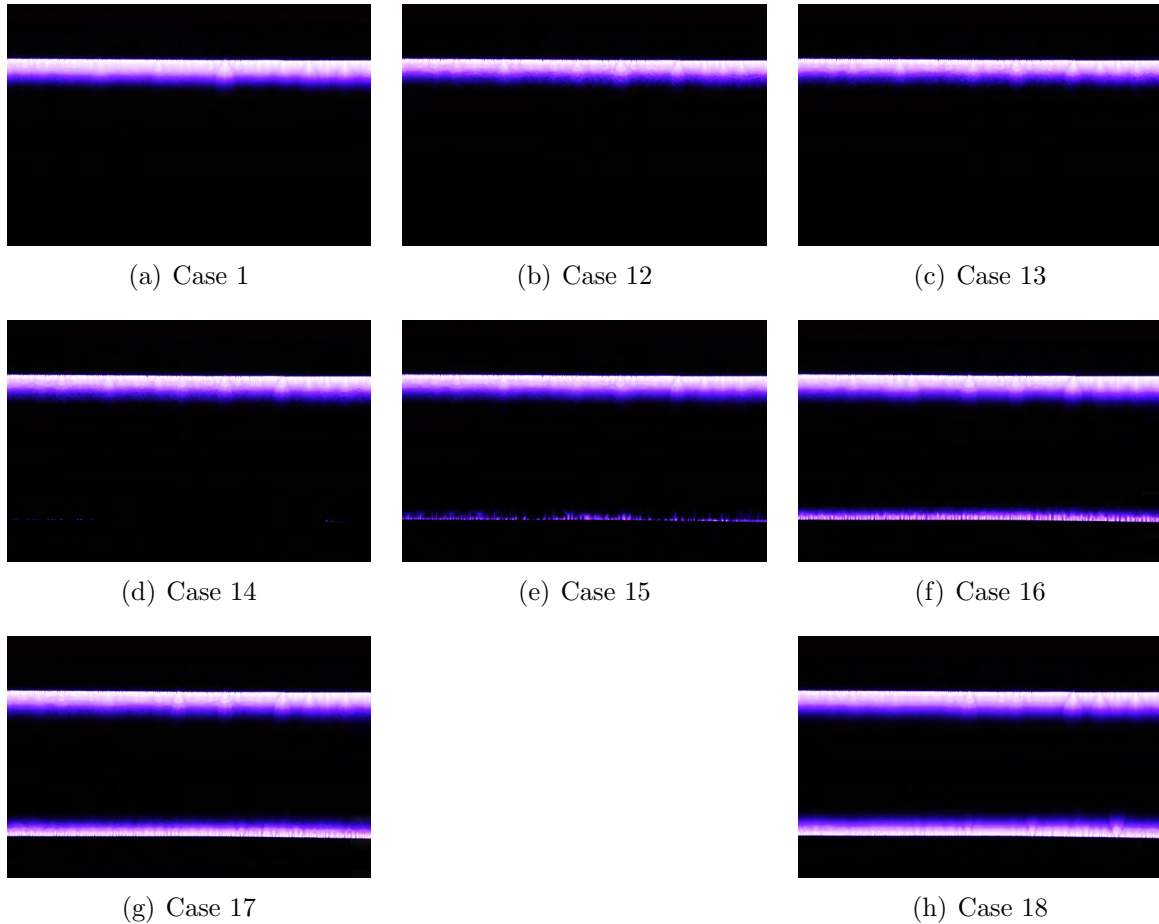


Figure 4.34: Case 1 shown for reference only. Cases 12-14 exhibit only a primary discharge with no discernible differences between the discharges. Cases 15-18 all exhibit both a primary and secondary plasma discharge. The secondary discharge increases in intensity as the the sliding discharge electrode potential is increased.

When the potential on the sliding electrode was increased further to 12.5 kV, the induced jet from the primary discharge fully separated from the wall after colliding with the secondary discharge jet. The vertical jet was similar to those in the Design of Experiments Phase but was angled towards the lower potential exposed electrode.

This suggested that a vertical steerable jet could be developed and controlled by relative potential changes on the two exposed electrodes. Figure 4.35 shows the near vertical jet that resulted.

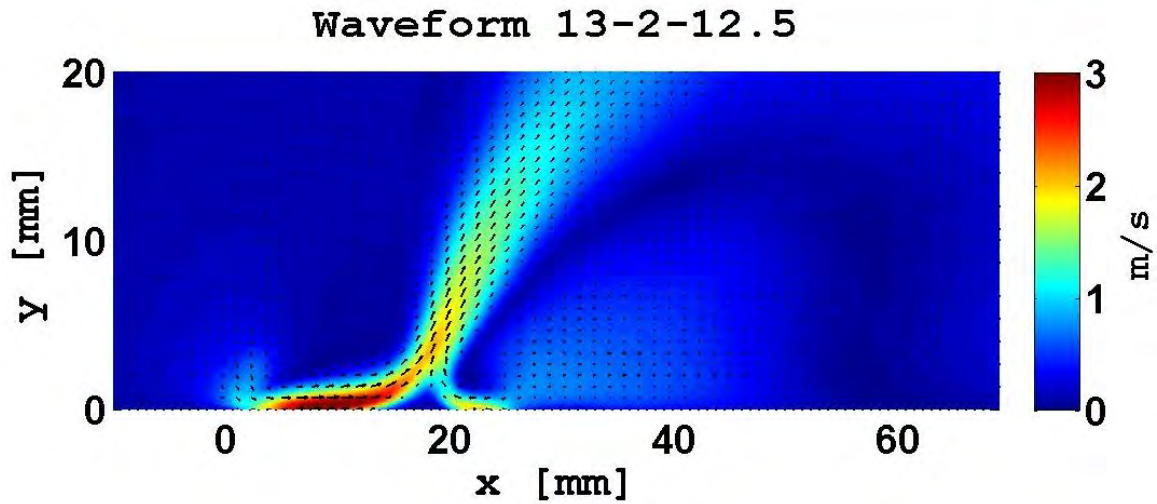


Figure 4.35: Vertical wall jet resulting from a 2.5 kV potential difference between the primary and sliding discharge electrodes.

4.5 Summary

A Final comparison between the three Test Phases was conducted to determine any trends caused by the changes in applied potentials. The velocity performance of the most efficient potential in each phase was examined at all test points. At all test points, Case 14 generated the greatest velocity per watt of input power but had an induced jet 30% shallower than Case 1 and Case 8. As the induced flow traveled downstream, the difference between the optimum cases in each phase decreased. A correlation can be observed between the initial jet height measured at the 31 mm point and the rate of dissipation in total velocity. The peak performance of Case 14 was 20% faster than any other case at the 31 mm point, but due to the shallow nature of its induced flow, it was only 10% faster by the 61 mm test point. The phase comparisons at the 31 and 61 mm test points can be seen in Figure 4.36.

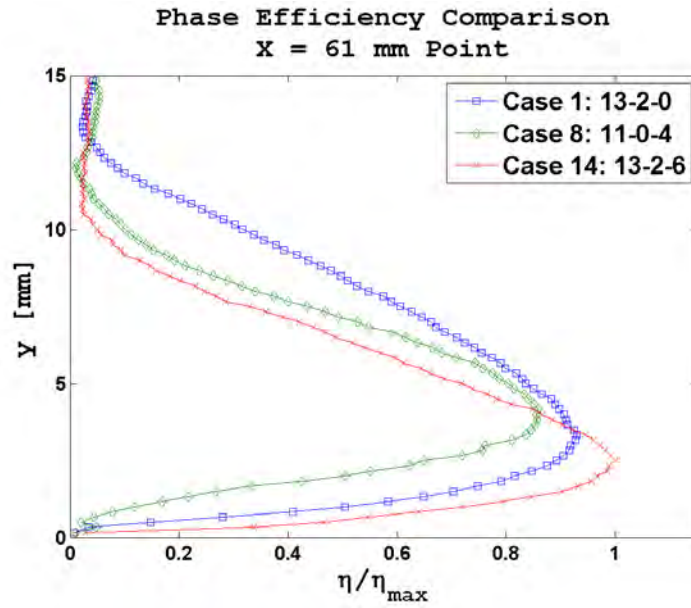
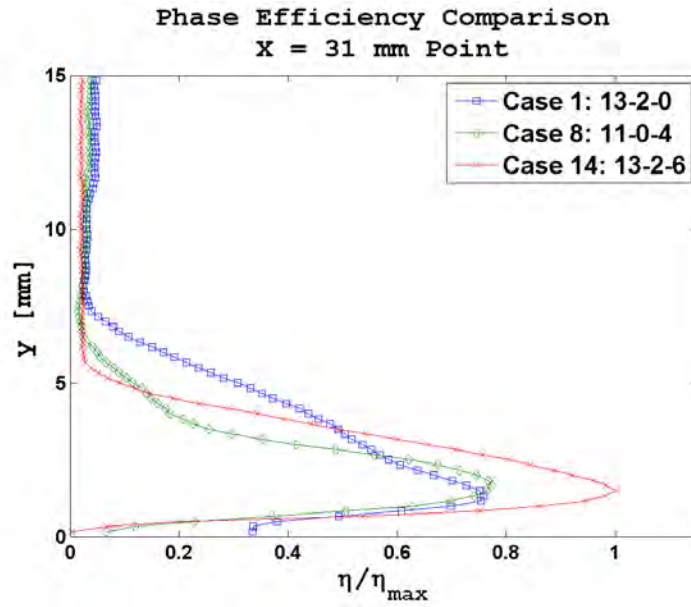


Figure 4.36

V. Conclusions

This chapter presents the preliminary findings of this body of work. Conclusions based on all the test phases are put forth and discussed. Suggestions for future tests and designs are also covered. This work encompassed an extensive examination of the induced velocity profile of a sliding discharge actuator and the effects of applying a third potential to the actuator and many parameters remain to be explored in future works.

5.1 Findings Review

The SDBD actuators most often tested create induced velocities on the order of 2 - 3 m/s and thrust on the orders of mN/m of array [31, 33]. However, surface charge buildup imposes performance limitations during the positive exposed electrode half-cycle. The addition of a third electrode, the sliding discharge electrode, to gather and disperse the surface charge, is examined in this work.

Phase I of this work examined the effects of splitting the primary waveform between the primary and secondary electrode. The results demonstrated that, in the absence of a secondary discharge along the sliding discharge electrode, there is no difference in induced velocity performance between similar split waveforms. Cases 1 and 2 delivered near identical profiles, as did Cases 5 and 6, although Cases 5 and 6 induced slightly higher velocities than Case 1 and 2. This will be discussed further in the section on future work recommendations. The range of applicable primary waveform split for the tested design was found to be such that any waveform with the secondary to sliding discharge electrode potential below 6 kV was acceptable. Any waveform with potential splits beyond that would result in the creation of a secondary discharge and decreased performance.

Phase II examined the effects of splitting the potential between the primary and sliding discharge electrode. The results clearly demonstrated that the primary factor in velocity performance is the potential difference between the primary and secondary electrode. Case 7 with a waveform of 13-0-2 kV produced a peak velocity

35% below that of Case 1 which had a waveform of 13-2-0. Conversely, Case 10 with applied waveforms of 17-0-2 kV induced a peak velocity 22% higher than that of Case 5 which had a waveform of 17-2-0 kV, although at the cost of a much higher power consumption. These results also clearly demonstrated the dramatic differences that resulted from even minor changes in the primary to secondary electrode potential differences.

Phase III explored the effects of applying a waveform to the sliding discharge electrode to alter the electric field in addition to dispersing any built up surface charge. Increasing the sliding discharge electrode potential resulted in increased velocities and shallower induced velocity profiles. Unfortunately the shallower profiles also yielded increased rates of velocity dissipation. Potential differences between the secondary electrode and the the sliding discharge electrode in excess of 6 kV again resulted in the creation of a secondary discharge. The trend of increasing velocity for increasing potential continued, even in the presence of a secondary discharge, until the strength of the secondary discharge was sufficient to cause the primary induced velocity to trip and separate away from the dielectric.

5.2 Future Work Recommendations

The sliding discharge actuator tested was robust and exhibited a peak performance on par with others that have been tested [31]. That being said, an actuator of similar configuration could be expected to achieve even greater performance with another dielectric material with properties superior to those of the silica glass tested. The silica glass demonstrated a tendency to experience failure, either 0.5 mm burn through holes or shattering, when exposed to large applied potentials. The author also believes that there were large fluctuations in the dielectric constant of the glass. The potentials measured on the encapsulated electrode fluctuated as the dielectric between the two exposed electrodes became warm. The silica glass utilized was also brittle, resulting in the minimum dielectric thickness of 1.8 mm.

A dielectric material with better thermal shock values and a higher dielectric constant such as quartz glass or borosilicate glass would have enabled further study and enhanced the actuator performance envelope by allowing greater potential splits to be applied before experiencing dielectric failure. The silica glass utilized required a warm up period of 10 minutes prior to operation to allow for the glass to achieve an even temperature distribution and allow the electrode potential fluctuations to level out. Application of potentials in excess of 17 kV without a warm up period resulted in the shattering of the dielectric. These dielectrics may also contain dielectric constants that are more constant across the operating frequencies and temperatures of the dielectric. A Macor dielectric ceramic should also be tested as it has a dielectric constant of 6.3, nearly twice that of silica glass, can be machined to thinner dielectric layers.

Several issues with the waveforms applied to the electrodes were encountered and two recommendations for the applied potentials are made for future examinations. While a sinusoidal input with no offset was easy to generate and apply, it proved challenging for power measurements and phase matching for any signals not either directly in phase or 180° out of phase with the primary signal. Several potentials with phase offsets of 45°, 90°, and 135° were attempted without success as the resulting inputs, both primary and secondary no longer possessed a sinusoidal form. A circuit containing one way blocking diodes incorporated into the system between the high voltage transformers and the electrodes may eliminate this issue and allow for a more in depth look at the affects of applied potentials to the third electrode.

Upon review of the Phase III results, the 13-2 primary to encapsulated electrode potential was not the ideal choice to examine in Phase III. The potential applied to the sliding discharge electrode acted as an accelerator to the induced velocity. A primary to secondary electrode waveform of 7.5-7.5 kV would have enabled a sliding discharge potential of 13 kV before a secondary discharge would have been initiated. An examination that includes larger secondary electrode potentials is therefore recommended.

The velocity and power consumption data generated as part of this research provide a useful tool for further investigations into the affects that changes in the electric field of a DBD actuator cause in terms of performance. Two pieces of experimental data would have great aid in the understanding of the mechanism and performance of the actuator: time resolved measurements of the accumulation of surface charge as has been measured by others [26,27] on SDBD's and time resolved thrust measurements. While the velocity improvements and the negation in the velocity difference between the positive and negative half cycles indicate a minimization in surface charge accumulation, without direct measurement no conclusions can be drawn as to whether the performance increases resulted solely from an increase in electric field strength or a change minimization in surface charge.

Thrust measurement data coupled with the surface charge data could then be utilized to examine the relative effects of positive and negative ions on the induced thrust and velocity of the actuator. It has been demonstrated that on an SDBD the accumulation of surfaces charges on the dielectric plays a direct role in the amount of thrust generated on each half cycle and that during the positive half cycle there appears to be more self-induced drag by the actuator limiting its thrust performance [26]. A direct examination and comparison between the electric fields and dielectric surface charging of an SDBD, sliding discharge actuator, and a three potential sliding discharge actuator would greatly enhance the understanding of the AC actuated DBD's mechanisms. This data would permit a math model to be constructed that would have taken into account electric field, residual charge on the dielectric surface, and experimental data.

Appendix A. Equipment and Settings

A.1 Waveform Generation Equipment Settings

Table A.1: Test Case Equipment Settings. All Function Generator settings Reported in V_{pp} . N/A settings indicate electrode connected directly to Earth ground. Amplifier settings marked with an * indicates a bridged amplification off of amplifier channels 3 and 4. All frequencies set to 10 kHz.

Equipment:					Function Generator			Amplifier			
					1	2	3	1	2	3	
Test Case	Actual Waveform				Settings			Settings			
Baseline	15	-	0	-	0	8.16 V	N/A	N/A	13	N/A	N/A
Case 1	12.6	-	2.7	-	0	7.0 V	640 mV	N/A	13	13	N/A
Case 2	10.6	-	4.6	-	0	5.68 V	1.927 V	N/A	13	13	N/A
Case 3	9.1	-	6.3	-	0	4.7 V	2.970 V	N/A	13	13	N/A
Case 4	7.6	-	7.8	-	0	3.880 V	3.980 V	N/A	13	13	N/A
Case 5	17.9	-	2.6	-	0	9.26 V	460 mV	N/A	13	14*	N/A
Case 6	18.6	-	3.4	-	0	9.9 V	581 mV	N/A	13	15*	N/A
Case 7	13.5	-	0	-	2.2	7.143 V	N/A	1.21	13	N/A	13
Case 8	11.4	-	0	-	4.4	6.053 V	N/A	2.69 V	13	N/A	13
Case 9	9.7	-	0	-	6.2	5.120 V	N/A	3.68 V	13	N/A	13
Case 10	18	-	0	-	1.8	9.32 V	N/A	585 mV	13	N/A	13
Case 11	18.8	-	0	-	2.7	9.67 V	N/A	1.135 V	13	N/A	13
Case 12	13.0	-	1.6	-	2.25	6.89 V	500 mV	1.0 V	13	13	13
Case 13	12.9	-	1.6	-	3.75	6.89 V	510 mV	2.05 V	13	13	13
Case 14	12.7	-	1.6	-	5.4	6.75 V	630 mV	3.15 V	13	13	13
Case 15	13.3	-	1.6	-	7.5	6.90 V	730 mV	4.35 V	13	13	13
Case 16	13.2	-	1.6	-	9.3	6.90 V	780 mV	5.3 V	13	13	13
Case 17	13.0	-	1.5	-	11.0	6.90 V	800 mV	6.6 V	13	13	13
Case 18	12.9	-	1.5	-	12.0	6.90 V	850 mV	7.0 V	13	13	13

A.2 *Equipment List*

Table A.2 lists the equipment the author utilized in this research.

Table A.2: Test Equipment

Equipment Type	Manufacturer	Model Number
Function Generators	Agilent	3522A
Amplifiers	Crown	XLS 1000
Transformers	Corona Magnetics Inc.	CMI 5530
Oscilloscope	Tektronix	DPO 4032
Voltage Probe	Tektronix	P6015A
Current Monitors	Pearson Electronics	Model 2100
Laser	New Wave Research	PIV 120
Camera	Megaplus	ES 4.0/E4

Appendix B. Data Compendium

The data compendium is comprised of four sections: Design of Experiment, Phase I, Phase II, and Phase III. The design of experiments section contains the full quiver plot and velocity profile results accumulated during that investigation for the SDBD to sliding discharge comparison, phase angle comparison, and the vertical wall jet comparison. The Phase I, II, and III sections all contain similar results. Each section begins with normalized velocity and efficiency profiles for the 31, 41, 51, and 61 mm Test Points. Each Test Case in the designated Test Phase then contains the following Figures:

- Test Case Velocity Profile Plot Versus Distance
- 10 Second Time Averaged Plasma Discharge Photograph
- Test Case Velocity Contour and Velocity Vectors Plot
- x Component Velocity Contour Plot
- y Component Velocity Contour Plot
- Turbulent Intensity Plot: u'/U_{max}
- Turbulent Intensity Plot: v'/V_{max}

B.1 Design of Experiment

SDBD to Sliding Discharge Actuator Comparison:

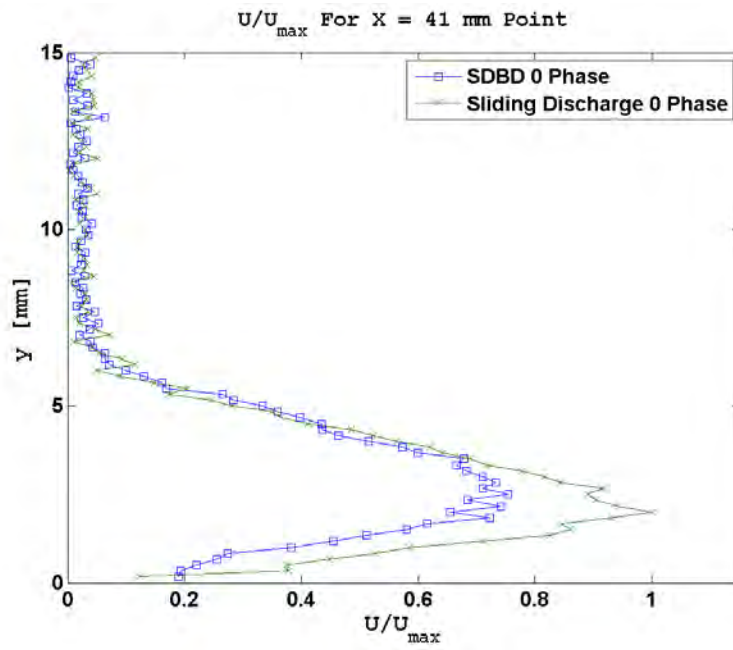


Figure B.1: 0° starting phase angle. Both actuators powered by a 12 kV potential.
 $U_{max} = 1.33$ m/s.

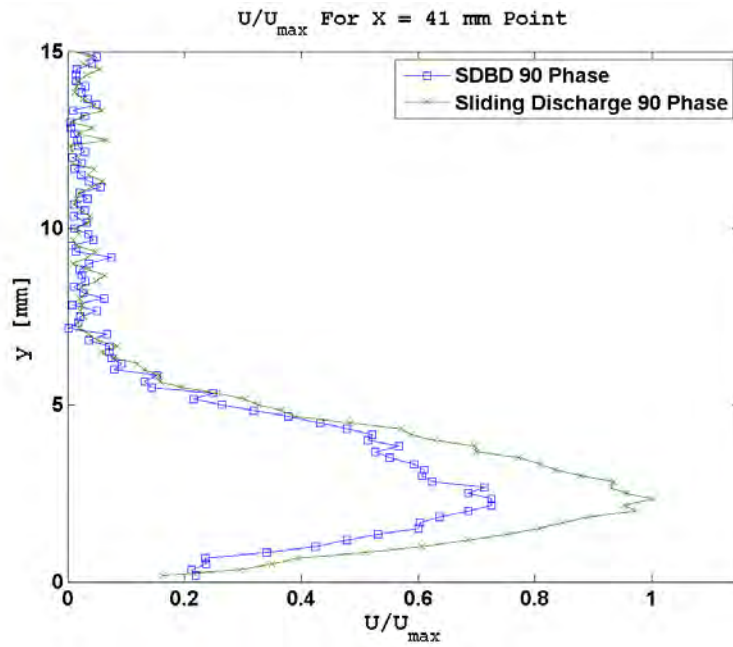


Figure B.2: 90° starting phase angle. Both actuators powered by a 12 kV potential.
 $U_{max} = 1.20$ m/s.

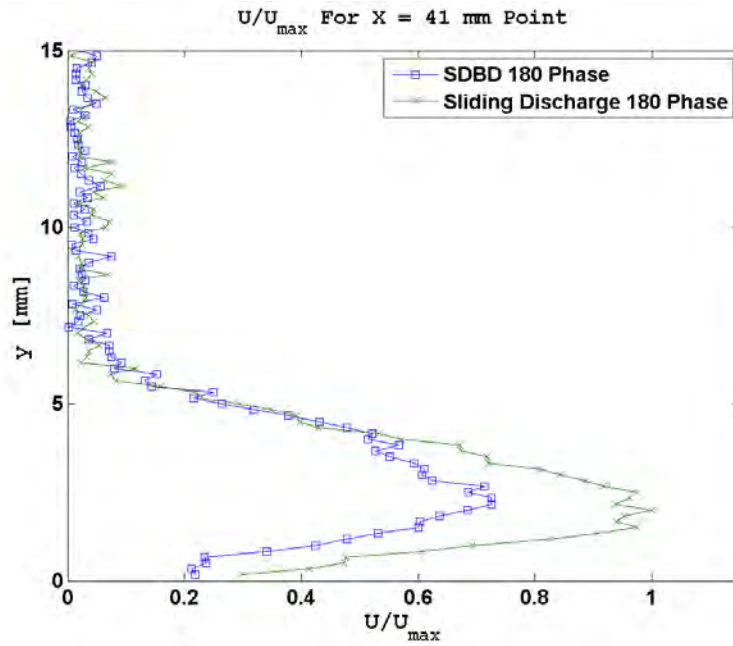
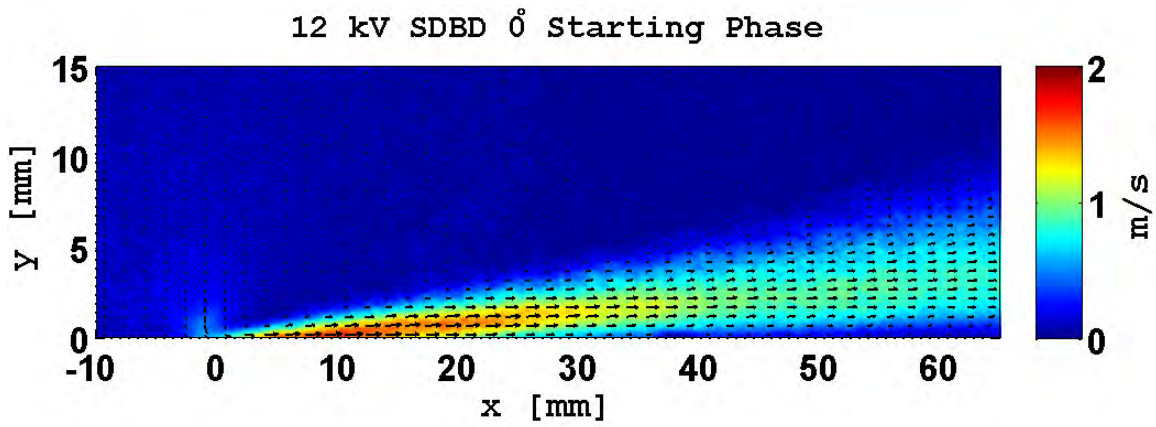
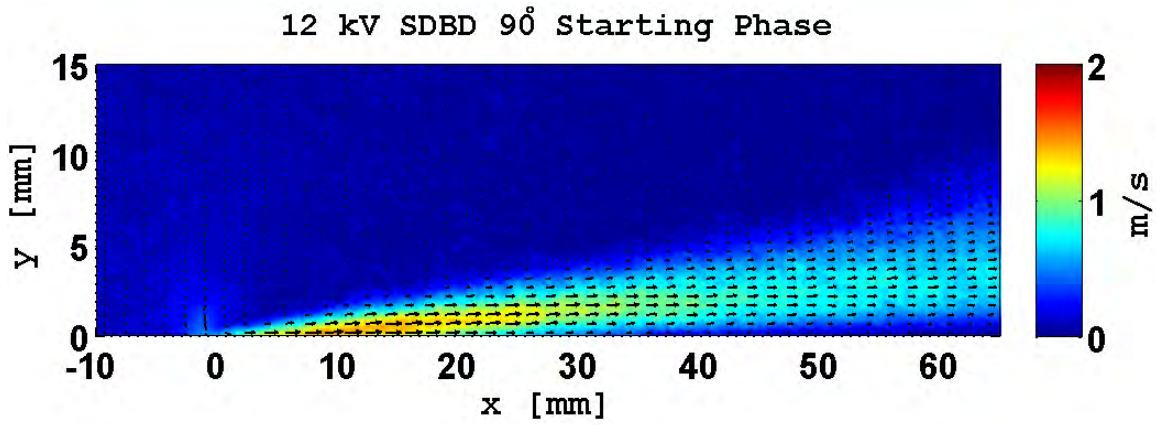


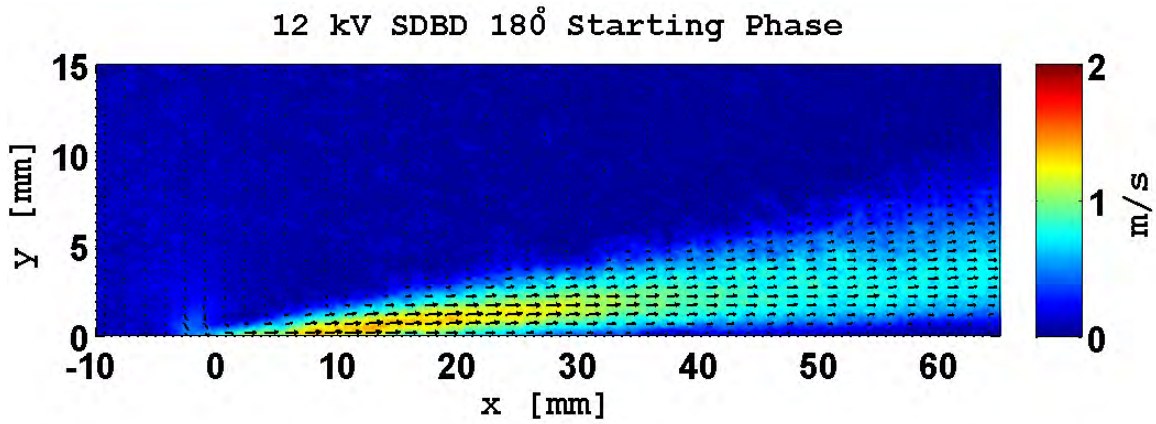
Figure B.3: 180° starting phase angle. Both actuators powered by a 12 kV potential.
 $U_{max} = 1.20$ m/s.



(a) SDBD Velocity Vectors and Contour Map 0° Starting Phase Angle

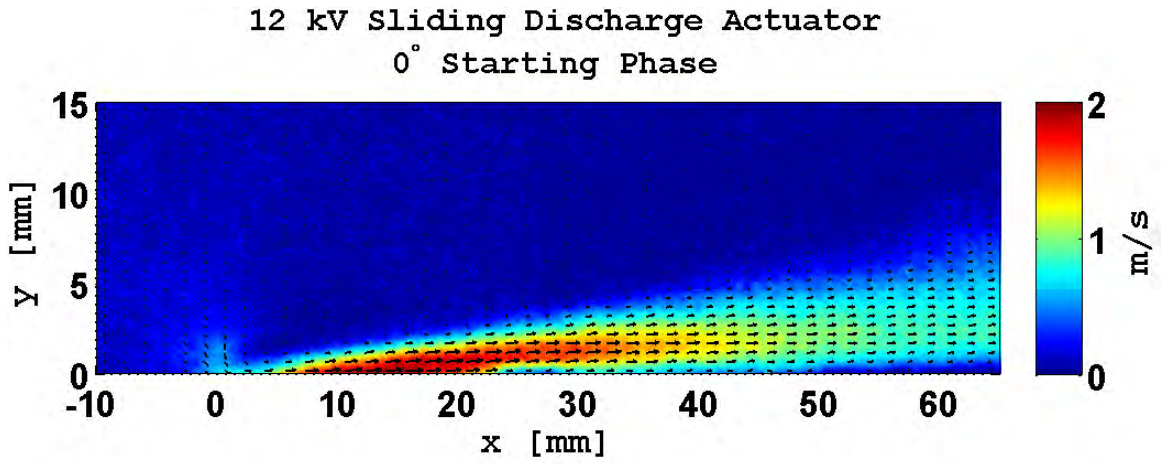


(b) SDBD Velocity Vectors and Contour Map 90° Starting Phase Angle

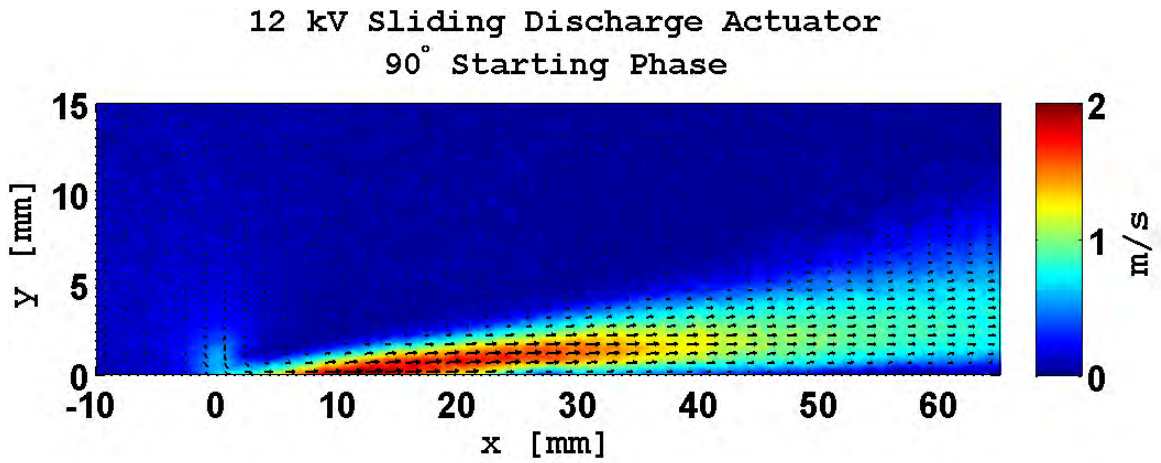


(c) SDBD Velocity Vectors and Contour Map 180° Starting Phase Angle

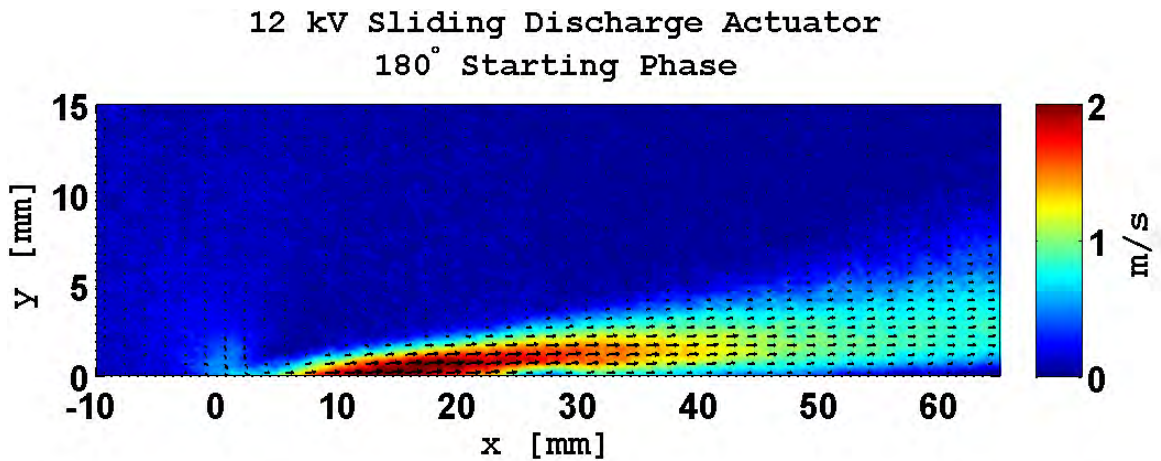
Figure B.4: 12 kV SDBD total velocity contours plots for various starting phase angles.



(a) Sliding Discharge Actuator Velocity Vectors and Contour Map 0° Starting Phase Angle



(b) Sliding Discharge Actuator Velocity Vectors and Contour Map 90° Starting Phase Angle

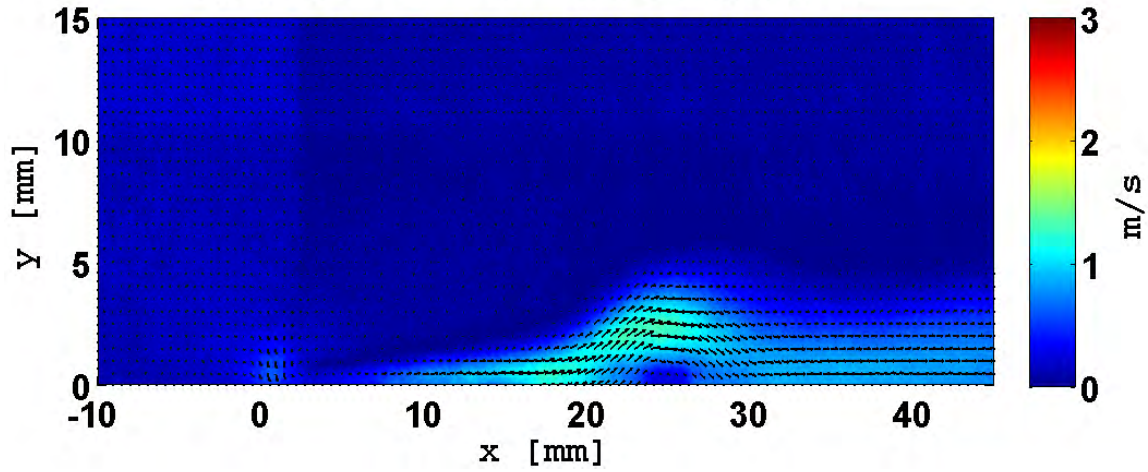


(c) Sliding Discharge Actuator Velocity Vectors and Contour Map 180° Starting Phase Angle

Figure B.5: 12 kV Sliding Discharge Actuator total velocity contours plots for various starting phase angles.

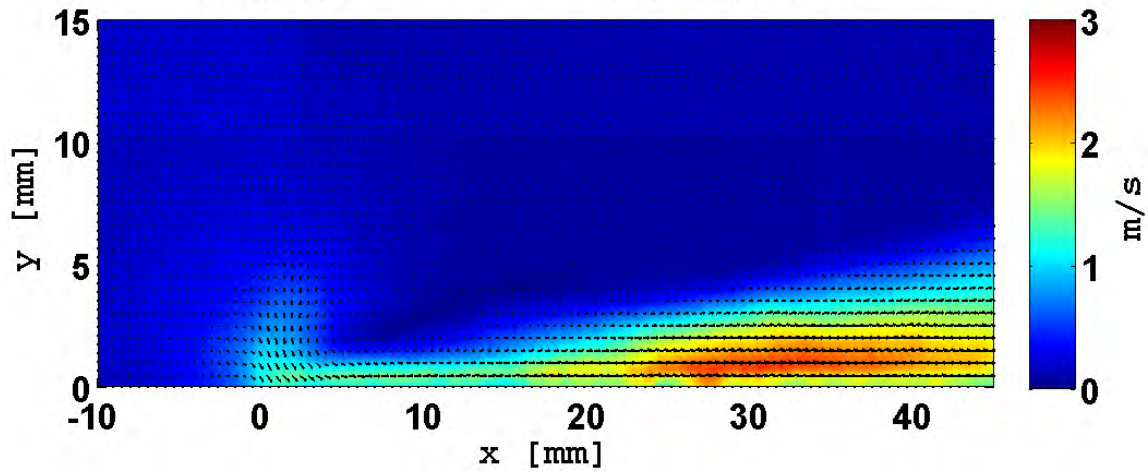
Sliding Discharge Actuator: Encapsulated Electrode Width Comparison

Case A: 12 - 0 - 8 kV Potential



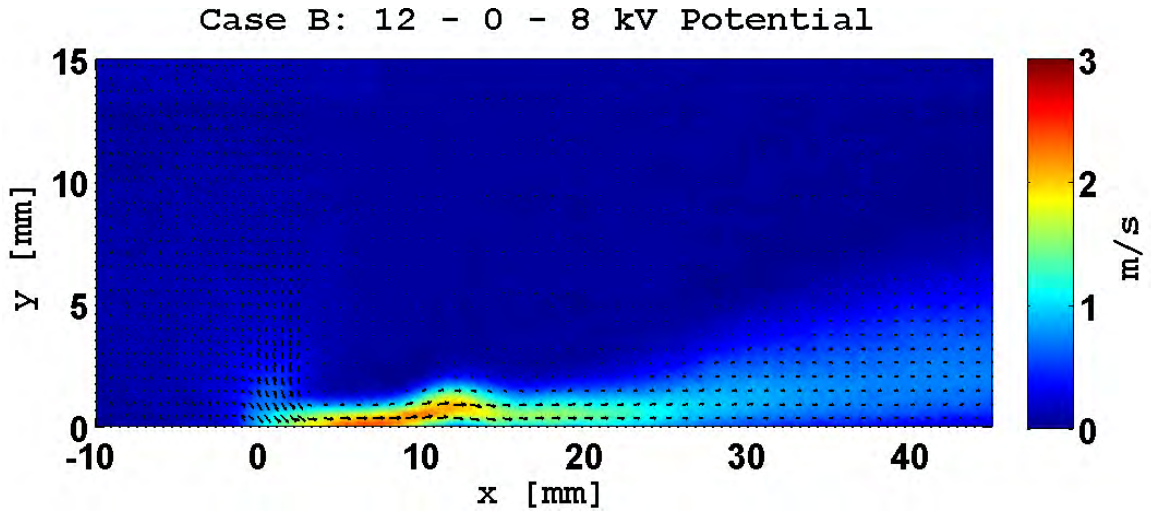
(a) Case A Sliding Discharge Actuator: 12-0-8 kV Waveform

Case A: 17 - 0 - 3 kV Potential

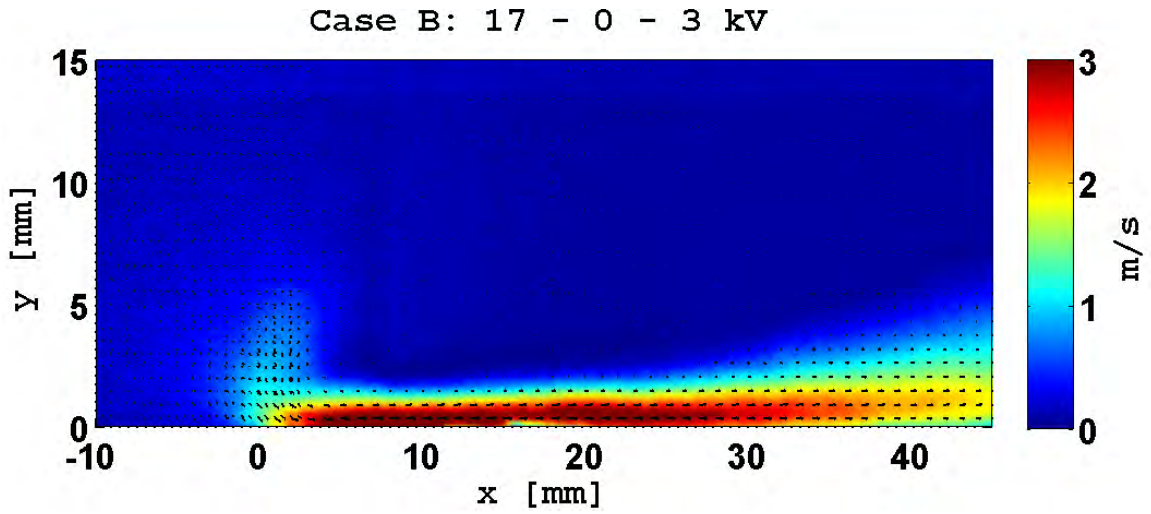


(b) Case A Sliding Discharge Actuator: 17-0-3 kV Waveform

Figure B.6: Case A Sliding Discharge Actuator: 12-0-8 and 17-0-3 kV waveform velocity contour plots.



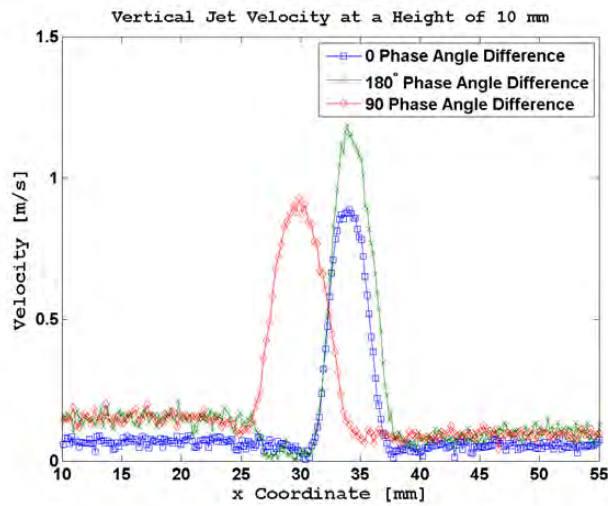
(a) Case B Sliding Discharge Actuator: 12-0-8 kV Waveform



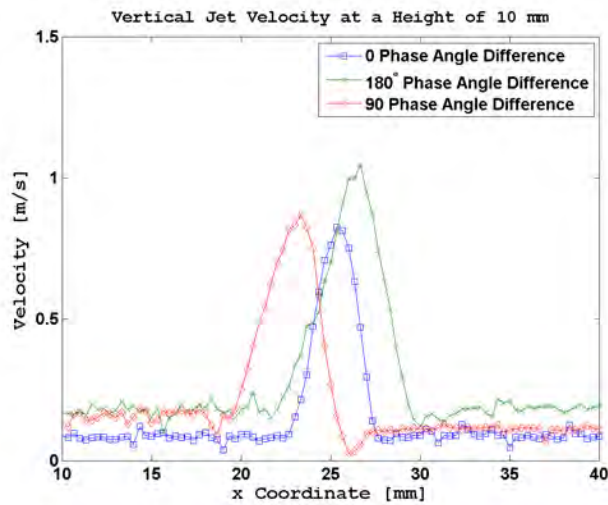
(b) Case B Sliding Discharge Actuator: 17-0-3 kV Waveform

Figure B.7: Case B Sliding Discharge Actuator: 12-0-8 and 17-0-3 kV waveform velocity contour plots.

Vertical Jet Comparisons:



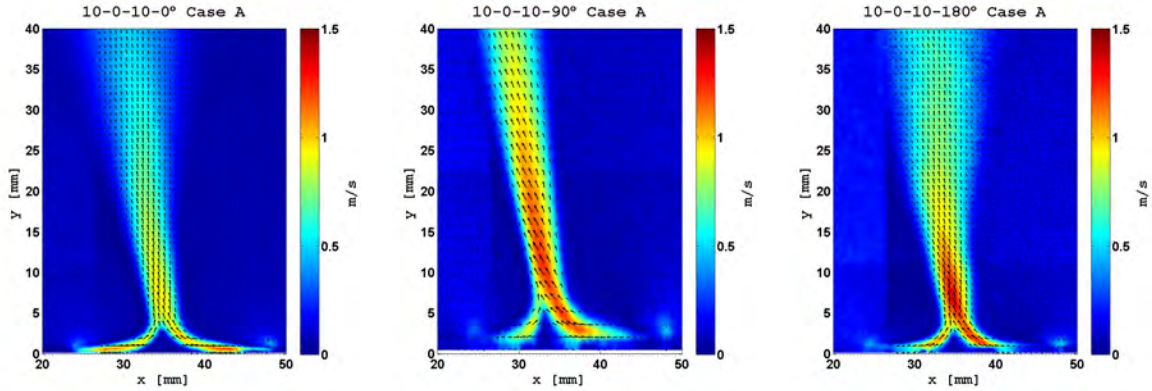
(a) Case A Vertical Profiles By Phase



(b) Case B Vertical Profiles By Phase

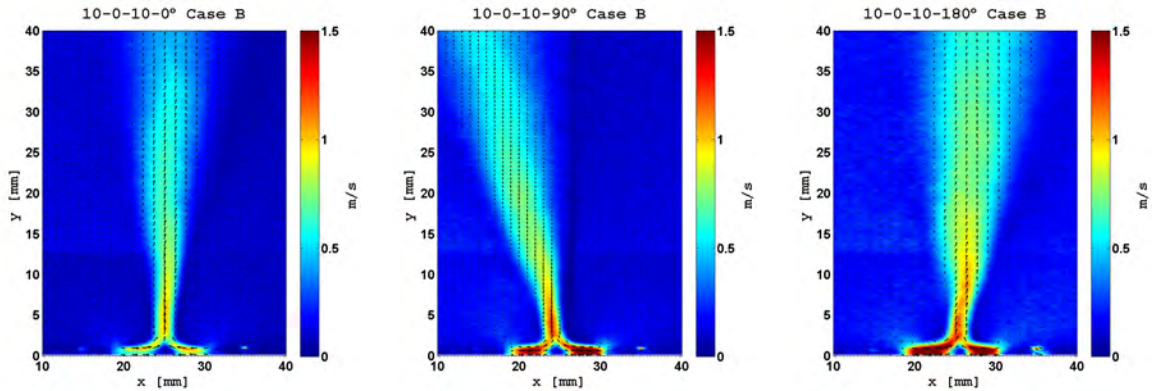
Figure B.8: Case A and Case B vertical velocity profile plots for a height of 10 mm above the dielectric surface.

Figures B.9 and B.10 show that the wider encapsulated electrode produced both higher vertical velocities and a thicker jet, 10 mm versus 5 mm.



(a) Case A Vertical Velocity Contour: 0° Phase Angle Difference (b) Case A Vertical Velocity Contour: 90° Phase Angle Difference (c) Case A Vertical Velocity Contour: 180° Phase Angle Difference

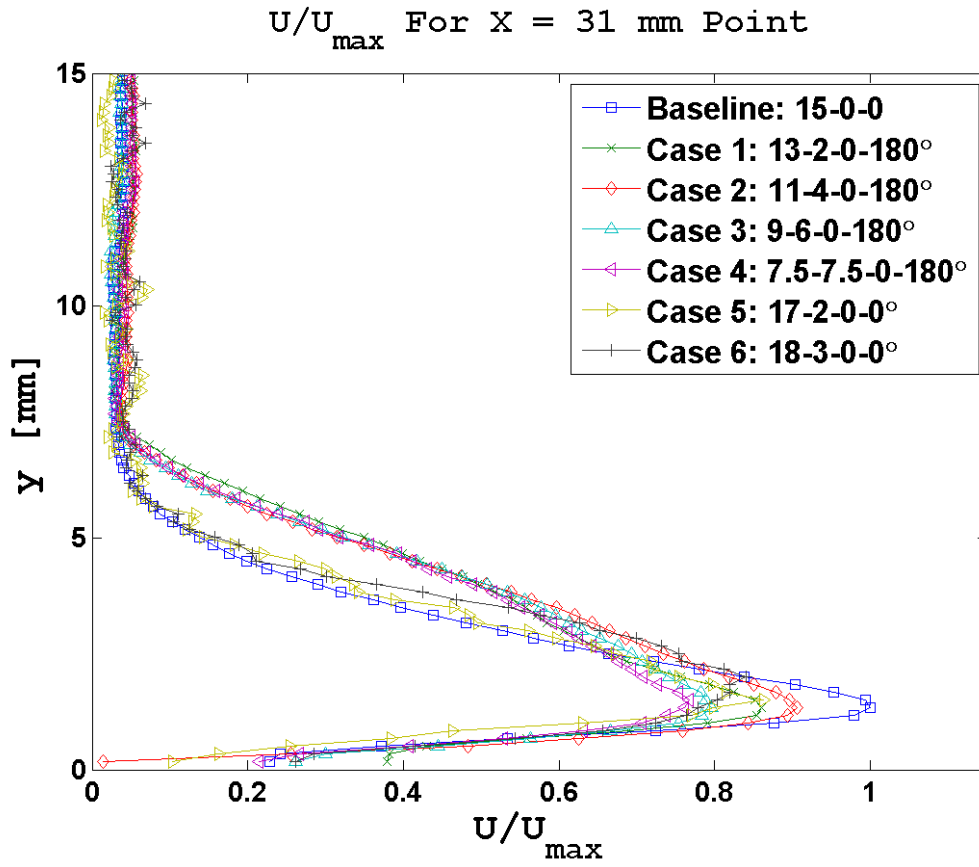
Figure B.9: Case A vertical velocity contours and vectors for phase angle differences of 0,90, and 180 degrees.



(a) Case B Vertical Velocity Contour: 0° Phase Angle Difference (b) Case B Vertical Velocity Contour: 90° Phase Angle Difference (c) Case B Vertical Velocity Contour: 180° Phase Angle Difference

Figure B.10: Case B vertical velocity contours and vectors for phase angle differences of 0,90, and 180 degrees.

B.2 Phase I



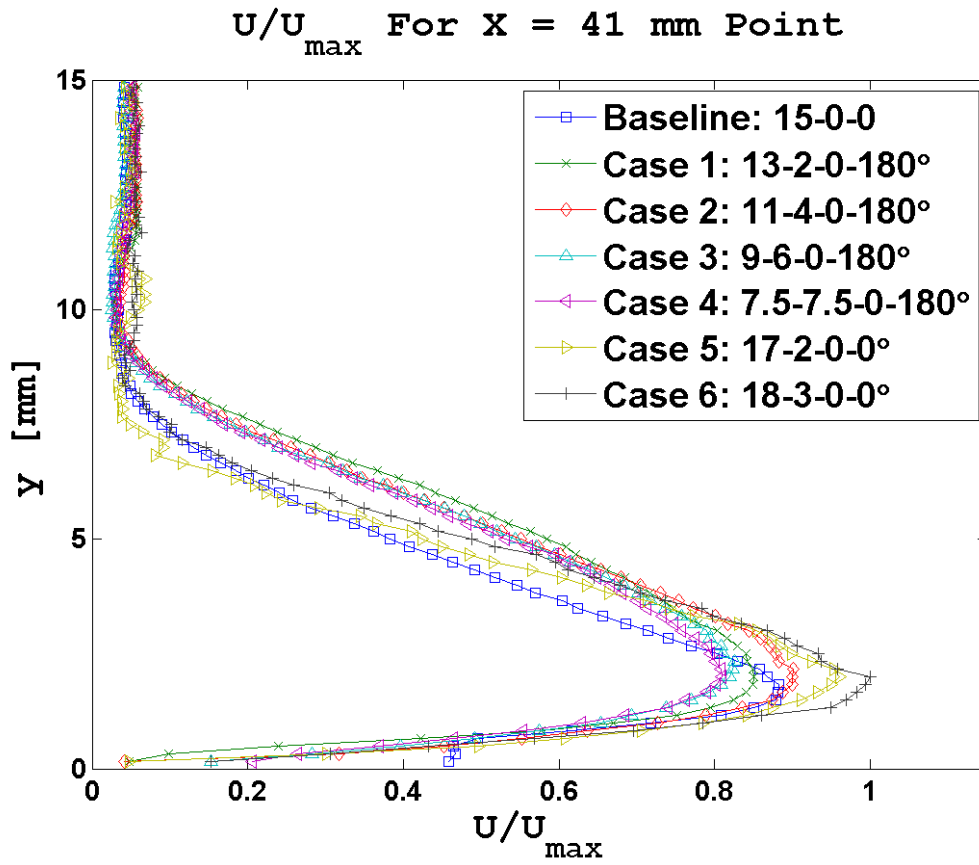


Figure B.12: Phase I Velocity Profiles: 41 mm Point. $U_{\max} = 1.65$ m/s.

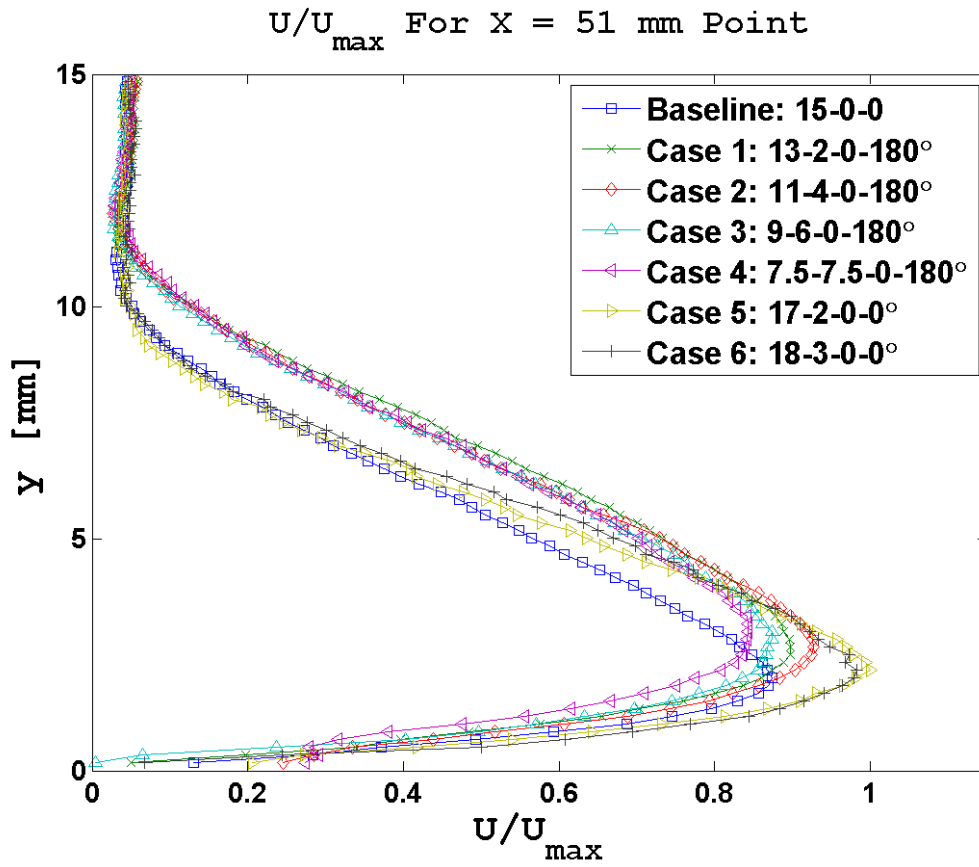


Figure B.13: Phase I Velocity Profiles: 51 mm Point. $U_{\max} = 1.49$ m/s.

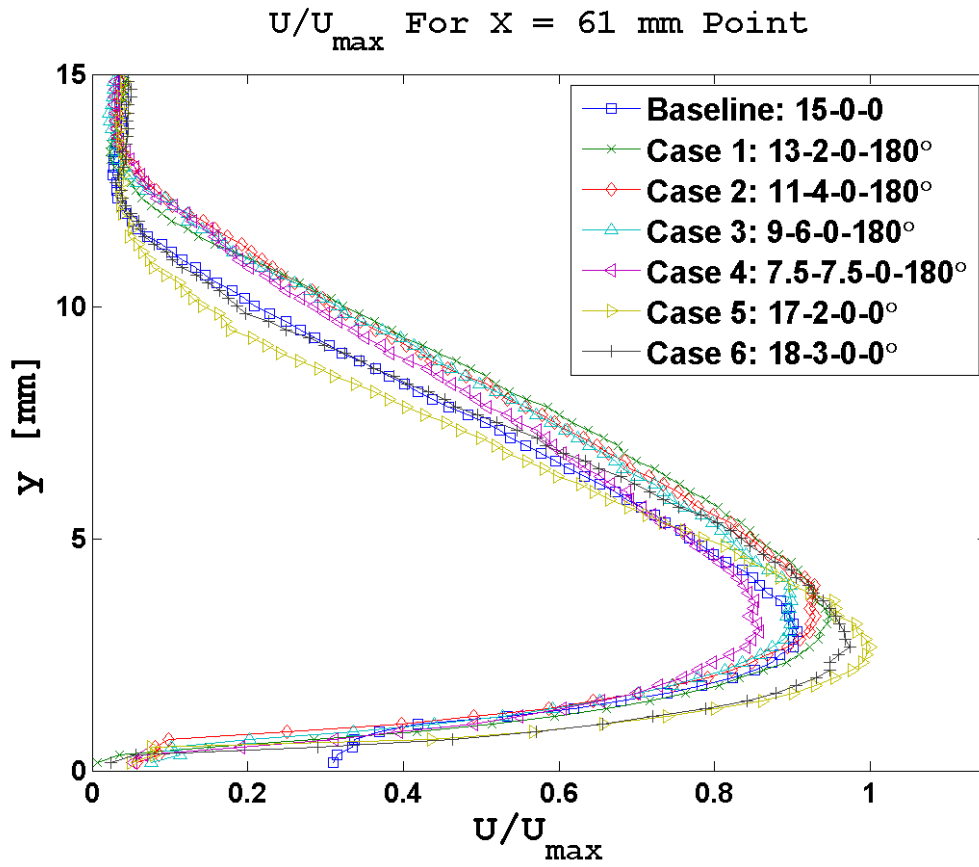


Figure B.14: Phase I Velocity Profiles: 61 mm Point. $U_{\max} = 1.33$ m/s.

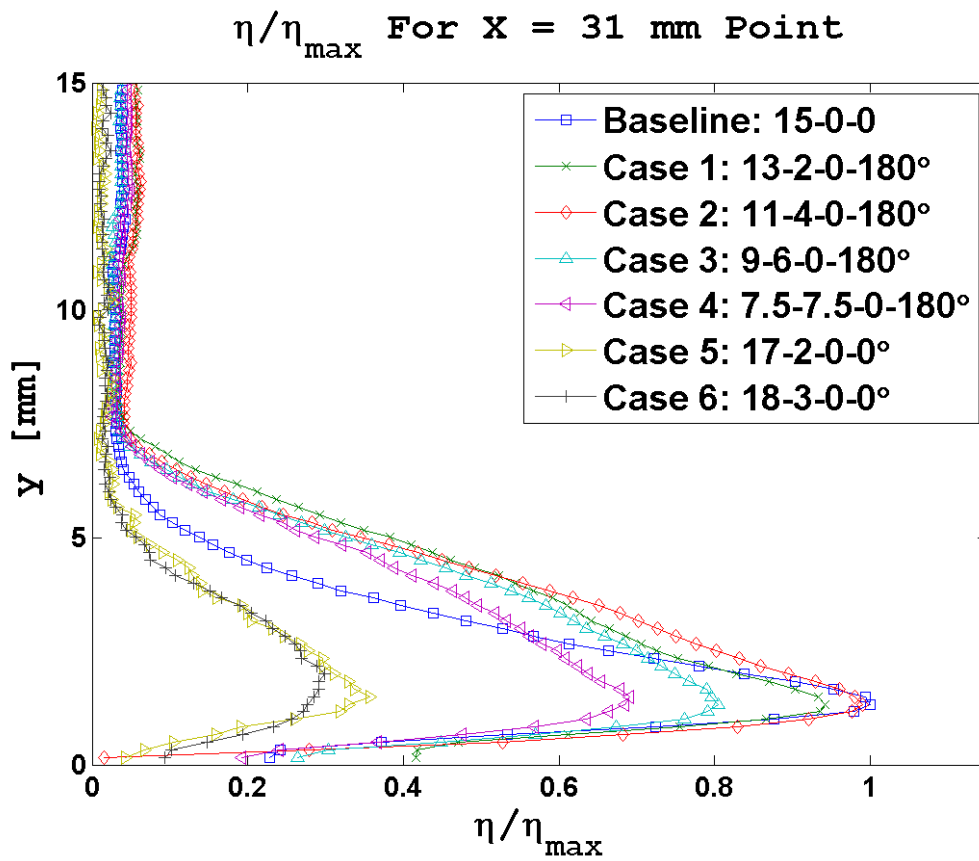


Figure B.15: Phase I Efficiency Profiles: 31 mm Point

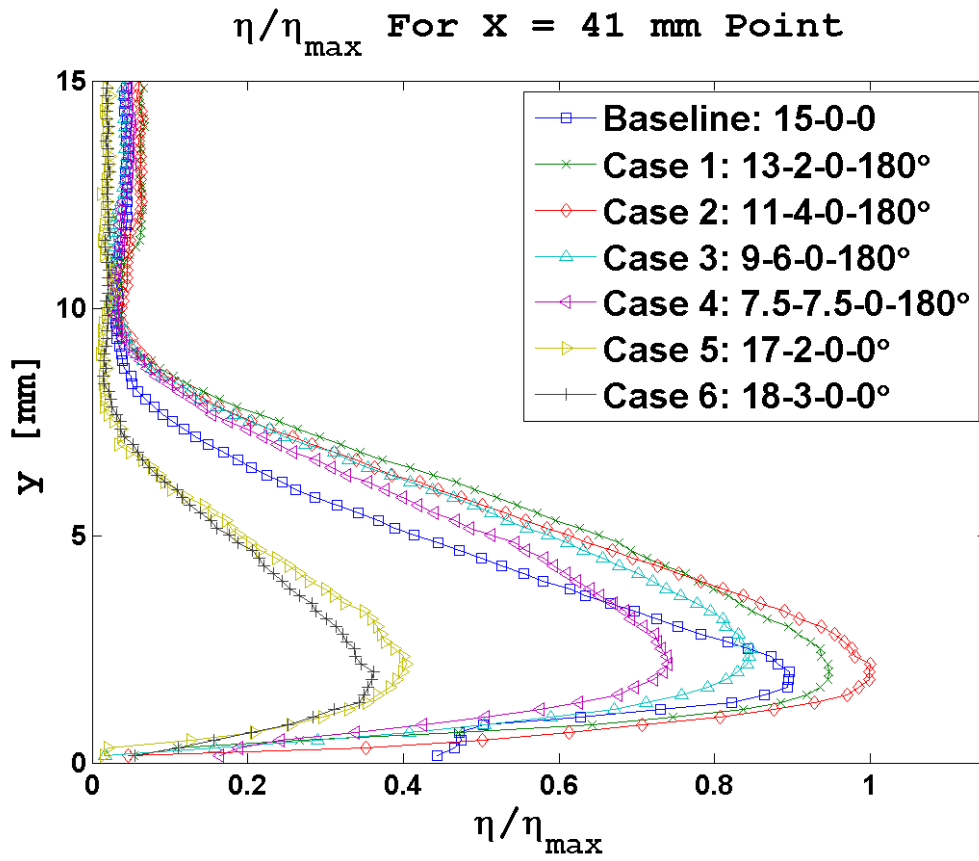


Figure B.16: Phase I Efficiency Profiles: 41 mm Point

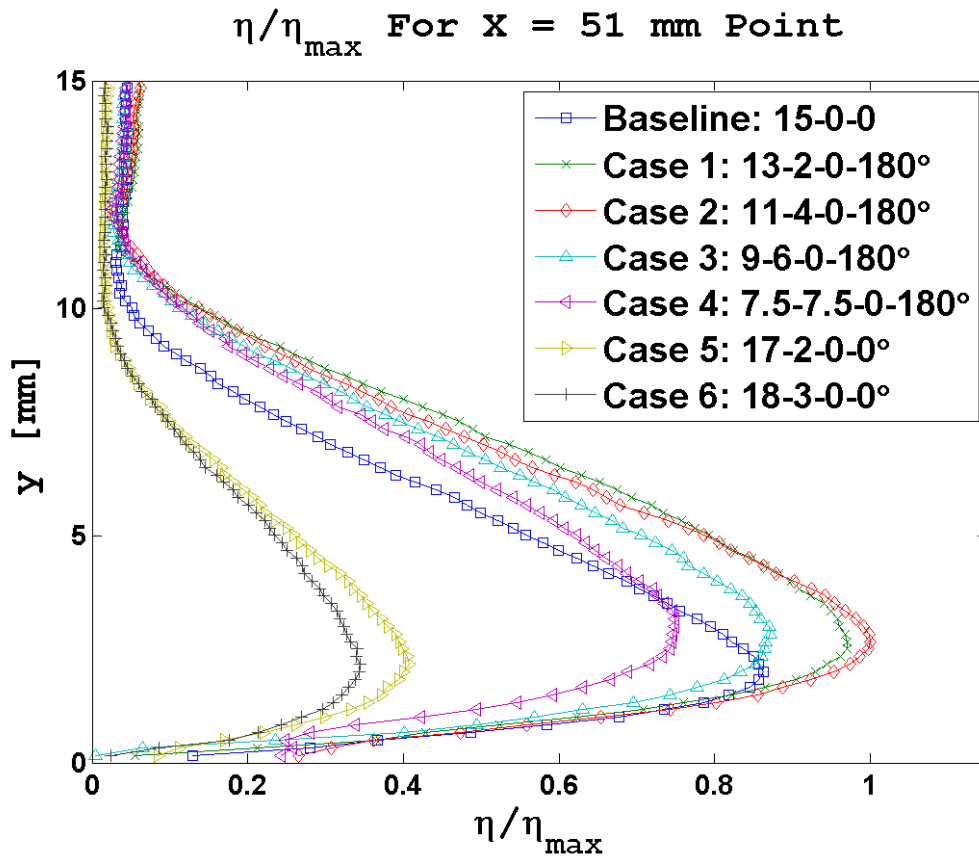


Figure B.17: Phase I Efficiency Profiles: 51 mm Point

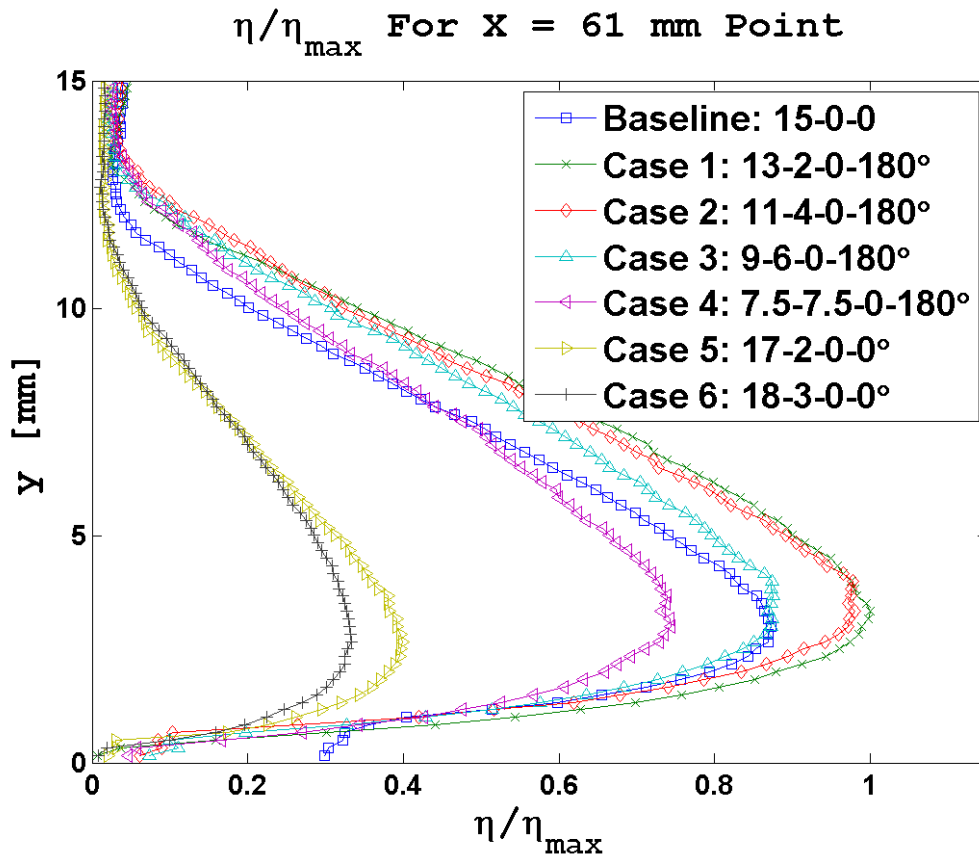


Figure B.18: Phase I Efficiency Profiles: 61 mm Point

Baseline Case: 15-0-0.

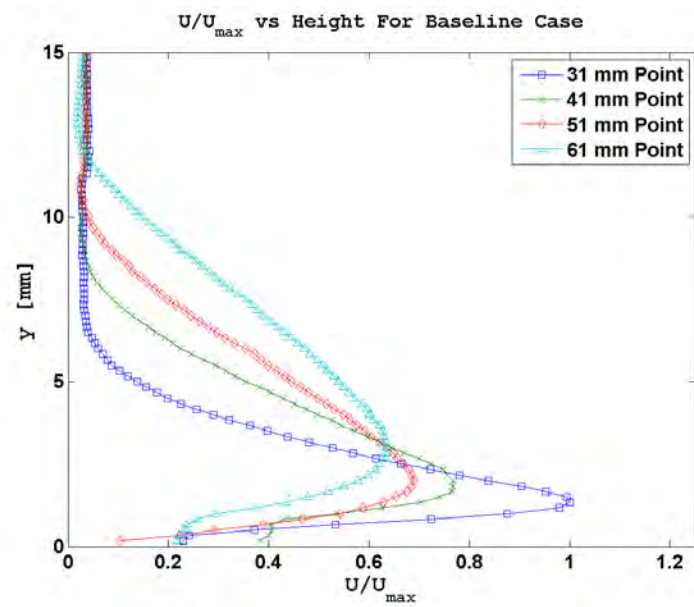


Figure B.19: Baseline Case: U vs Height

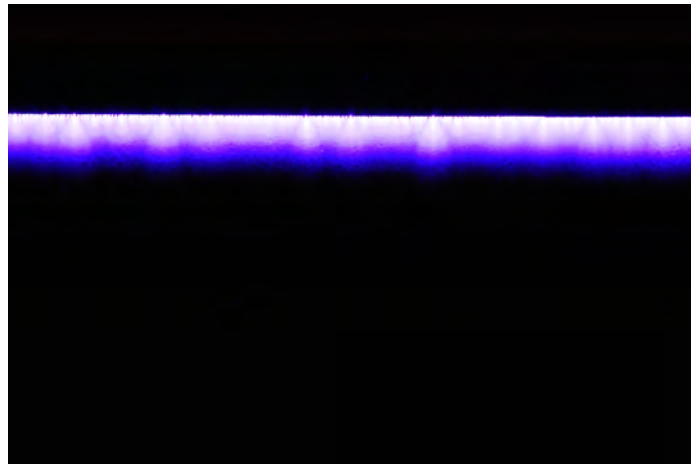


Figure B.20: Baseline Case: Discharge Plume

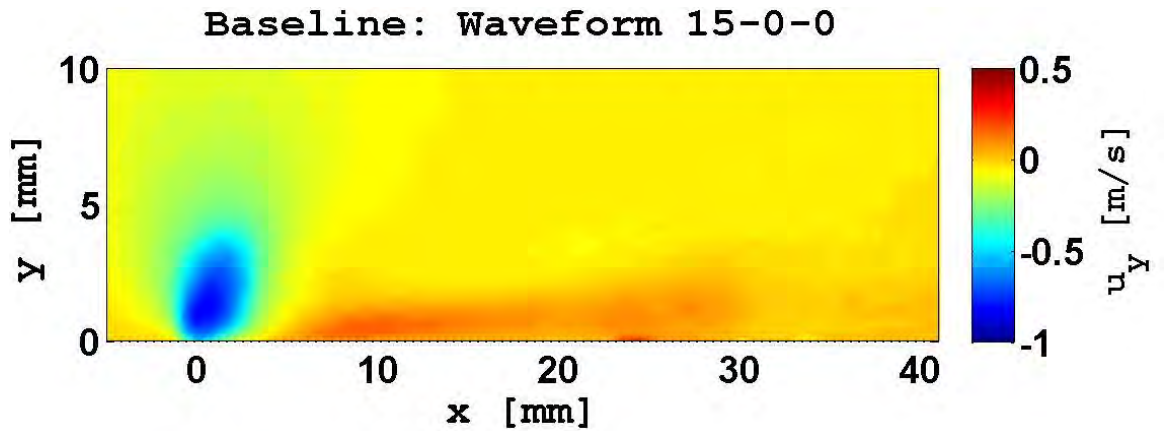
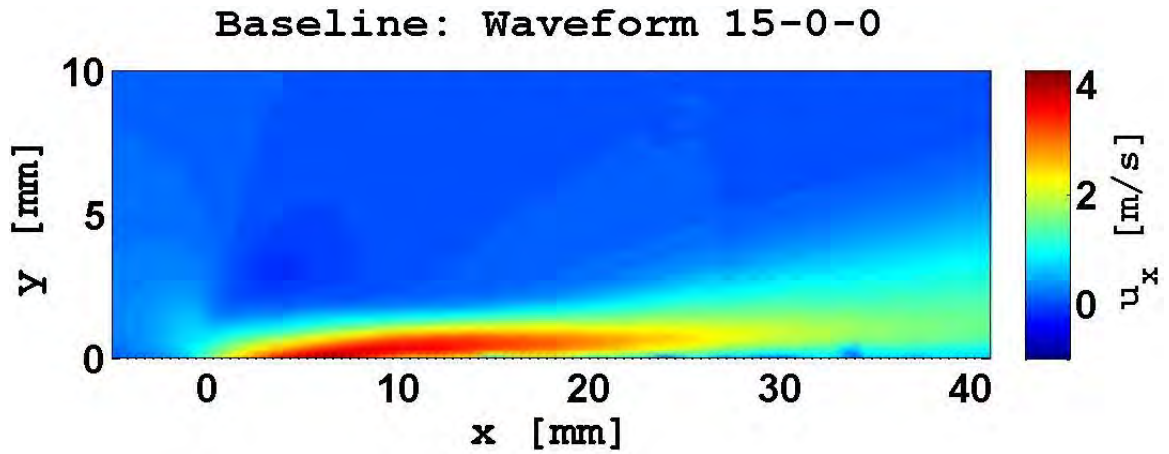
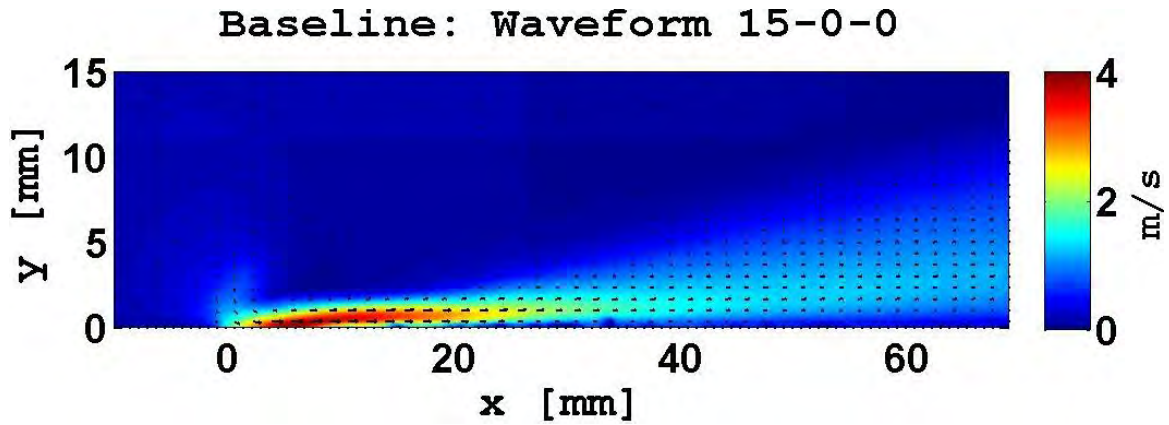


Figure B.21: Baseline Case: Velocity Vectors and Components

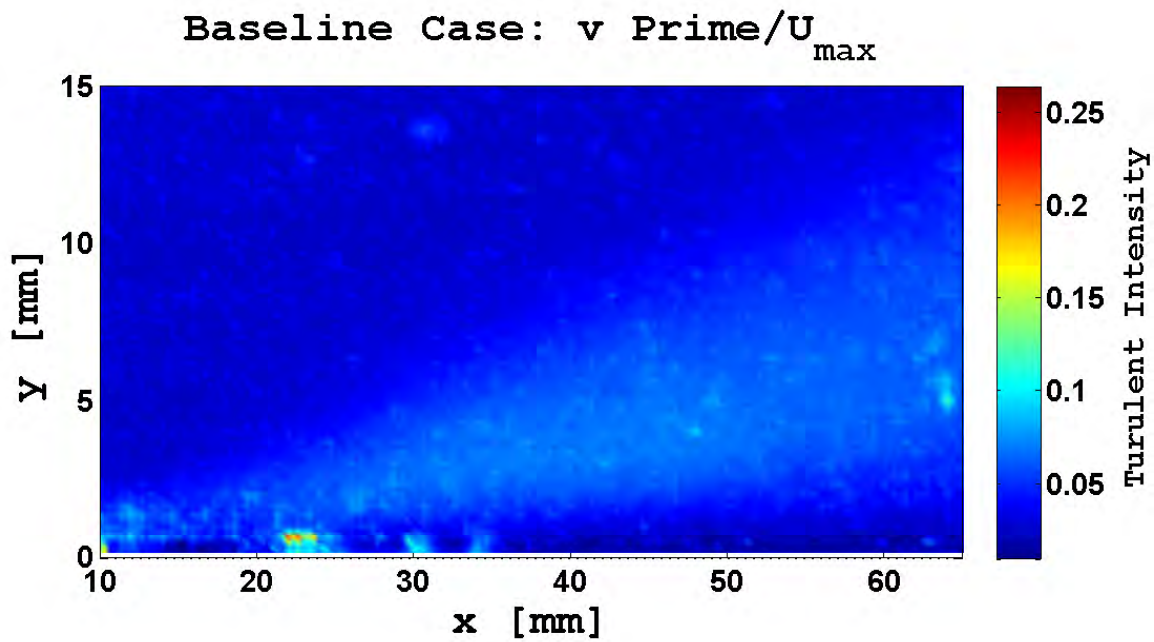
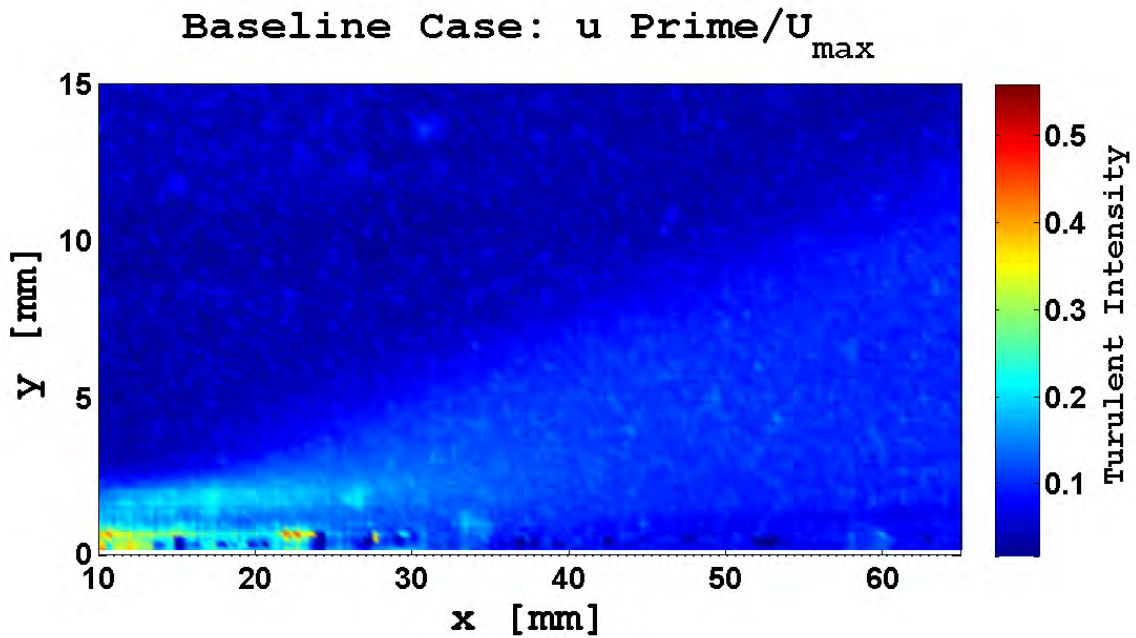


Figure B.22: Baseline Case: Turbulent intensities. The x component intensity is fairly constant but the induced jet boundary is clearly demarcated. The y component intensities are larger, but the induced jet boundary is still clearly demarcated.

Test Case 1: 13-2-0.

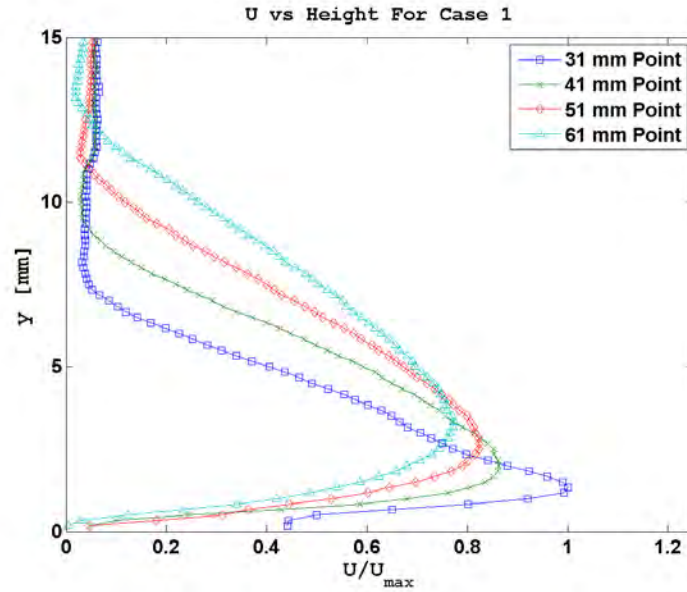


Figure B.23: Case 1: U vs Height

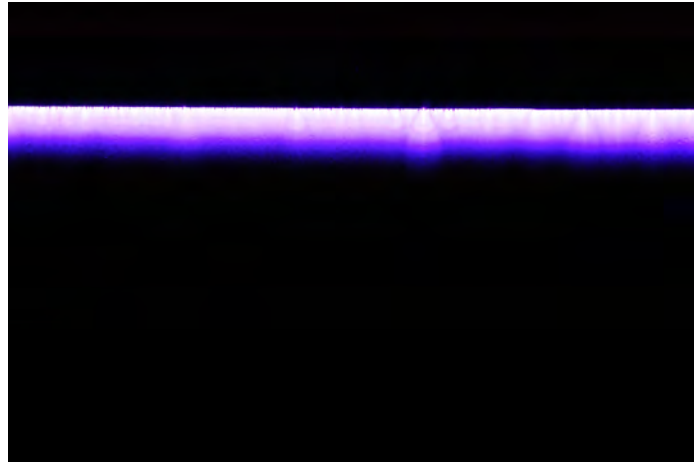


Figure B.24: Case 1: Discharge Plume

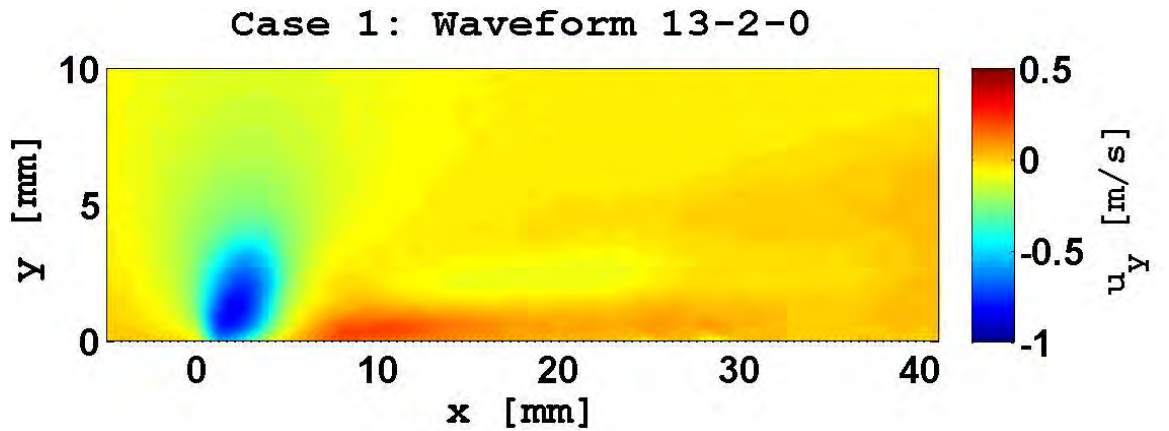
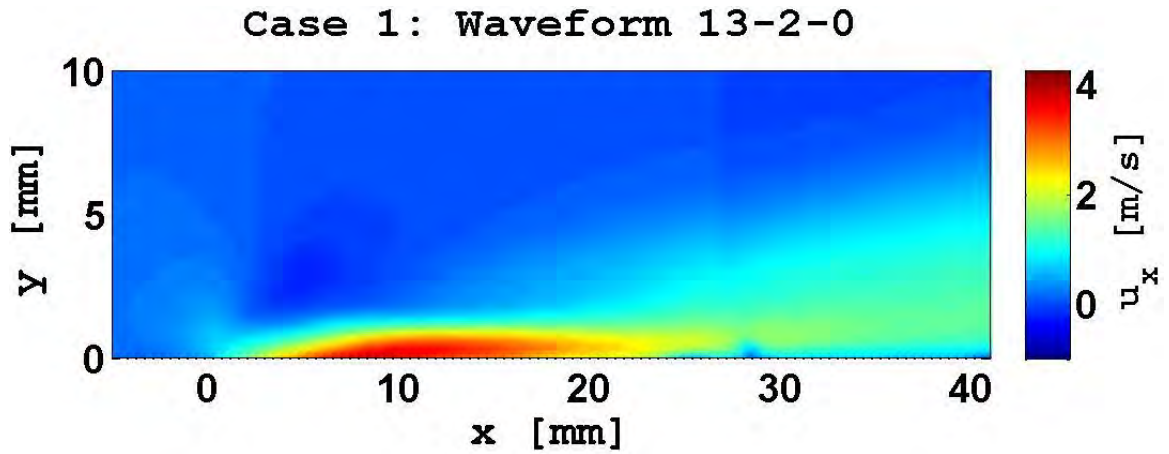
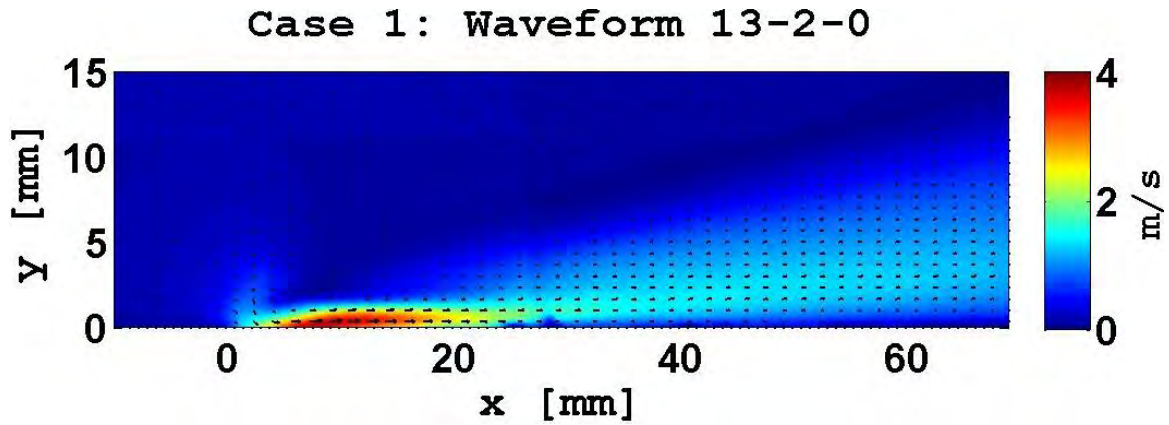
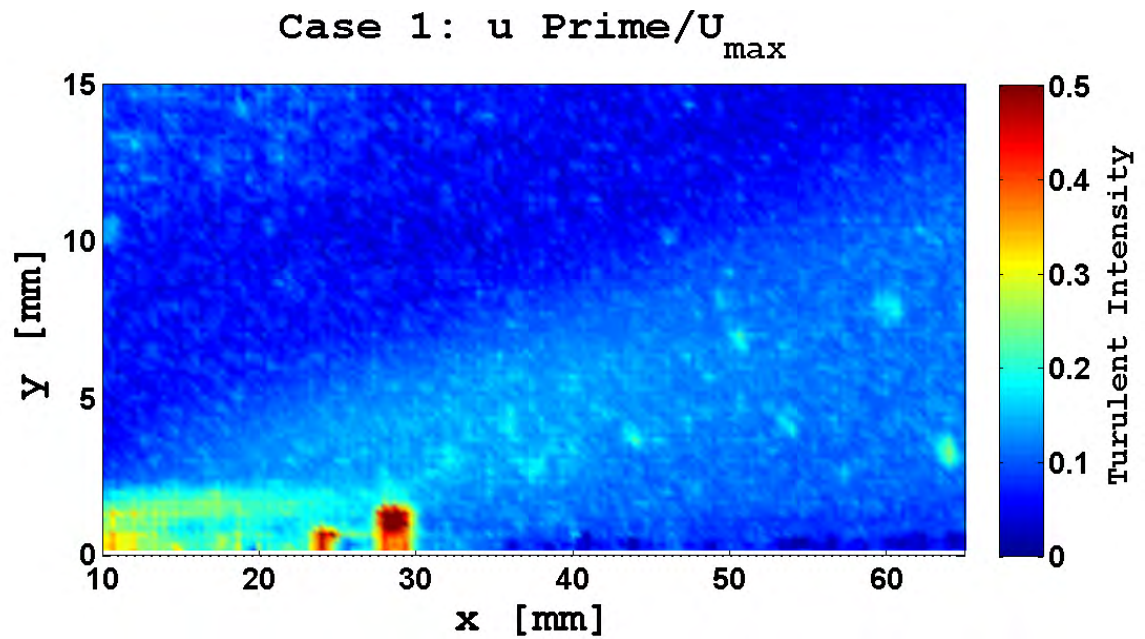
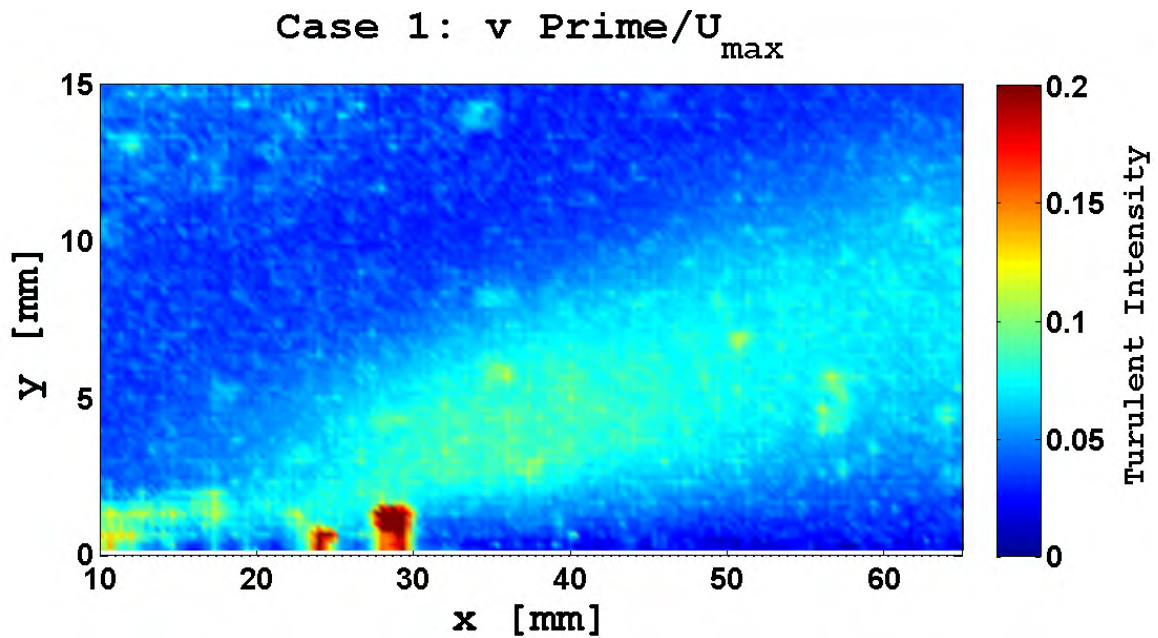


Figure B.25: Case 1: Velocity Vectors and Components



(a) Turbulent Intensity: u' / U_{max}



(b) Turbulent Intensity: v' / U_{max}

Figure B.26: Case 1: Turbulent intensities. The x component intensity is fairly constant but the induced jet boundary is clearly demarcated. The y component intensities are larger, but the induced jet boundary is still clearly demarcated.

Case 2: 11-4-0

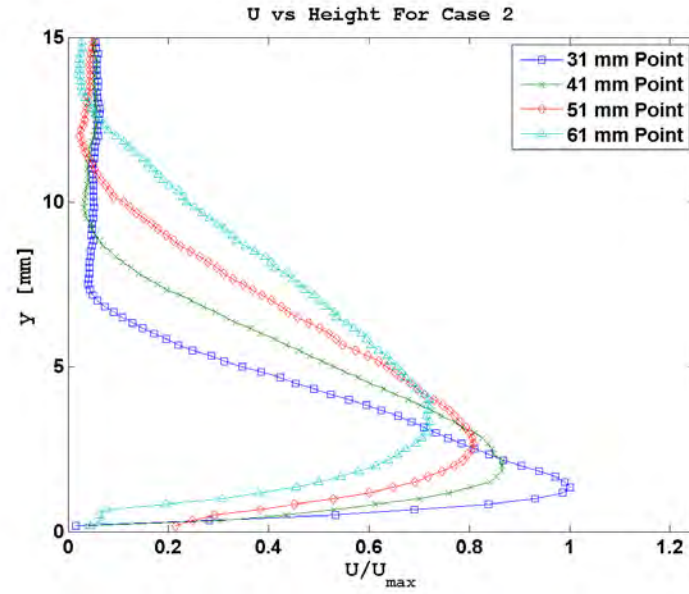


Figure B.27: Case 2: U vs Height

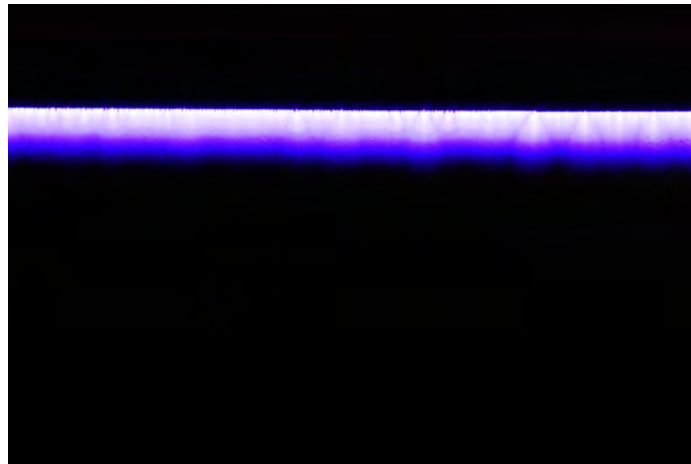


Figure B.28: Case 2: Discharge Plume

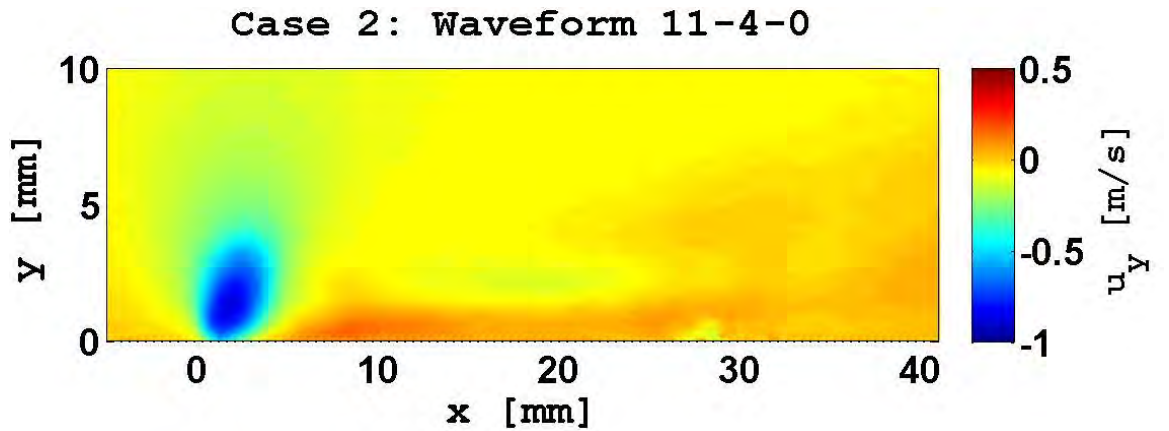
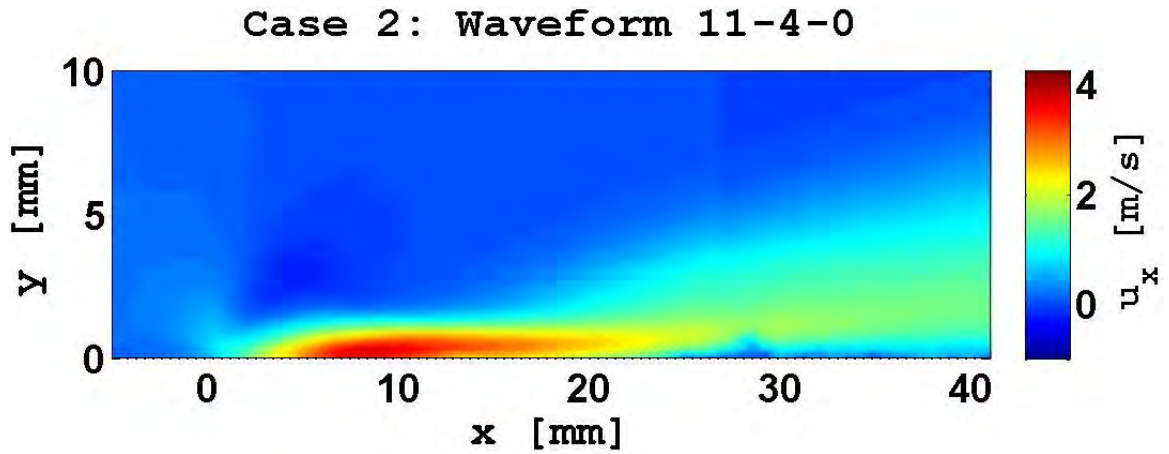
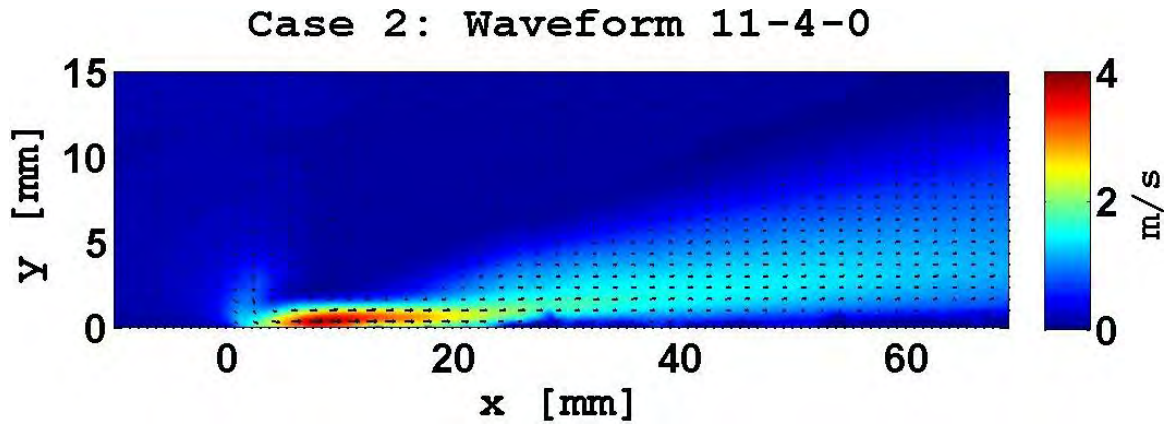


Figure B.29: Case 2: Velocity Vectors and Components

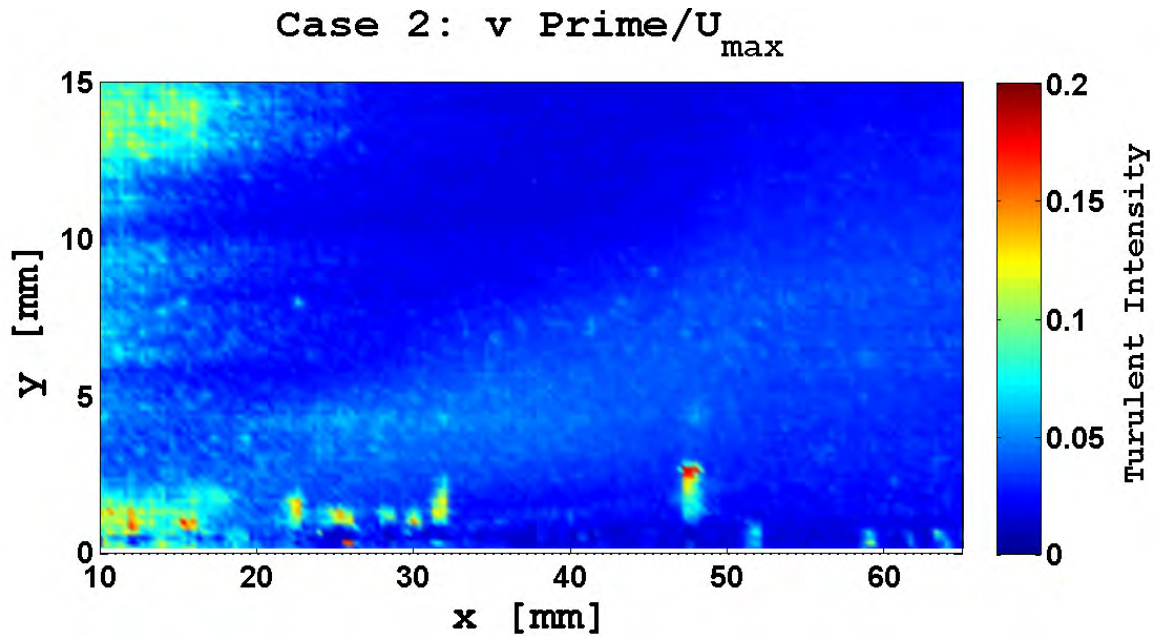
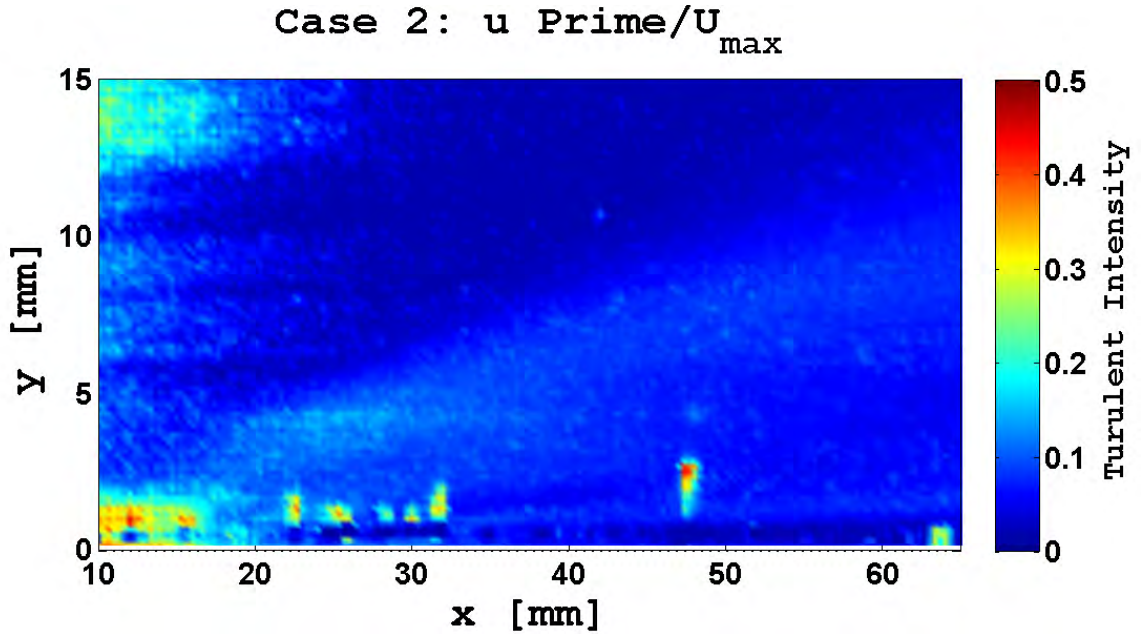


Figure B.30: Case 2: Turbulent intensities. The x component intensity is fairly constant but the induced jet boundary is clearly demarcated. The y component intensities are larger, but the induced jet boundary is still clearly demarcated. At the 0 mm point the small suction cone can be seen as an outline.

Case 3: 9-6-0

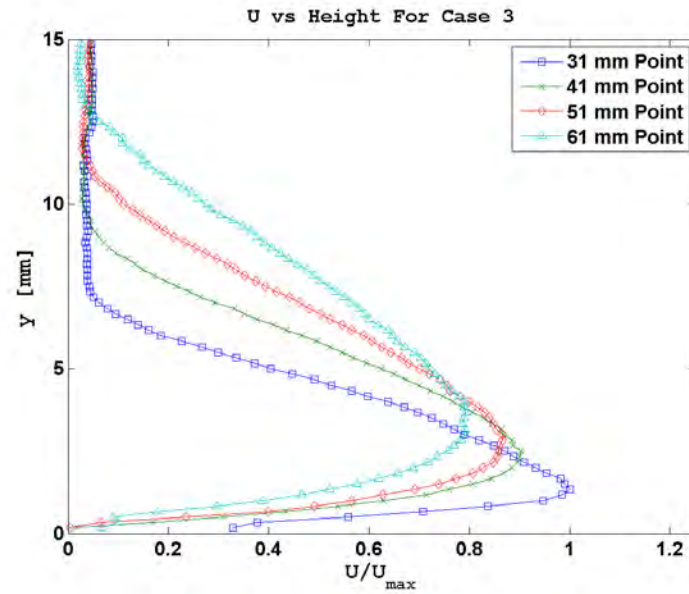


Figure B.31: Case 3: U vs Height

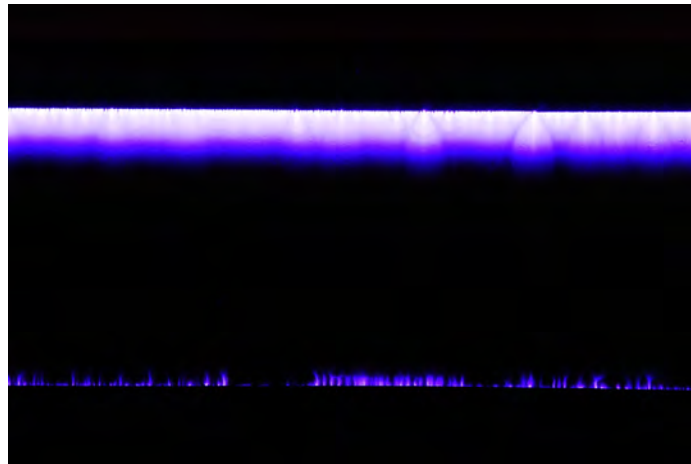


Figure B.32: Case 3: Discharge Plume

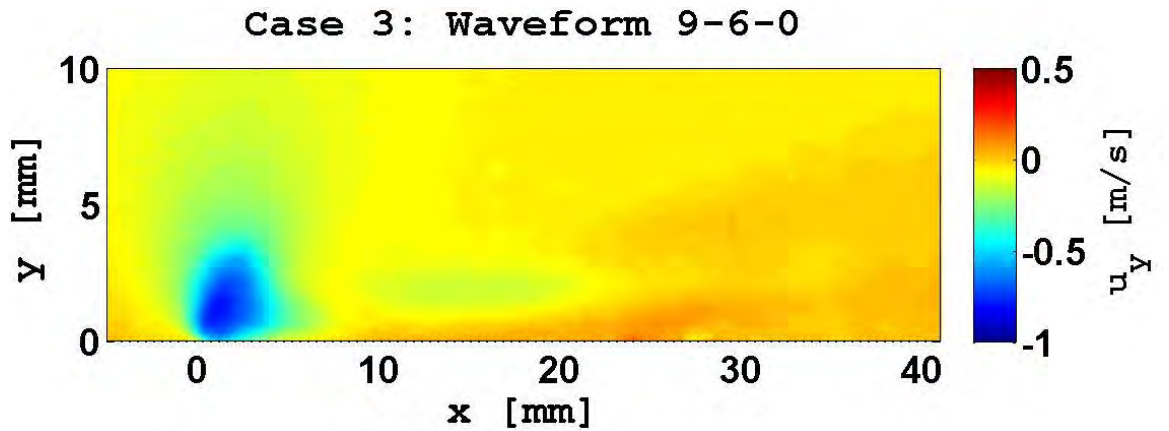
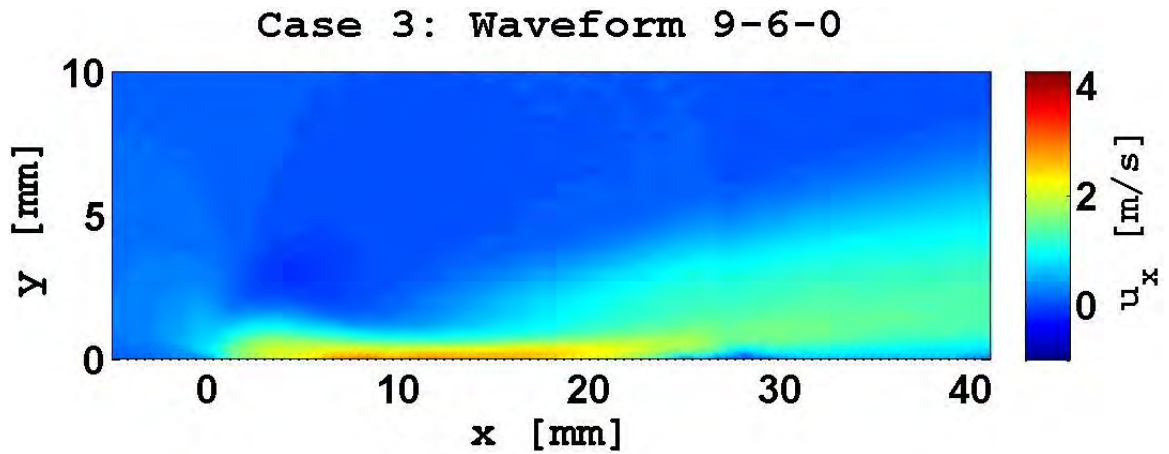
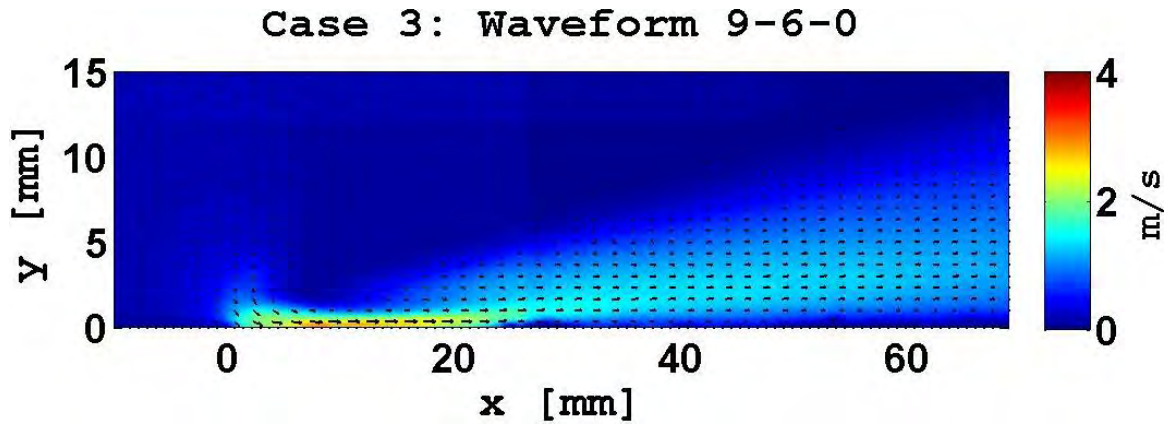


Figure B.33: Case 3: Velocity Vectors and Components

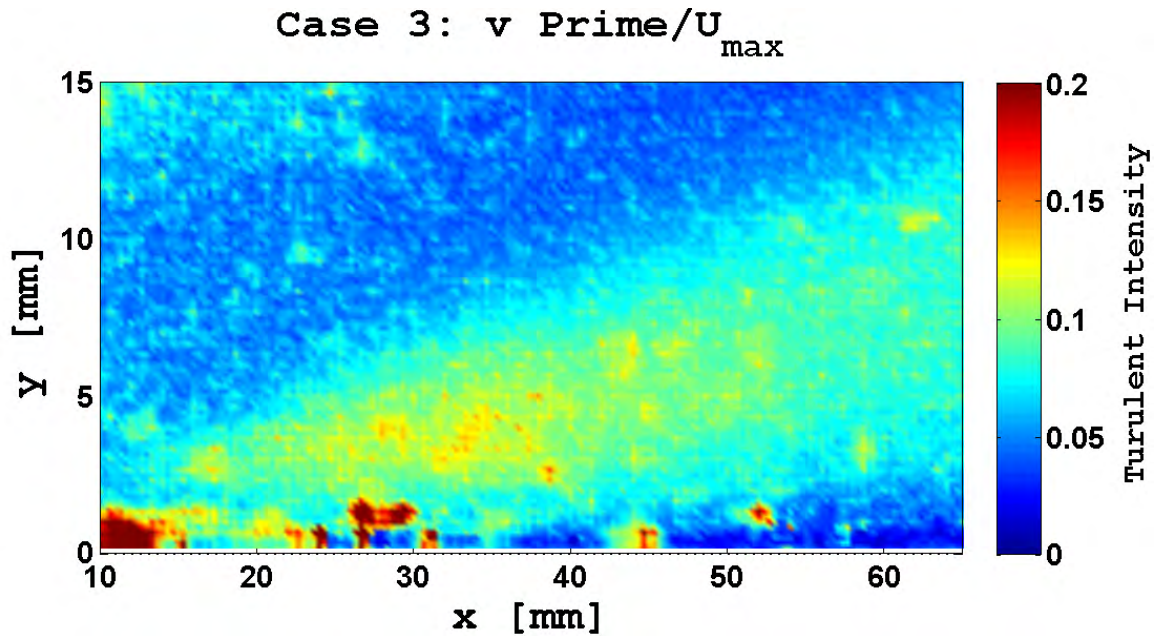
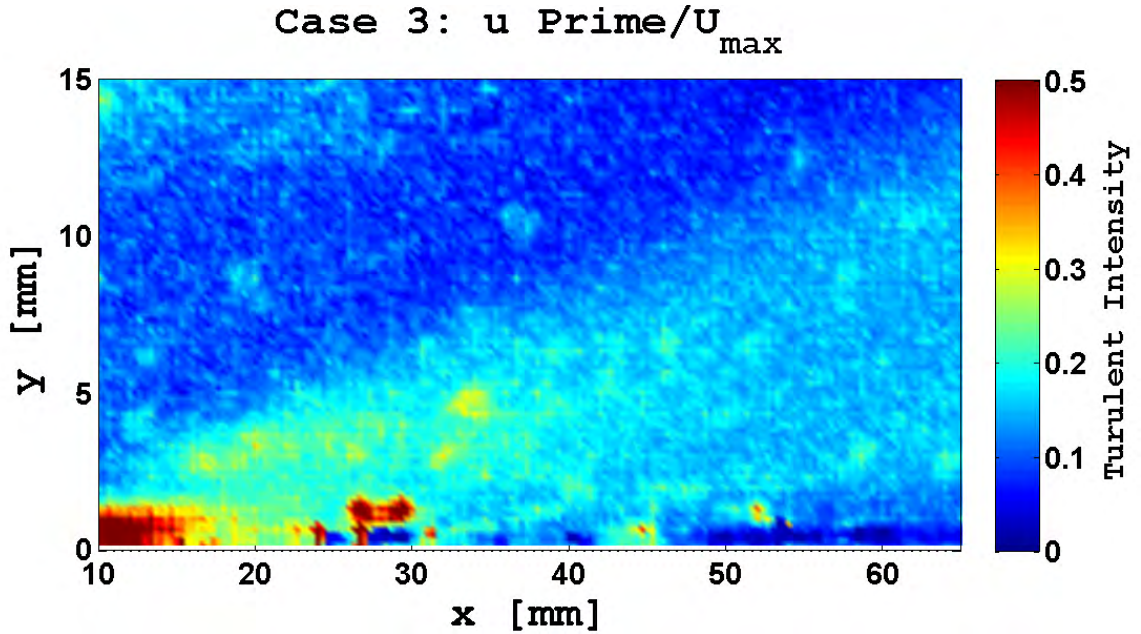


Figure B.34: Case 3: Turbulent intensities. The x component intensity peaks between the primary and sliding discharge electrode but is fairly constant but the induced jet boundary is clearly demarcated. The y component intensities are larger, but the induced jet boundary is still clearly demarcated. At the 0 mm point the small suction cone can be seen as an outline.

Case 4: 7.5-7.5-0

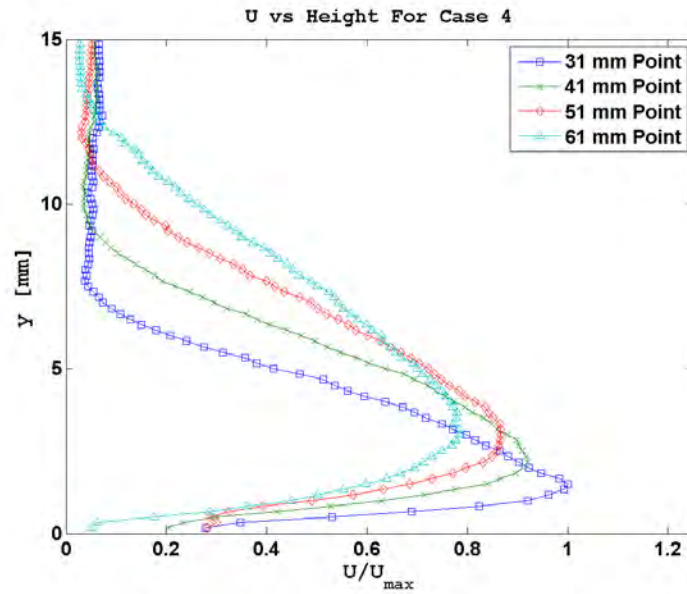


Figure B.35: Case 4: U vs Height

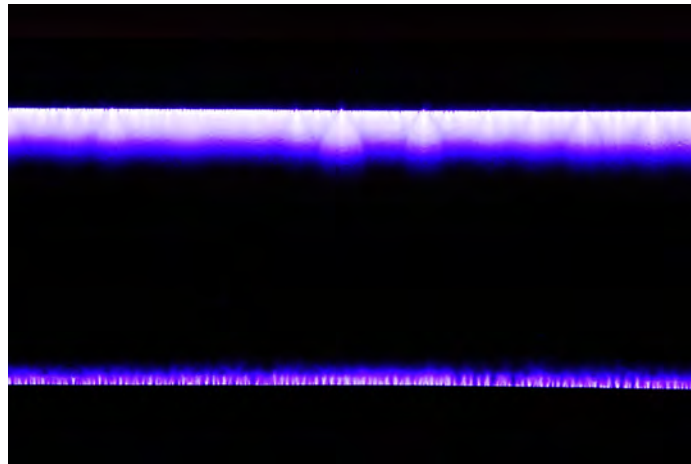


Figure B.36: Case 4: Discharge Plume

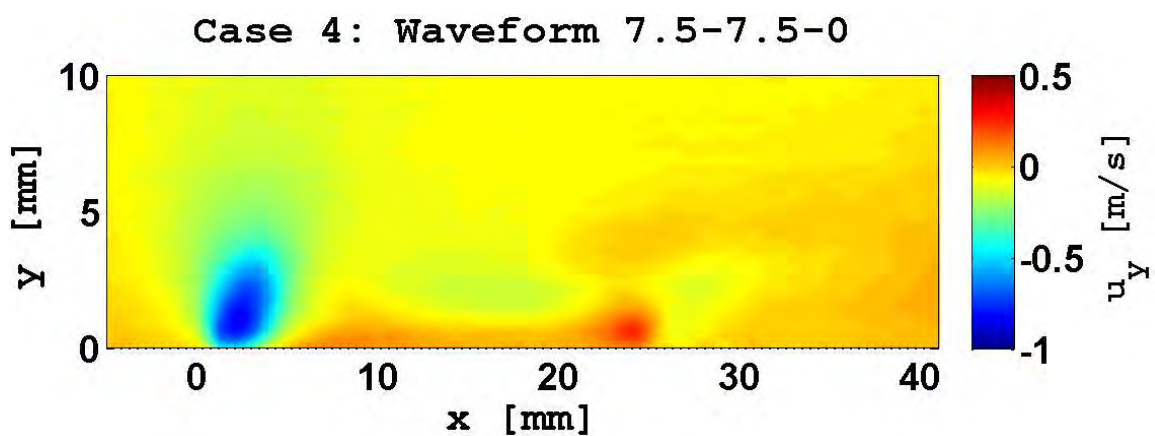
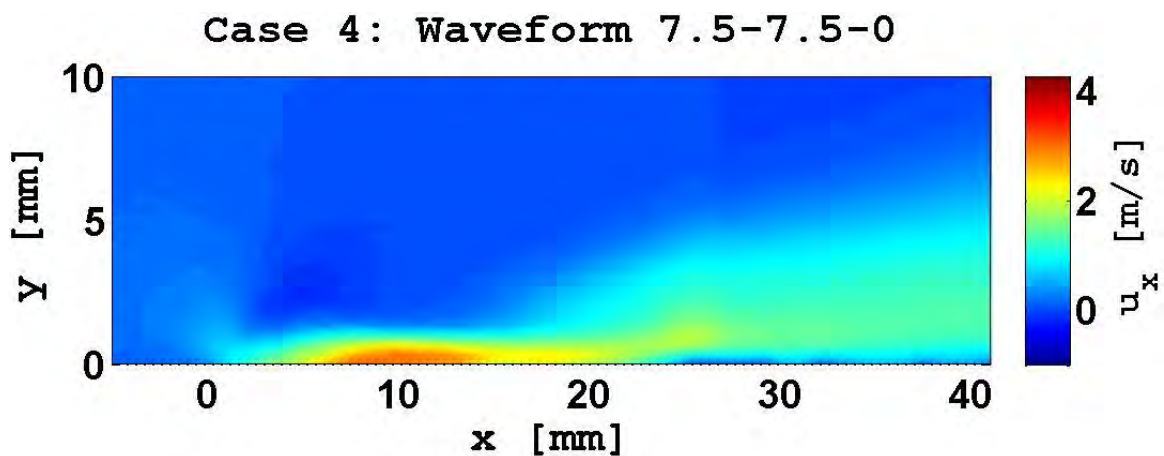
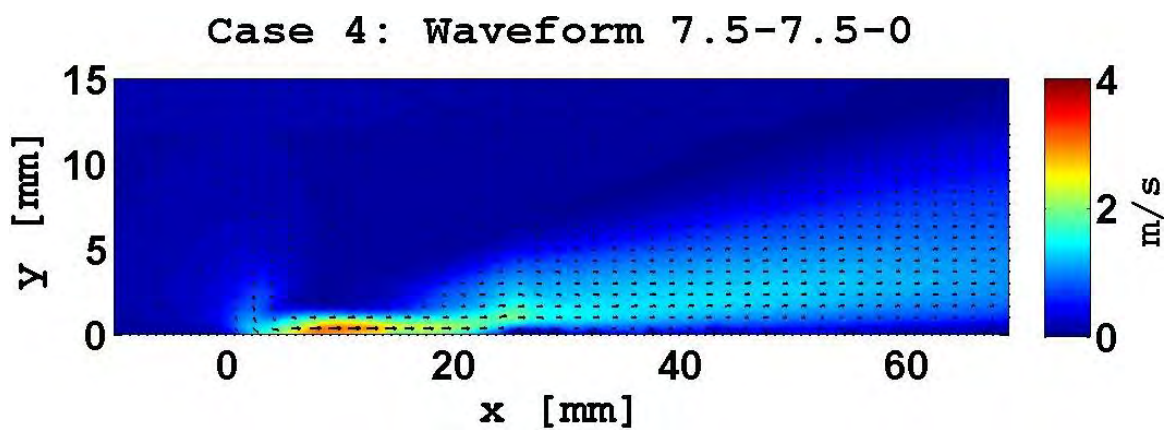
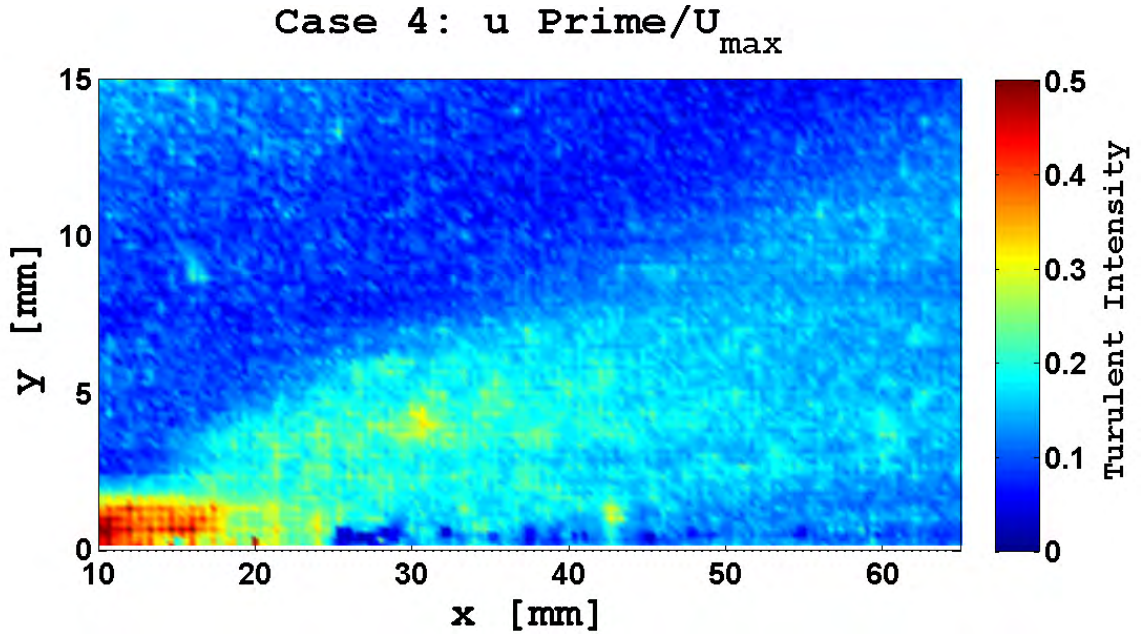
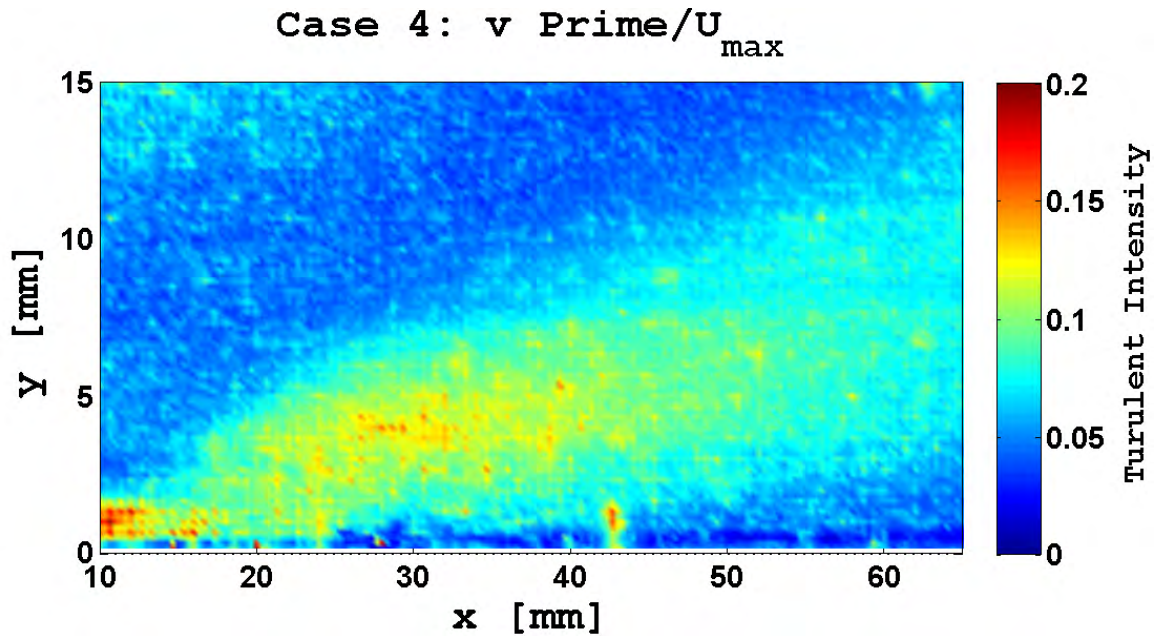


Figure B.37: Case 4: Velocity Vectors and Components



(a) Turbulent Intensity: u' / U_{max}



(b) Turbulent Intensity: v' / U_{max}

Figure B.38: Case 4: Turbulent intensities. The x component intensity peaks between the primary and sliding discharge electrode but is fairly constant but the induced jet boundary is clearly demarcated. The y component intensities are larger, but the induced jet boundary is still clearly demarcated. At the 0 mm point the small suction cone can be seen as an outline.

Case 5: 17-2-0

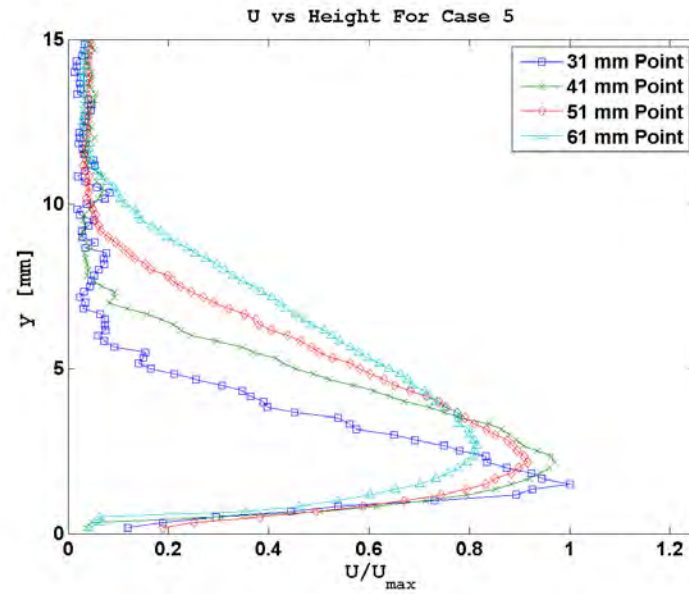


Figure B.39: Case 5: U vs Height

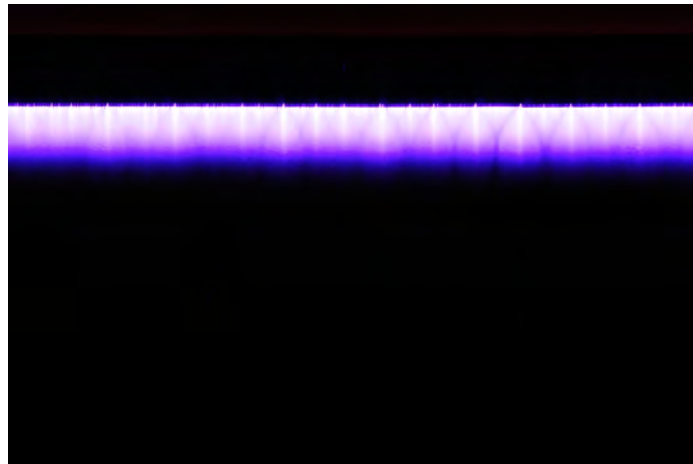


Figure B.40: Case 5: Discharge Plume

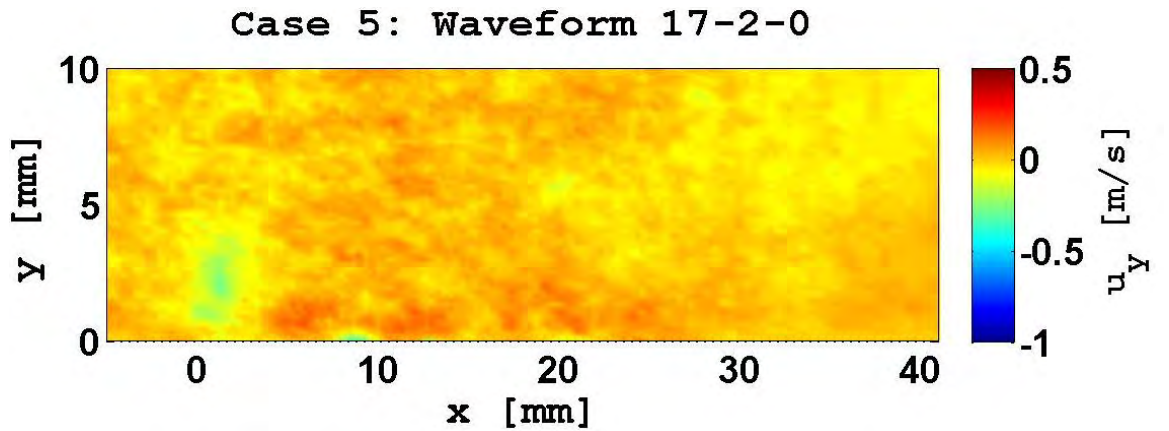
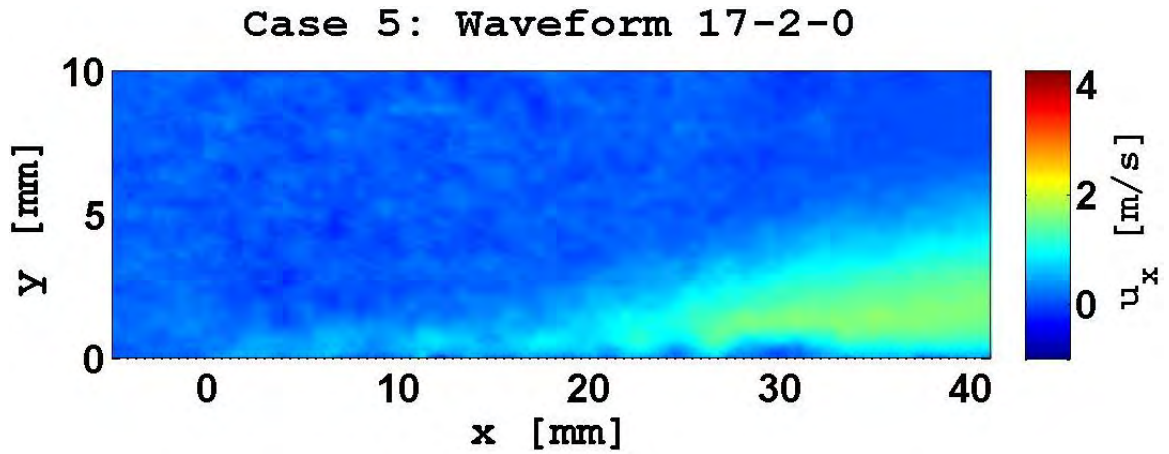
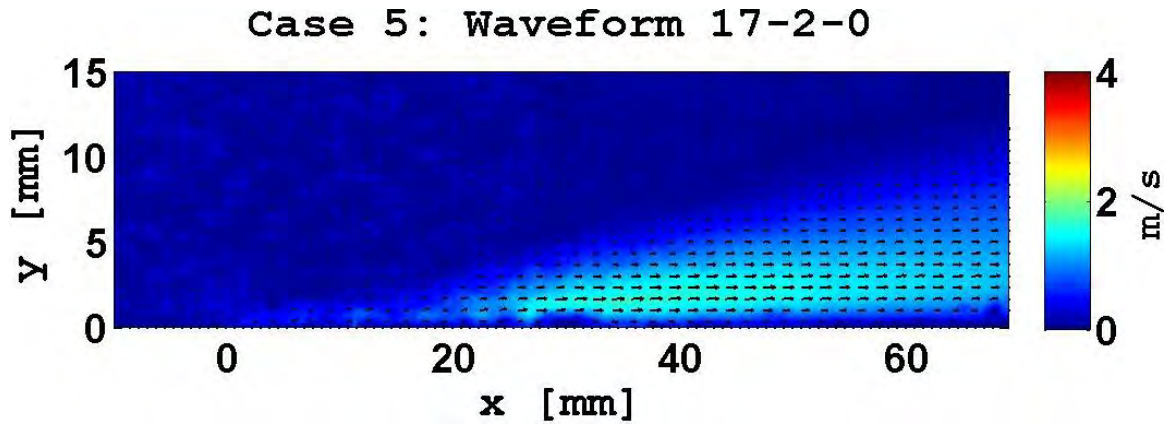
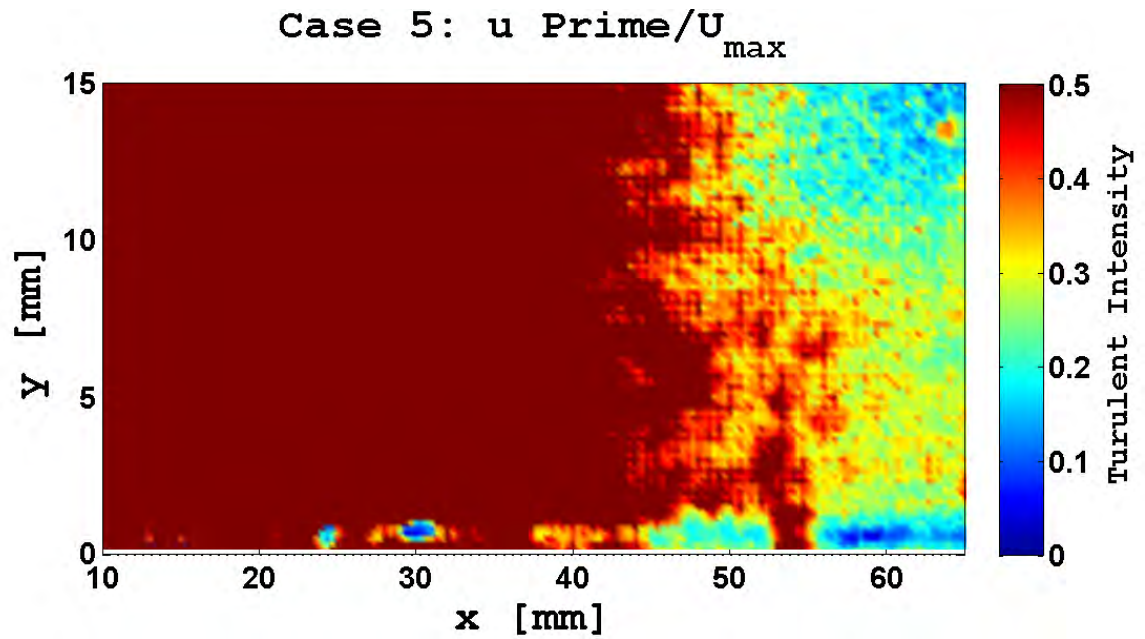
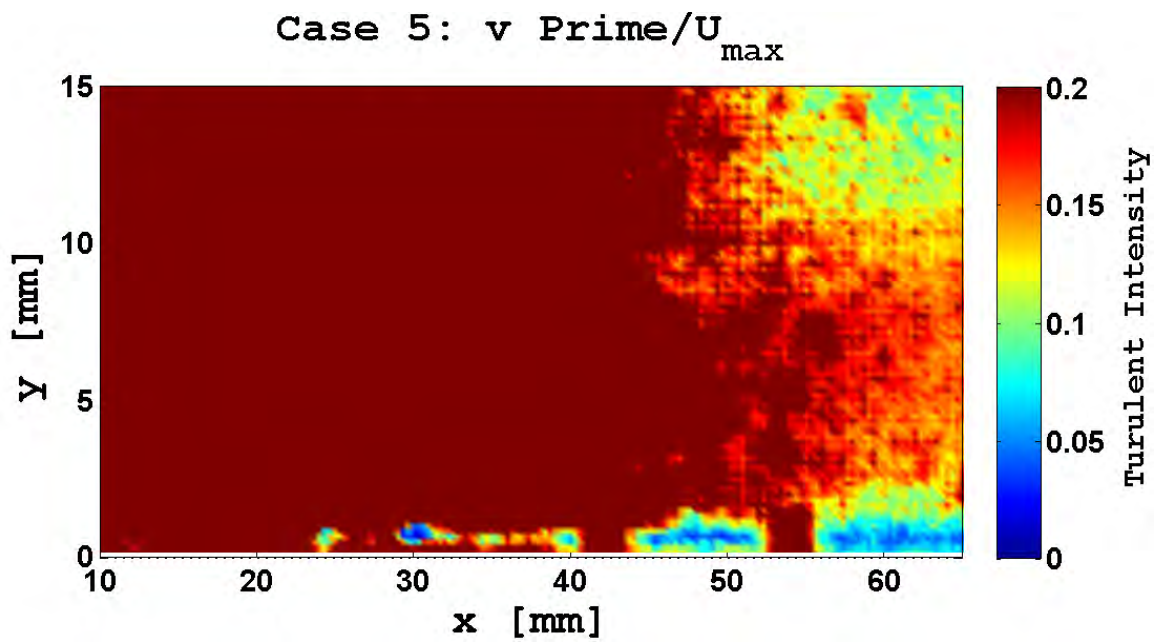


Figure B.41: Case 5: Velocity Vectors and Components



(a) Turbulent Intensity: u' / U_{max}



(b) Turbulent Intensity: v' / V_{max}

Figure B.42: Case 5: Turbulent intensities. The turbulent intensities are no longer constant but the outline of the jet can still be seen.

Case 6: 18-3-0

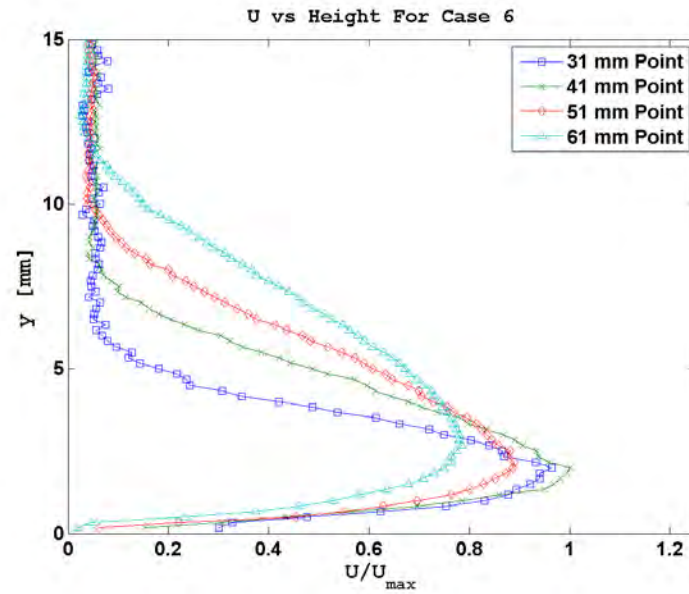


Figure B.43: Case 6: U vs Height

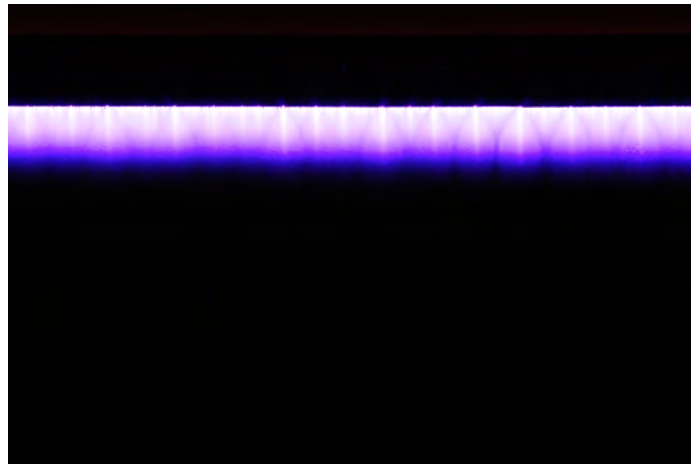


Figure B.44: Case 6: Discharge Plume

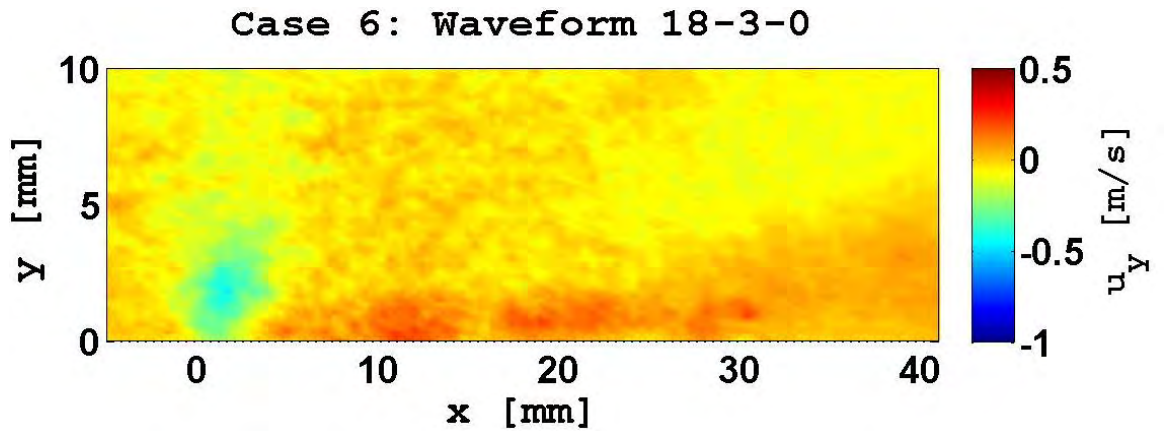
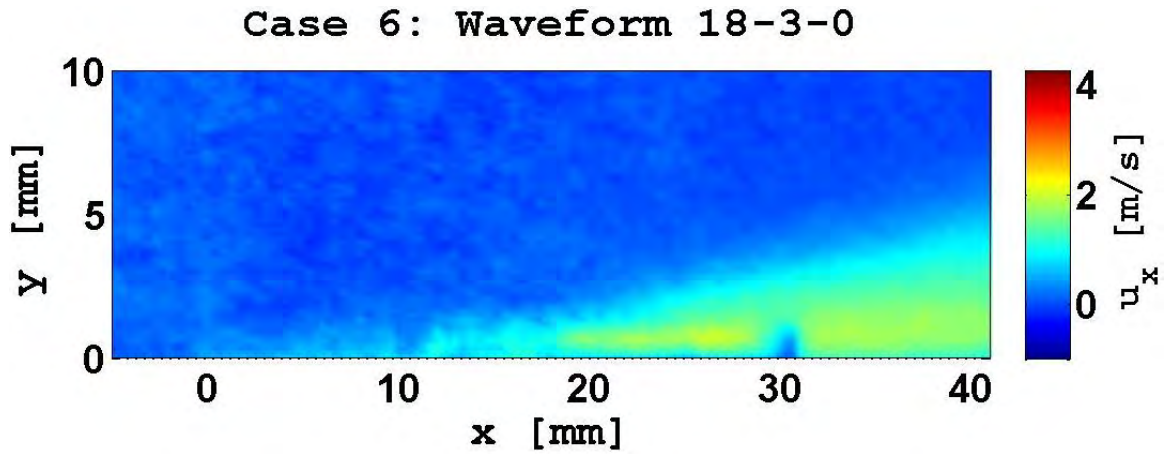
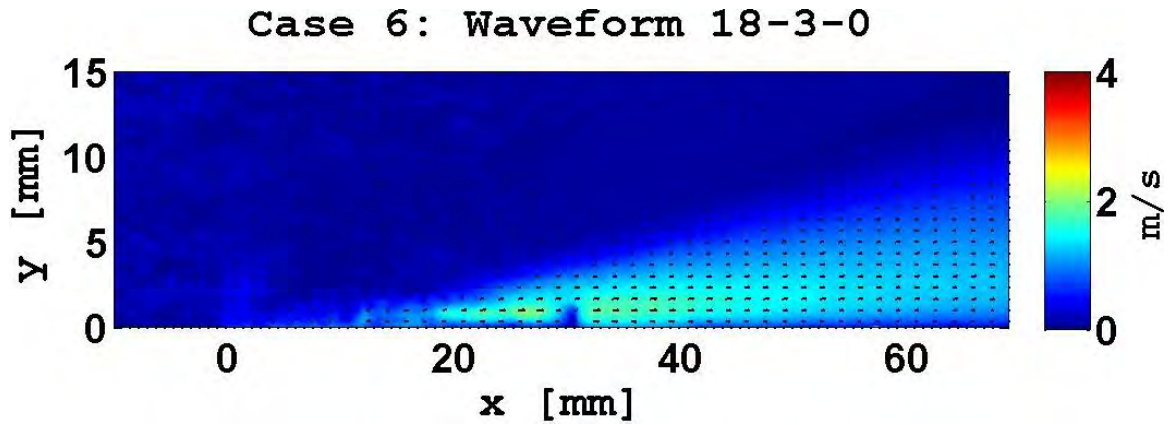
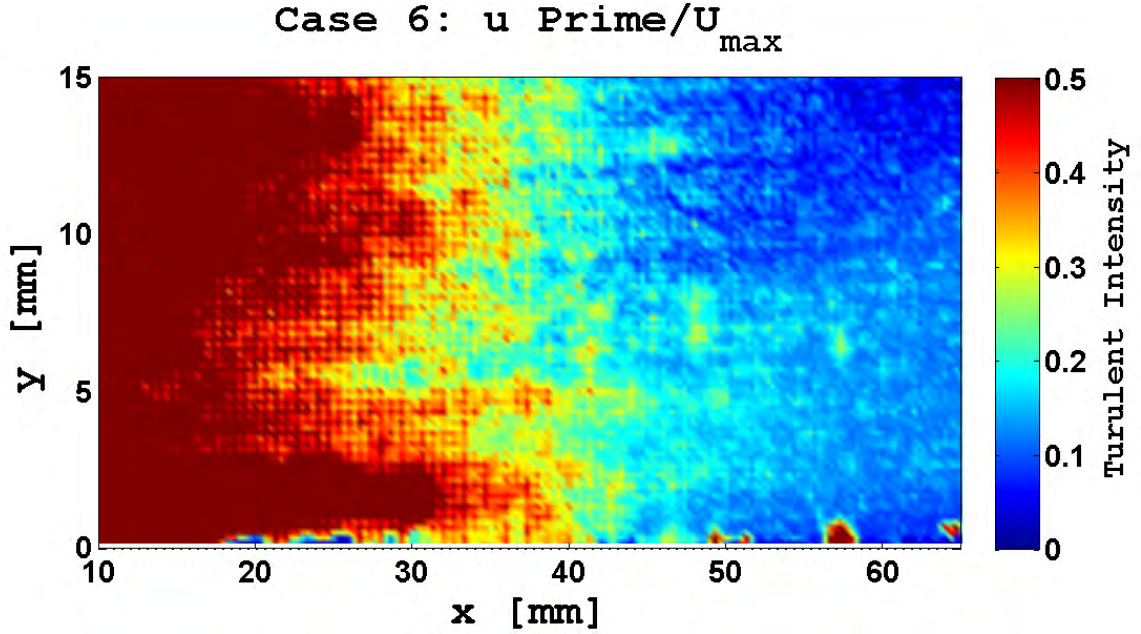
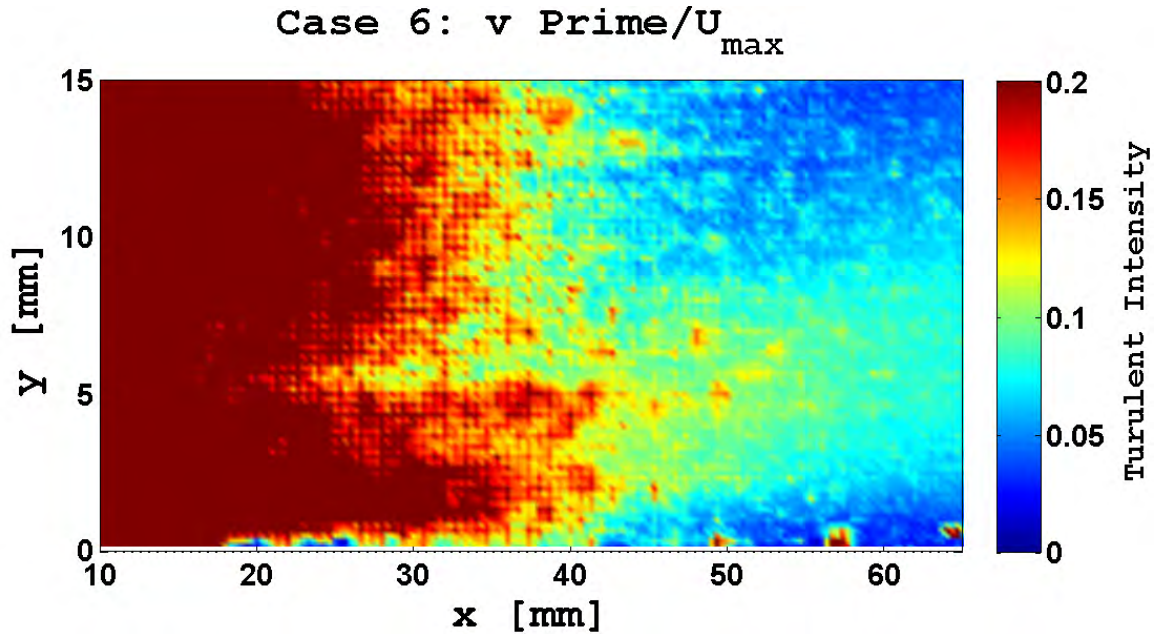


Figure B.45: Case 6: Velocity Vectors and Components



(a) Turbulent Intensity: u' / U_{max}



(b) Turbulent Intensity: v' / U_{max}

Figure B.46: Case 6: Turbulent intensities. The x component intensity peaks between the primary and sliding discharge electrode and the intensities are fairly constant in the jet, the induced jet boundary is clearly demarcated. The y component intensities are larger, but the induced jet boundary is still clearly demarcated. At the 0 mm point the small suction cone can be seen and is larger than the one in Cases 1-4.

B.3 Phase II

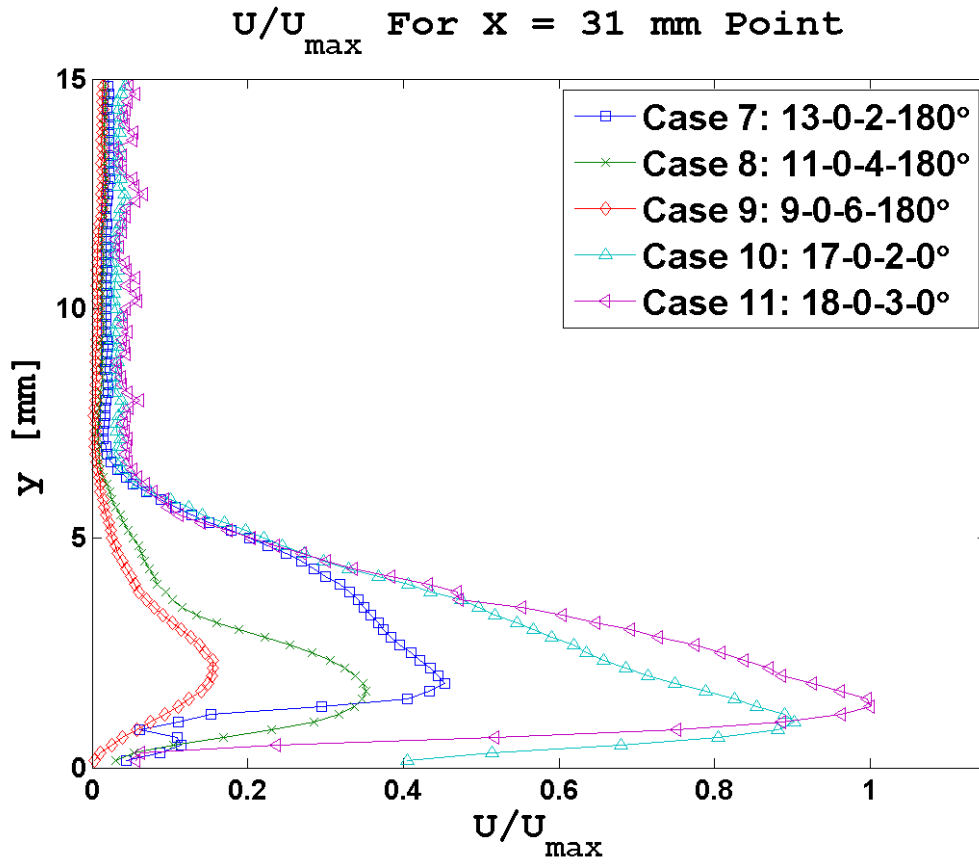


Figure B.47: Phase II Velocity Profiles: 31 mm Point. $U_{\max} = 2.28$ m/s.

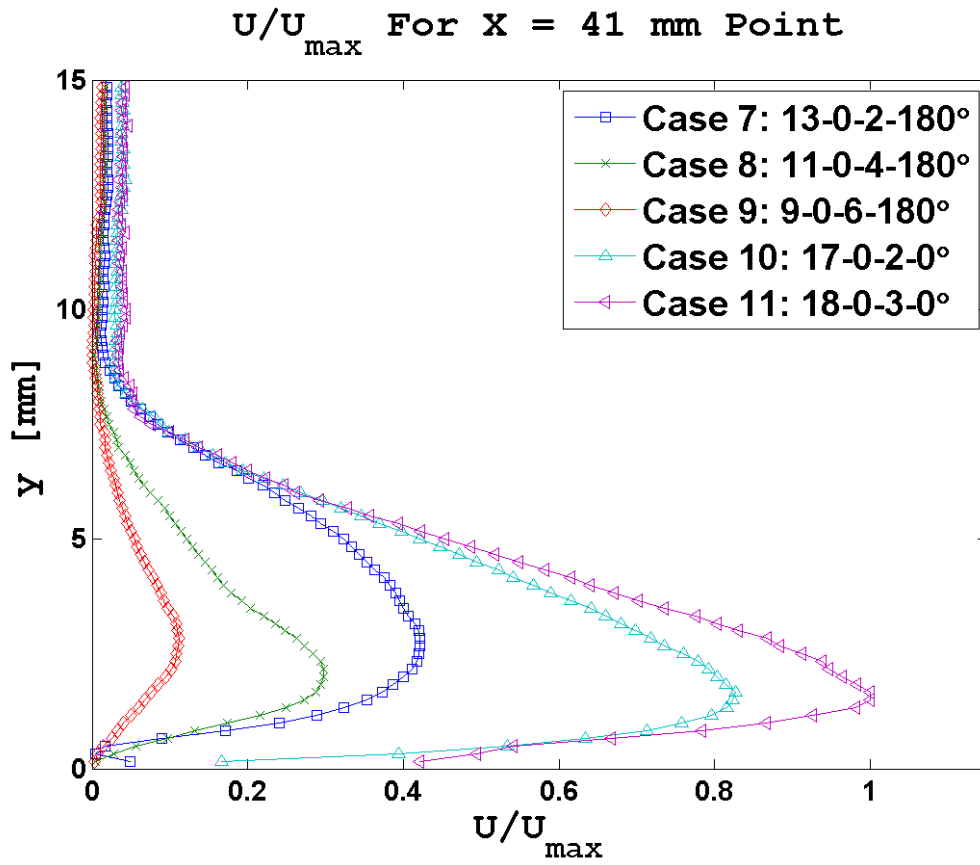


Figure B.48: Phase II Velocity Profiles: 41 mm Point. $U_{\max} = 2.27$ m/s.

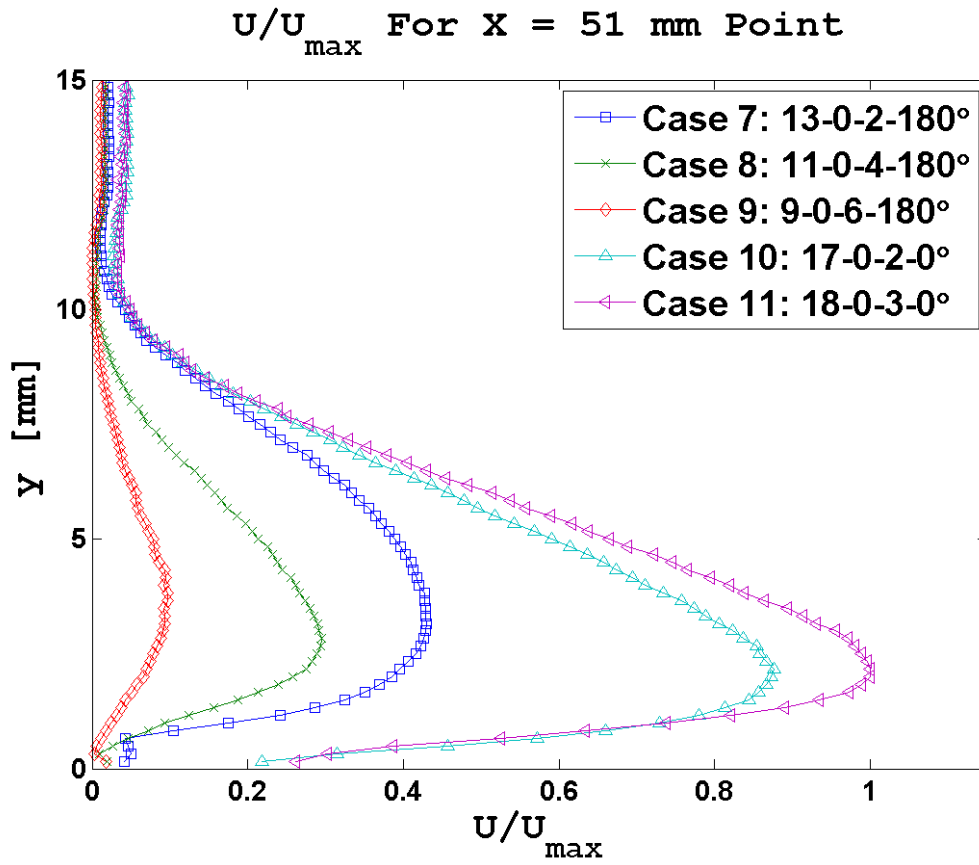


Figure B.49: Phase II Velocity Profiles: 51 mm Point. $U_{\max} = 2.05$ m/s.

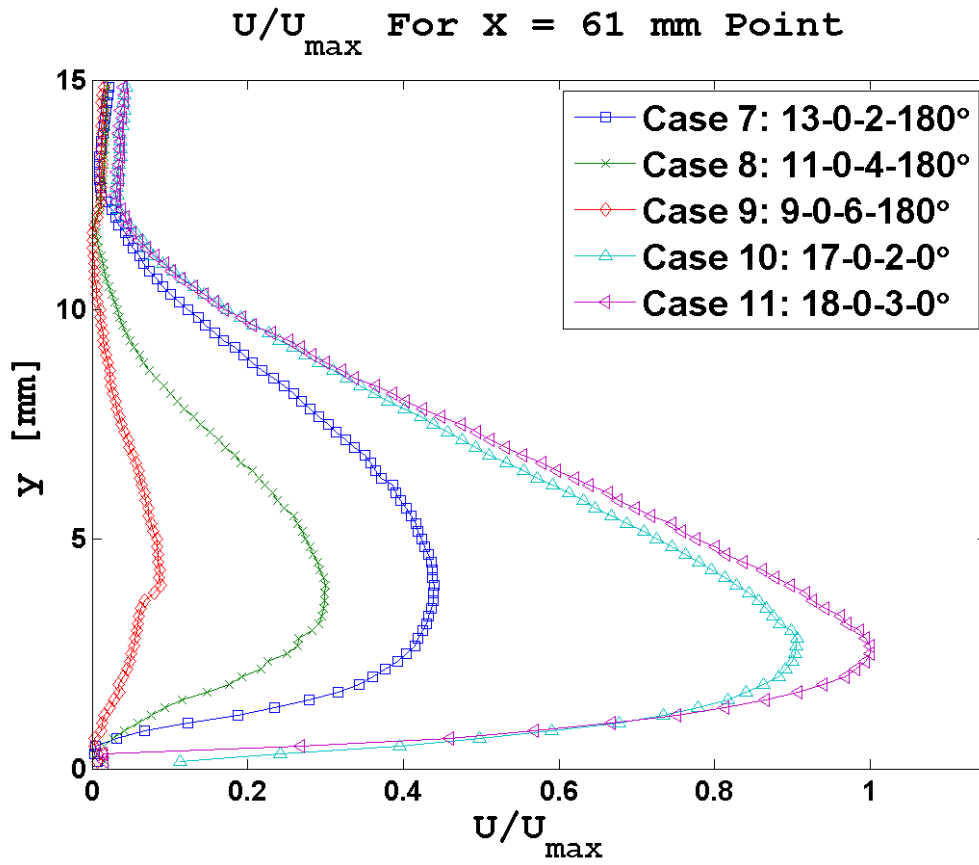


Figure B.50: Phase II Velocity Profiles: 61 mm Point. $U_{\max} = 1.87$ m/s.

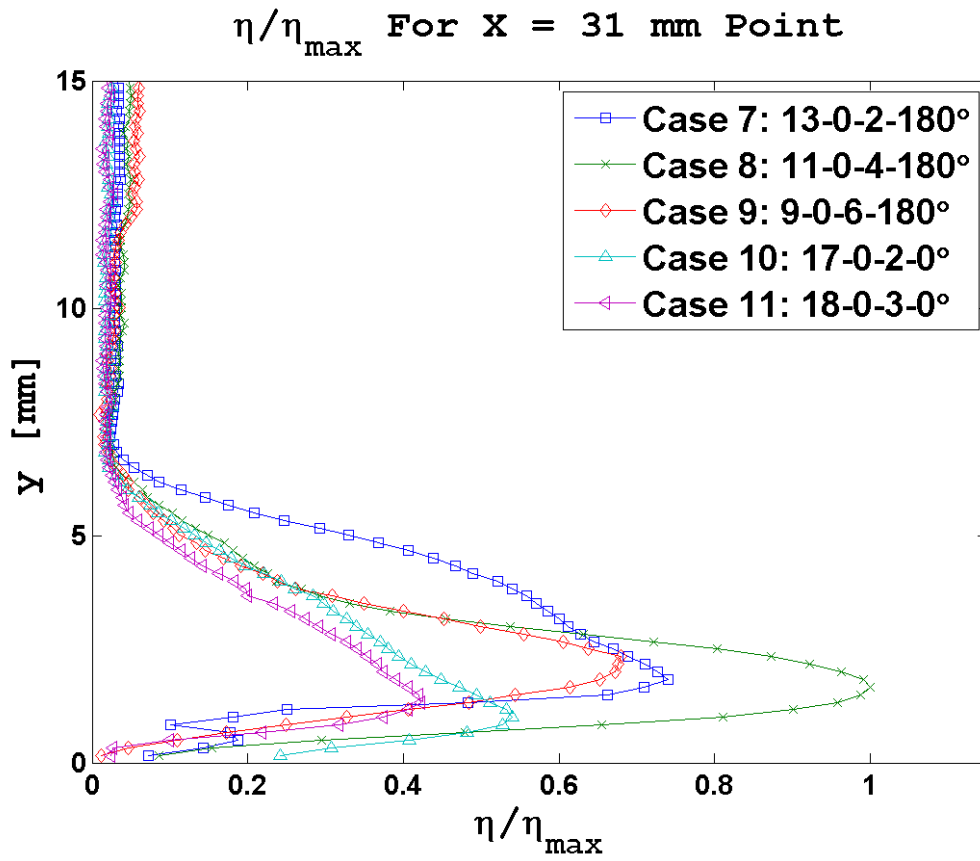


Figure B.51: Phase II Efficiency Profiles: 31 mm Point

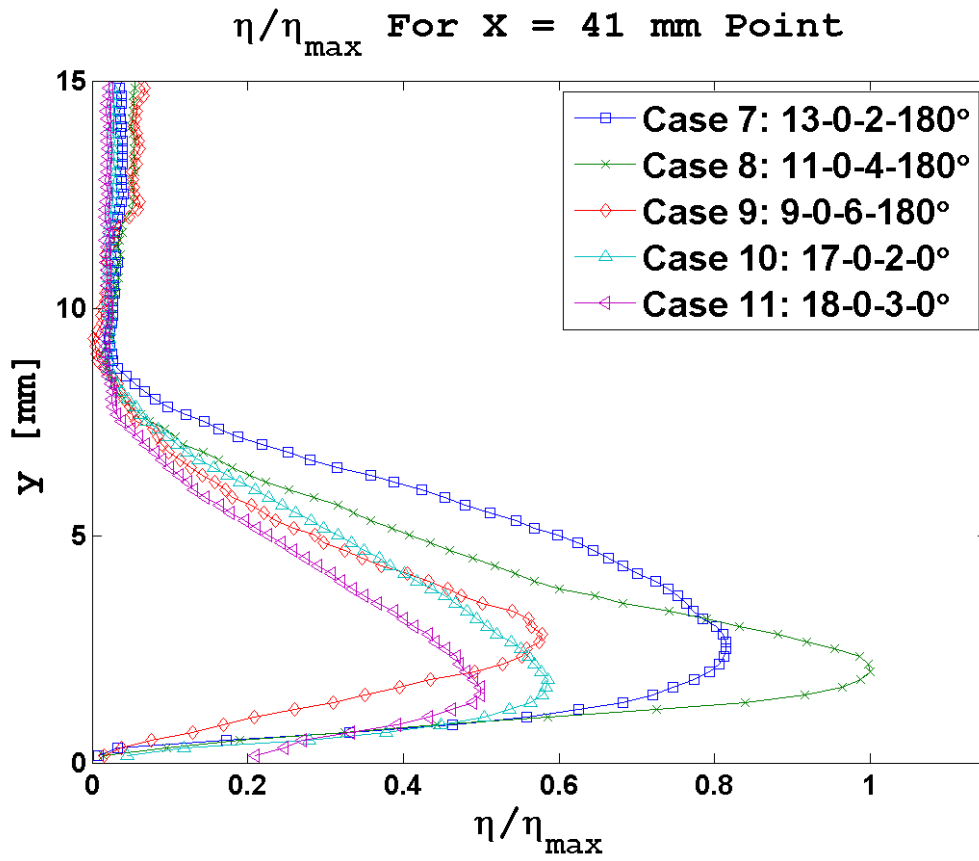


Figure B.52: Phase II Efficiency Profiles: 41 mm Point

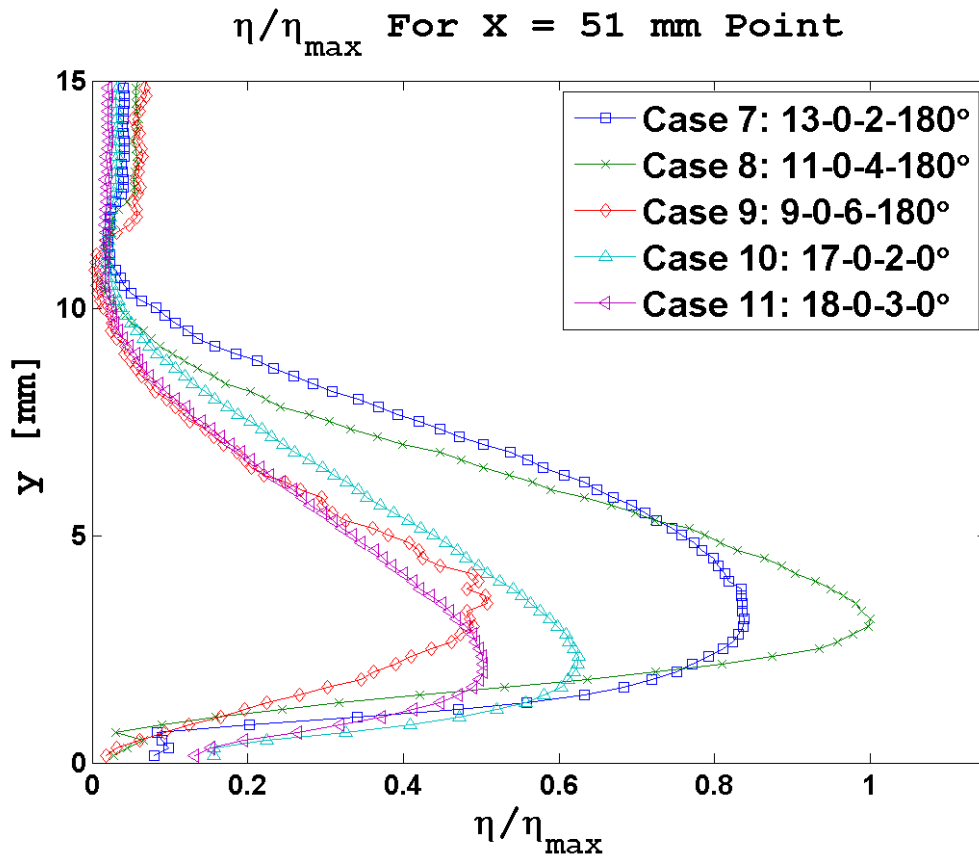


Figure B.53: Phase II Efficiency Profiles: 51 mm Point

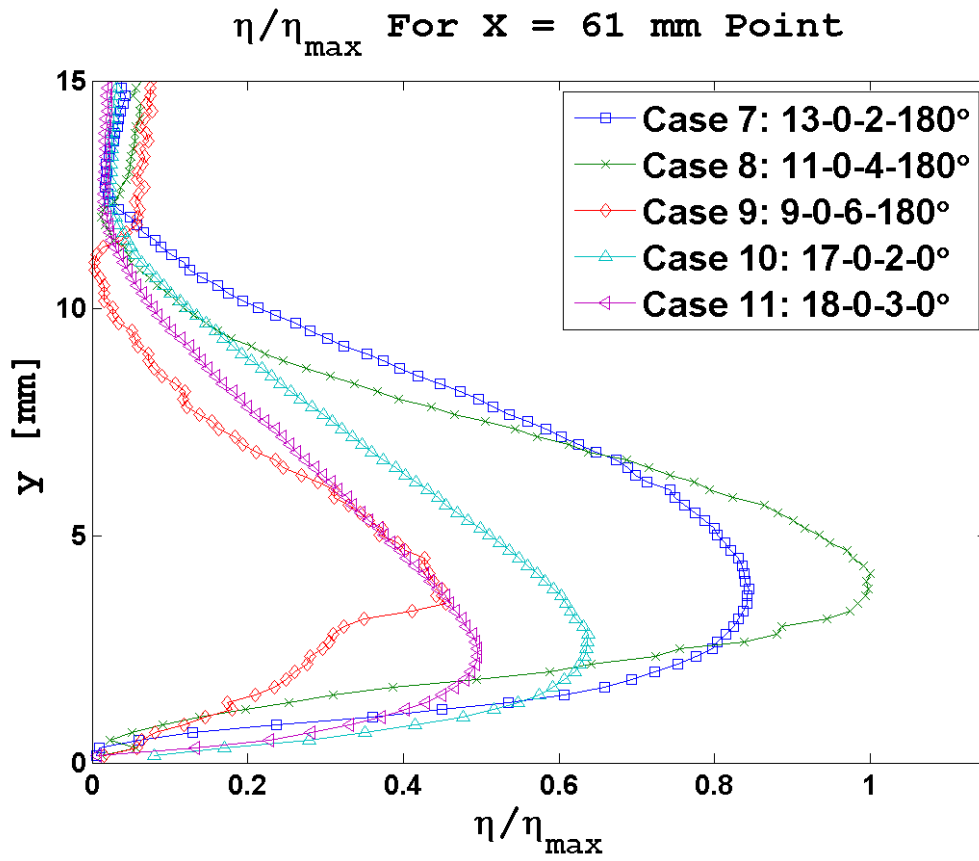


Figure B.54: Phase II Efficiency Profiles: 61 mm Point

Case 7: 13-0-2

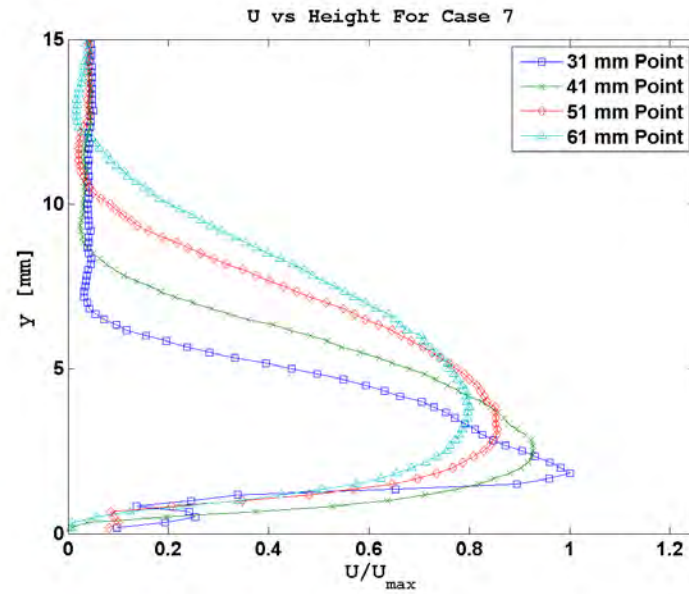


Figure B.55: Case 7: U vs Height

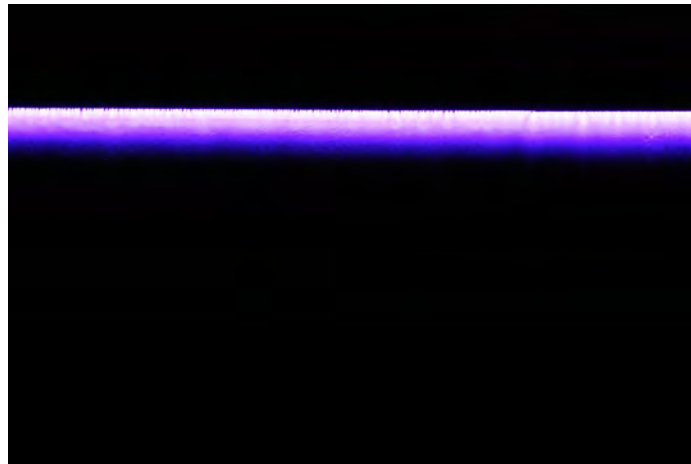
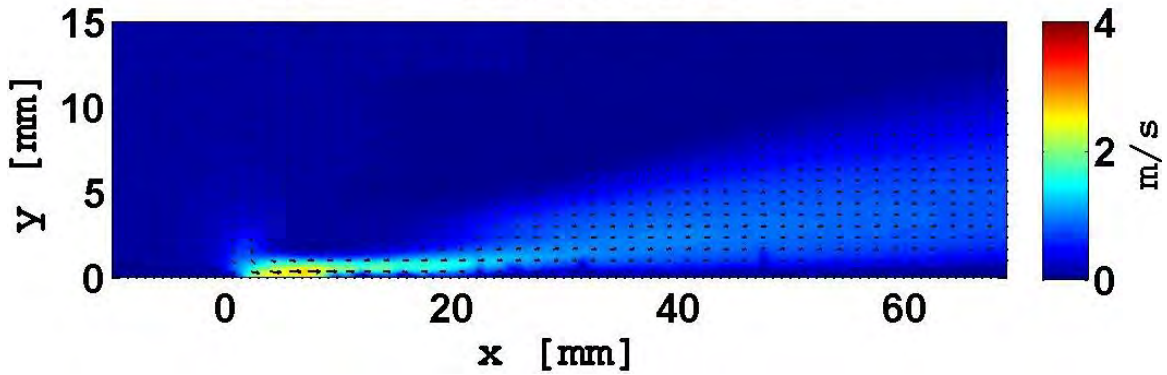


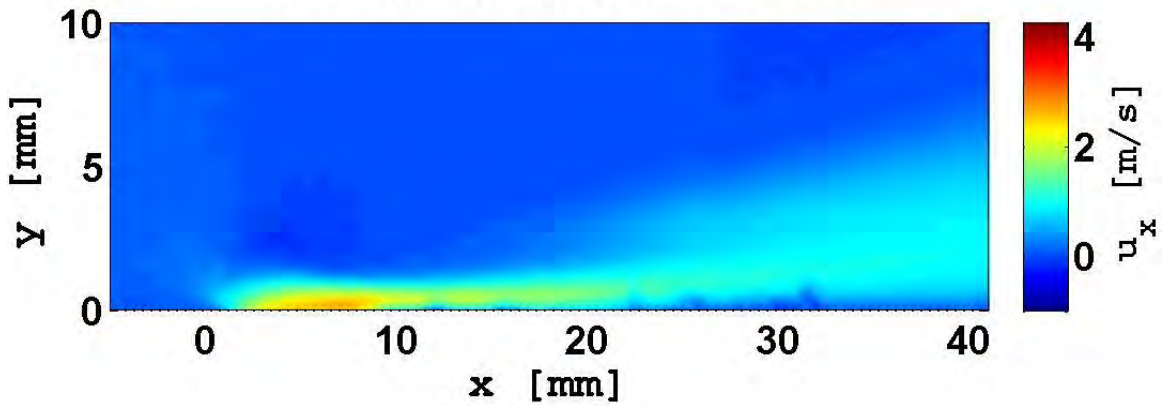
Figure B.56: Case 7: Discharge Plume

Case 7: Waveform 13-0-2



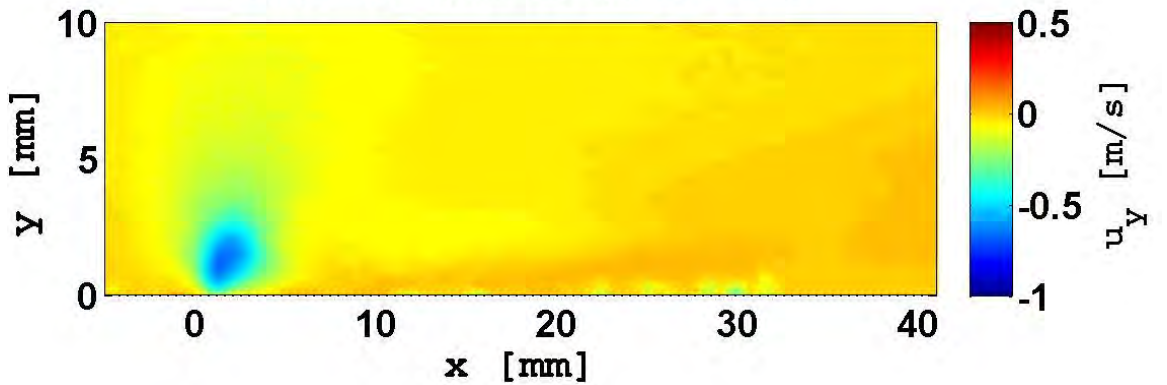
(a) Velocity Contours and Vectors

Case 7: Waveform 13-0-2



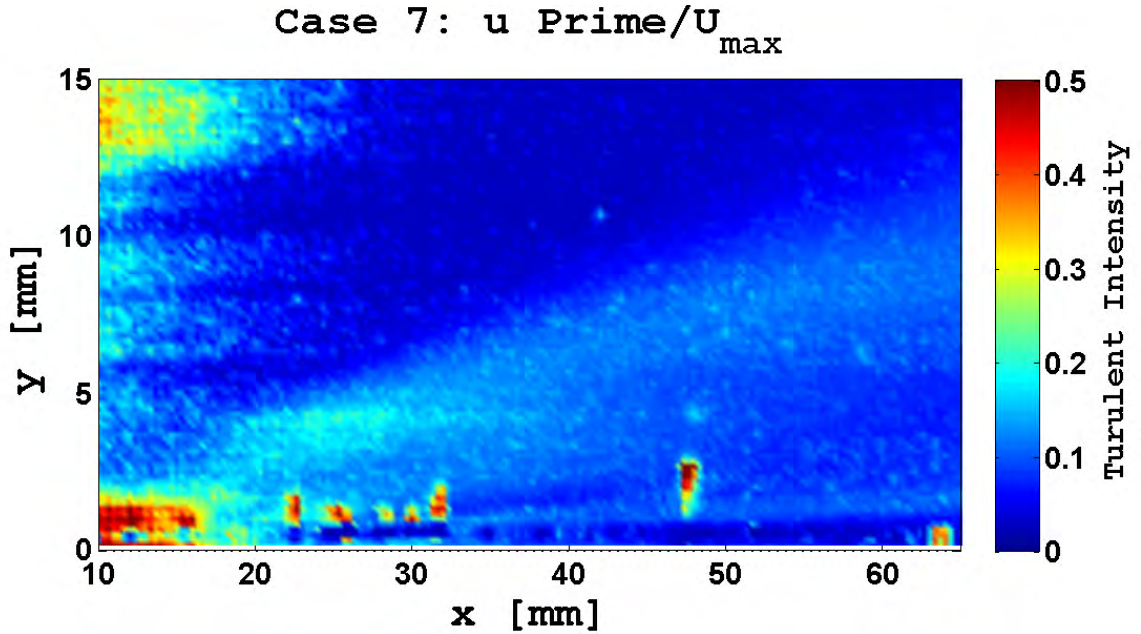
(b) x Velocity Component

Case 7: Waveform 13-0-2

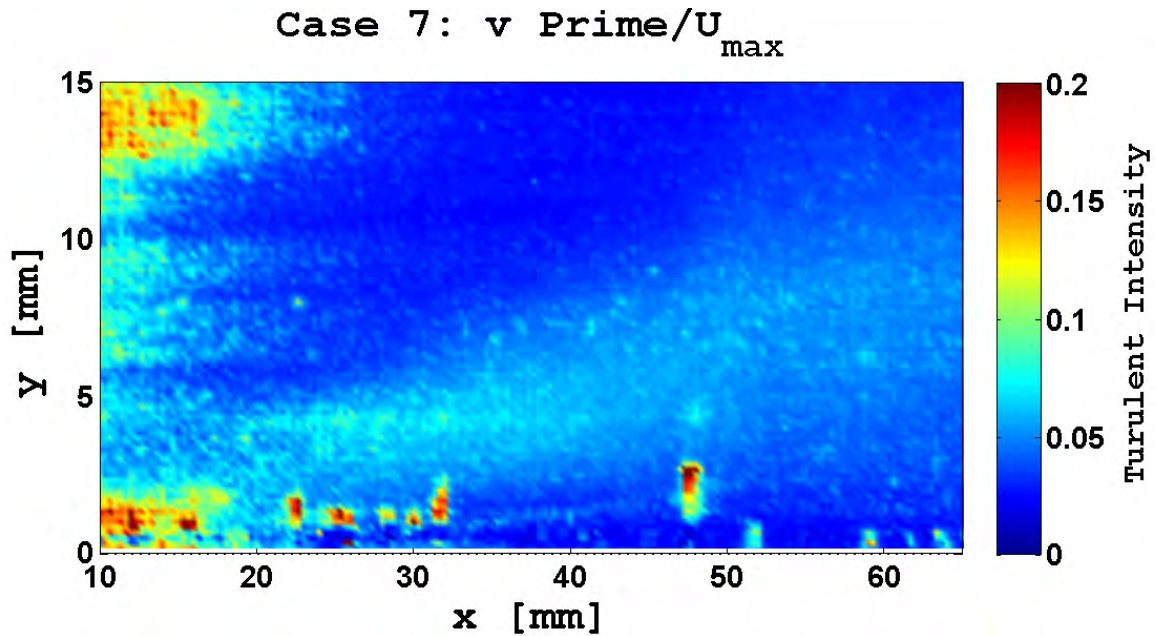


(c) y Velocity Component

Figure B.57: Case 7: Velocity Vectors and Components



(a) Turbulent Intensity: u' / U_{max}



(b) Turbulent Intensity: v' / U_{max}

Figure B.58: Case 7: Turbulent intensities. The x component intensity peaks above the suction zone and the intensities are fairly constant in the jet, the induced jet boundary is clearly demarcated. The y component intensities are larger, but the induced jet boundary is still clearly demarcated with a marked shift in intensity.

Case 8: 11-0-4

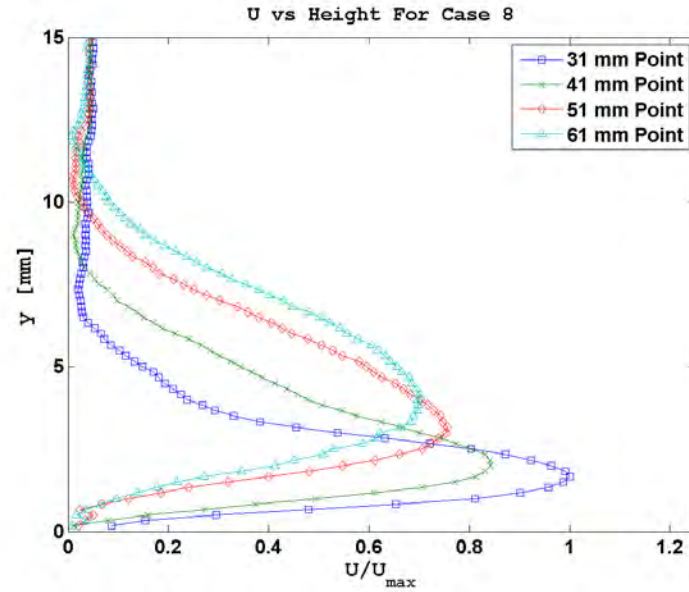


Figure B.59: Case 8: U vs Height

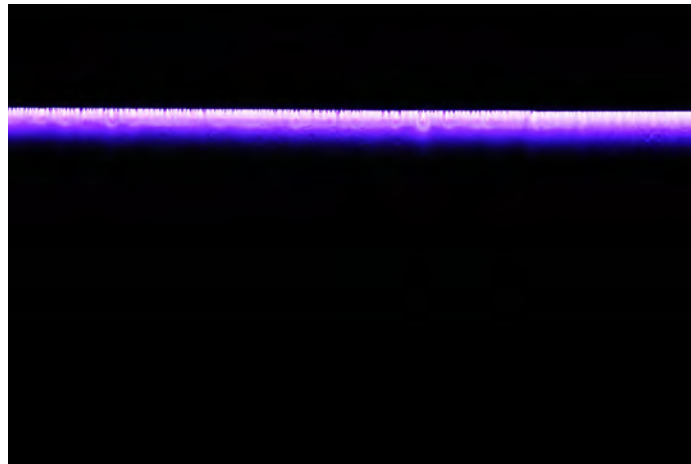


Figure B.60: Case 8: Discharge Plume

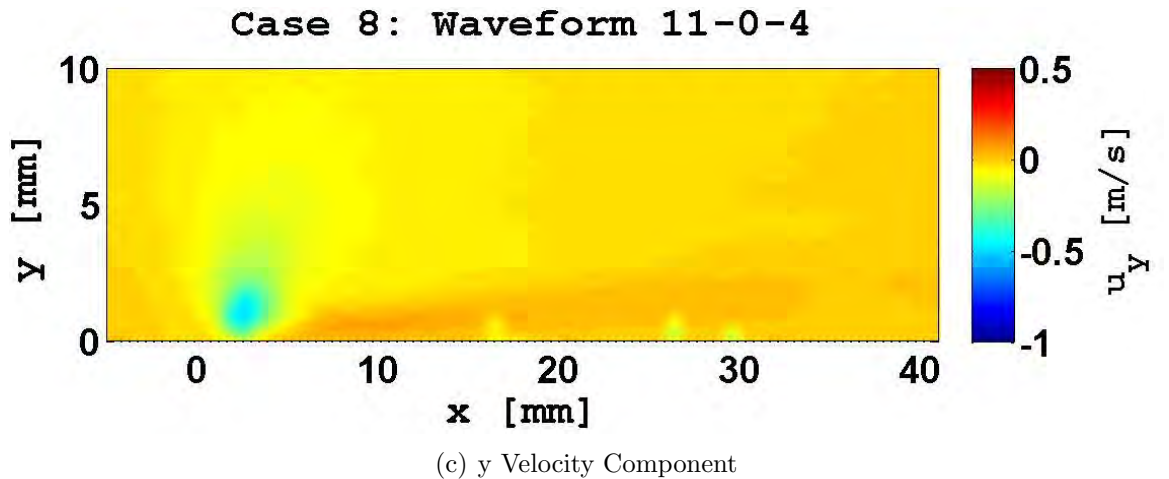
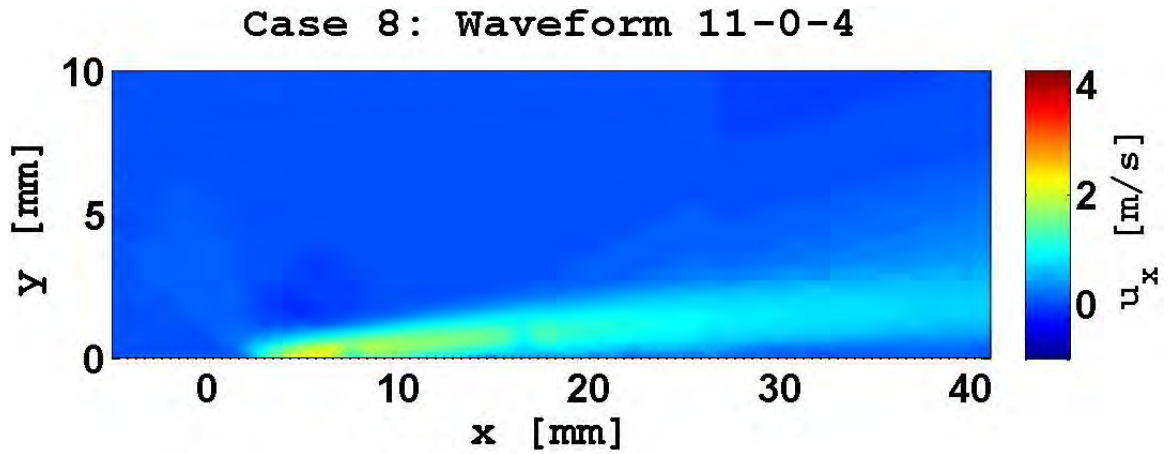
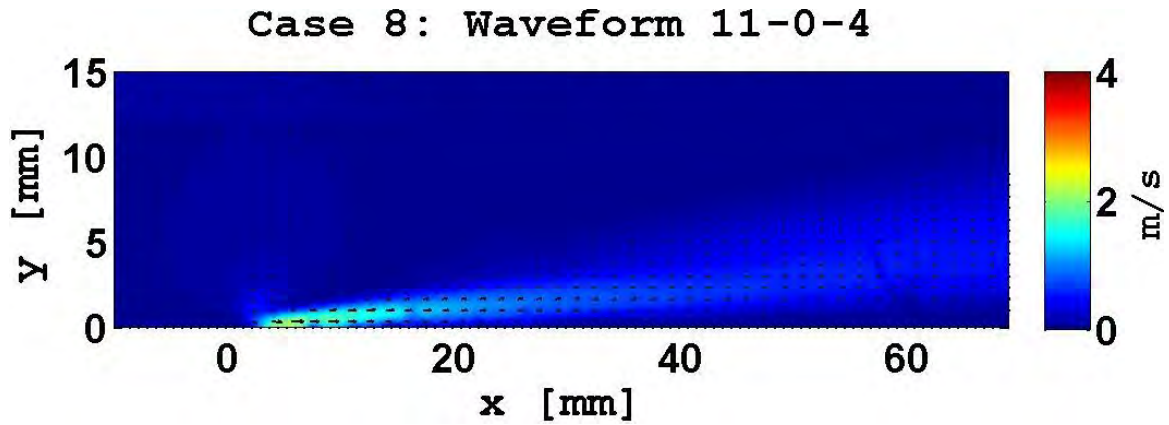


Figure B.61: Case 8: Velocity Vectors and Components

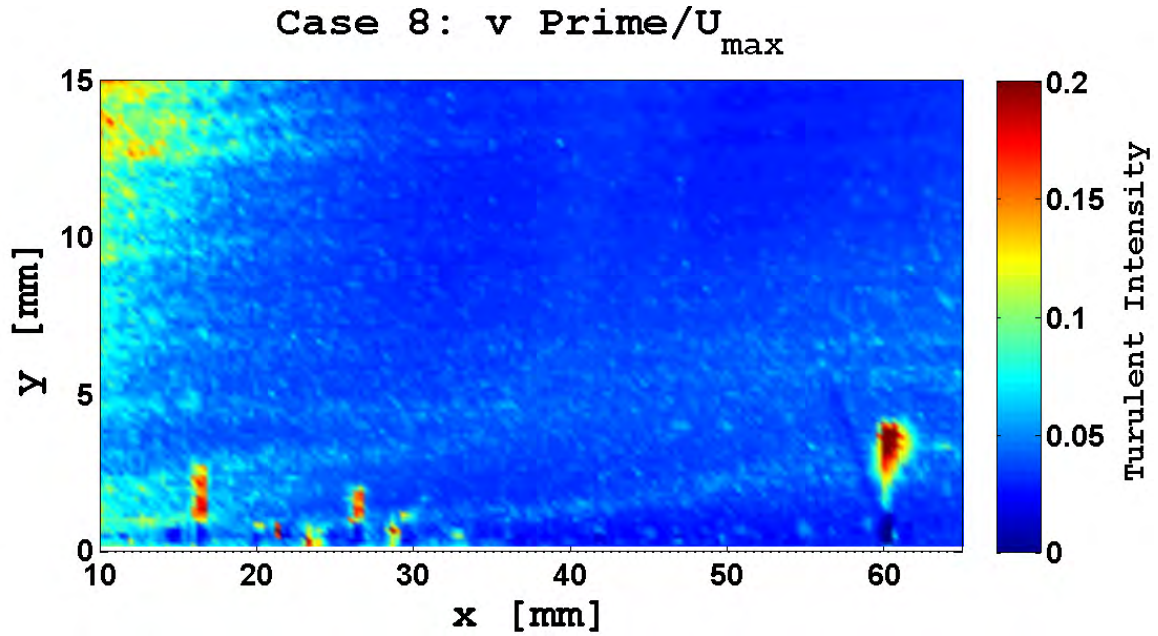
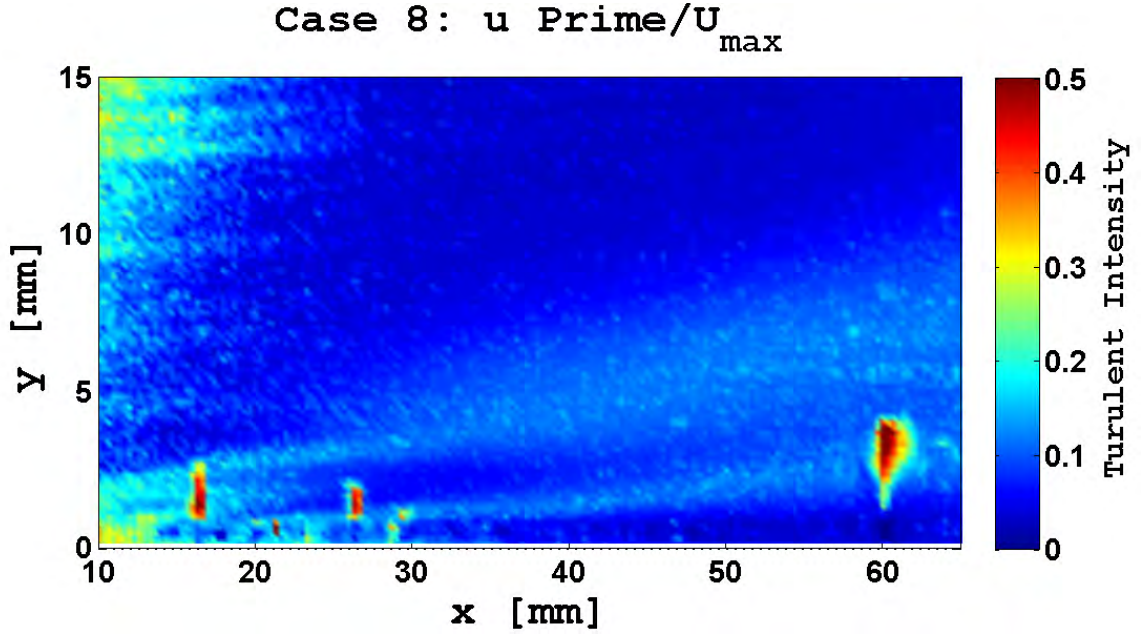


Figure B.62: Case 8: Turbulent intensities. The x component intensity peaks above the suction zone and the intensities are fairly constant in the jet, the induced jet boundary is clearly demarcated. The y component intensities are larger, but the induced jet boundary is still clearly demarcated with a marked shift in intensity. The turbulence in the suction zone is clearly seen near the 0 mm point.

Case 9: 9-0-6

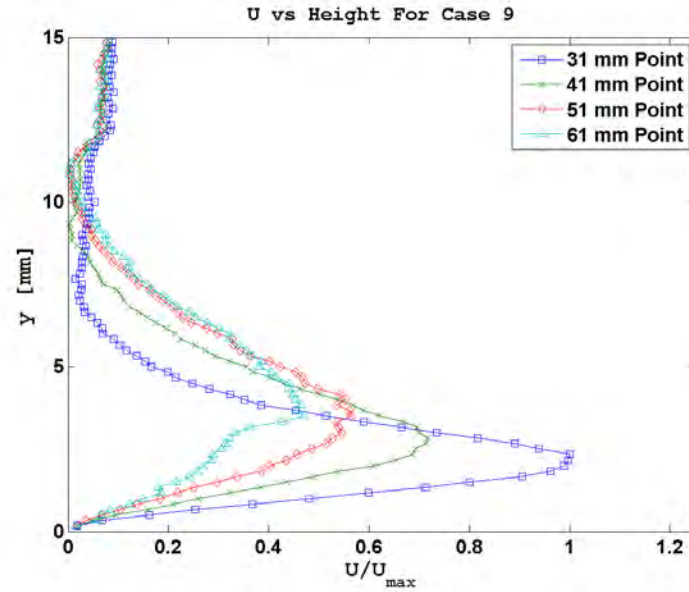


Figure B.63: Case 9: U vs Height

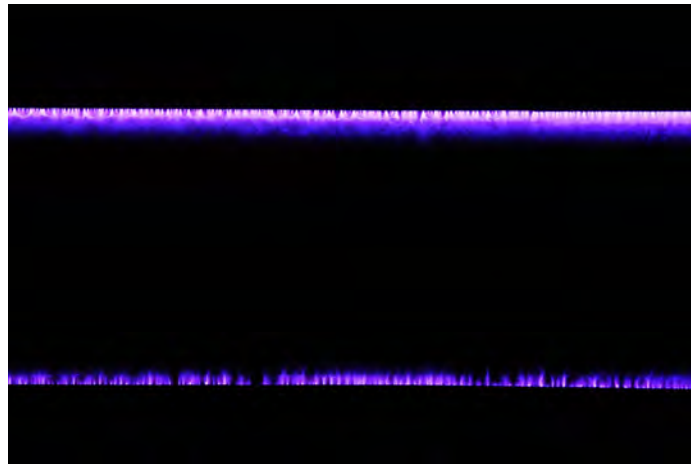


Figure B.64: Case 9: Discharge Plume

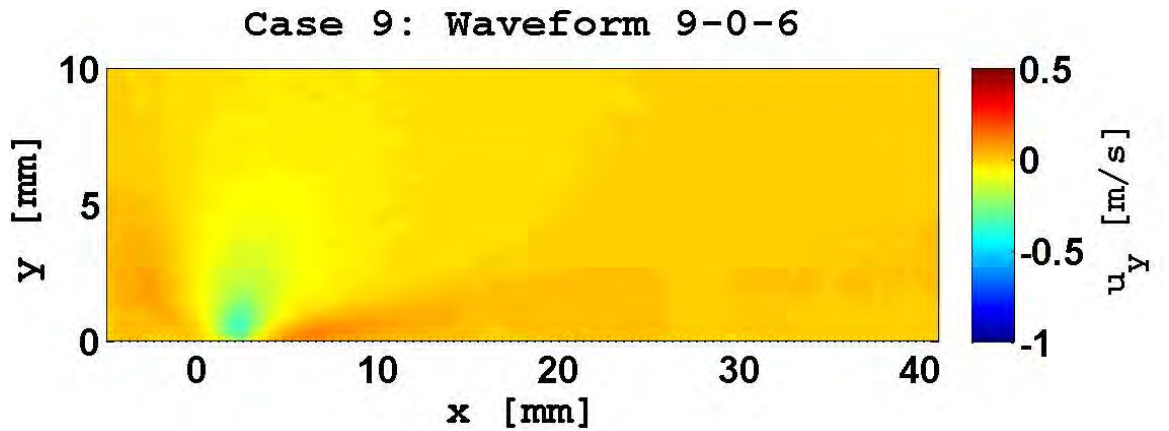
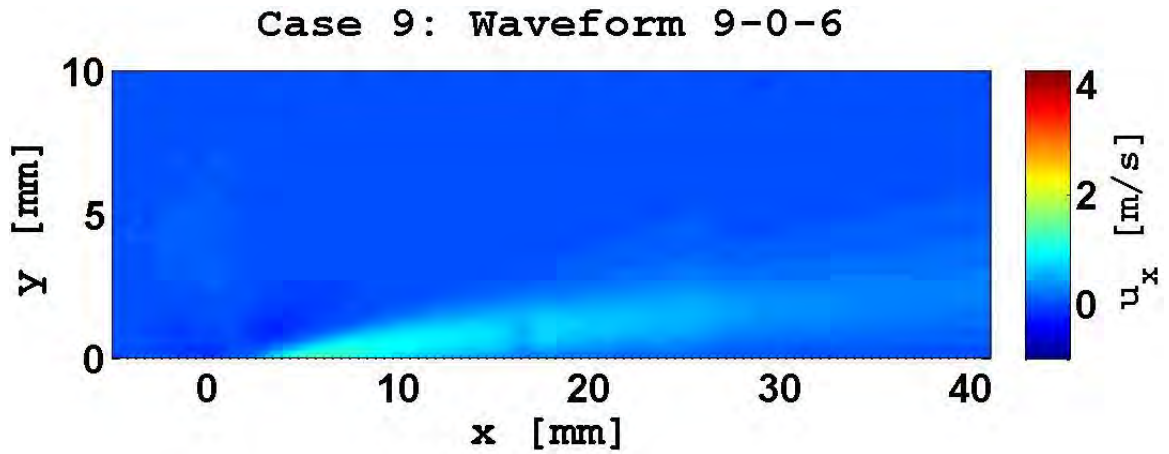
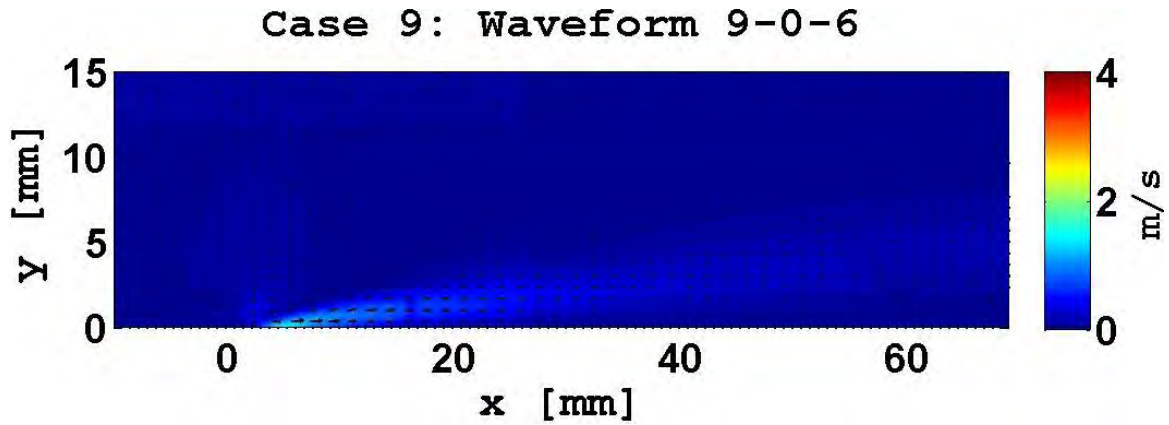


Figure B.65: Case 9: Velocity Vectors and Components

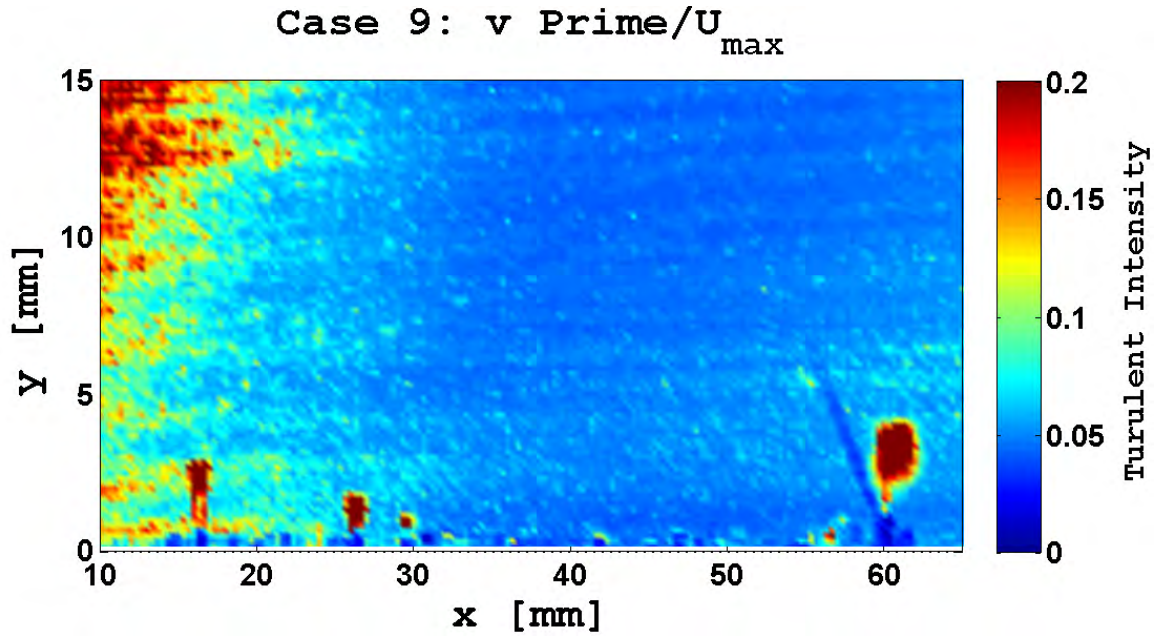
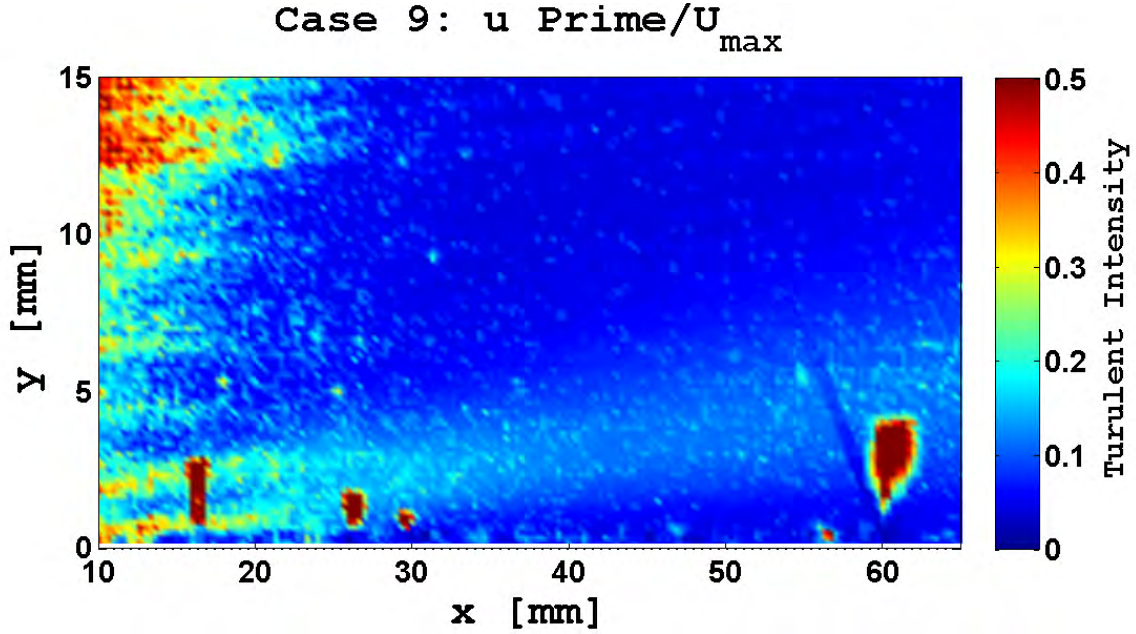


Figure B.66: Case 9: Turbulent intensities. The x component intensity peaks above the suction zone, but the intensities outside this region are very small and there is no clear demarcation of the induced flow boundary. The y component intensities are larger and the induced jet boundary is now clearly demarcated with a marked shift in intensity. The turbulence in the suction zone is clearly seen near the 0 mm point.

Case 10: 17-0-2

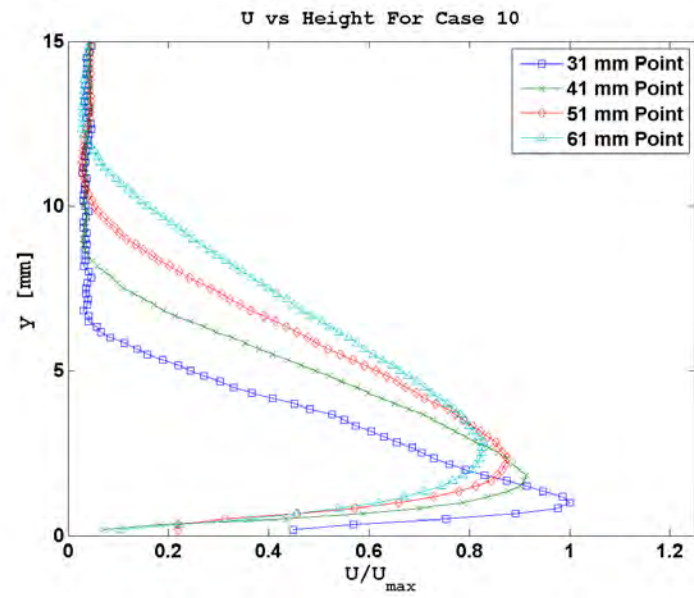


Figure B.67: Case 10: U vs Height

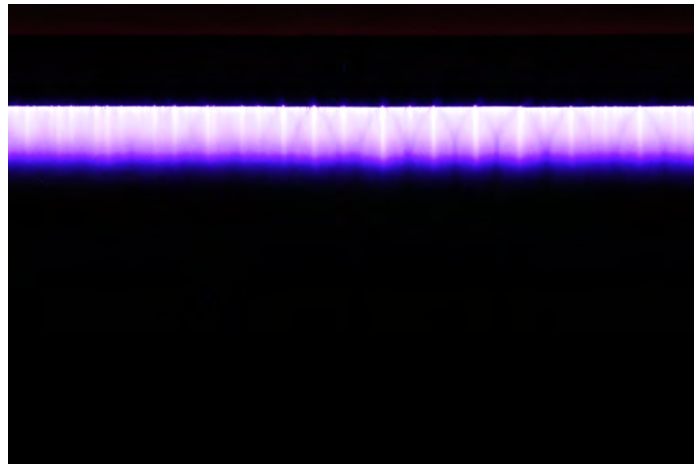


Figure B.68: Case 10: Discharge Plume

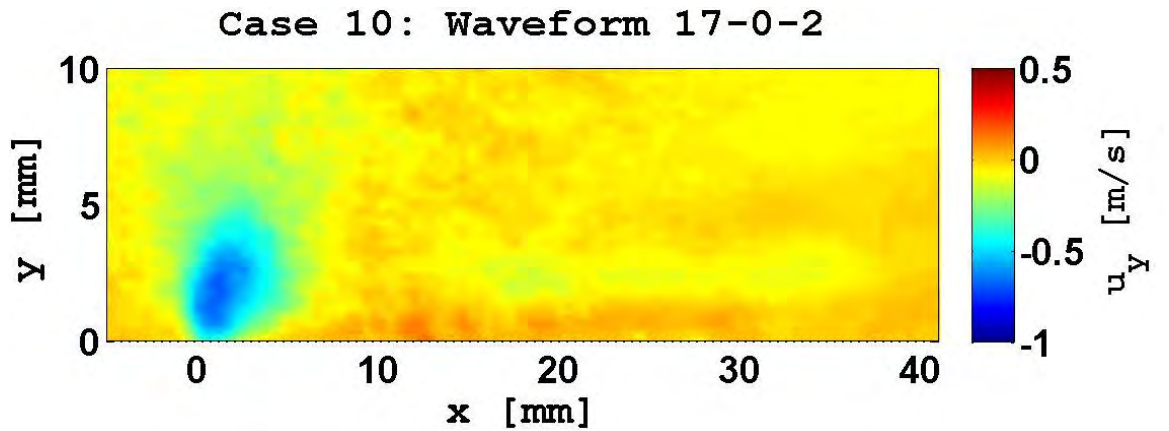
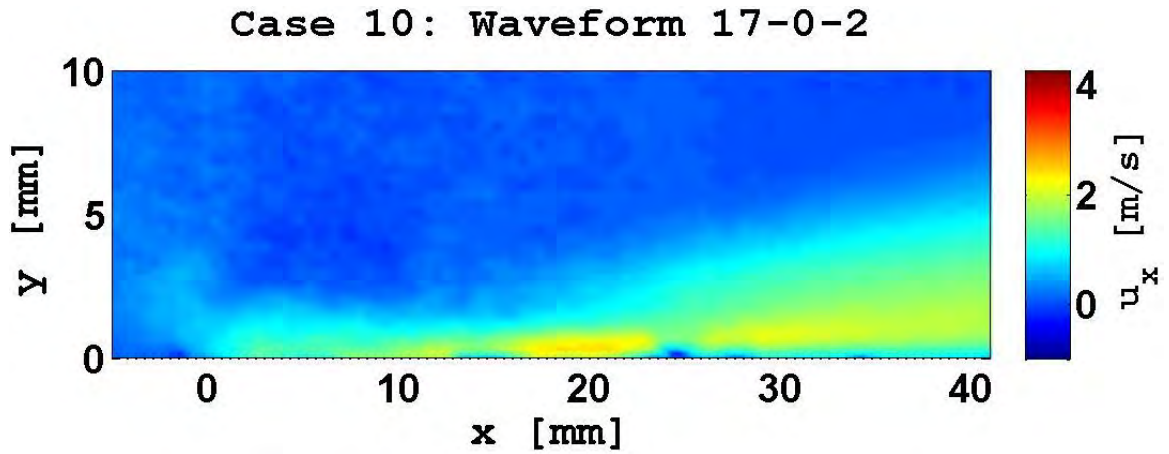
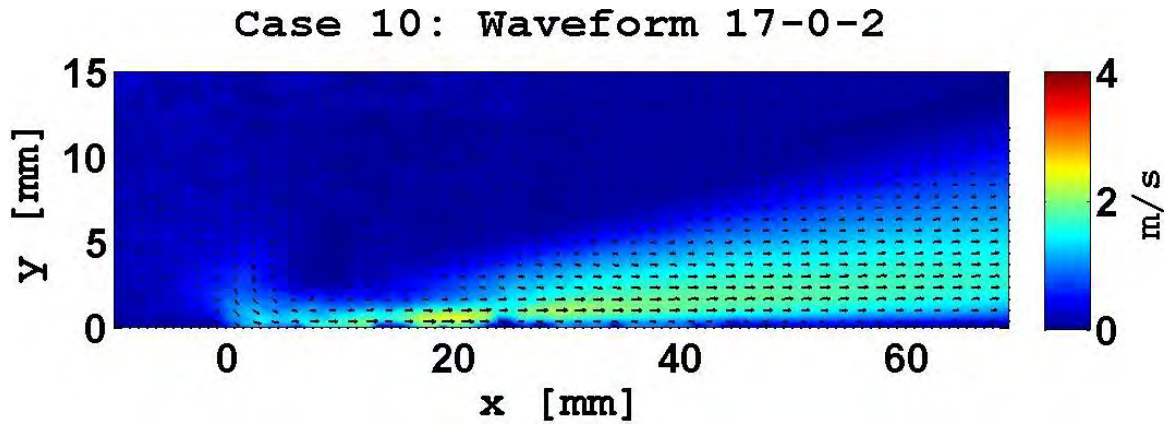
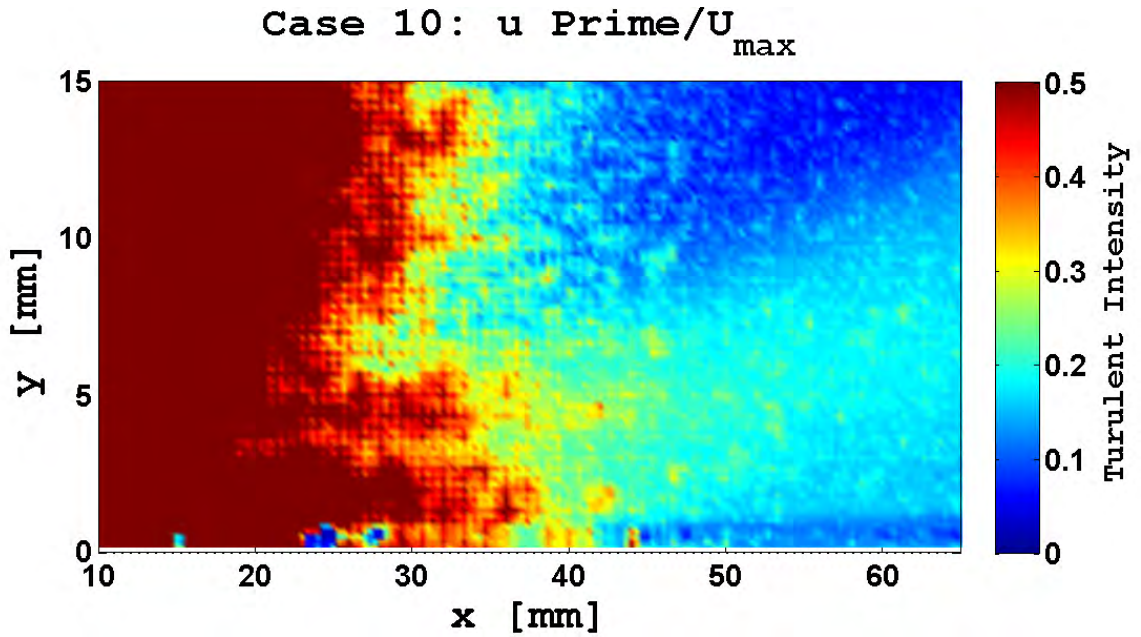
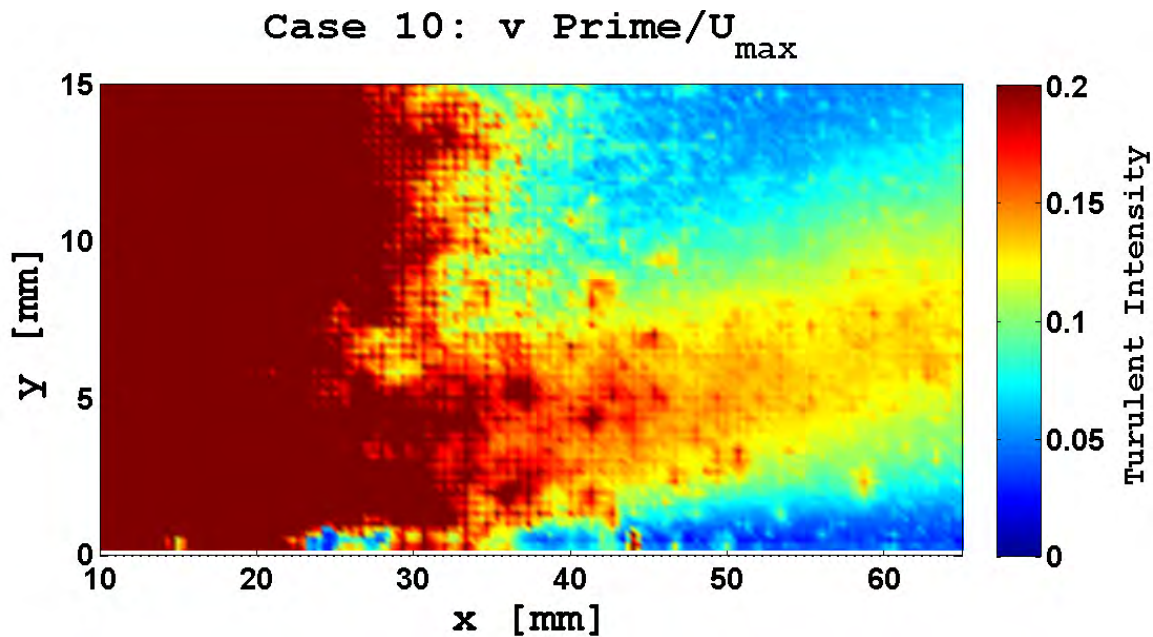


Figure B.69: Case 10: Velocity Vectors and Components



(a) Turbulent Intensity: u' / U_{max}



(b) Turbulent Intensity: v' / U_{max}

Figure B.70: Case 10: Turbulent intensities. The x component intensity peaks above the suction zone, but the intensities outside this region are very small and there is a clear demarcation of the induced flow boundary. The y component intensities are larger and the induced jet boundary is now clearly demarcated with a marked shift in intensity. The turbulence in the suction zone is clearly seen near the 0 mm point. The filamentary nature of this discharge has caused an increase in the turbulence of the induced flow.

Case 11: 18-0-3

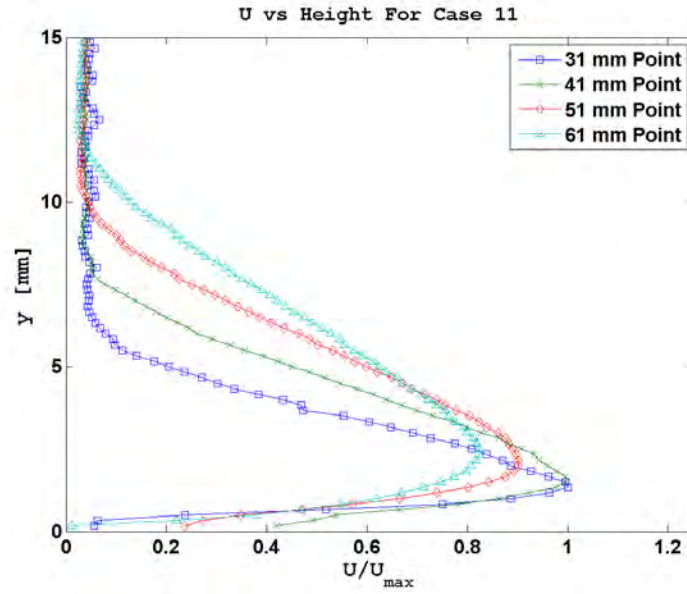


Figure B.71: Case 11: U vs Height

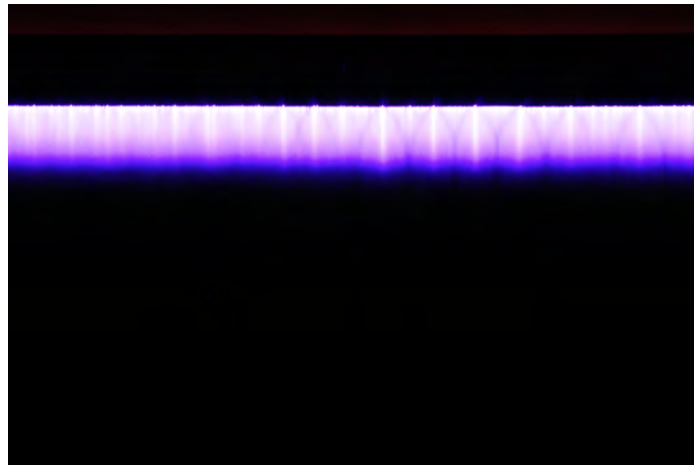


Figure B.72: Case 11: Discharge Plume

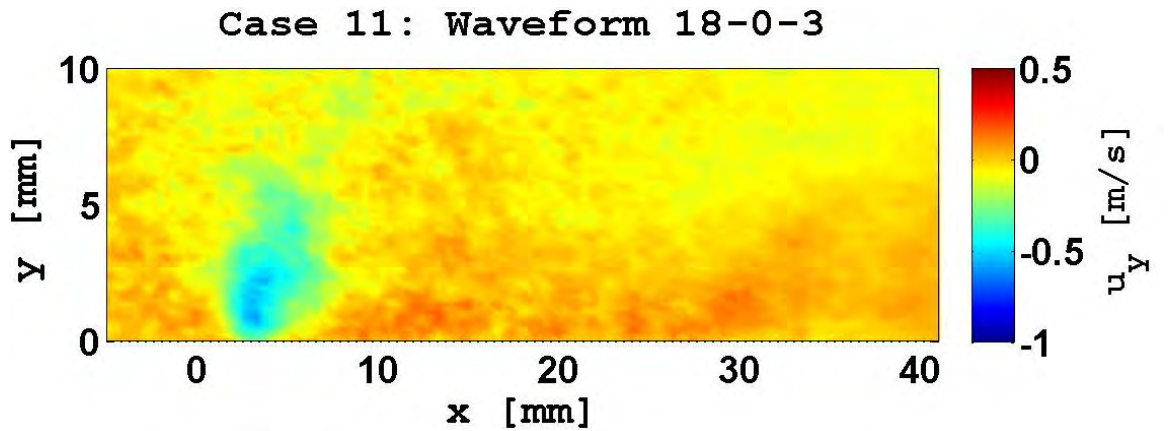
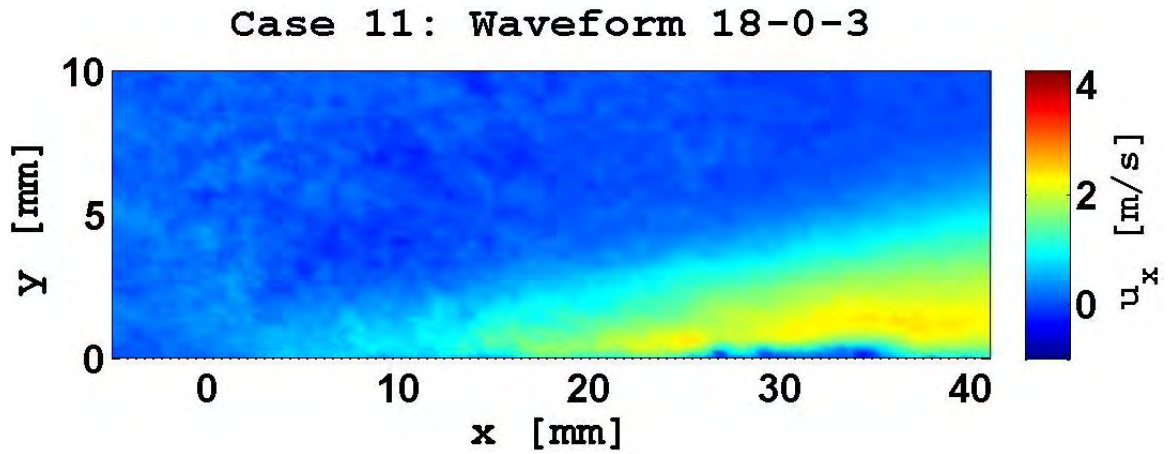
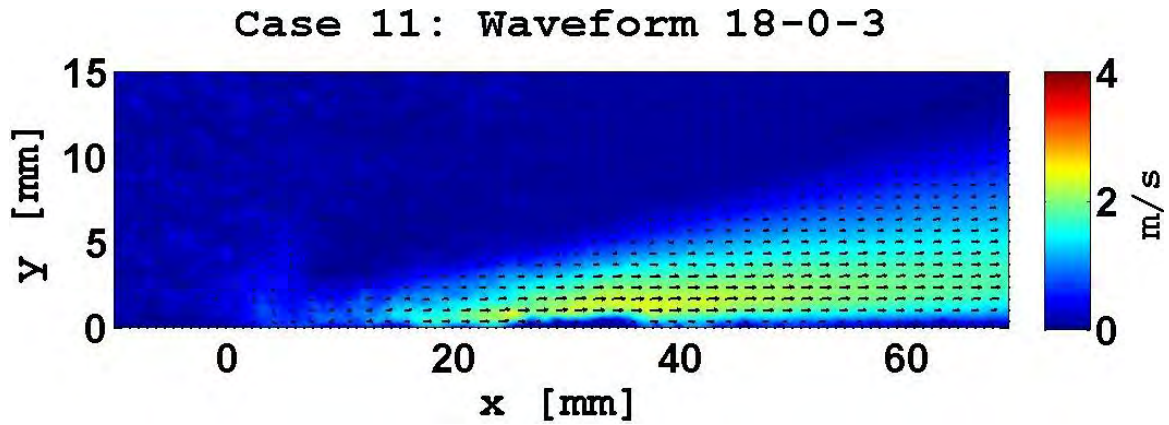


Figure B.73: Case 11: Velocity Vectors and Components

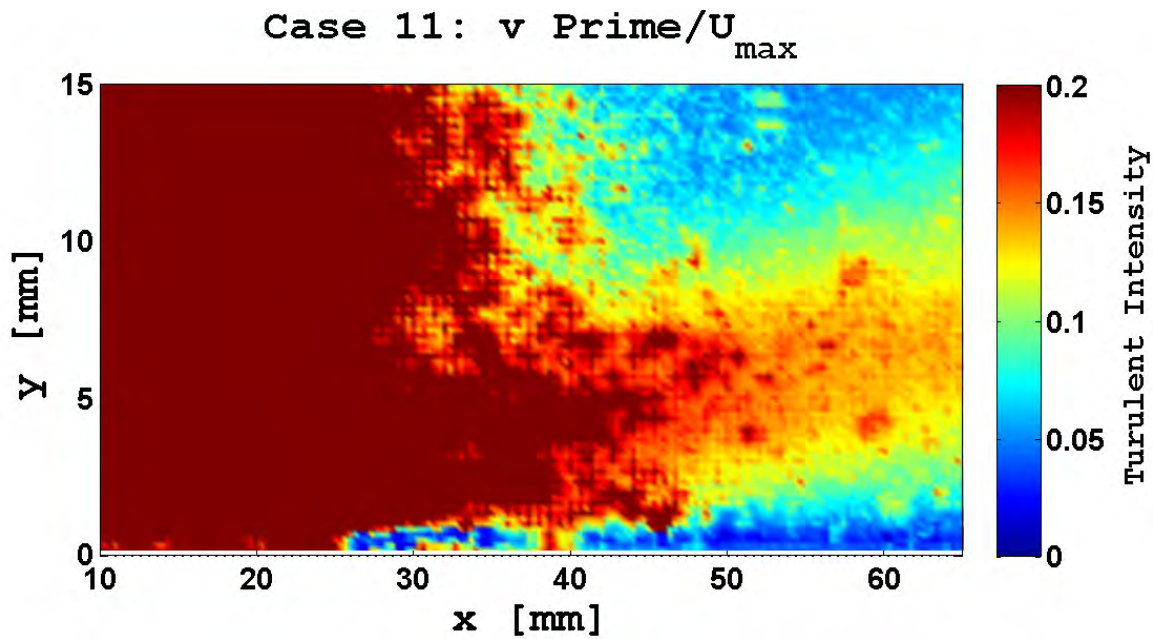
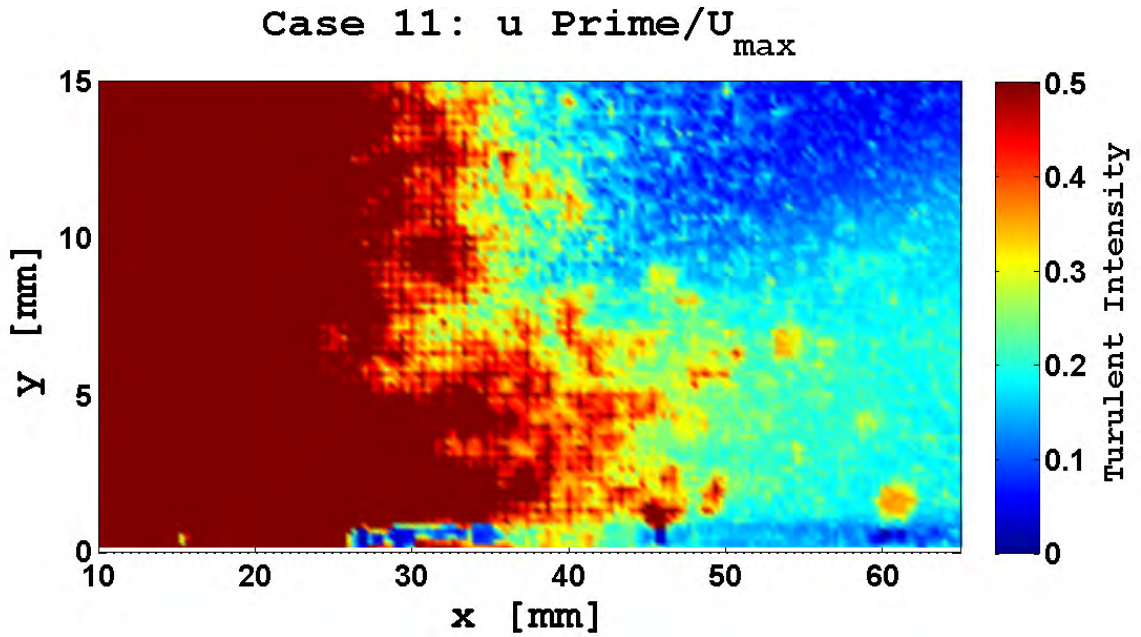


Figure B.74: Case 11: Turbulent intensities. The x component intensity peaks above the suction zone, but the intensities in the jet outside this region are still present and there is a clear demarcation of the induced flow boundary. The y component intensities are larger and the induced jet boundary is now clearly demarcated with a marked shift in intensity. The turbulence in the suction zone is clearly seen near the 0 mm point and is much stronger than was present in earlier cases. The intense filamentary nature of this discharge has caused an increase in the turbulence of the induced flow.

B.4 Phase III

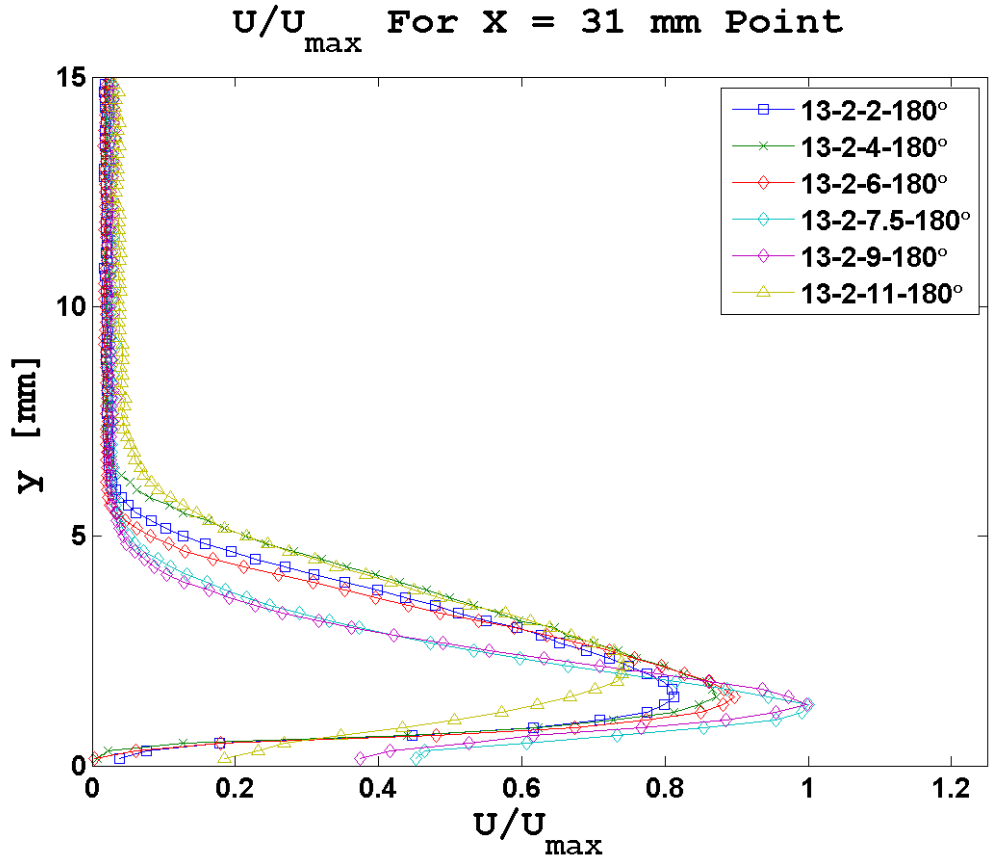


Figure B.75: Phase III Velocity Profiles: 31 mm Point. $U_{\max} = 2.41$ m/s.

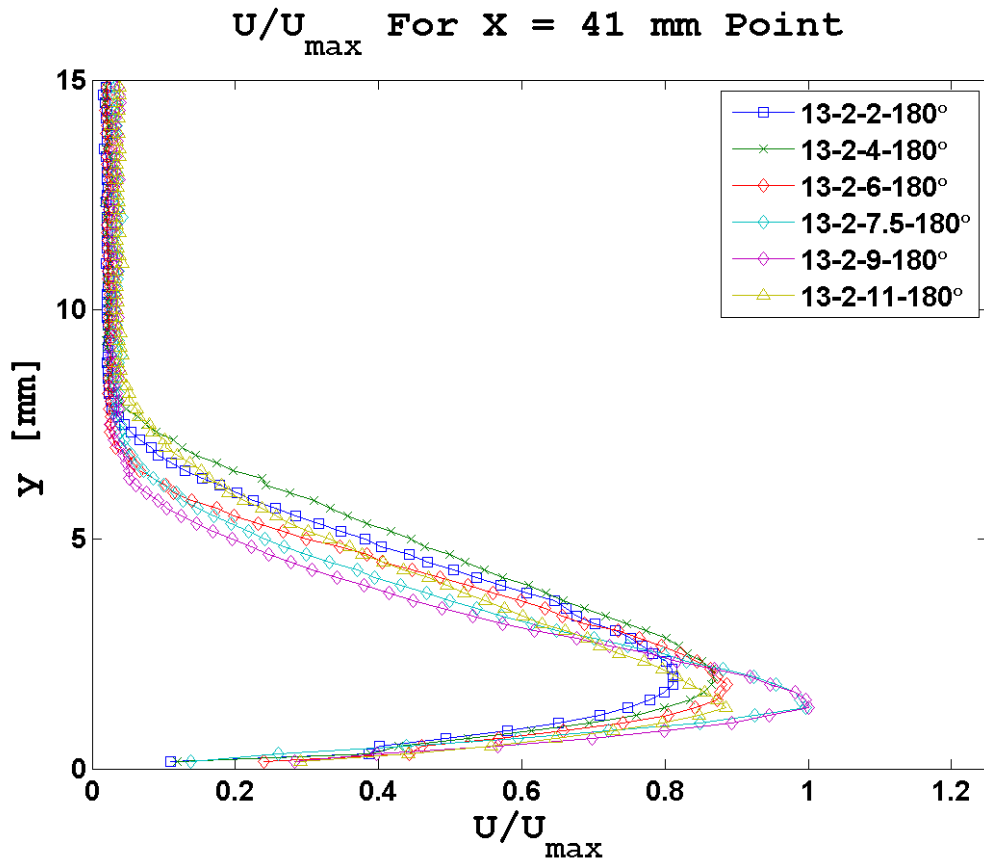


Figure B.76: Phase III Velocity Profiles: 41 mm Point. $U_{\max} = 1.98$ m/s.

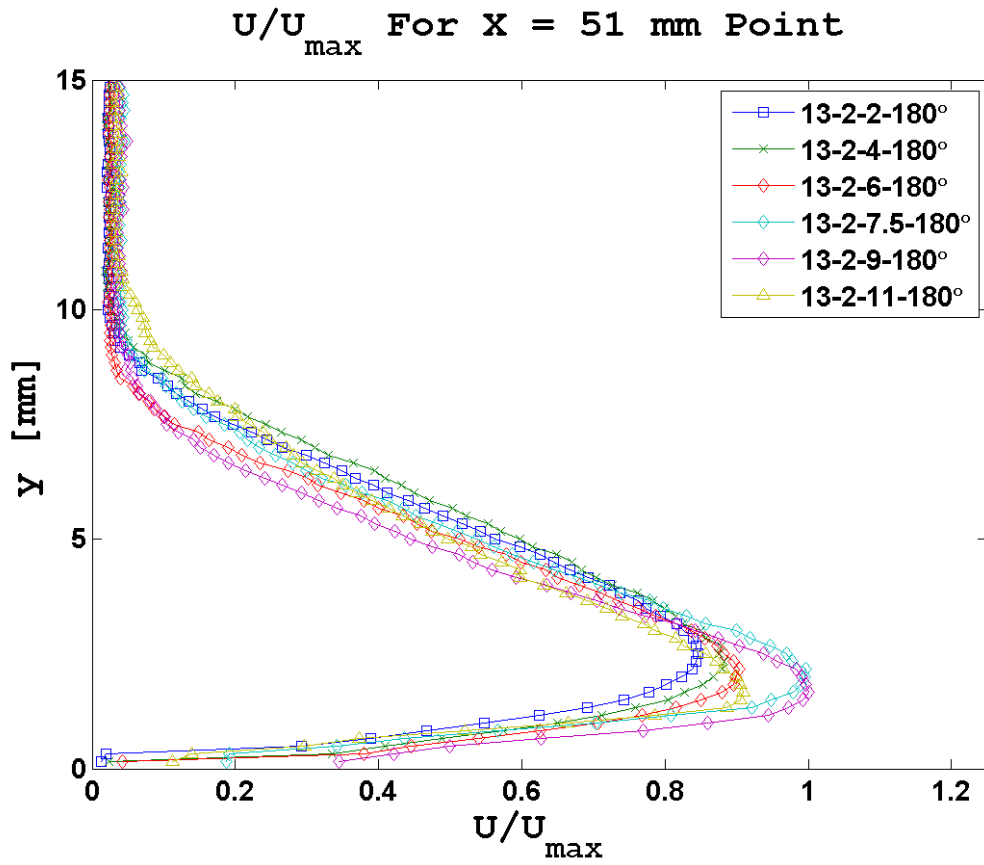


Figure B.77: Phase III Velocity Profiles: 51 mm Point. $U_{\max} = 1.71$ m/s.

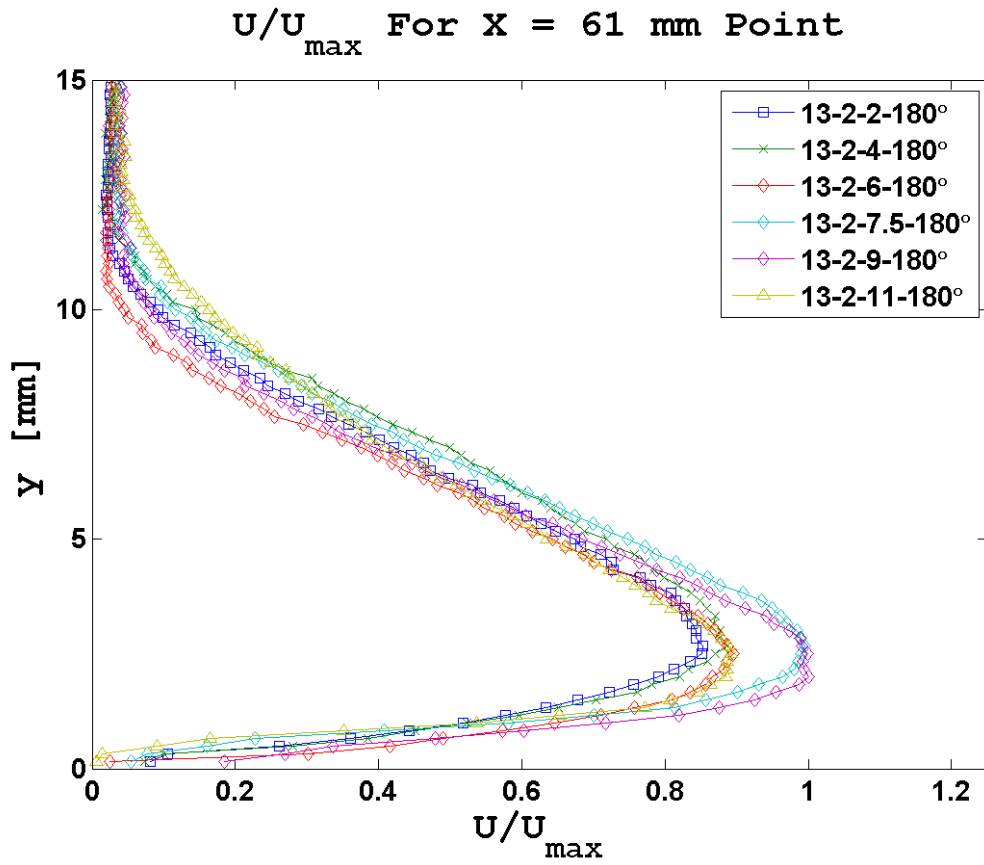


Figure B.78: Phase III Velocity Profiles: 61 mm Point. $U_{\max} = 1.52$ m/s.

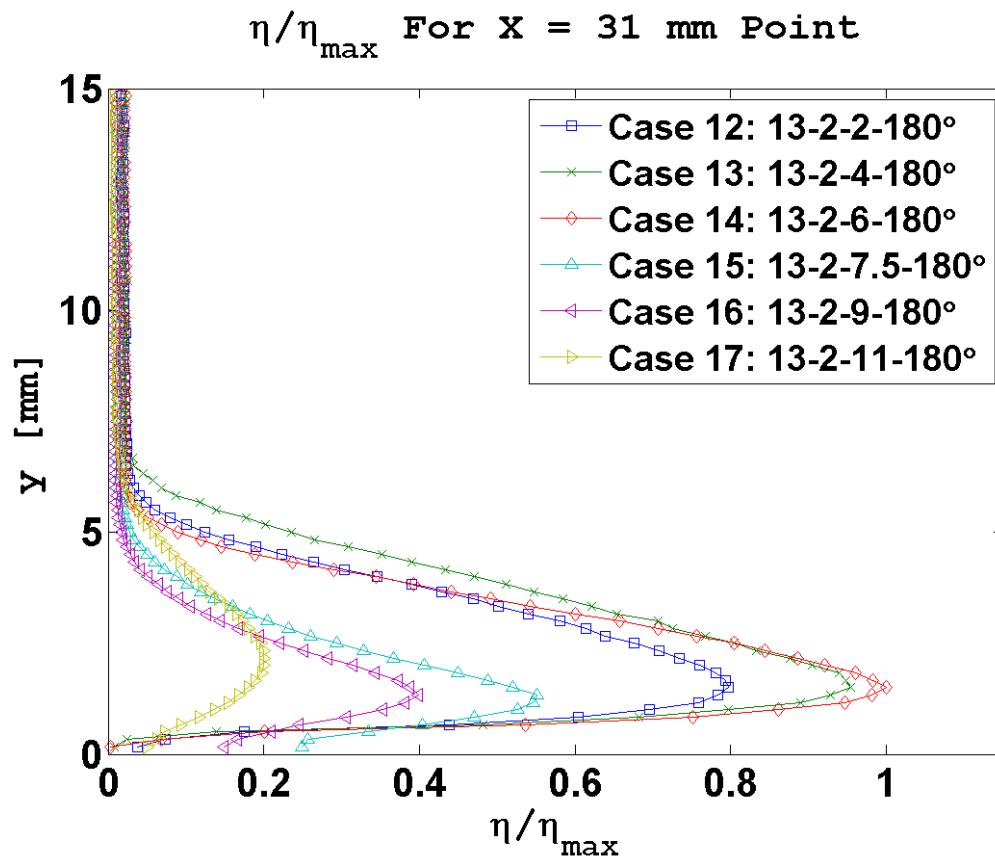


Figure B.79: Phase III Efficiency Profiles: 31 mm Point

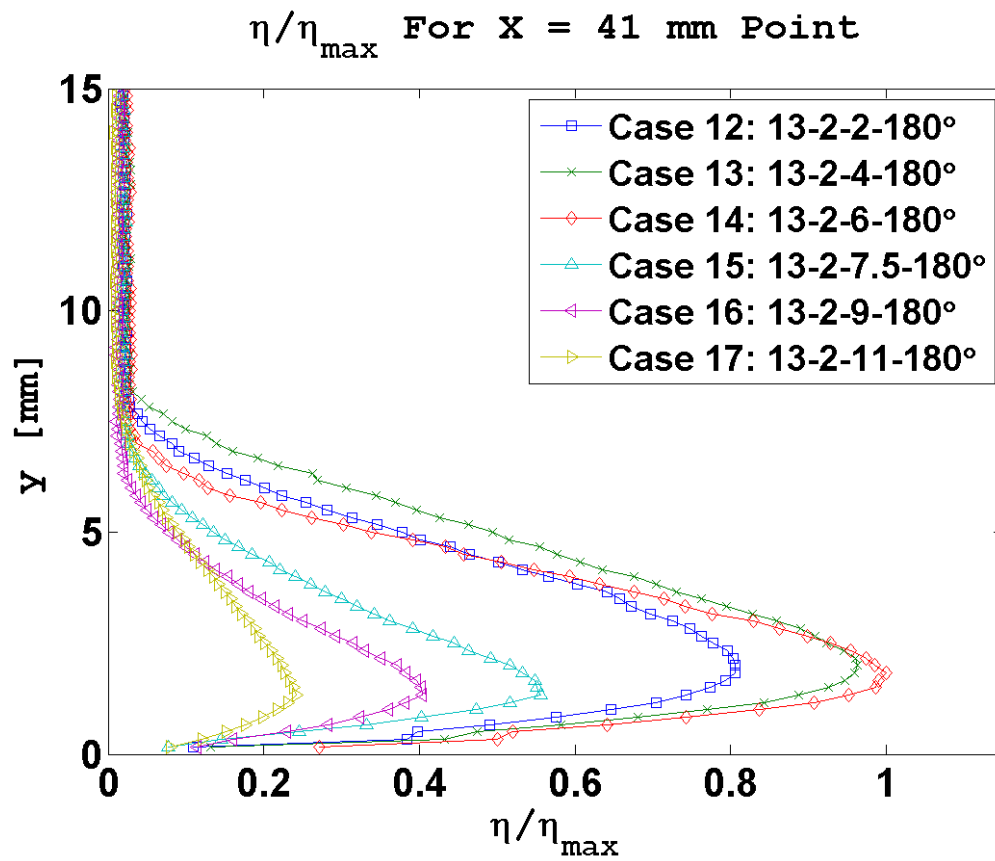


Figure B.80: Phase III Efficiency Profiles: 41 mm Point

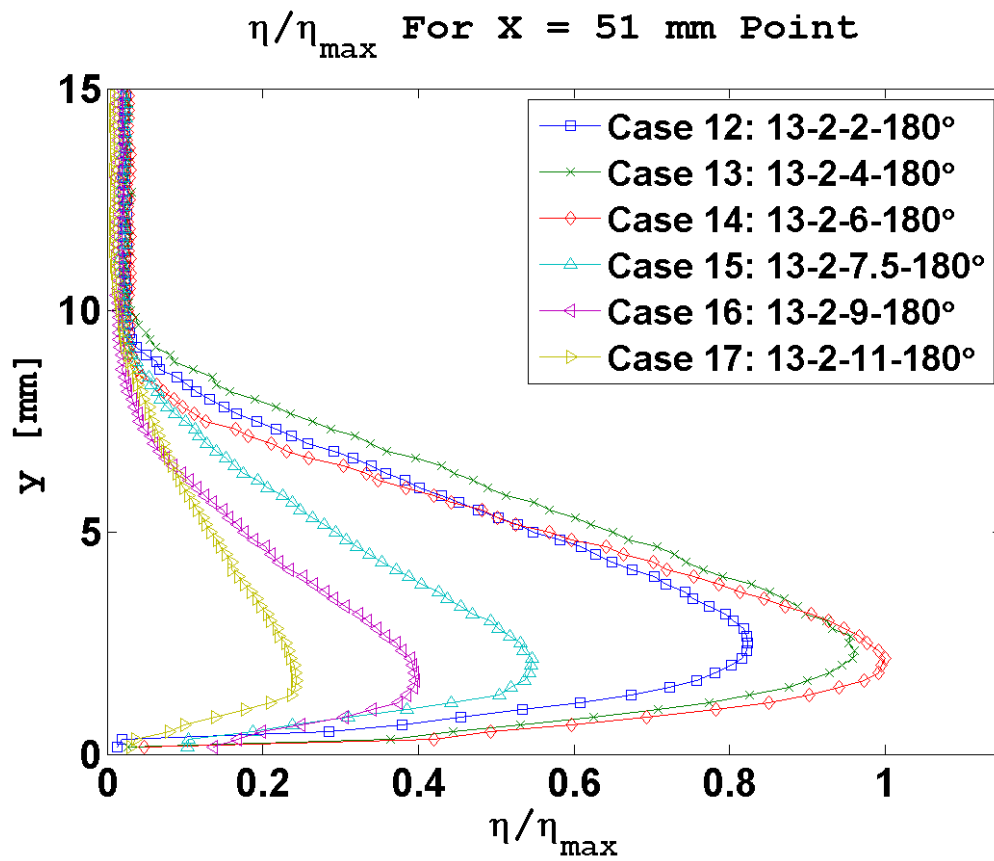


Figure B.81: Phase III Efficiency Profiles: 51 mm Point

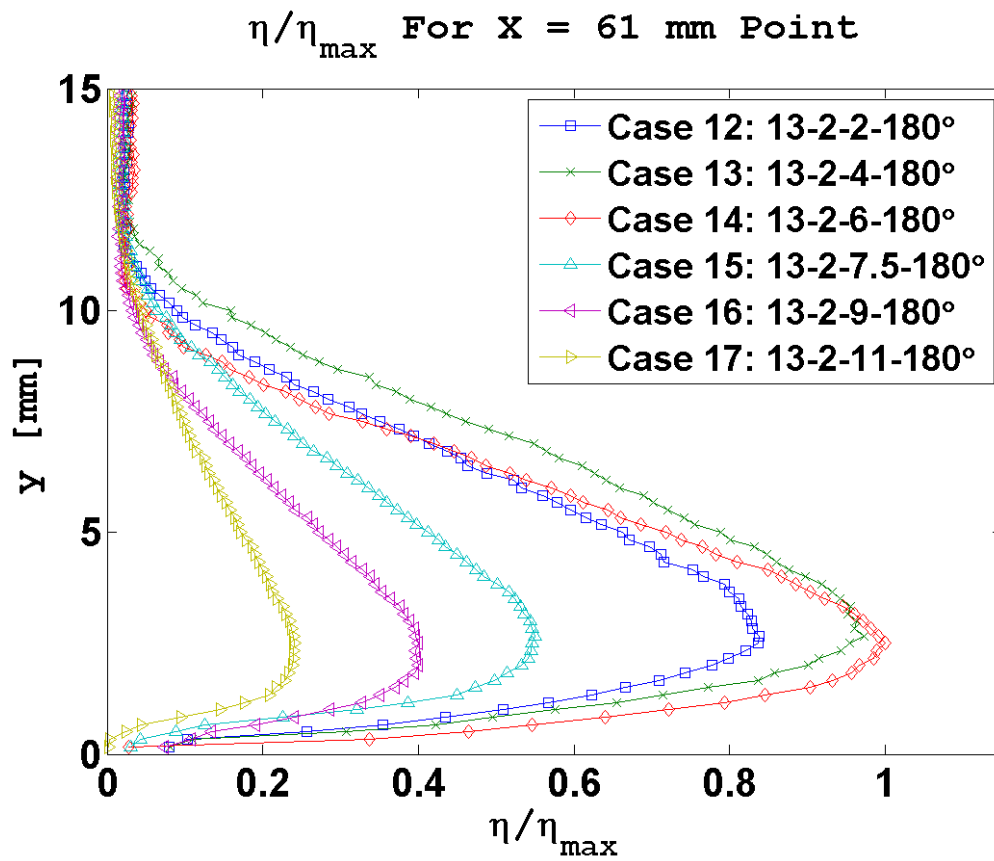


Figure B.82: Phase III Efficiency Profiles: 61 mm Point

Case 12: 13-2-2

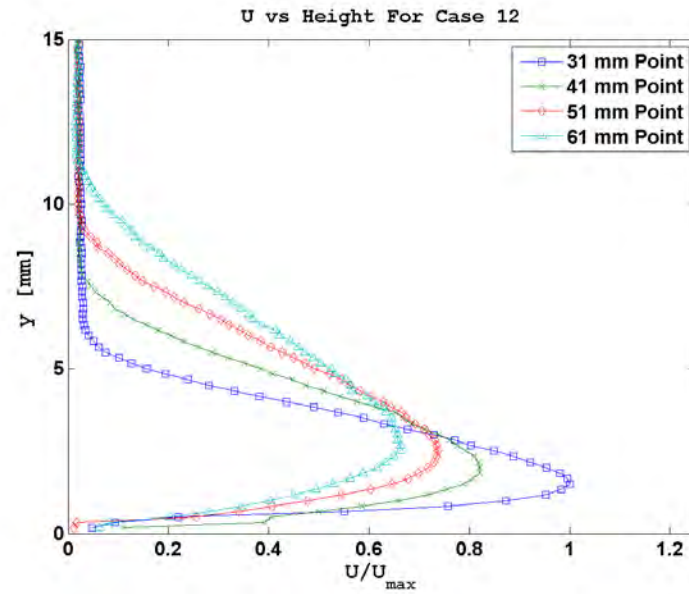


Figure B.83: Case 12: U vs Height

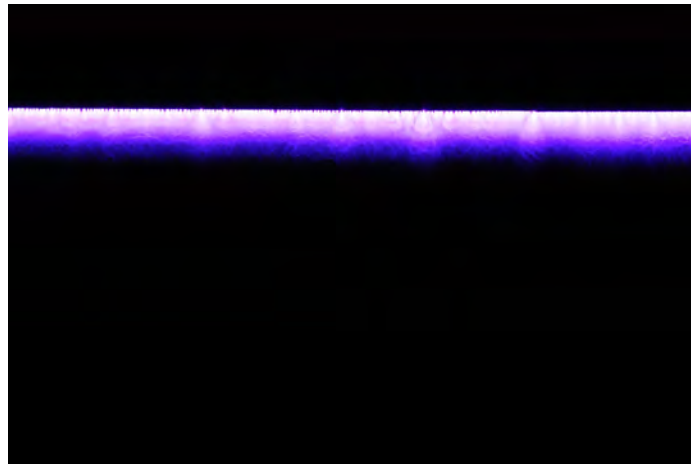


Figure B.84: Case 12: Discharge Plume

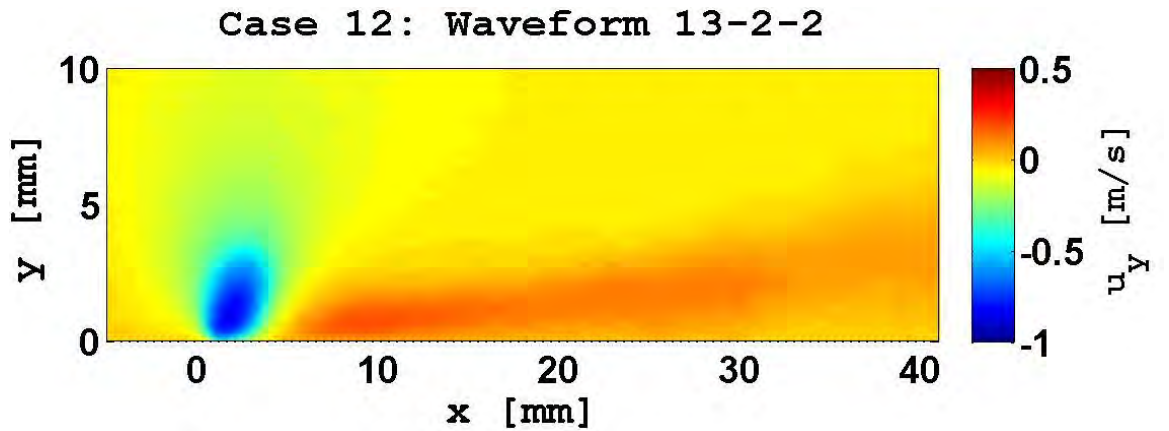
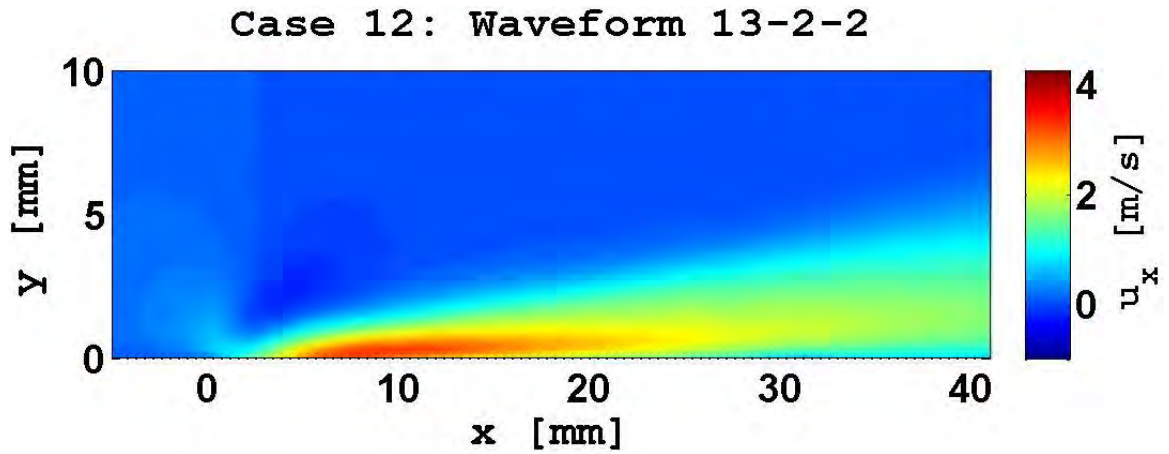
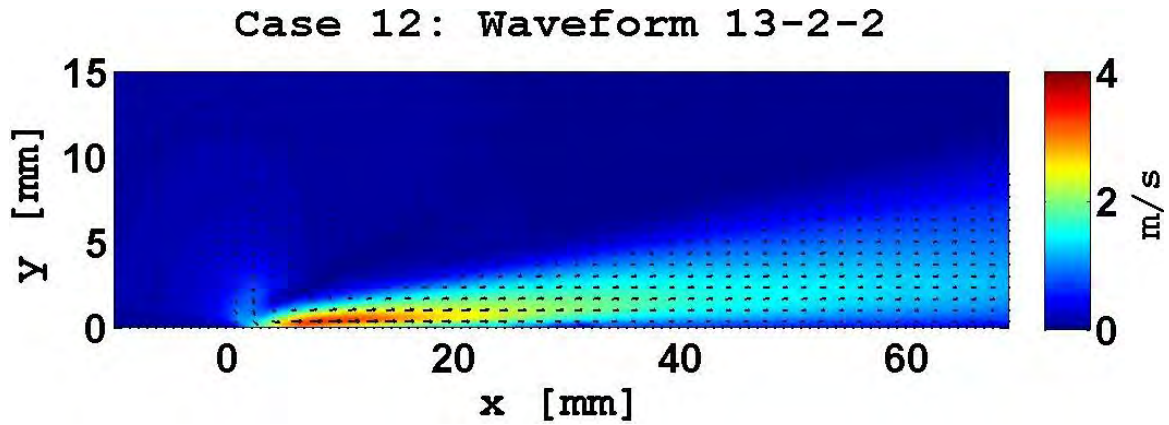
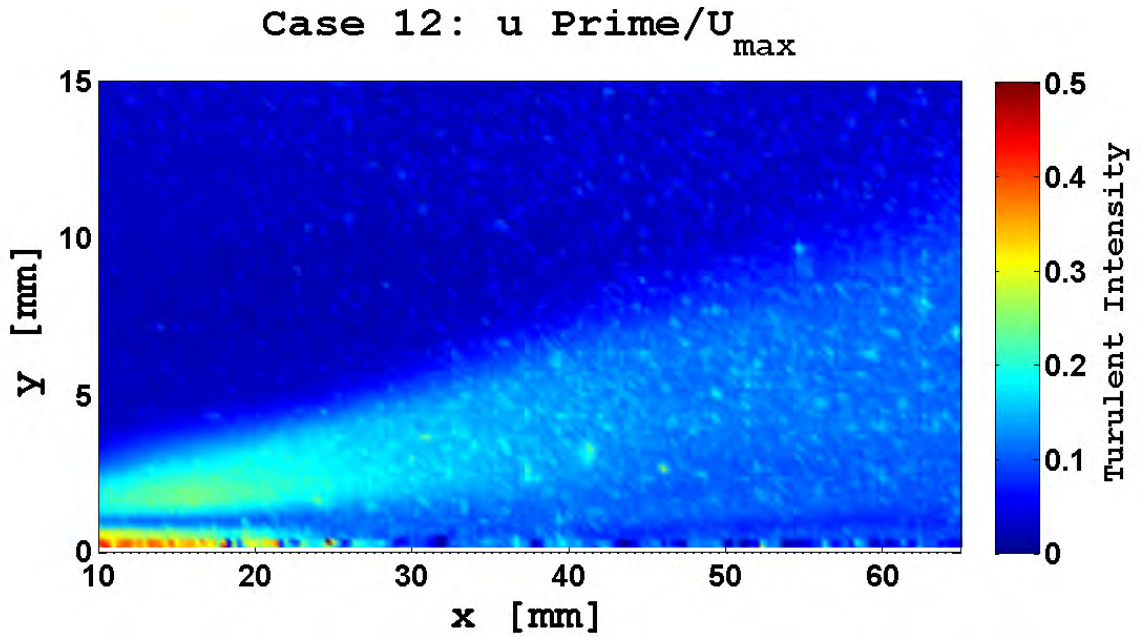
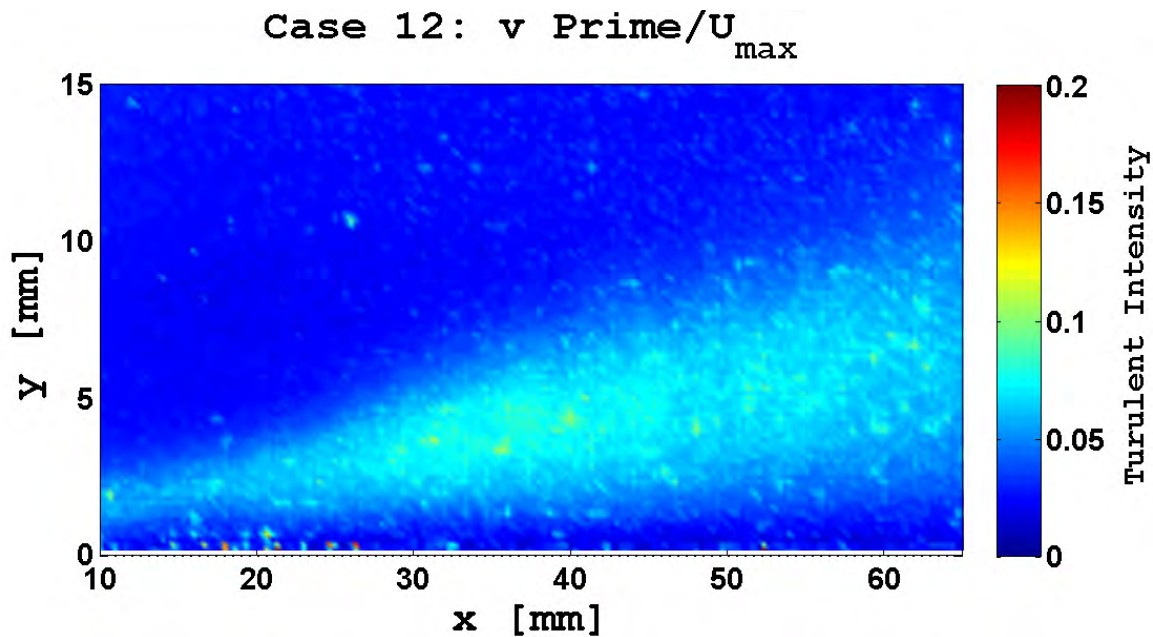


Figure B.85: Case 12: Velocity Vectors and Components



(a) Turbulent Intensity: u' / U_{max}



(b) Turbulent Intensity: v' / U_{max}

Figure B.86: Case 12: Turbulent intensities. The x component intensity peaks between the exposed electrodes and the intensities in the jet outside this region are still present with a clear demarcation of the induced flow boundary and the far field region. The y component intensities are smaller and the induced jet boundary is now clearly demarcated with a marked shift from negative to positive intensity. The turbulence in the suction zone is no longer seen near the 0 mm point. The large negative values of the y component is present in all of the Phase III Test Cases.

Case 13: 13-2-4

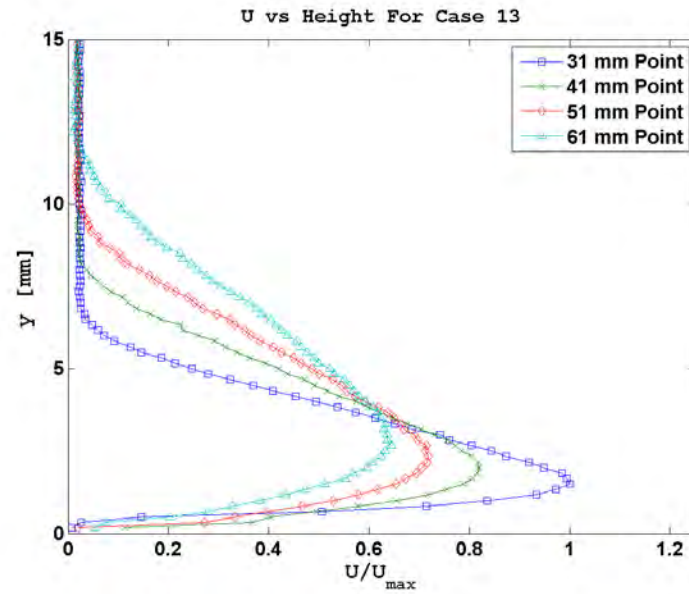


Figure B.87: Case 13: U vs Height

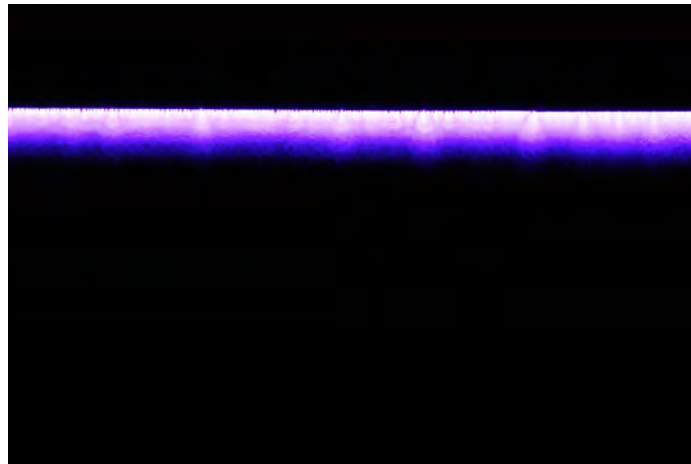


Figure B.88: Case 13: Discharge Plume

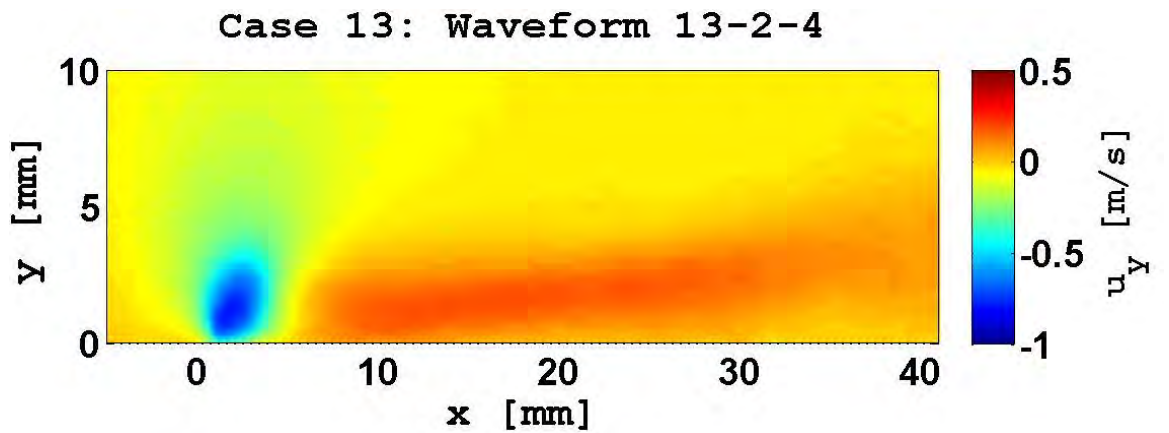
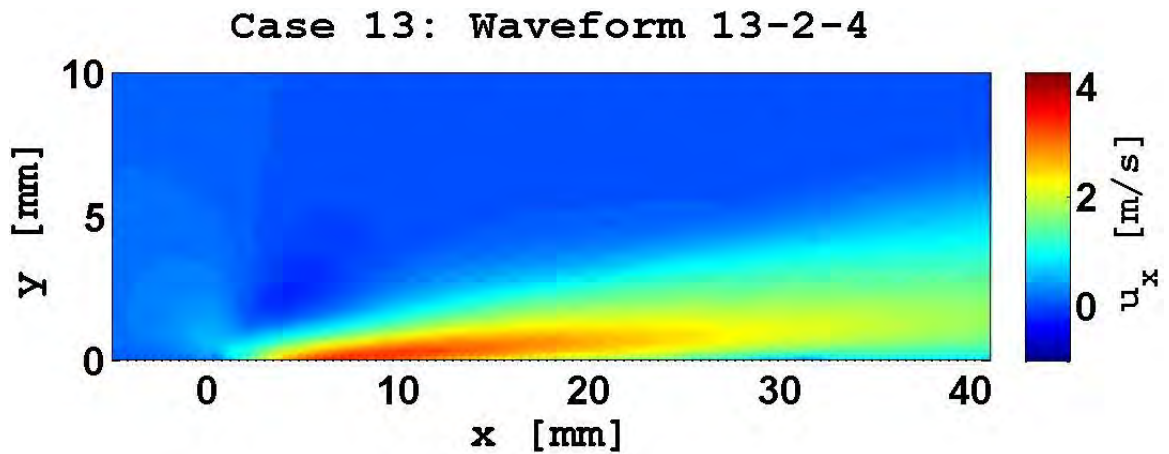
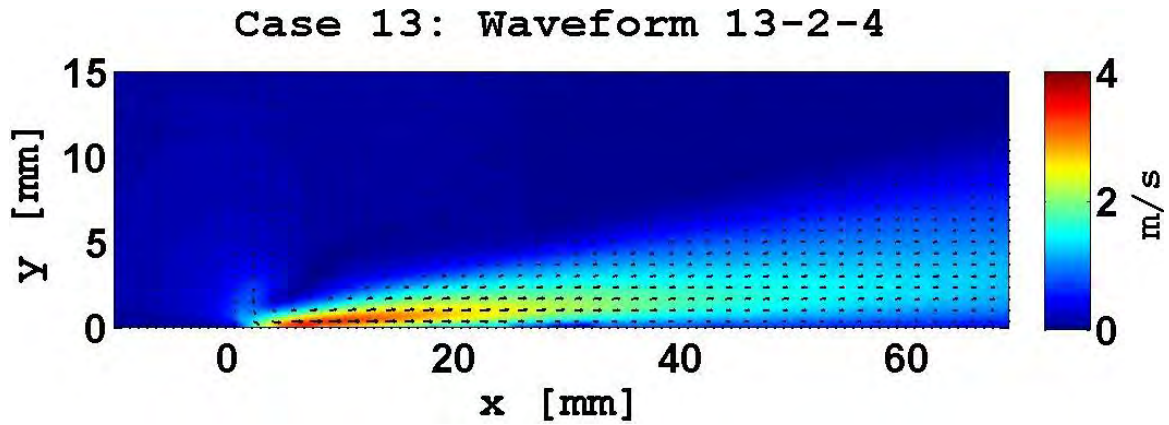
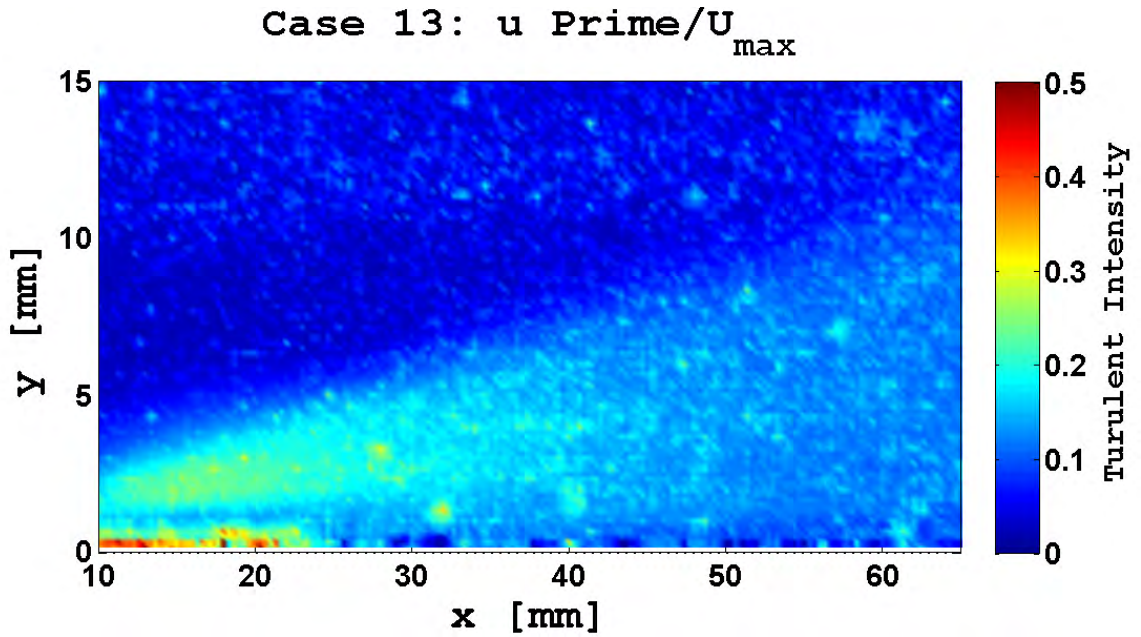
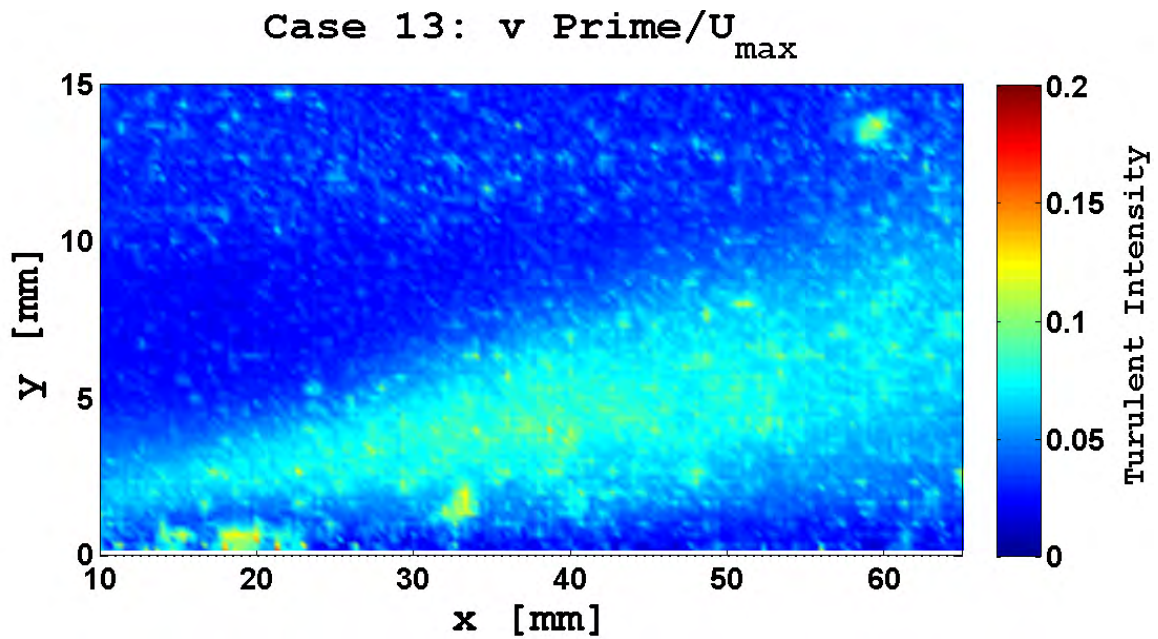


Figure B.89: Case 13: Velocity Vectors and Components



(a) Turbulent Intensity: u' / U_{max}



(b) Turbulent Intensity: v' / U_{max}

Figure B.90: Case 13: Turbulent intensities. The x component intensity peaks between the exposed electrodes and the intensities in the jet outside this region are still present with a clear demarcation of the induced flow boundary and the far field region. The y component intensities are smaller and the induced jet boundary is now clearly demarcated with a marked shift from negative to positive intensity. The turbulence in the suction zone is no longer seen near the 0 mm point. The large negative values of the y component is present in all of the Phase III Test Cases.

Case 14: 13-2-6

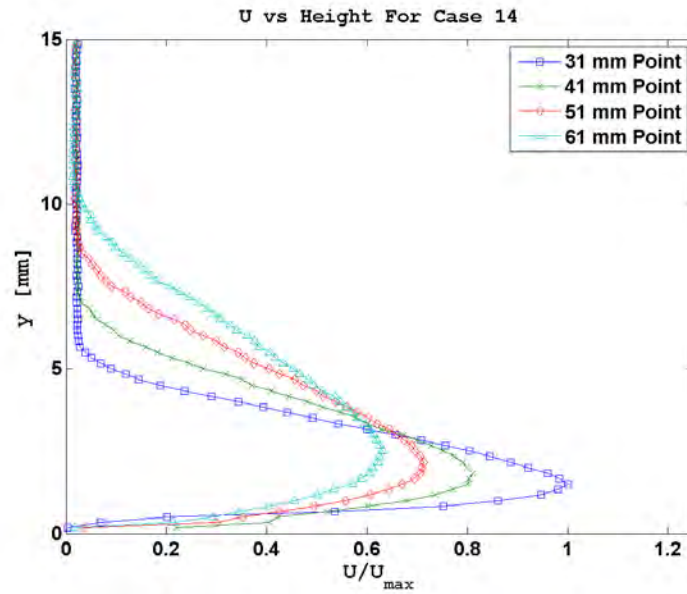


Figure B.91: Case 14: U vs Height

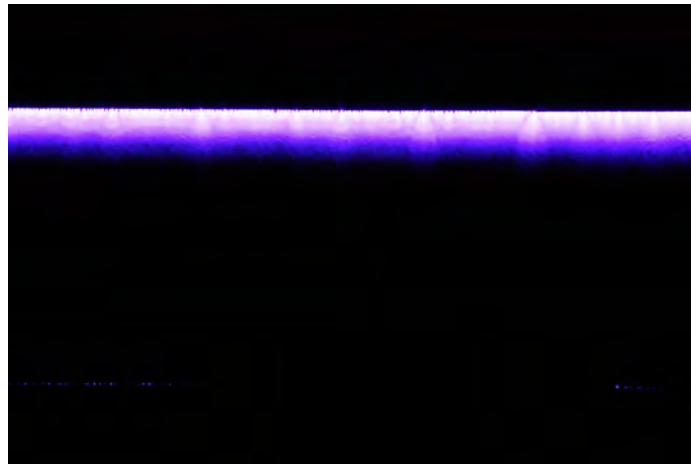


Figure B.92: Case 14: Discharge Plume

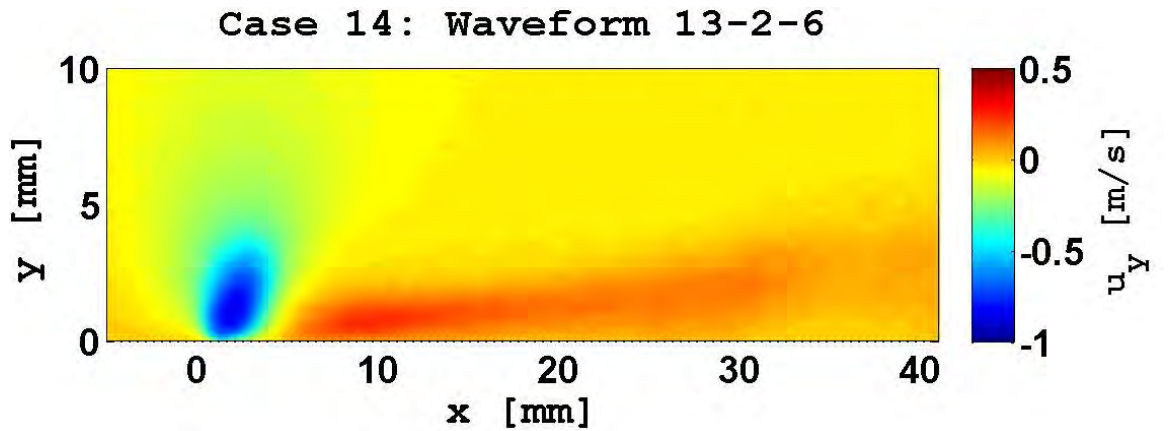
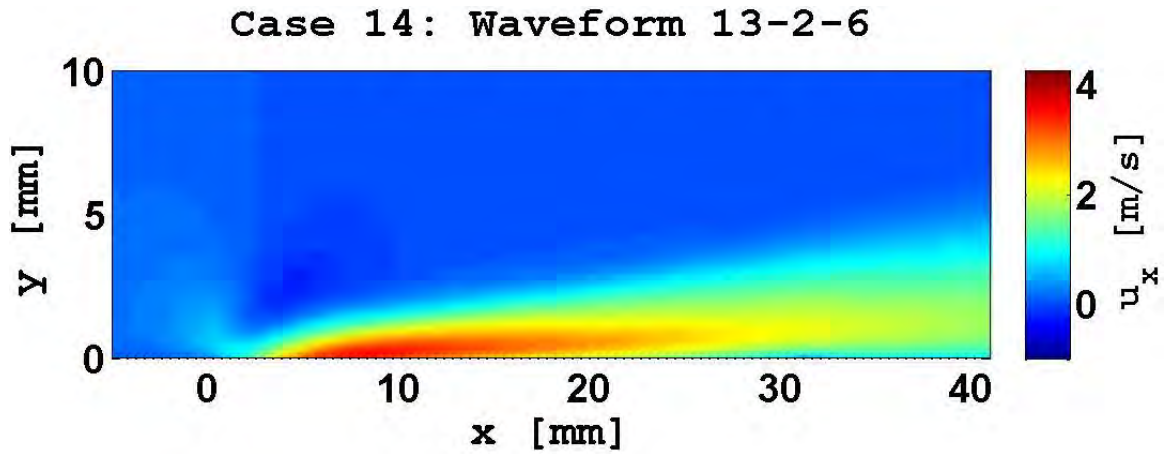
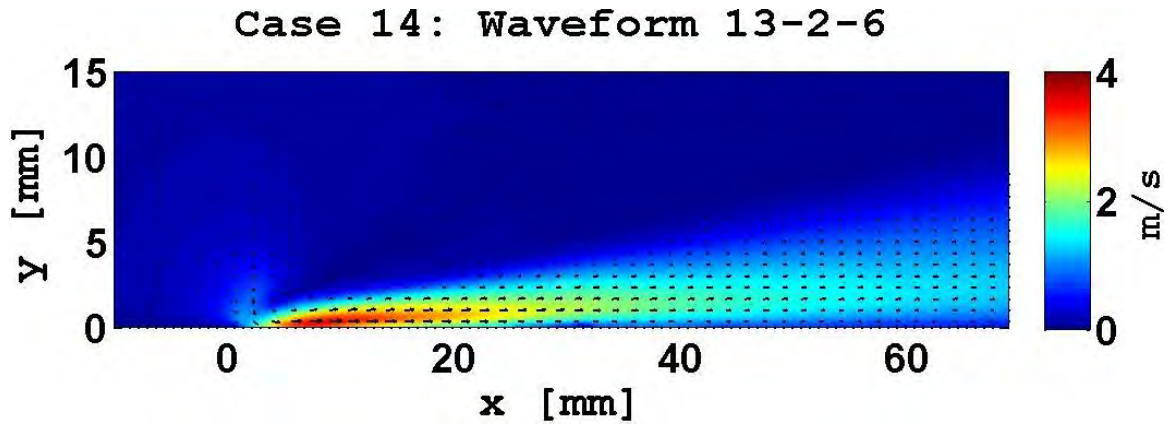
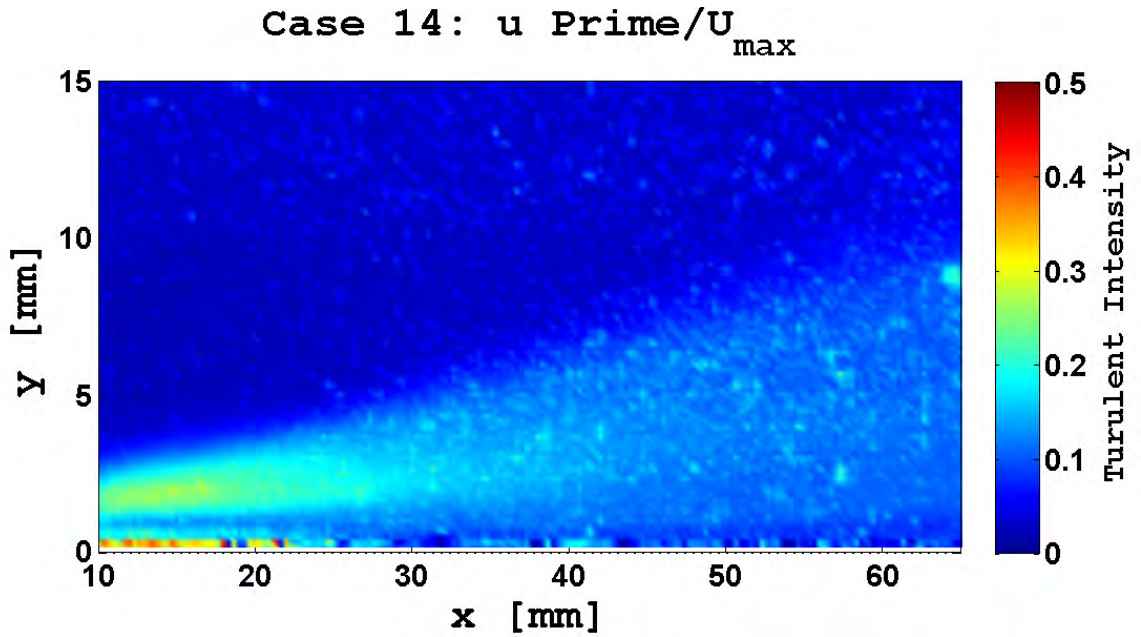
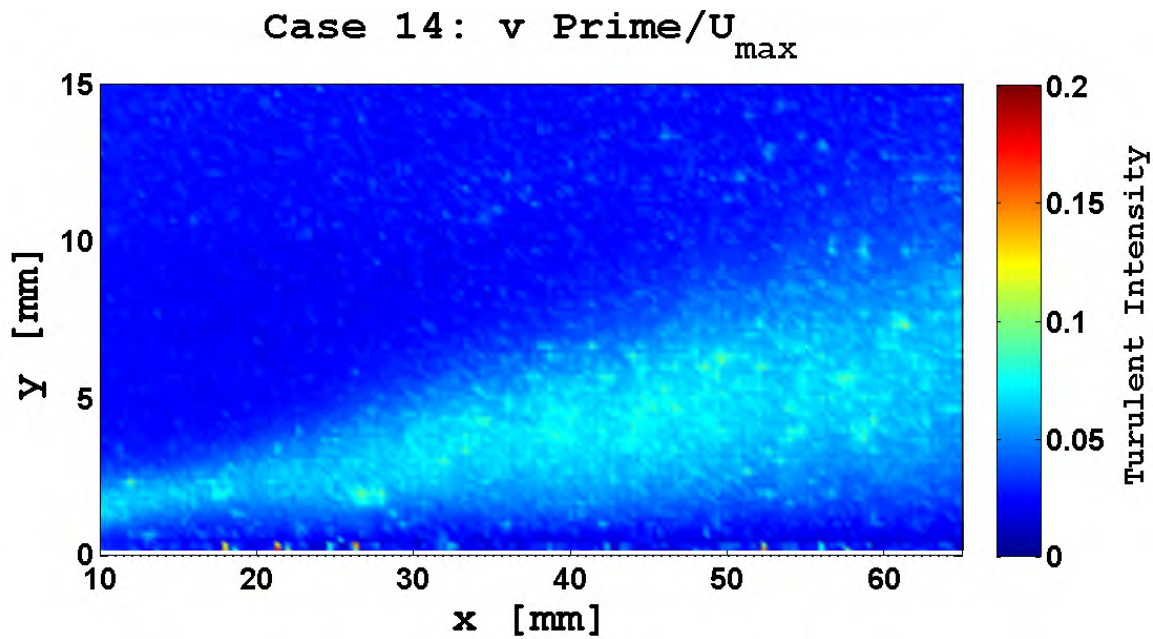


Figure B.93: Case 14: Velocity Vectors and Components



(a) Turbulent Intensity: u' / U_{max}



(b) Turbulent Intensity: v' / U_{max}

Figure B.94: Case 14: Turbulent intensities. The x component intensity peaks between the exposed electrodes and the intensities in the jet outside this region are still present with a clear demarcation of the induced flow boundary and the far field region. The y component intensities are smaller and the induced jet boundary is now clearly demarcated with a marked shift from negative to positive intensity. The turbulence in the suction zone is no longer seen near the 0 mm point. The large negative values of the y component is present in all of the Phase III Test Cases.

Case 15: 13-2-7.5

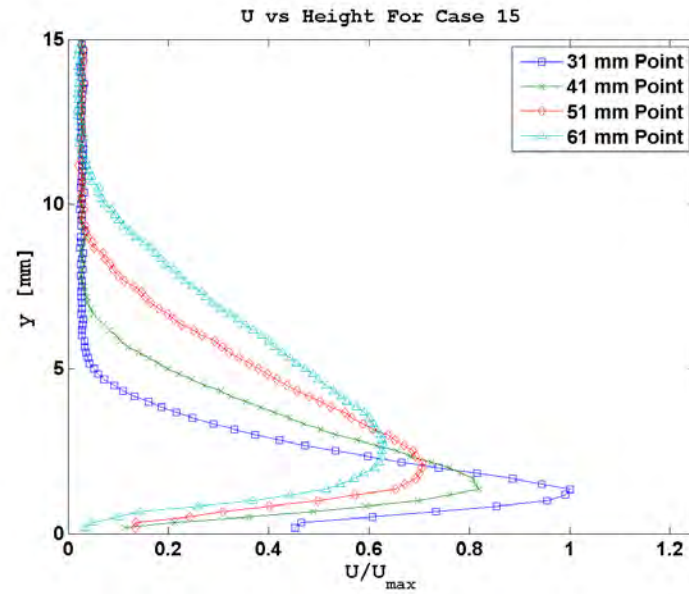


Figure B.95: Case 15: U vs Height

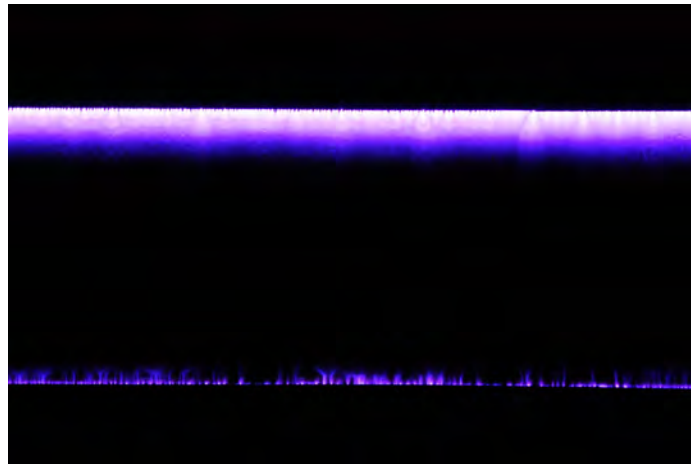
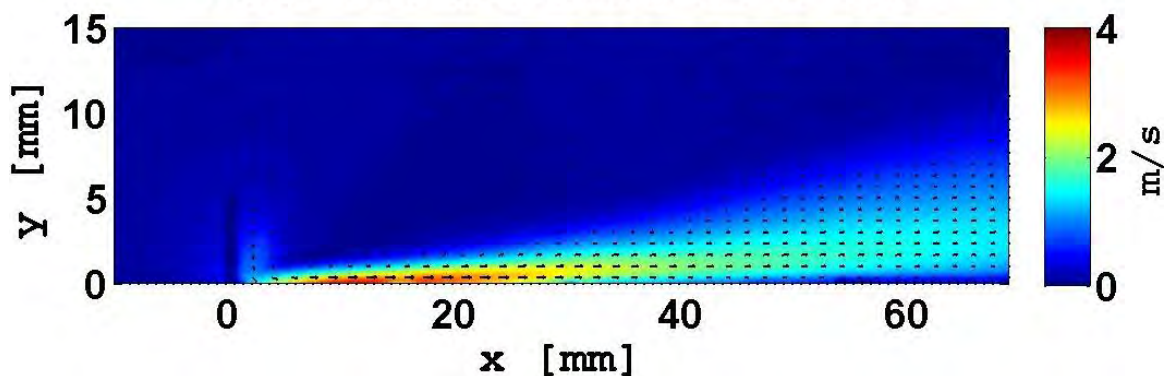


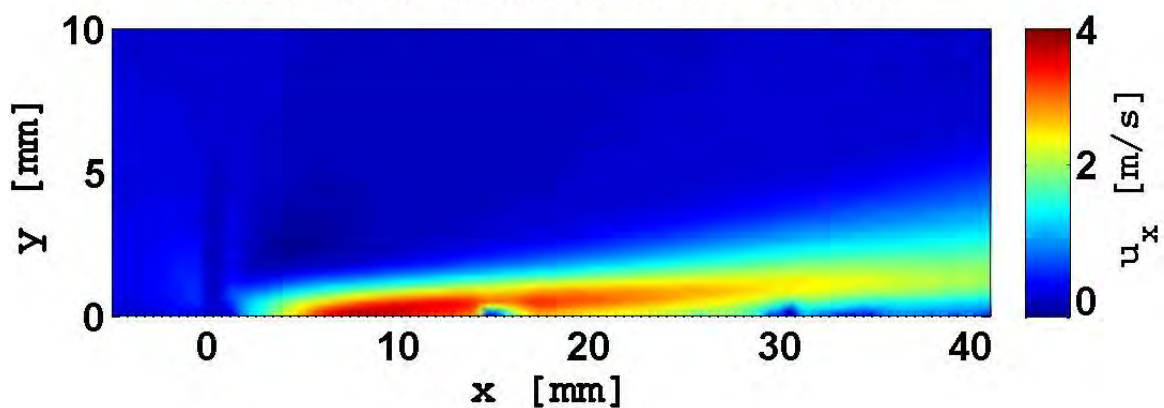
Figure B.96: Case 15: Discharge Plume

Case 15: Waveform 13-2-7.5



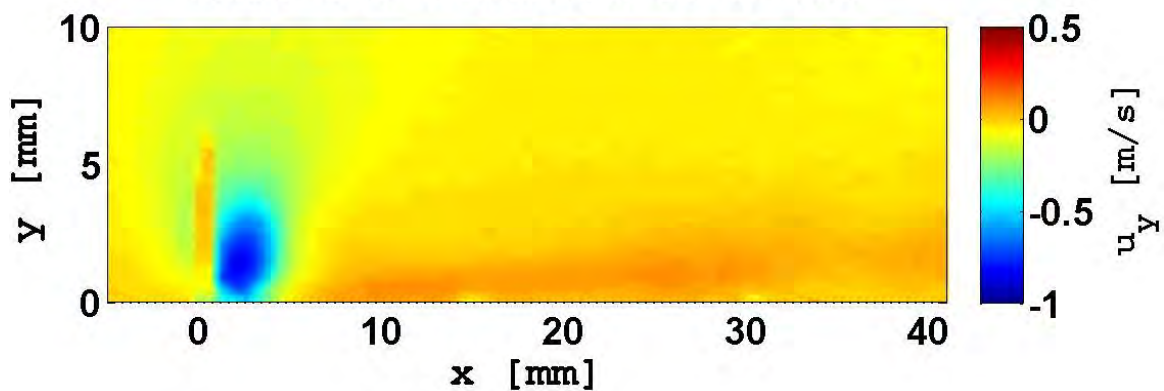
(a) Velocity Contours and Vectors

Case 15: Waveform 13-2-7.5



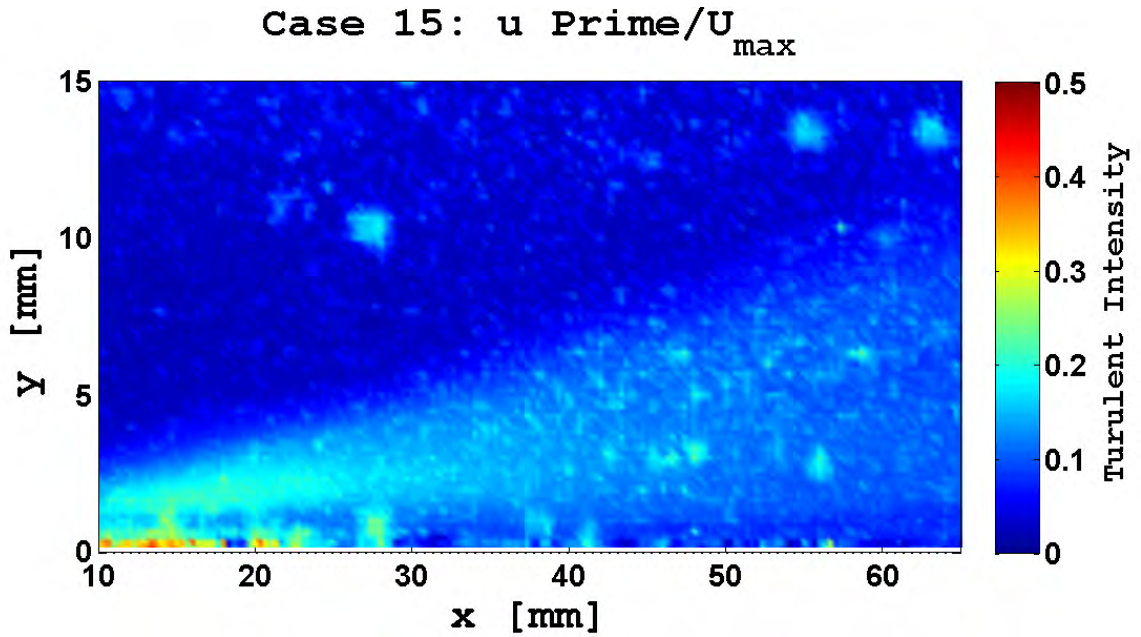
(b) x Velocity Component

Case 15: Waveform 13-2-7.5

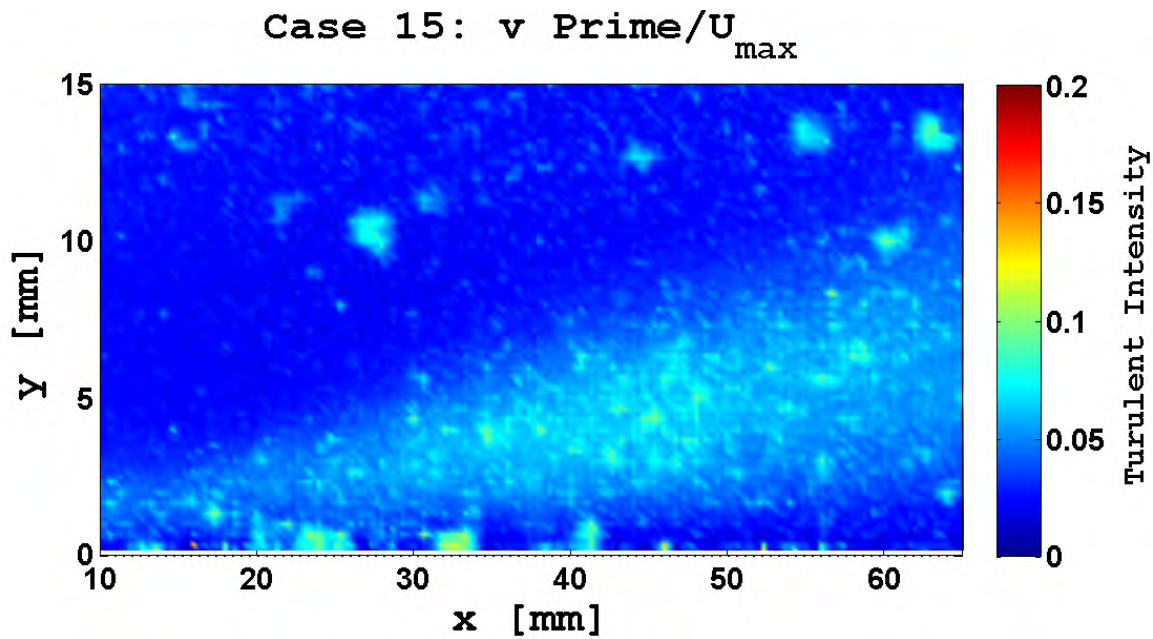


(c) y Velocity Component

Figure B.97: Case 15: Velocity Vectors and Components



(a) Turbulent Intensity: u' / U_{max}



(b) Turbulent Intensity: v' / U_{max}

Figure B.98: Case 15: Turbulent intensities. The x component intensity peaks between the exposed electrodes and the intensities in the jet outside this region are still present with a clear demarcation of the induced flow boundary and the far field region. The y component intensities are smaller and the induced jet boundary is now clearly demarcated with a marked shift from negative to positive intensity. The turbulence in the suction zone is no longer seen near the 0 mm point. The large negative values of the y component is present in all of the Phase III Test Cases.

Case 16: 13-2-9

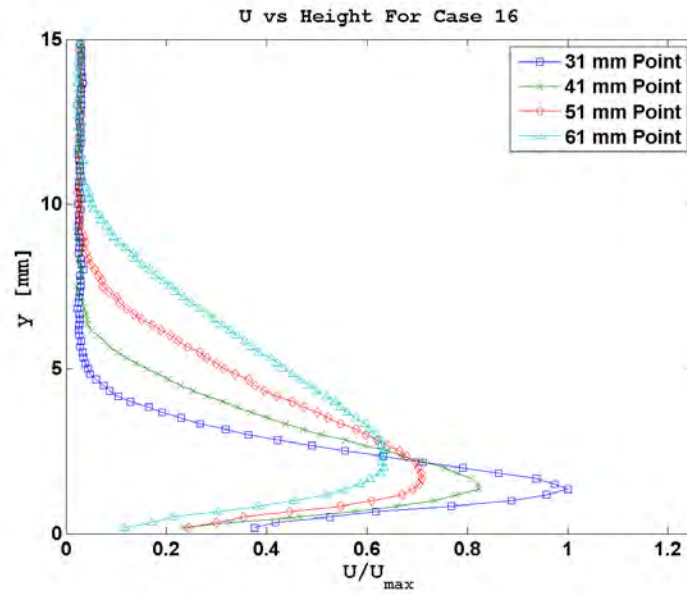


Figure B.99: Case 16: U vs Height

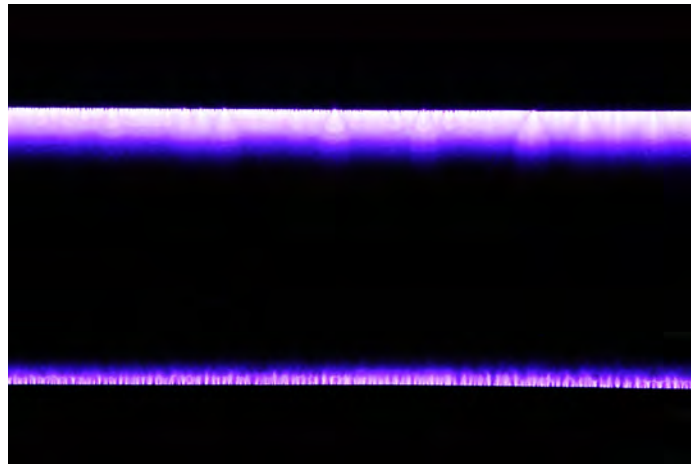


Figure B.100: Case 16: Discharge Plume

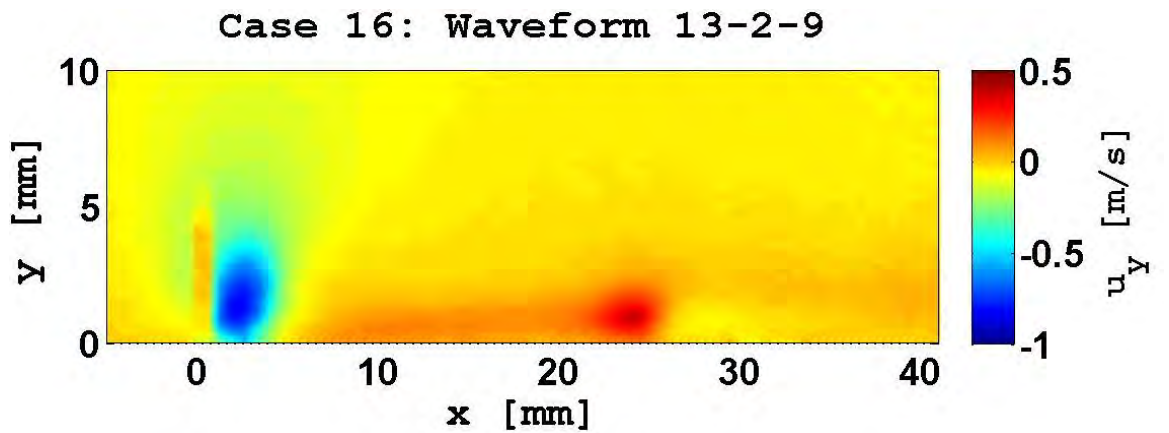
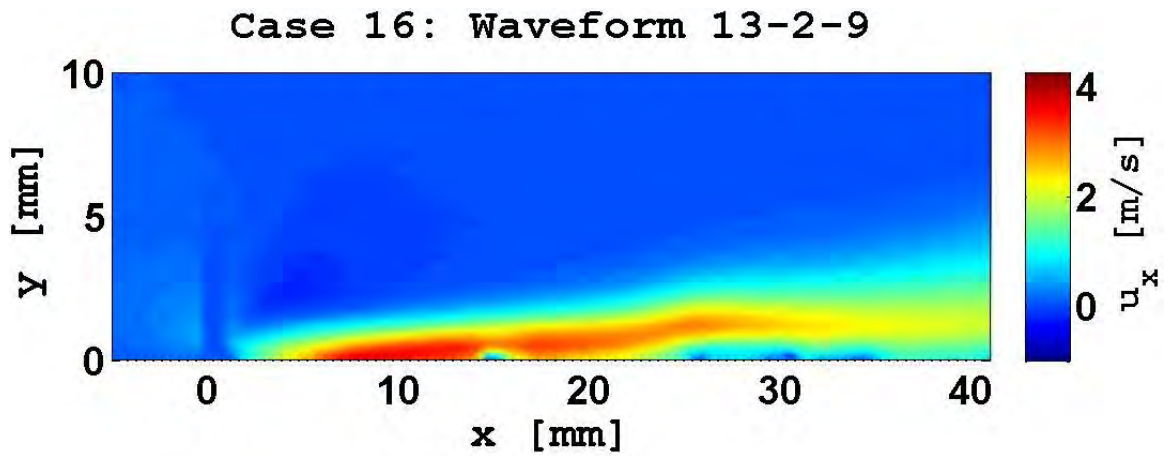
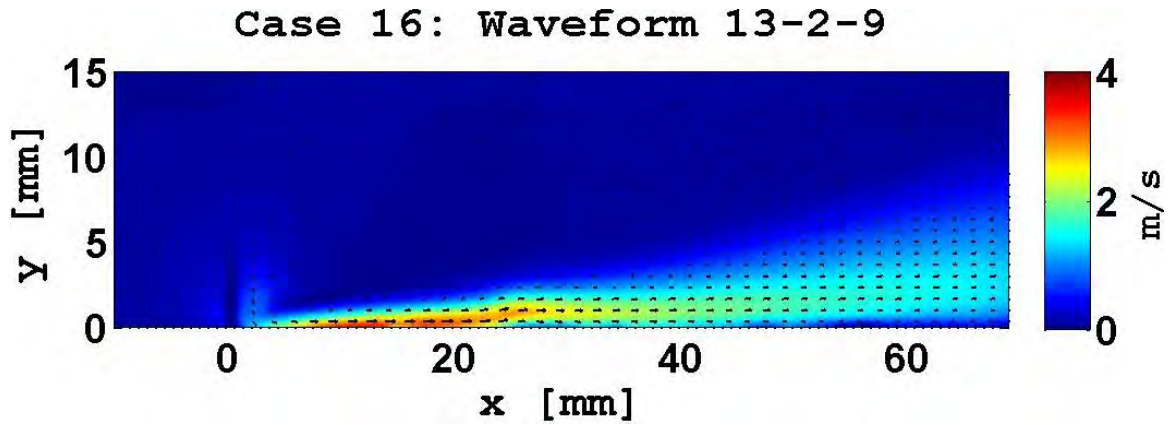
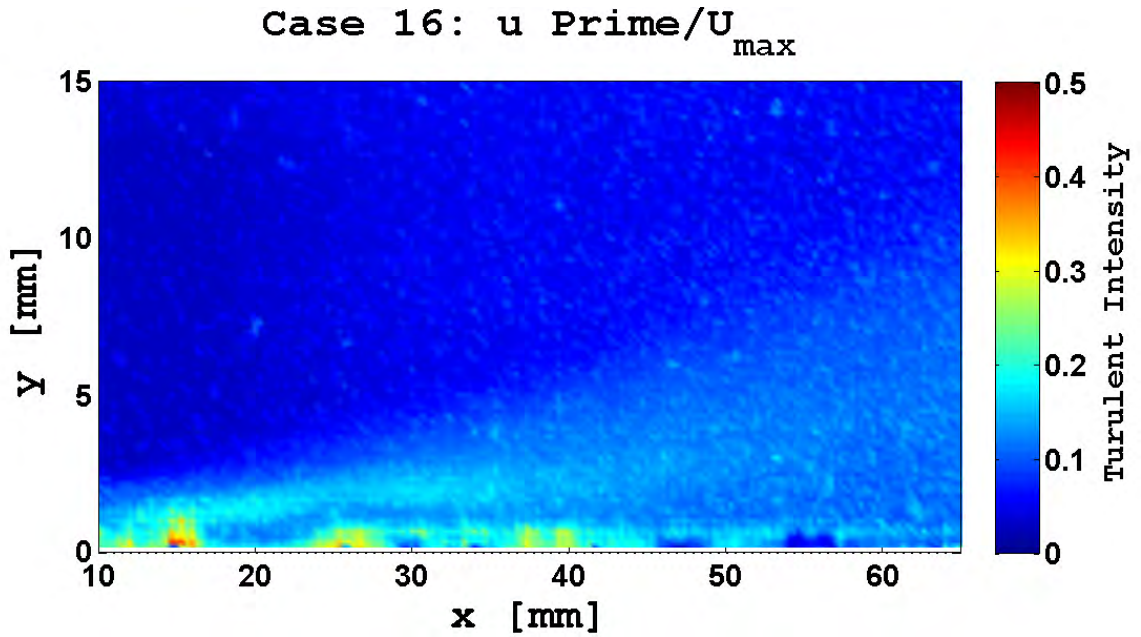
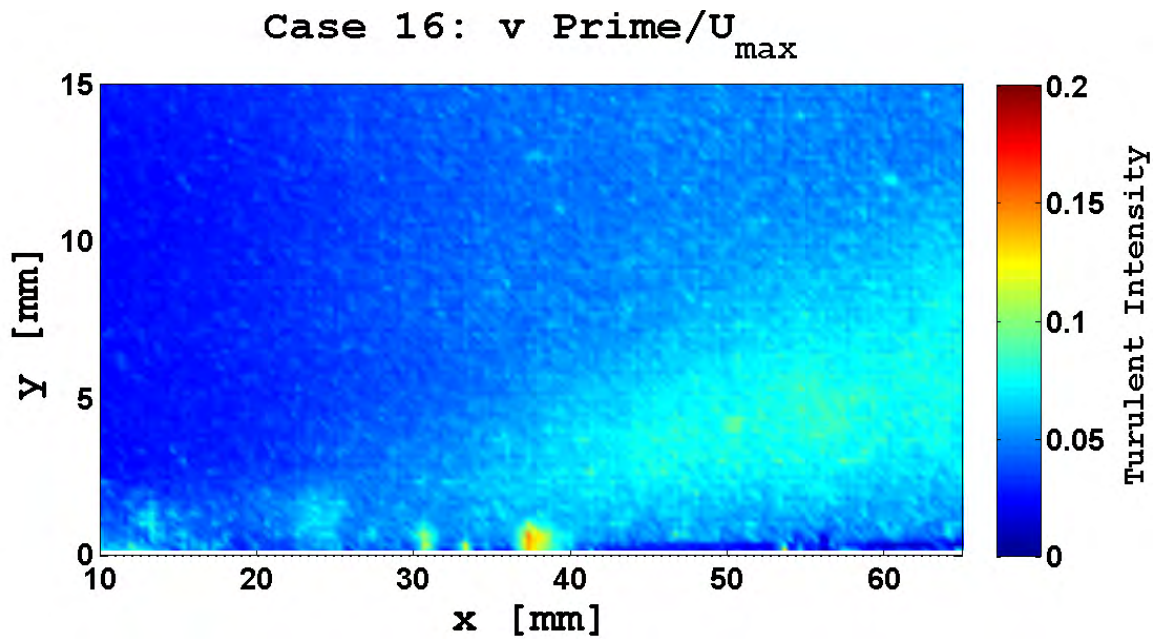


Figure B.101: Case 16: Velocity Vectors and Components



(a) Turbulent Intensity: u' / U_{max}



(b) Turbulent Intensity: v' / U_{max}

Figure B.102: Case 16: Turbulent intensities. The x component intensity peaks between the exposed electrodes and the intensities in the jet outside this region are still present with a clear demarcation of the induced flow boundary and the far field region. The y component intensities are smaller and the induced jet boundary is now clearly demarcated with a marked shift from negative to positive intensity. The turbulence in the suction zone is no longer seen near the 0 mm point. At the 31 mm point the shift in y turbulent intensities begins to mark the development of the secondary discharge.

Case 17: 13-2-11

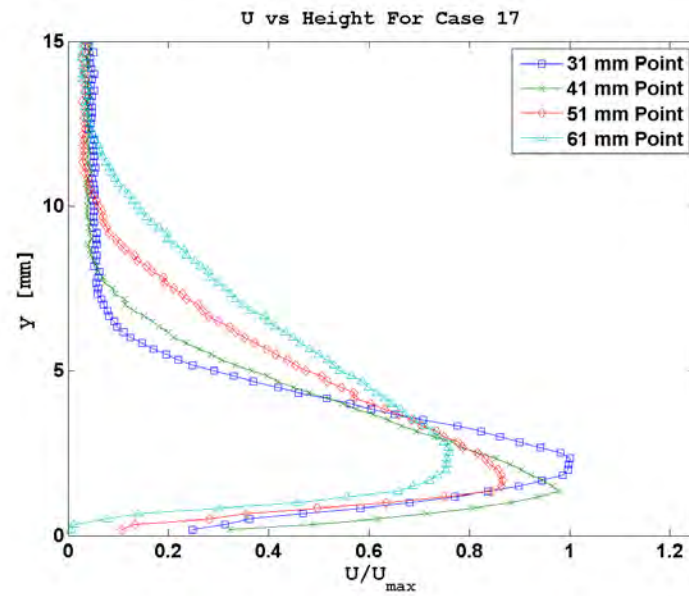


Figure B.103: Case 17: U vs Height

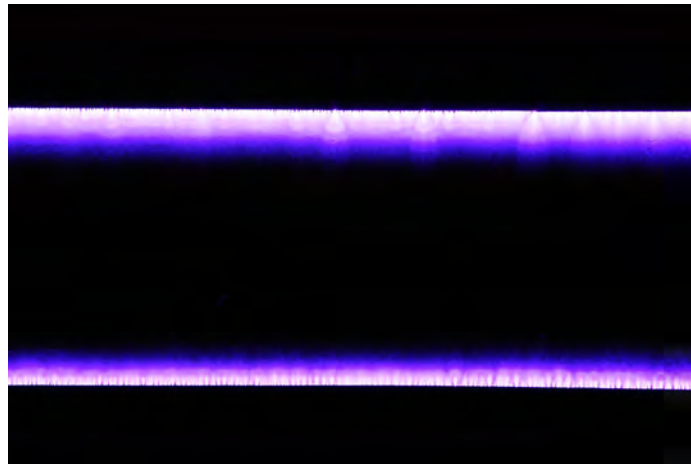
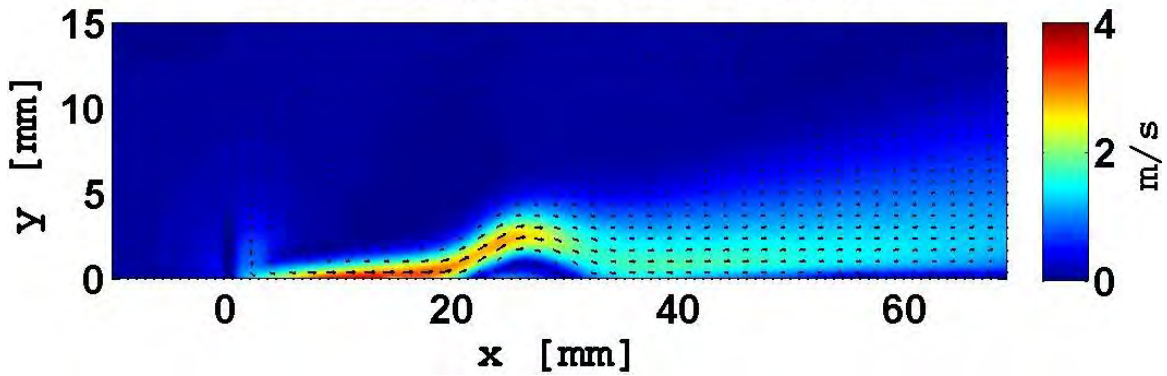


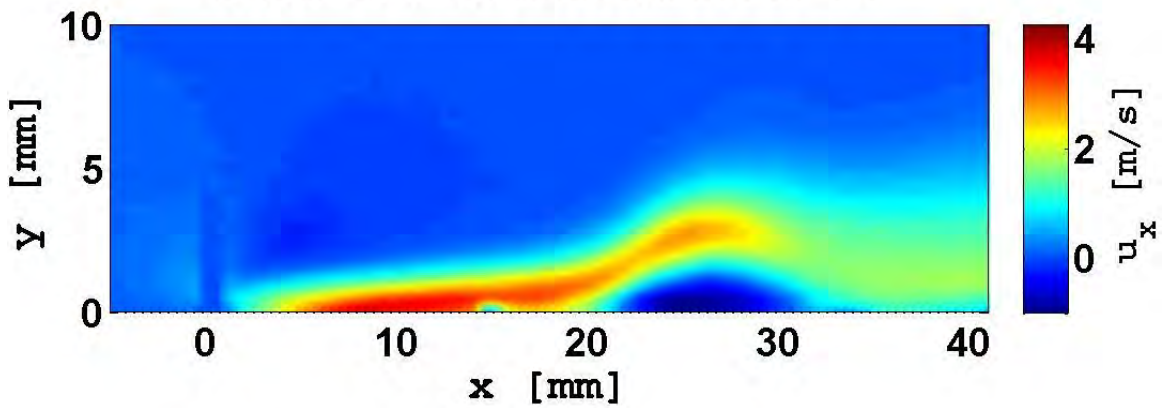
Figure B.104: Case 17: Discharge Plume

Case 17: Waveform 13-2-11



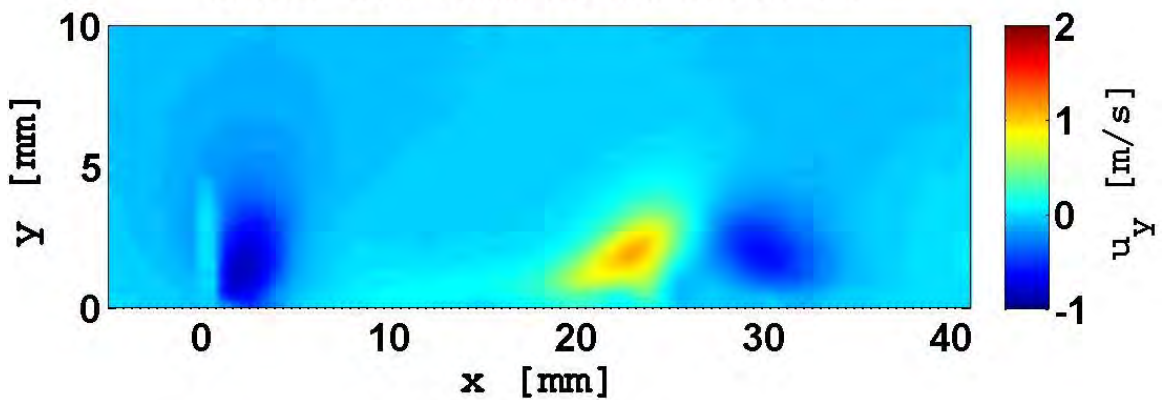
(a) Velocity Contours and Vectors

Case 17: Waveform 13-2-11



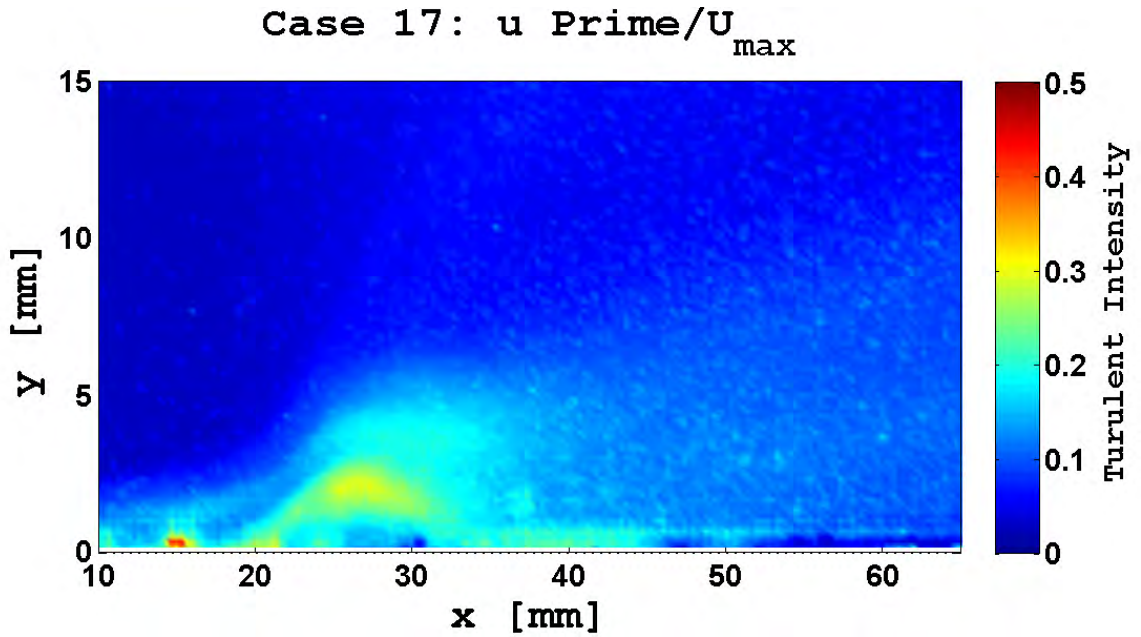
(b) x Velocity Component

Case 17: Waveform 13-2-11

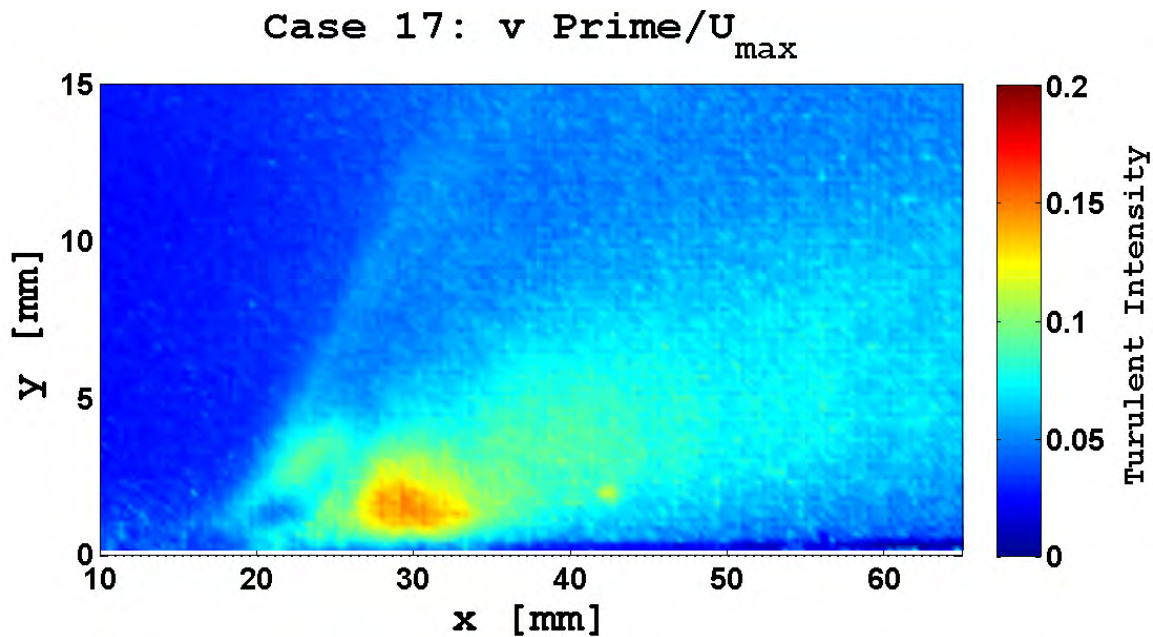


(c) y Velocity Component

Figure B.105: Case 17: Velocity Vectors and Components



(a) Turbulent Intensity: u' / U_{max}



(b) Turbulent Intensity: v' / U_{max}

Figure B.106: Case 17: Turbulent intensities. The x component intensity peaks between the exposed electrodes and the intensities in the jet outside this region are still present with a clear demarcation of the induced flow boundary and the far field region. At the 25 mm point the beginnings of the boundary layer trip can be seen. The y component intensities are smaller and the induced jet boundary is now clearly demarcated with a marked shift from negative to positive intensity. The turbulence in the suction zone is no longer seen near the 0 mm point. At the 31 mm point the shift in y turbulent intensities clearly marks the boundary layer trip caused by the secondary discharge.

Case 18: 13-2-12

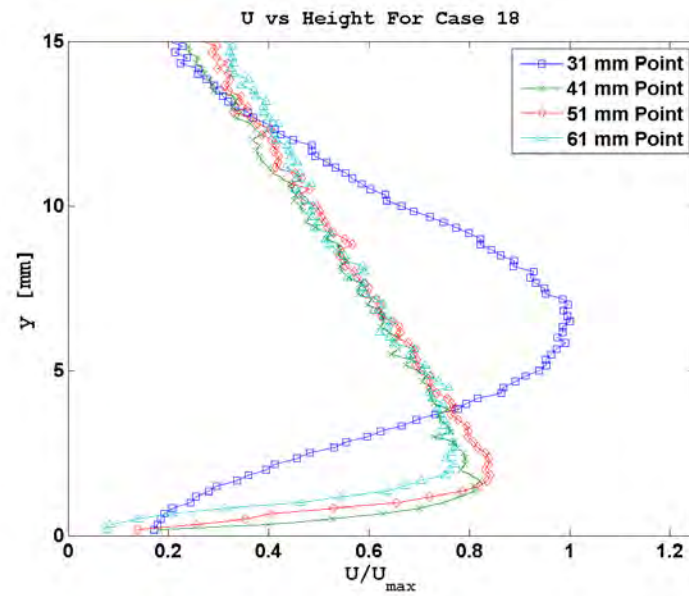


Figure B.107: Case 18: U vs Height

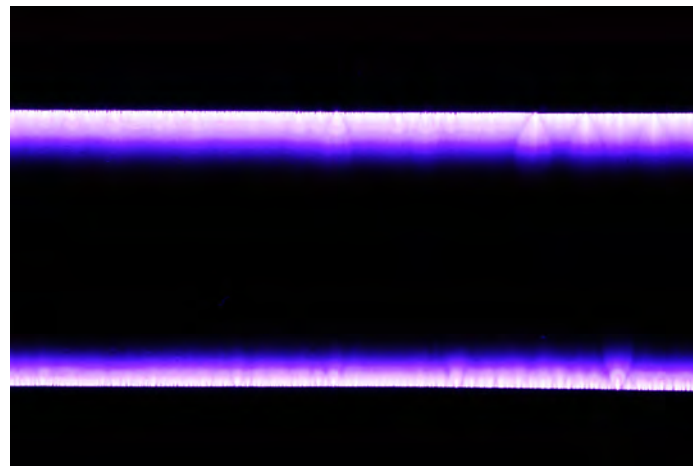
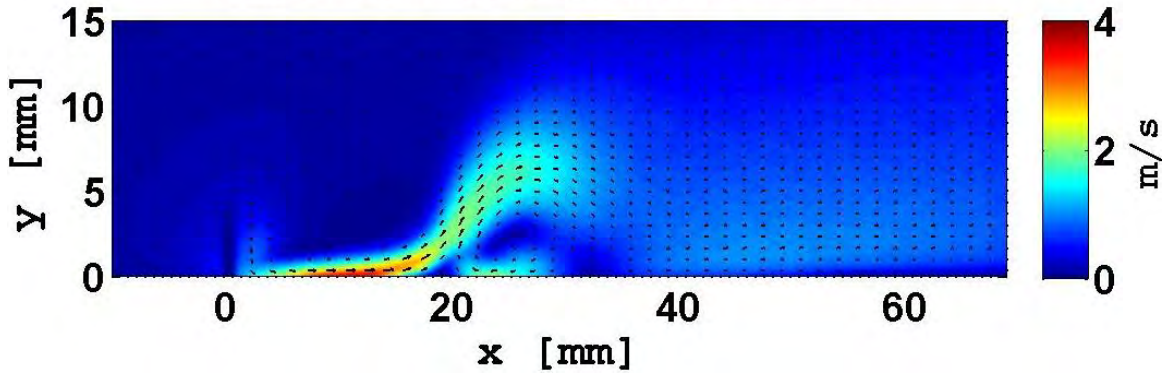


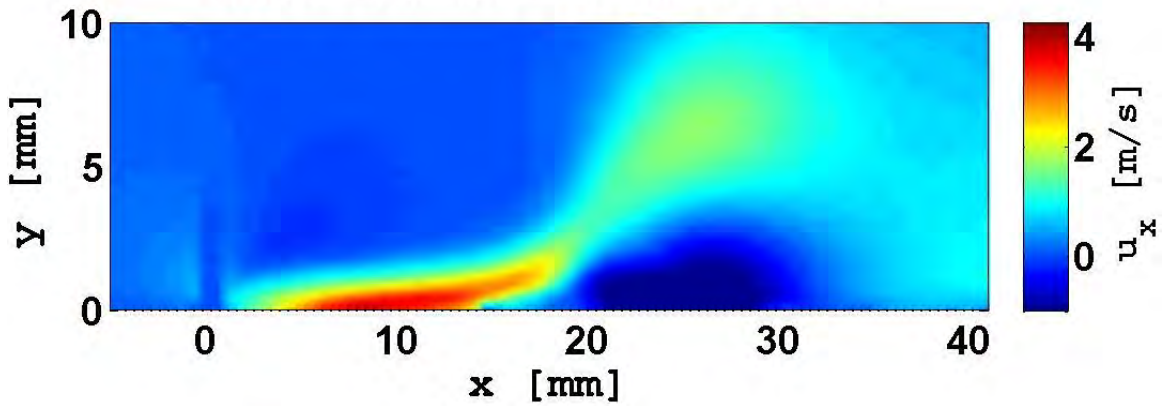
Figure B.108: Case 18: Discharge Plume

Case 18: Waveform 13-2-12



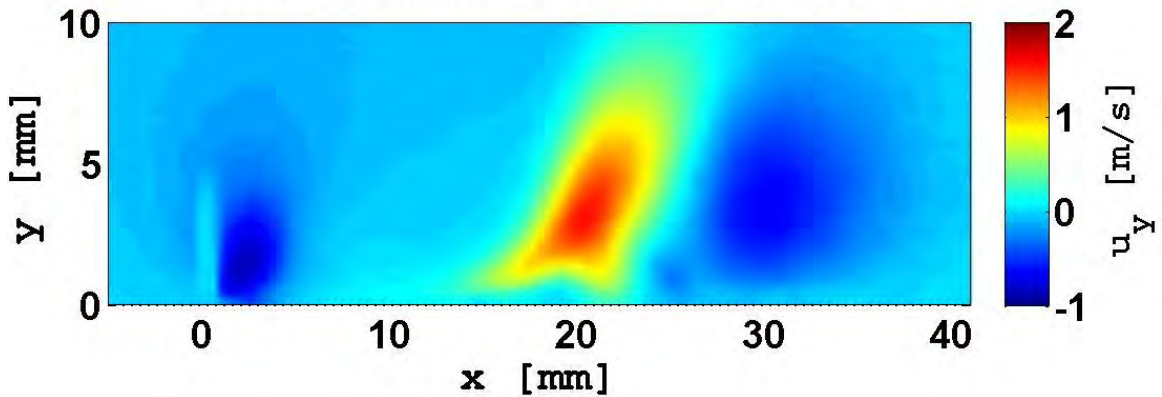
(a) Velocity Contours and Vectors

Case 18: Waveform 13-2-12



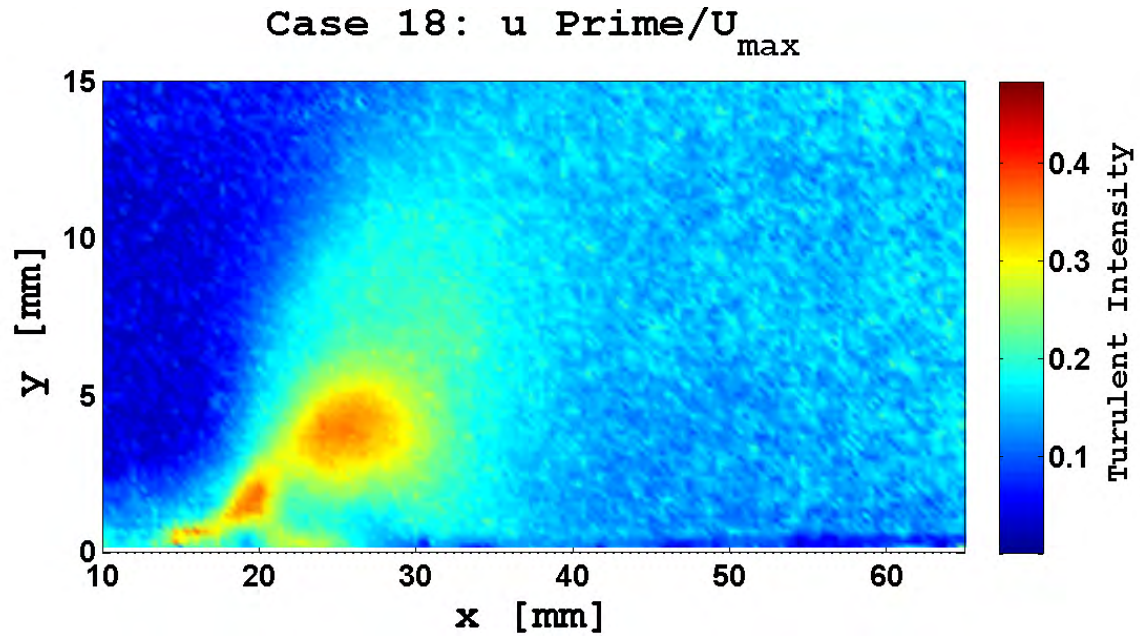
(b) x Velocity Component

Case 18: Waveform 13-2-12

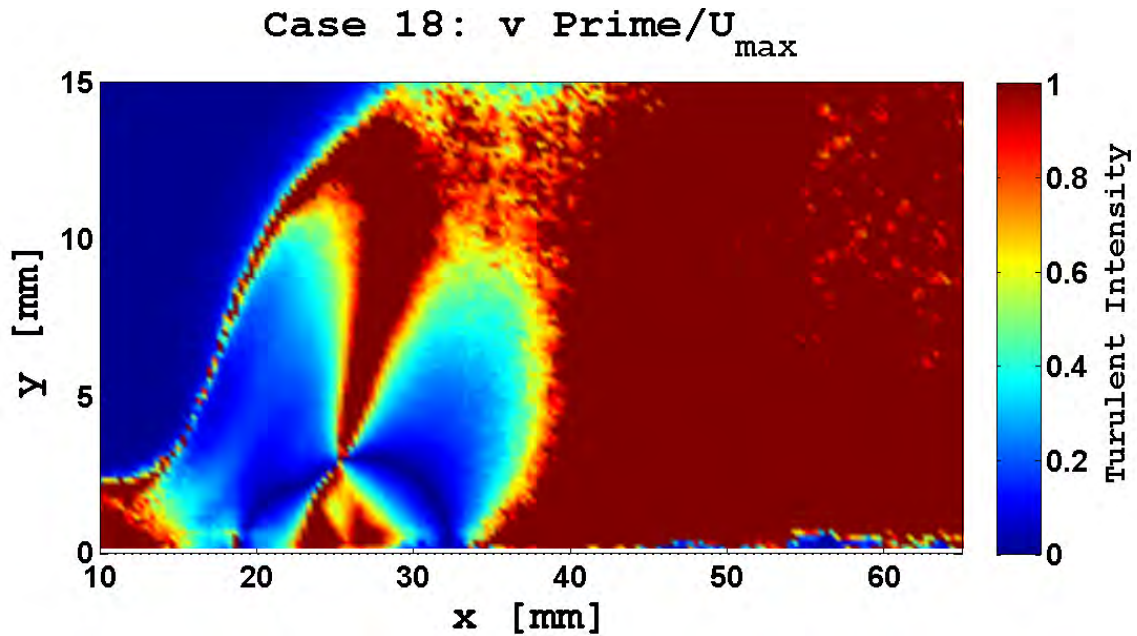


(c) y Velocity Component

Figure B.109: Case 18: Velocity Vectors and Components



(a) Turbulent Intensity: u' / U_{max}



(b) Turbulent Intensity: v' / U_{max}

Figure B.110: Case 18: Turbulent intensities. The x component intensity peaks between the exposed electrodes and there is no longer a clear demarcation of the induced flow. At the 20 mm point the angle of the induced nearly vertical wall jet can be seen. The y component intensities vary greatly and no clear pattern emerges.

Appendix C. Matlab Code

C.1 Vector Continuity Check

Listing C.1: Momentum Continuity Vector Check (Appendix3/thesisvectorchecks3.m)

```
1 %Thesis vector analysis script

clear all;
clc;

6 %Now I am going to do a rolling average over a three by three ...
  window of
  %vectors, not pixel positions. I am NOT going to validate on the ...
  boundary.
  %Each vector is going to be compared to the mean of its nearest ...
  eight
  %neighbors. If that vector is outside of a given number of ...
  standard
  %deviations, as specified by variable epsilon, it will be removed ...
  from the
11 %data set.
load 'C:\Users\Steve\Documents\MATLAB\Thesis\Results matrices\180 ...
    0 3 matrix.mat'
%
tstart = tic
bbbb = 0;

16 epsilon = 4; %Numer of standard deviations. If vector is outside...
    of this
    %it is discarded.

replaced = 0;
vector_z = 1;

21 n = length(xmat(1,1,:));

for z = 1:n
    z
26 for y = 2:254
    for x = 2:248

        x_mag_vec = [xmat((x-1),(y-1),z) xmat((x),(y-1),z) xmat((x+1)...
            ,(y-1),z)...
            xmat((x-1),(y),z) xmat((x+1),y,z) xmat((x-1),(y+1),z) ...
            xmat((x),(y+1),z)...
31 xmat((x+1),(y+1),z)];

        x_mean = nanmean(x_mag_vec);
        x_std_dev = nanstd(x_mag_vec);

36 y_mag_vec = [ymat((x-1),(y-1),z) ymat((x),(y-1),z) ymat((x+1)...
            ,(y-1),z)...
```

```

        ymat((x-1),(y),z) ymat((x+1),y,z) ymat((x-1),(y+1),z) ...
            ymat((x),(y+1),z)...
        ymat((x+1),(y+1),z)];

    y_mean = nanmean(y_mag_vec);
41    y_std_dev = nanstd(y_mag_vec);

    diff_x = abs(xmat(x,y,z) - x_mean);
    diff_y = abs(yamat(x,y,z) - y_mean);

46    x_limit = epsilon*x_std_dev;
    y_limit = epsilon*y_std_dev;

    if diff_x >= x_limit
        xmat(x,y,z) = NaN;
51    ymat(x,y,z) = NaN;
        replaced = replaced + 1; %This lets me track how many ...
            vectors
                                %I am discarding

    elseif diff_y >= y_limit
        xmat(x,y,z) = NaN;
56    ymat(x,y,z) = NaN;
        replaced = replaced + 1;
    end
end
end
end
61 end

%Now I am putting good_xmat and good_yamat into m/s from pixels/...
    frame. the
%24.1 is derived from the number of pixels per mm of my field of ...
    regard in
%the PIV setup: 24.1 = 2048/85.0.
66 x_mat_meters = xmat/24.1/(50*10^(-6))/1000;
    y_mat_meters = ymat/24.1/(50*10^(-6))/1000;
    tf = toc(tstart)

%
71 tstart = tic
    %Now save the results to a .mat file so I dont have to do this all...
        the time
    dir = 'C:\Users\Steve\Documents\MATLAB\Thesis\Results matrices\';
    filename = '180 0 3 meters matrix.mat';
    save([dir filename], 'x_mat_meters', 'y_mat_meters')
76 tf = toc(tstart)
%
    clear xmat ymat x_mag_vec y_mag_vec
%
    results = zeros(249,255,5);
81
    %Now I am creating a results matrix that will allow for easy ...
        comparison

```

```

    %between test cases and faster plotting then plotting above meters...
    matrix.
    %results(i,i,1) = x mean vel.
    %results(i,i,2) = x std dev.
86 %results(i,i,3) = y mean vel.
    %results(i,i,4) = y std vel.
    %results(i,i,5) = vector magnitude.

    %This script cascades through the vector map taking the standard ...
    deviation
91 %and average at all points in the vector map.
    for count = 1:255
        for count2 = 1:249
            results(count,count2,1) = nanmean(x_mat_meters(count,...
                count2,:));
            results(count,count2,2) = nanstd(x_mat_meters(count,count2...
                ,:));
96         results(count,count2,3) = nanmean(y_mat_meters(count,...
                count2,:));
            results(count,count2,4) = nanstd(y_mat_meters(count,count2...
                ,:));
        end
    end
end

101 results(:,:,5) = sqrt(results(:,:,1).^2 + results(:,:,3).^2);

tstart = tic
%Now save the results to a .mat file so I dont have to do this all...
the time
dir = 'C:\Users\Steve\Documents\MATLAB\Thesis\Results matrices\';
106 filename = '180 0 3 results matrix.mat';
save([dir filename],'results')
tf = toc(tstart)

```

Bibliography

1. Klein, T., *Macroscopic Computational Model of Dielectric Barrier Discharge Plasma Actuators*, AFIT/GAP/ENP/06-07, Master's thesis, School of Engineering and Management, Air Force Institute of Technology, Wright-Patterson AFB OH, February 2006.
2. Corke, T., Post, M., and Orlov, D., "Single Dielectric Barrier Discharge Plasma Enhanced Aerodynamics: Physics, Modeling and Applications," *Progress In Aerospace Sciences*, Vol. 43, 2007, pp. 193–217.
3. Orlov, D., Font, G., and Edelstein, D., "Characterization of Discharge Modes of Plasma Actuators," *American Institute of Aeronautics and Astronautics Journal*, Vol. 46, No. 12, December 2008.
4. Abe, T., Takizawa, Y., Sato, S., and Kimura, N., "Experimental Study for Momentum Transfer in a Dielectric Barrier Discharge Plasma Actuator," *American Institute of Aeronautics and Astronautics Journal*, Vol. 46, No. 9, September 2008.
5. Abe, T. and Takagaki, M., "Momentum Coupling and Flow Induction in a DBD Plasma Actuator," AIAA Paper 2009-4068, 2009.
6. Balcer, B., Franke, M., and Rivir, R., "Effects Of Plasma Induced Velocity On Boundary Layer Flow," AIAA Paper 2006-875, 2006.
7. Corke, T., Jumper Jr., E., Post, M., and Orlov, D., "Application of Weakly-Ionized Plasma As Wing Flow-Control Devices," AIAA Paper 2002-0350, 2002.
8. Corke, T. and Mertz, B., "Plasma Flow Control Optimized Airfoil," AIAA Paper 2006-1208, 2006.
9. Corke, T. and Post, M., "Overview of Plasma Flow Control: Concepts, Optimization, and Application," AIAA Paper 2005-563, 2005.
10. Enloe, C., McLaughlin, T., VanDyken, R., and Fischer, J., "Plasma Structure in the Aerodynamic Plasma Actuator," Tech. rep., 2004.
11. Enloe, C., McLaughlin, T., VanDyken, R., Kachner, K., Jumper, E., and Corke, T., "Mechanisms and Responses of a Single Dielectric Barrier Plasma Discharge," AIAA Paper 2003-1021, 2003.
12. Enloe, C., McHarg, M., Font, G., and McLaughlin, T., "Plasma-induced Force and Self-induced Drag in the Dielectric Barrier Discharge Aerodynamic Plasma Actuator," AIAA Paper 2009-1622, 2009.
13. He, C. and Corke, T., "Plasma Flaps and Slats: An Application of Weakly Ionized Plasma Actuators," *Journal of Aircraft*, Vol. 46, No. 3, May-June 2009.
14. Jayaraman, B., Lian, Y., and Shyy, W., "Low-Reynolds Number Flow Control Using Dielectric Barrier Discharge Actuators," AIAA Paper 2010-3974, 2007.

15. Likhanskii, A., Shneider, M., Opaits, D., Miles, R., and Macheret, S., "Limitations of the DBD Effects on the External Flow," AIAA Paper 2010-470, 2010.
16. Yamada, S., Shibata, K., Ishikawa, H., Honami, S., and Motosuke, M., "Flow Behavior Behind a Circular Cylinder by DBD Plasma Actuators in Low Reynolds Number," AIAA Paper 2010-549, 2010.
17. Pavon, S., *Interaction Between a Surface Dielectric Barrier Discharge and Transonic Airflow*, Ph.D. thesis, Ecole Polytechnique Federale de Lusanne, 2008.
18. Charles, C., *Computational Modeling of the Dielectric Barrier Discharge DBD Device for Aeronautical Applications*, Master's thesis, School of Engineering and Management, Air Force Institute of Technology, Wright-Patterson AFB OH, June 2006.
19. Fridman, A. and Kennedy, L., *Plasma Physics and Engineering*, Taylor and Francis, New York, New York, 2004.
20. Stanfield II, S., *A Spectroscopic Investigation Of A Surface-Discharge-Mode, Dielectric Barrier Discharge*, Ph.D. thesis, School of Graduate Studies, Wright State University, Dayton, OH, September 2009.
21. Barckmann, K., Grundmann, S., Tropea, C., and Kriegseis, J., "Dielectric-Barrier Discharge Plasmas for Flow Control at Higher Mach Numbers," AIAA Paper 2010-4258, 2010.
22. Poggie, J., Tilmann, C., Flick, P., Silkey, J., Osborne, B., Ervin, G., and et. al., "Closed-Loop Stall Control on a Morphing Airfoil Using Hot-Film Sensors and DBD Actuators," AIAA Paper 2010-547, 2010.
23. Takashima, K., Zouzou, N., Mizuno, A., and Touchard, G., "Generation of Extended Surface Barrier Discharge on Dielectric Surface - Electrical Properties," *International Journal of Plasma Environmental Science & Technology*, Vol. 1, No. 1, March 2007.
24. Guo, S., Simon, T., Ernie, D., and Kortshagen, U., "Separation Control Using DBD Plasma Actuators: Thrust Enhancement Studies," AIAA Paper 2010-1090, 2010.
25. Huba, J. D., *NRL Plasma Formulary*, Naval Research Laboratory Publication, Washington, D.C. 20375, 2006.
26. Enloe, C., Font, G., McLaughlin, T., and Orlov, D., "Surface Potential and Longitudinal Electric Field Measurements in the Aerodynamic Plasma Actuator," *AIAA Journal*, Vol. 46, No. 11, November 2008, pp. 2730-2740.
27. Enloe, C., McLaughlin, T., Gregory, J., Medina, R., and Miller, W., "Surface Potential and Electric Field Structure in the Aerodynamic Plasma Actuator," AIAA Paper 2008-1103, 2008.

28. Corke, T., Post, M., and Orlov, D., "Single-Dielectric Barrier Discharge Plasma Enhanced Aerodynamics: Concepts, Optimization, and Applications," *Journal of Propulsion and Power*, Vol. 5, No. 24, September-October 2008.
29. VanDyken, R., McLaughlin, T., and Enloe, C., "Parametric Investigations Of A Single Dielectric Barrier Plasma Actuator," Tech. rep., 2004.
30. Zito, J., Arnold, D., Durscher, R., and Roy, S., "Investigation of Impedance Characteristics and Power Delivery for Dielectric Barrier Discharge Plasma Actuators," AIAA Paper 2010-964, 2010.
31. Thomas, F., Corke, T., Iqbal, M., Kozlov, A., and Schatzman, D., "Optimization of Dielectric Barrier Discharge Plasma Actuators for Active Aerodynamic Flow Control," *American Institute of Aeronautics and Astronautics Journal*, Vol. 47, No. 9, September 2009.
32. Hale, C., Erfani, R., and Kontis, K., "Plasma Actuators with Multiple Encapsulated Electrodes to Influence the Induced Velocity," AIAA Paper 2010-1223, 2010.
33. Hale, C., Erfani, R., and Kontis, K., "Multiple Encapsulated Electrode Plasma Actuators to Influence the Induced Velocity: Further Configurations," AIAA Paper 2010-5106, 2010.
34. Enloe, C., McLaughlin, T., Font, G., and Baughn, J., "Frequency Effects on the Efficiency of the Aerodynamic Plasma Actuator," AIAA Paper 2006-166, 2006.
35. Enloe, C., McLaughlin, T., VanDyken, R., Kachner, K., Jumper Jr., E., Corke, T., Post, M., and Haddad, O., "Mechanisms and Responses of a Single Dielectric Barrier Plasma Discharge: Geometric Effects," *American Institute of Aeronautics and Astronautics Journal*, Vol. 42, No. 3, March 2004.
36. Durscher, R. and Roy, S., "Novel Multi-Barrier Plasma Actuators for Increased Thrust," AIAA Paper 2010-965, 2010.
37. Likhanskii, A., Shneider, M., Macheret, S., and Miles, R., "Optimization of Dielectric Barrier Discharge Plasma Actuators Driven By Repetitive Nanosecond Pulses," AIAA Paper 2007-644, 2007.
38. Opaits, D., Neretti, G., Zaidi, S., Shneider, M., Miles, R., Likhanskii, A., and Macheret, S., "DBD Plasma Actuators Driven by a Combination of Low Frequency Bias Voltage and Nanosecond Pulses," AIAA Paper 2008-1372, 2008.
39. Opaits, D., Zaidi, S., Shneider, M., Miles, R., Likhanskii, A., and Macheret, S., "Improving Thrust by Suppressing CHarge Build-up in Pulsed DBD Plasma Actuators," AIAA Paper 2009-487, 2009.
40. Font, G., Enloe, C., Newcomb, J., Vasso, A., and McLaughlin, T., "Effect of Oxygen Content on the Behavior of the Dielectric Barrier Discharge Aerodynamic Actuator," AIAA Paper 2009-4285, 2009.

41. Humble, R., Henry, G., and Larson, W., *Space Propulsion Analysis and Design*, McGraw Hill Companies, New York, New York, 1995.
42. Boeuf, J. P. and Pitchford, L. C., "Electrohydrodynamic Force and Aerodynamic Flow Acceleration in Surface Dielectric Barrier Discharge," *Journal of Applied Physics*, Vol. 97, 2005.
43. Tavoularis, S., *Measurement in Fluid Mechanics*, Cambridge University Press, New York, New York, 2009.
44. Post, M. and Corke, T., "Separation Control on High Angle of Attack Airfoil Using Plasma Actuators," AIAA Paper 2003-1024, 2003.
45. Anderson, R. and Roy, S., "Preliminary Experiments of Barrier Discharge Plasma Actuators using Dry and Humid Air," AIAA Paper 2006-369, 2006.
46. Porter, C., Abbas, A., Cohen, K., McLaughlin, T., and Enloe, C., "Spatially Distributed Forcing and Jet Vectoring with a Plasma Actuator," *AIAA Journal*, Vol. 47, No. 6, June 2009.
47. Huimin, S., Min, J., Hua, L., and Yun, W., "Experimental Investigation of the Plasma Aerodynamic Actuation Generated by Nanosecond-pulse Sliding Discharge," Third international conference on measuring technology and mechatronics automation, 2011.
48. Raffel, M., Willert, C., and Kompenhans, J., *Particle Image Velocimetry: A Practical Guide*, Springer, 1998.
49. Forte, M., Jolibois, J., Pons, J., Moreau, E., Touchard, G., and Cazalens, M., "Optimization of a Dielectric Barrier Discharge Actuator by Stationary and Non-stationary Measurements of the Induced Flow Velocity - Application to Airflow Control," *Experimental Fluids*, Vol. 43, August 2007, pp. 917-928.
50. de La Harpe, J., *Performance Characterization of a Novel Plasma Thruster to Provide a Revolutionary Operationally Responsive Space Capability With Micro and Nano-Satellites*, Master's thesis, School of Engineering and Management, Air Force Institute of Technology, Wright-Patterson AFB OH, March 2011.
51. Fleming, S., Bolitho, M., and Jacob, J., "Separation Control Using Vectoring Plasma Actuators," AIAA Paper 2010-468, 2010.

Vita

LCDR Steven D. Seney Jr attended Worcester Polytechnic Institute under the Naval Reserve Officers' Training Corps scholarship program graduating with a Bachelor of Science degree in Mechanical Engineering in 2001. He was commissioned an Ensign in the United States Navy and was selected for Naval Aviator training, earning his "Wings of Gold" in 2002.

Upon completion of flight school, he commenced a tour flying the P-3C Orion with VP-45 in Jacksonville, FL completing a deployment split between Africa and the Mediterranean Sea and a second deployment split between Japan and Iraq. Following this tour he reported to Naval Personnel Command for duty as a Rating Assignments Officer overseeing of the career progression and detailing of 40,000 enlisted aviation sailors. During this tour LCDR Seney completed an IA assignment as an embedded training team member serving with the Afghan National Army in Kandahar, Afghanistan.

In 2008 LCDR Seney was selected for duty as an Aviation Engineering Duty Officer (AEDO) and given orders to report to the Air Force Institute of Technology. Following his graduation from AFIT he will be reporting PEO NAVAIR in Patuxent River Maryland for a tour as IPTE Assistant Lead for the BAMS UAV Program.

Permanent address: 2950 Hobson Way
Air Force Institute of Technology
Wright-Patterson AFB, OH 45433

REPORT DOCUMENTATION PAGE			Form Approved OMB No. 0704-0188	
The public reporting burden for this collection of information is estimated to average 1 hour per response, including the time for reviewing instructions, searching existing data sources, gathering and maintaining the data needed, and completing and reviewing the collection of information. Send comments regarding this burden estimate or any other aspect of this collection of information, including suggestions for reducing this burden to Department of Defense, Washington Headquarters Services, Directorate for Information Operations and Reports (0704-0188), 1215 Jefferson Davis Highway, Suite 1204, Arlington, VA 22202-4302. Respondents should be aware that notwithstanding any other provision of law, no person shall be subject to any penalty for failing to comply with a collection of information if it does not display a currently valid OMB control number. PLEASE DO NOT RETURN YOUR FORM TO THE ABOVE ADDRESS.				
1. REPORT DATE (DD-MM-YYYY) 15-09-2011		2. REPORT TYPE Master's Thesis		3. DATES COVERED (From — To) Aug 2009 – Sep 2011
4. TITLE AND SUBTITLE Increasing The Performance of a Sliding Discharge Actuator Through The Application of Multiple Potentials			5a. CONTRACT NUMBER	
			5b. GRANT NUMBER	
			5c. PROGRAM ELEMENT NUMBER	
6. AUTHOR(S) LCDR Steven D Seney Jr			5d. PROJECT NUMBER	
			5e. TASK NUMBER	
			5f. WORK UNIT NUMBER	
7. PERFORMING ORGANIZATION NAME(S) AND ADDRESS(ES) Air Force Institute of Technology Graduate School of Engineering and Management (AFIT/ENY) 2950 Hobson Way WPAFB OH 45433-7765			8. PERFORMING ORGANIZATION REPORT NUMBER AFIT/GA/GAE/ENY/11-S01	
9. SPONSORING / MONITORING AGENCY NAME(S) AND ADDRESS(ES) Dr. John Schmisser Air Force Office of Scientific Rresearch 875 North Randolph St, Suite 325 Rm 3112 Arlington, VA 22203 Tele: (703) 696-6962 DSN 426-6962 FAX (703) 696-7320 Email: john.schmisser@afosr.af.mil			10. SPONSOR/MONITOR'S ACRONYM(S) AFOSR	
			11. SPONSOR/MONITOR'S REPORT NUMBER(S)	
12. DISTRIBUTION / AVAILABILITY STATEMENT APPROVED FOR PUBLIC RELEASE; DISTRIBUTION UNLIMITED				
13. SUPPLEMENTARY NOTES This material is declared a work of the U.S. Government and is not subject to copyright protection in the United States.				
14. ABSTRACT <p>This work encompasses a comparison between a sliding discharge DBD actuator with grounded and AC biased sliding electrode driven at kHz frequency. The induced velocity in the bulk flow was recorded with PIV and compared for multiple potential splits between two test configurations and a baseline sliding discharge actuator over three test phases. In the first test phase, varying potential splits were examined between the primary and secondary electrode with the sliding electrode grounded. The potential splits induced a thicker induced jet than the baseline case with similar peak velocities on the order of 1.25 m/s at the 61 mm test point. The second test phase encompassed an examination of the effects of varying the potentials applied to the primary and sliding discharge electrode with the potential difference between the electrodes maintained at 15 kV. Induced velocities ranged from a low of 0.17 m/s to a high of 1.87 m/s. The data suggests that the induced velocity is primarily dependent upon the primary to secondary electrode potential split. Phase three examined the effect of applying an AC potential to the sliding discharge electrode. The induced jet decreases in height and the vertical velocity component decreases with an increasing bias on the sliding discharge electrode. Peak jet velocity increases with increasing bias on the sliding electrode until such bias reaches the ionization thresh-hold of the bulk flow.</p>				
15. SUBJECT TERMS DBD, plasma actuator, PIV				
16. SECURITY CLASSIFICATION OF:			17. LIMITATION OF ABSTRACT UU	18. NUMBER OF PAGES 209
a. REPORT U	b. ABSTRACT U	c. THIS PAGE U		
			19b. TELEPHONE NUMBER (Include Area Code) (937)255-3636, ext	